Knowledge Based Process Development of Bobbin Tool Friction Stir Welding

(Vom Promotionsausschuss der Technischen Universität Hamburg-Harburg als Dissertation angenommene Arbeit))

J. Hilgert

wissen
schafft
nutzen

Helmholtz-Zentrum
Geesthacht
Zentrum für Material- und Küstenforschung

Knowledge Based Process Development of Bobbin Tool Friction Stir Welding

(Vom Promotionsausschuss der Technischen Universität Hamburg-Harburg als Dissertation angenommene Arbeit)

J. Hilgert

Knowledge Based Process Development of Bobbin Tool Friction Stir Welding

(Vom Promotionsausschuss der Technischen Universität Hamburg-Harburg als Dissertation angenommene Arbeit)

Jakob Hilgert

173 pages with 92 figures and 15 tables

Abstract

Over the last twenty years Friction Stir Welding (FSW) has proven to be a very promising new joining technique. Especially high strength aluminium alloys can be welded with large advantages as compared to conventional fusion welding processes. For some joint configurations and desired applications bobbin tool welding is a process variant that can circumvent limitations arising from the high process forces in conventional tool FSW. As bobbin tools are highly mechanically loaded, in-depth understanding of the evolution of temperatures and forces is desirable to avoid tool failure and extend the range of applicable process parameters together with overall productivity. Up to now the process and tool development has been mostly empirical. A transition to a science based approach is highly necessary.

The work presented here was conducted to establish a set of numerical models that can be used in process development of bobbin tool FSW. The first model covers the transient temperature fields that are needed as input for any further model. The material flow model predicts the acting forces and shear layer shape. Finally the mechanical loads on the tool are predicted by a mechanical model. The models predict very time and position dependent conditions for the investigated specimen sizes and welding speeds. This explains the instability that can be observed experimentally under certain conditions. A control strategy is needed to produce sound welds at reasonable productivity. A versatile controller has been successfully designed, implemented and tested as part of the work presented here.

The models are applied to the existing tools and validated experimentally. A novel tool design is developed based on the experimental results and further improved using the models predictions. Finally the new tool design is tested. The results have shown that the productivity of the process as well as the joint quality could be significantly improved. The knowledge about the thermal history and extent of plastic deformation gained from the process model is a valuable input to the understanding of microstructure formation and the development of residual stress fields.

Wissensbasierte Prozessentwicklung des Rührreibschweißens mit Bobbin Tool

Zusammenfassung

Das Rührreibschweißen hat sich in den letzten 20 Jahren als vielversprechender Fügeprozess herausgestellt. Insbesondere beim Fügen hochfester Aluminium Legierungen zeigen sich große Vorteile gegenüber konventionellen Schweißverfahren. Die Prozessvariante des Bobbin Werkzeuges (Zweischulterwerkzeug) kann in einigen Fällen genutzt werden um die Einschränkungen des konventionellen Verfahrens durch übermäßige Prozesskräfte zu umgehen. Da Bobbin Werkzeuge mechanisch sehr hoch belastet sind sollten die wirkenden Kräfte und Temperaturen möglichst exakt bekannt sein um die Zerstörung der Werkzeuge zu verhindern und das Prozessfenster und die Produktivität zu optimieren. Bis jetzt basierte die Prozess- und Werkzeugentwicklung auf empirischen Erwägungen. Ein Übergang hin zu einem wissensbasierten Ansatz erscheint dringend erforderlich.

Die vorliegende Arbeit präsentiert eine Reihe numerischer Modelle die für die Prozessentwicklung des Reibrührschweißens mit Bobbin Werkzeug eingesetzt werden können. Das grundlegende Modell ermöglicht die zeitaufgelöste Vorhersage der Temperaturverläufe innerhalb des Prozesses und wird für alle weiterführenden Vorhersagen benötigt. Der Materialfluss wird modelliert, um Aussagen über die wirkenden Kräfte und die Form der Scherschicht zu ermöglichen. Diese mechanischen Lasten finden Eingang in ein Modell zur Vorhersage des Spannungszustandes im Werkzeug.

Die Vorhersagen ergeben im Falle der verwendeten Probengeometrie und Prozessparametern sehr zeit- und ortsabhängige Verläufe der Prozessgrößen. Dies erklärt die zu beobachtende Instabilität für ungeregelte Versuche. Eine Regelstrategie ist unerlässlich, um fehlerfreie Verbindungen mit akzeptabler Produktivität zu erreichen. Ein solcher Regelalgorithmus wird im Rahmen der Arbeit erfolgreich entworfen, implementiert und angewendet.

Die numerischen Modelle werden auf die verfügbaren Werkzeuge angewendet und die Vorhersagen experimentell überprüft. Auf den Ergebnissen aufbauend wird eine verbesserte Werkzeuggeometrie entwickelt, produziert und getestet. Die Ergebnisse zeigen, dass die Produktivität des Verfahrens und die Qualität der Verbindungen erheblich verbessert werden können. Erst das Wissen um die exakten Temperaturverläufe im Material und das Ausmaß der plastischen Verformung ermöglicht weiterführende Untersuchungen der Entwicklung der Mikrostrukur und der Eigenspannungen.

Acknowledgments

This work is the result of three years of research on bobbin tool friction stir welding at Helmholtz-Zentrum Geesthacht (former GKSS). The results presented here could not have been achieved without the help and support of many dear colleagues and friends. I would like to thank

- head of institute Prof. Dr. Norbert Huber for the supervision of the work

- Dr. Jorge F. dos Santos for his help in scientific and all other questions

- Dr. Arne Roos for his warm welcome to the team and countless tips and tricks along the way

- Leon L. Hütsch and Julia Hapke for hours of discussion and a great time

- my students Daniela Raminger, Diego Bettoni, Joao Luis Bilia Lopes, Lucio Correa and Amauri Mosquen for their effort, commitment, patience and hours of work

- all members of WMP for keeping up motivation and a productive environment

- my family for getting me here in the first place

- my wife Luisa for her patience and support in all matters

- and last but not least, Mark-Uwe Kling for the kangaroo

Jakob Hilgert

KNOWLEDGE BASED PROCESS DEVELOPMENT OF BOBBIN TOOL FRICTION STIR WELDING

Abstract

Over the last twenty years Friction Stir Welding (FSW) has proven to be a very promising new joining technique. Especially high strength aluminium alloys can be welded with large advantages as compared to conventional fusion welding processes. For some joint configurations and desired applications bobbin tool welding is a process variant that can circumvent limitations arising from the high process forces in conventional tool FSW. As bobbin tools are highly mechanically loaded, in-depth understanding of the evolution of temperatures and forces is desirable to avoid tool failure and extend the range of applicable process parameters together with overall productivity. Up to now the process and tool development has been mostly empirical. A transition to a science based approach is highly necessary.

The work presented here was conducted to establish a set of numerical models that can be used in process development of bobbin tool FSW. The first model covers the transient temperature fields that are needed as input for any further model. The material flow model predicts the acting forces and shear layer shape. Finally the mechanical loads on the tool are predicted by a mechanical model.

The models predict very time and position dependent conditions for the investigated specimen sizes and welding speeds. This explains the instability that can be observed experimentally under certain conditions. A control strategy is needed to produce sound welds at reasonable productivity. A versatile controller has been successfully designed, implemented and tested as part of the work presented here.

The models are applied to the existing tools and validated experimentally. A novel tool design is developed based on the experimental results and further improved using the models predictions. Finally the new tool design is tested. The results have shown that the productivity of the process as well as the joint quality could be significantly improved. The knowledge about the thermal history and extent of plastic deformation gained from the process model is a valuable input to the understanding of microstructure formation and the development of residual stress fields.

Zusammenfassung

Das Rührreibschweißen hat sich in den letzten 20 Jahren als vielversprechender Fügeprozess herausgestellt. Insbesondere beim Fügen hochfester Aluminium Legierungen zeigen sich große Vorteile gegenüber konventionellen Schweißverfahren. Die Prozessvariante des Bobbin Werkzeuges (Zweischulterwerkzeug) kann in einigen Fällen genutzt werden um die Einschränkungen des konventionellen Verfahrens durch übermäßige Prozesskräfte zu umgehen. Da Bobbin Werkzeuge mechanisch sehr hoch belastet sind sollten die wirkenden Kräfte und Temperaturen möglichst exakt bekannt sein um die Zerstörung der Werkzeuge zu verhindern und das Prozessfenster und die Produktivität zu optimieren. Bis jetzt basierte die Prozess- und Werkzeugentwicklung auf empirischen Erwägungen. Ein Übergang hin zu einem wissensbasierten Ansatz erscheint dringend erforderlich.

Die vorliegende Arbeit präsentiert eine Reihe numerischer Modelle die für die Prozessentwicklung des Reibrührschweißens mit Bobbin Werkzeug eingesetzt werden können. Das grundlegende Modell ermöglicht die zeitaufgelöste Vorhersage der Temperaturverläufe innerhalb des Prozesses und wird für alle weiterführenden Vorhersagen benötigt. Der Materialfluss wird modelliert, um Aussagen über die wirkenden Kräfte und die Form der Scherschicht zu ermöglichen. Diese mechanischen Lasten finden Eingang in ein Modell zur Vorhersage des Spannungszustandes im Werkzeug.

Die Vorhersagen ergeben im Falle der verwendeten Probengeometrie und Prozessparametern sehr zeit- und ortsabhängige Verläufe der Prozessgrößen. Dies erklärt die zu beobachtende Instabilität für ungeregelte Versuche. Eine Regelstrategie ist unerlässlich, um fehlerfreie Verbindungen mit akzeptabler Produktivität zu erreichen. Ein solcher Regelalgorithmus wird im Rahmen der Arbeit erfolgreich entworfen, implementiert und angewendet.

Die numerischen Modelle werden auf die verfügbaren Werkzeuge angewendet und die Vorhersagen experimentell überprüft. Auf den Ergebnissen aufbauend wird eine verbesserte Werkzeuggeometrie entwickelt, produziert und getestet. Die Ergebnisse zeigen, dass die Produktivität des Verfahrens und die Qualität der Verbindungen erheblich verbessert werden können. Erst das Wissen um die exakten Temperaturverläufe im Material und das Ausmaß der plastischen Verformung ermöglicht weiterführende Untersuchungen der Entwicklung der Mikrostrukur und der Eigenspannungen.

Symbols and Abbreviations

AMGM	Advanced moving geometry model	34, 42, 50, 117
ANN	Artificial neural network	56
ASLM	Analytical shear layer model	37, 117
BT-FSW	Friction Stir Welding using a bobbin tool	4, 6, 11, 70, 93
CFD	Computational Fluid Dynamics	19, 20, 50, 54, 57, 62, 66, 80
c_p	specific heat	14
c_p	Specific heat capacity	37, 41
CSM	Computational Solid Mechanics	19, 22
δ	Contact state variable	ii, 16, 53, 59, 62
dr	Normal distance to the tool pin surface	38
dT_{500}	Amount of time a defined material point has a temperature above 500K	42
dz	Normal distance to the nearest tool shoulder surface	38
$\dot{\epsilon}$	Effective strain rate	51
η	Material viscosity	20
η_{eff}	Effective viscosity	ii, 52
F	Process force acting on the tool	15
F_g	Forging force acting between the two shoulders of a bobbin tool	ii, 57, 65, 82
FSW	Friction Stir Welding	2, 3, 8, 117
f_v	Viscous force per area acting on a location on the pin surface	59
F_x	Force in welding direction	31, 57, 59, 81, 82
F_y	Force in lateral direction	31, 57, 81, 82
$\dot{\gamma}$	Shear rate	18
GKSS		*see* HZG
h	Heat transfer coefficient	41
HAZ	Heat Affected Zone	11, 24, 108, 113
HZG	Helmholz Zentrum Geesthacht, Zentrum für Material- und Küsten-forschung	93

k	thermal conductivity	14, 37, 41
K_0	Modified Bessel function of the 2nd kind and 0th order	14
L	Characteristic length	37
λ	$\frac{\rho c_p}{2k}$	14
m_r	ASLM parameter	39, 56, 62
m_{shape}	ASLM parameter	38, 56, 62
M_T	Machine torque applied to the tool	ii, 18, 45, 57, 59, 82
μ	Coulomb's friction coefficient	15, 18
m_z	ASLM parameter	38, 56, 62
∇	Nabla operator defined as $\left(\frac{\partial}{\partial x}, \frac{\partial}{\partial y}, \frac{\partial}{\partial z} \right)$	20
n_{conv}	Convergence parameter	52
ω	Angular velocity	15, 17, 31
ω_{matrix}	Angular velocity of the Matrix	16
ω_{tool}	Angular velocity of the tool	16, 53
p	(Uniform) contact pressure	18
π	(constant)$\approx$3.1415	14
Q	Total input of heat from the tool	14, 15
$q_{friction}$	Heat flow/generation per area due to friction	17
q_l	Line energy applied by the tool	ii, 46
q_{total}	Total heat flow per area	18, 41
R	Universal gas constant: 8.3144621 $\frac{J}{mol K}$	23
r	Distance from assumed heat source center	14, 15, 17, 38, 53
R_*	ASLM variable: shear layer outer boundary radius	38
RFPM	Rotating featured pin model	50, 54, 59, 80, 81, 118
ρ	ASLM variable: normalized dr	37, 38, 41
ρ_{mat}	materials density	14
R_m	ASLM parameter	38, 56, 60
R_p	Tool pin radius	38
RPM	Tool rotations per minute	50, 117
$Rprop$	Resilient backpropagation algorithm for the training of ANNs	56
R_s	Tool shoulder radius	38
$\bar{\sigma}$	Effective deviatoric flow stress	51
SSBT-FSW	Stationary Shoulder Bobbin Tool Friction Stir Welding	113, 114
SZ	Stir Zone	11, 108, 110
T	Temperature	41
T_0	Initial temperature	14
$\tau_{friction}$	Shear stress due to friction	17, 18

Contents

Chapter 1

Introduction

1.1   Motivation

One of the major challenges of our modern societies is the apparent conflict between economic growth and a considerate exploitation of the limited resources. In the last decade the focus of public interest was drawn to the consumption of fossil fuels and the emission of greenhouse gases. Under the impression of the urgent nature of climate change there is a strongly perceived need to reduce energy consumption. At the same time mobility of commodities as well as people is getting more important by the minute and there is a growing demand for sustainable and environmentally friendly high performance products on the global markets. This has increased the driving force for engineers and scientists to develop advanced materials and technologies to improve the efficiency of manufacturing and transportation. A result of this is the ongoing development of light-weight materials with very high specific strength like fibre reinforced polymers and high strength aluminium and magnesium alloys. Along with these materials, novel joining technologies where developed. A very promising technology is Friction Stir Welding (FSW see Section 1.2). As this is a very young process, there is still a lack of precise knowledge of the physical interactions involved. A possible approach to filling these knowledge gaps is numerical simulation.

Early work on process modelling of FSW was published by Frigaard et al. [1] in 2001. The author has adopted this topic in 2009 [2] with a focus on FSW with bobbin tools. The result obtained in this work revealed the need for a more intense study of the transient nature of bobbin tool welds, not only in terms of temperature but also in terms of material flow and process forces. The experimental work by Neumann [3] that was available in this field at that time also indicated a need for improved tooling as a consequence of the high process loads. It was understood that a science based approach is needed to achieve further development of the process with an efficient and sustainable use of resources. This need was the basis for the presented work.
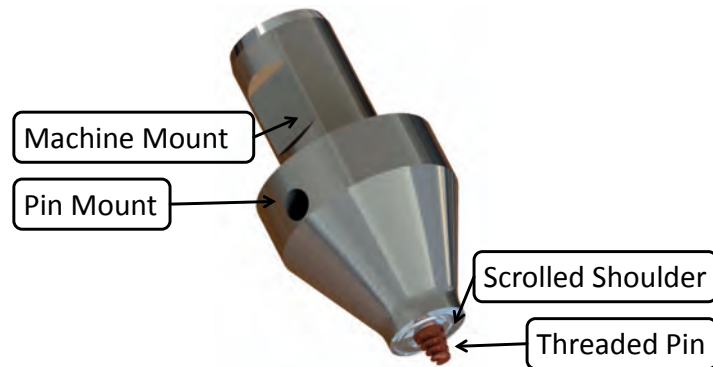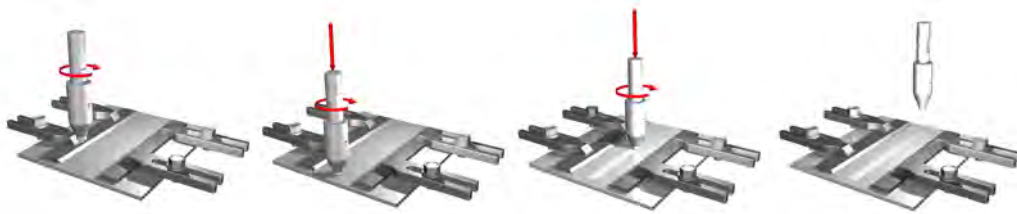
Figure 1.1: Standard FSW tool

Figure 1.2: Basic principle of the FSW process
[Courtesy of HZG]

1.2 Friction Stir Welding (FSW)

FSW is a solid state joining process invented and patented in 1991 by Thomas et al. [4]. The process is carried out by plunging a rotating tool made of a wear-resistant and high-temperature-resistant material into the material to be joined and translating it along the desired weld line. The heat generated by friction at the tool surface and plastic dissipation in the deforming regions of the work pieces soften the material to a plasticised state. It is then extruded around the tool and consolidates to form a weld. It must be emphasised that there is no bulk melting of the material. In most cases a single sided joining approach is taken. For this the standard tool design consists of a shoulder and a pin. This configuration and the process variant of FSW carried out with such tools will be referred to as standard FSW throughout this work. During the process the shoulder is in intimate contact with the work piece surfaces and prevents the material from being expelled from the weld. Such a tool configuration can be seen in Fig. 1.1. The basic principle of the FSW process and the process steps approach, tool plunge, welding and tool retreat are illustrated in Fig. 1.2. More details on standard FSW and its applications can be found in Section 3.1. There is a special class of FSW tools called bobbin tools. The name refers to the shape of these tools, which consist of two shoulders connected by a pin. The upper shoulder and the pin act similarly to the shoulder and pin in standard FSW. The lower shoulder that is attached to the tip of the pin is in contact with the opposing surface of the work piece. Such a tool configuration can be

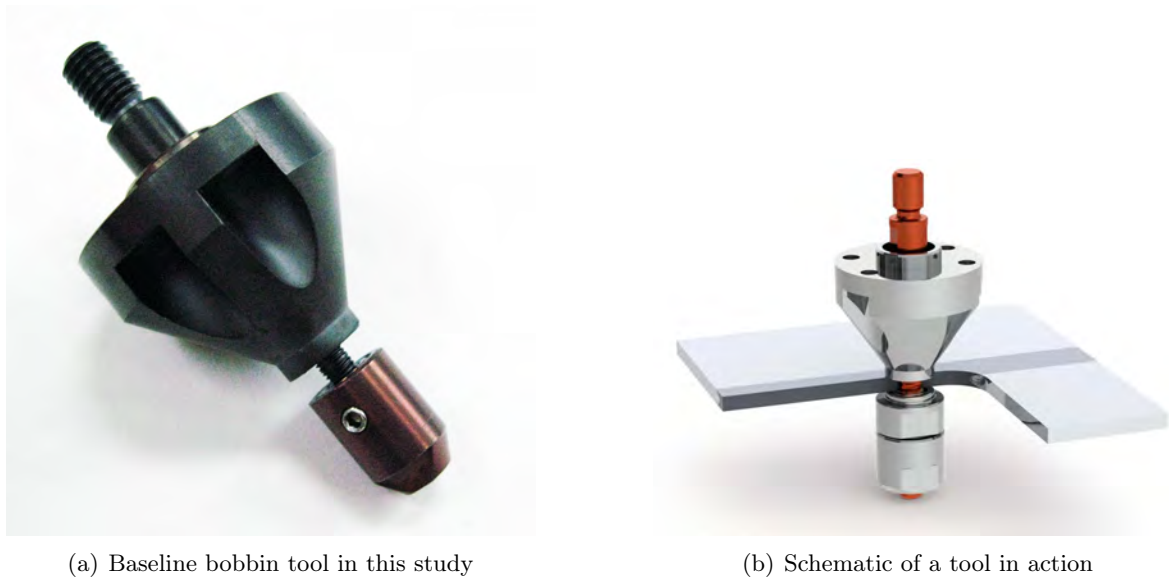(a) Baseline bobbin tool in this study   (b) Schematic of a tool in action

Figure 1.3: FSW bobbin tool

seen in Fig. 1.3.

Although the concept has already been described in the first patent on FSW [4] in 1991, very little work has been published in the field of bobbin tool FSW (abbreviated BT-FSW) as compared to FSW with standard tools. This is due to the fact that there have been practical issues when applying BT-FSW in the past (see Fig. 3.4). When using a bobbin tool, there is no need for a backing plate or anvil as the loads act between the two shoulders and have to be carried by the pin instead. This allows for welding machines with substantially lower stiffness but also yields a challenge in terms of tool design, material and lifetime. The first bobbin tools had a fixed distance between their shoulders (so called Fixed-Gap bobbin tools). This resulted in thermal stresses because of incompatible thermal extension coefficients between the tool and work piece materials (see Section 6.1.4.1). As the pin already carries a substantial load resulting from the pressure applied to both shoulders, the additional load favoured pin fracture [5].

There is still a great potential to be realised in BT-FSW if the present limitations are to be overcome by a deeper understanding of the process and its specific challenges. More details on BT-FSW and its applications can be found in Section 3.1.

1.3 Modelling of FSW

It is desirable to understand the physical relationship between the process parameters and the process result for any given process. This is especially true if the relationship can be predicted before conducting the process so that undesirable results can be avoided. An example of a schematic diagram of such relationships is presented in Fig. 1.4. This has been detailed to
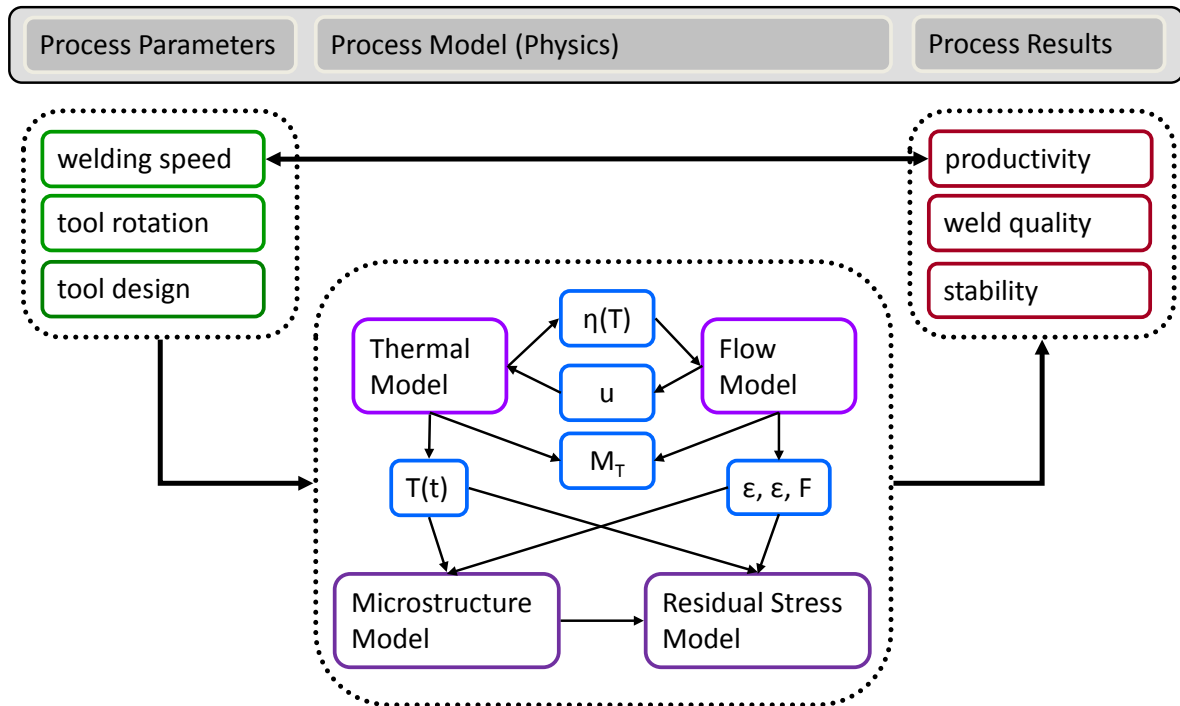
Figure 1.4: Schematic diagram of a physical model for parameter-result-relationships

cover a great amount of physical interactions by Colligan and Mishra [6]. FSW is still a very young technology. In the first decade after its invention, the main efforts went into technology development [5]. Limited detail is yet known about the physical interactions involved in the joint formation in FSW. A deeper understanding of the process can be gathered by numerical modelling [7]. There is an active community contributing to the field of numerical simulation. Models of the standard FSW process are under continuous development, including thermal, flow and stress phenomena (see Section 3.2). First approaches on modelling defect formation have been reported by Arbegast [8] and Ke et al. [9]. There have been sophisticated investigations by Zhu and Chao [10] on effects of input data on the modelling of welding processes in general. These investigations can provide useful support for any more specific models. Numerical analysis may also help to find improved tool geometry, to estimate and to minimise the required process power, and to increase the welding speed without diminishing the strength of the joint [11]. A complete framework covering all aspects needed to understand and predict the process results based on the controllable inputs and the physical properties of the used materials has not yet been established. An extended overview of the present state of modelling in FSW along with the specific challenges and gaps in knowledge is given in Chapter 3.

Chapter 2

Objectives and Structure

2.1 Objectives

The focus of this study is set on simulation based process development. In order to avoid excessive experimental effort when developing a bobbin tool welded structure, the basic interactions of process parameters (welding speed, tool rotation, tool geometry) and process variables (temperature evolution, material flow, process forces) should be known in advance. These can be predicted using numerical models. This study describes an approach that uses a number of experimentally validated models to achieve a science based process development strategy that can be used to choose tool design and process parameters for a given application. The objectives of the work can be defined as:

- Develop a numerical process model for BT-FSW.

- Demonstrate the capabilities of the model in process development.

The milestones in the course of the work are:

- Produce and evaluate baseline experimental bobbin tool welds.

- Define important physical quantities of the process.

- Develop numerical models for these quantities.

- Define and implement necessary changes and improvements to the experimental setup (hardware and software) to allow for measurement and control of the relevant variables.

- Calibrate and validate numerical models.

- Apply numerical models to tool design, parameter selection and process control strategy.

- Define, manufacture and implement tools with improved performance.

- Validate the improved tools and experimental setup.

2.2 Structure

Chapter 3 gives a brief introduction to the present state of the art of FSW, BT-FSW and modelling work available for these processes. The different modelling approaches are compared and the open questions and knowledge gaps are pointed out.

Chapter 4 describes the experimental setup for the welding and deals with material-characterisation experiments conducted to validate the numerical models and test the process control and tool design developed in this study.

Chapter 5 describes the numerical models developed and used in this work. A transient moving geometry thermal model for temperature field prediction and machine torque prediction is described first. It can be used as a basis for all other numerical models. Two versions of a CFD material flow model are presented. They are used for the prediction of forces and the contact state (ratio of slipping to sticking) at the tool interface. They also predict the shape and velocity profile of the material shear layer around the tool, which is fed back as an input to the thermal model. Finally a mechanical model of the tool is described. It can be run based on the predictions of the thermal and flow models. The predicted stresses in the tool can be used to find the limits of operation for a given tool design or to compare different tool design candidates.

Chapter 6 gives a detailed explanation of the challenges of bobbin tool design. Tool material, loading, feature design and cleaning are discussed. The empirical baseline tool used at the beginning of the work is compared to the improved tool design. The limitations of tool optimisation due to the limits imposed by machining and manufacturing technologies are discussed.

Section 6.3.1 deals with process control. Based on the needs found in the preceding chapters, different parameter control strategies are explained and discussed. The software controller implemented for the welding machine used in the experiments is described and selected controller outputs are presented.

Chapter 7 presents the results of the welding experiments relevant for process development. The visual and mechanical properties are compared for the different welding campaigns. The quality improvement that was gained within this study is discussed.

Chapter 8 gives a summary of the process development procedure based on numerical simulations used in this study. The results of modelling and process development are discussed, conclusions are drawn and future research work is recommended.

Chapter 3

State of the Art

3.1   Friction Stir Welding Processes

Comprehensive reviews on FSW have been published by Mishra and Ma [12], Nandan et al. [13] and most recently by Cam [14]. Therefore only a brief description of the process itself is included in this work. Standard FSW can be divided into three process steps. In the initial plunging step the rotating tool makes contact with the work piece. Due to frictional heating the temperature is increased. The tool plasticises the work piece surface and plunges in. As the height of the pin is just short of the thickness of the plates, the shoulder of the tool comes in contact with the plate surface before the pin penetrates through the plates. In the welding step the tool is translated along the weld line. Material is extruded around the pin and mixed behind the tool thus forming the joint. In the final exit step the tool is retracted leaving an exit hole (see Fig. 3.1(a)). There are several approaches to avoid an exit hole including post machining of excess run-out areas and retractable pin tool technology [15].

(a) Standard tool

(b) Bobbin tool

Figure 3.1: Typical exit holes and run-outs

The main driver for the development of FSW was the need for a joining process suited for high strength aluminium alloys like the 2XXX and 7XXX series. These were considered hard to weld or not weldable at all with most conventional techniques. FSW offers an excellent

alternative to conventional fusion welding and provides good joint properties and a high degree of repeatability. It was soon found that apart from the aluminium alloys mentioned above FSW is also capable of joining a great number of other materials. These include Al, Pb, Mg, Ti, Cu, Zn, steels [7, 16] and especially hard to weld alloys [17] including ODS aluminium alloys [18]. Many joints between dissimilar materials are possible as well [19].

The potentials and benefits of FSW can be grouped in three major families [12]. First there are a great number of metallurgical benefits resulting from the solid state nature of the process with no bulk melting of the joined materials. Solidification cracking is not an issue. No loss of alloying elements due to evaporation are expected as temperatures stay far below the critical range. The considerably lower temperatures, as compared to any fusion welding process, also help to reduce the distortion [20, 7, 21, 22, 17, 23, 24] generated by constrained thermal expansion. In this context a reduction of residual stresses has been reported by Su et al. [17]. Good dimensional stability and repeatability can be achieved [20, 7]. The terminology of FSW has been summarised by Threadgill [25] and an ISO standard will be issued shortly.

The micro structure in the centre of the joint is very fine-grained and recrystallised for most materials. This yields excellent metallurgical properties. High ductility welds can be achieved [20]. Lomolino et al. [26] report good fatigue and fracture toughness properties. Any welding position is possible without influence on the joint quality. A good surface finish can be achieved [20] (see Fig. 7.1) and no post weld treatments is needed for many applications [7].

These characteristics alone make FSW a very attractive alternative to fusion welding processes for engineers, yet there are more beneficial aspects when it comes to environmental sustainability. There is no need for shielding gas for many materials including aluminium alloys 2xxx and 7xxx. Only basic surface cleaning is required. Toxic solvents are not required for oxide removal. There is a great economic saving potential for consumable materials, such as filler wire or process gas. There are no fumes and virtually no noise [7, 23] emission.

Finally, there are advantages when it comes to energy consumption and efficiency. The FSW process has an efficiency of up to 97% compared to 17-20% of a CO2 LBW [12]. A more efficient use of material strength resulting from the higher joint quality (i.e efficiency) allows a weight reduction of the welded structure. The same effect can be obtained by joining parts with different thickness to tailor welded blanks [27]. This helps to decrease fuel consumption in light weight aircraft, automotive and marine applications. Apart for many materials and material combinations, FSW has been developed for many different joint geometries and configurations as shown in Fig. 3.2.

Many aspects of the process have been investigated in detail. Kamp et al. [28] and Sullivan and Robson [29] deal with the microstructure and precipitation evaluation. Xu et al. [30] describe the mechanical properties, Dong et al. [31] the shear layer evolution and Reynolds [32] describes material flow visualisation. Hattingh et al. [33] and Colligan and Pickens [34] investigate the influence of the tool design and Derry and Robson [35] investigate the toughness

(a) square butt   (b) edge butt   (c) T butt

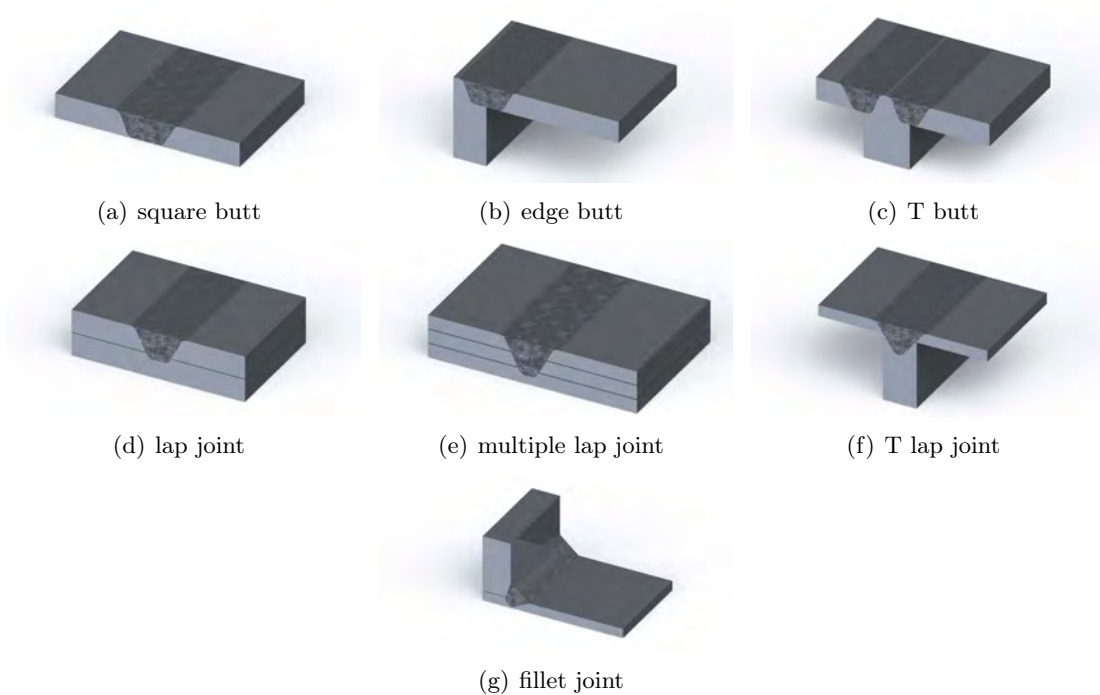(d) lap joint   (e) multiple lap joint   (f) T lap joint

(g) fillet joint

Figure 3.2: Joint configurations for FSW

of joints.

Although a relatively young technology, FSW has already found many potential applications. Because of its potential in hard-to-weld series 2XXX and 7XXX aluminium alloys that are widely used in aircraft [36], aerospace companies took the lead in evaluating and adopting the technology. Standard FSW is considered a maturing process [5] that has already been implemented in the maritime, automotive, and aerospace fabrication industries [7, 21]. The process is approved for maritime applications by DNV, Germanischer Lloyd and RINA [37]. An overview of potential application fields is given by Cook et al. [23] and Schöfer [37] and is summarised below:

aerospace *(military/civilian aircraft, aircraft parts, fuel tanks, rockets),* **land transportation** *(tailored blanks, truck bodies, armor plate vehicles, wheel rims, engine and chassis cradles, fuel tankers, motorcycle and bicycle frames),* **railway** *(tankers and wagons, container bodies, underground carriages and trams),* **shipbuilding and marine** *(panels for decks, sides, bulkheads and floors, helicopter landing pads, offshore accommodation, hulls and superstructures, aluminum extrusions),* **construction** *(aluminum bridges, window frames, aluminum pipelines, heat exchangers, facade panels),* **electrical** *(bus bars, electrical connectors, electric motor housings, encapsulation of electronics), and* **gas** *(tanks and cylinders).*

For this study the bobbin tool variant of the FSW process is used. The concept of the bobbin

tool is as old as FSW itself. The first patent by Thomas et al. [4] already describes a bobbin tool. The main advantage of this technique is the ability to weld closed sections without the need for a rigid backing [38]. The reason for this is that the forging forces needed to confine the material act between the two shoulders only and do not contribute to the loading of the machine or clamping. On the other hand these loads have to be carried by the pin which gives rise to the largest challenge of BT-FSW (see Chapter 6).

When using BT-FSW the process can be divided into three process steps similar to those in standard FSW: The plunging step is somewhat different by nature, as it is not possible to insert a bobbin tool into a work piece from above because of the lower shoulder. Therefore the plunging step should rather be described as running-in step. There are two possibilities to start a bobbin tool weld. One is to drill a hole into the work piece, insert the pin and mount the lower shoulder. Then start the weld by starting the tool rotation and slowly beginning translational movement. The other option is to run into the work piece from a side with a fully assembled tool. When the pin makes contact a dwelling time may be necessary to soften the material. Then the translational motion is slowly started and accelerated to the desired welding speed. The second option has been adopted in this study. The welding step in BT-FSW is essentially the same as in standard FSW. The rotating tool is translated along the welding line. The exit step is again different from standard FSW as the tool cannot be retracted in an out-of-plane direction from the workpiece because of the lower shoulder. Therefore the tool can either be stopped at its final position, disassembled and retracted to both sides or simply run out of the side of the workpiece thus leaving a bobbin tool style exit hole as shown in Fig. 3.1(b). The first option is usually not feasible in practise as a featured pin that has been stopped while welding is geometrically trapped in the work piece. Even if there was no surface adhesion, only very simple pin designs could be retracted. Therefore the second option is selected for this study.

While the first tools where monolithic and had a fixed gap size, a major improvement in BT technologie was the Auto-Adjustable Pin Tool invented by Ding and Oelgoetz in 1999 [15] (see also Campbell et al. [39], Carter [40] and Loitz et al. [41]). It allows force controlled welds by having an adjustable distance between the two shoulders. These tools have also been commercialised [42]. Several patents reveal designs for bobbin tool welding setups: Smith et al. [43] describe a self clamping machine and Eller et al. [44] describe details of bobbin tooling. Loitz et al. [41] present a bobbin tool welding head featuring independent pin and shoulder operation (compare to Burton and Matlack [45] who also describe a counter rotating spindle). The overall patent situation can be considered rather complex as several international patents contain mutually exclusive claims.

In a typical BT-FSW weld, the same microstructural zones can be observed as in standard FSW (see Fig. 3.3) [8]. These include the SZ (Stir Zone), the TMAZ (Thermal-Mechanically Affected Zone) and the HAZ (Heat Affected Zone). There are two main challenges in bobbin
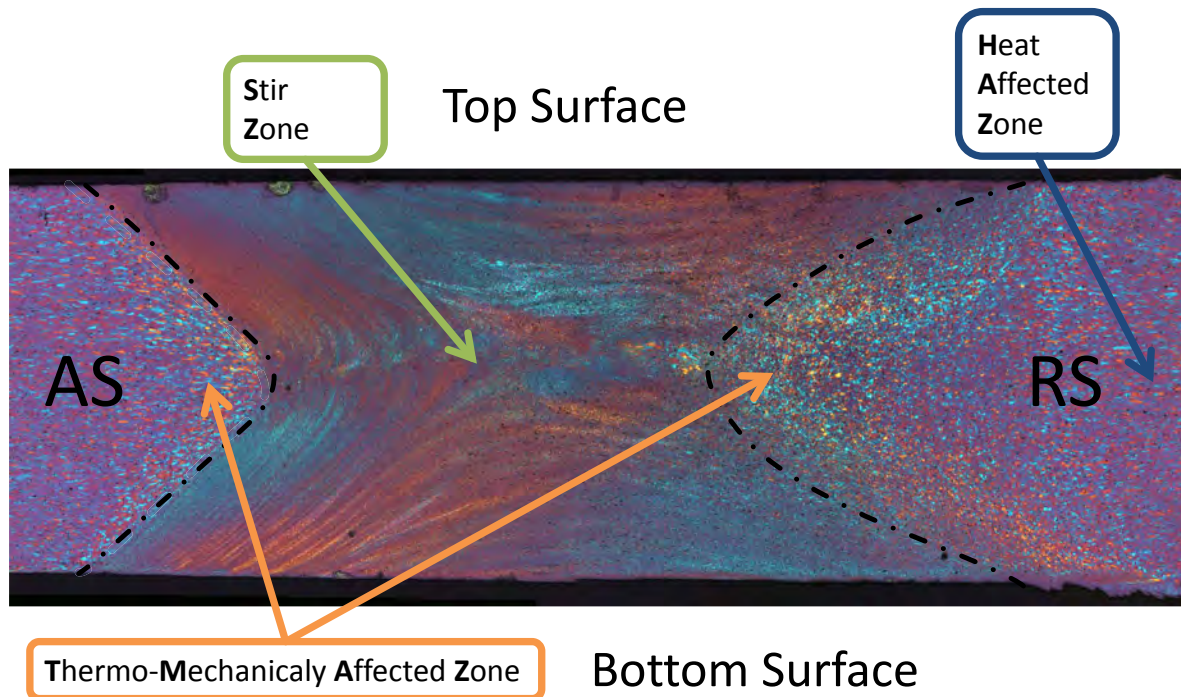
Figure 3.3: Microstructural zones (BT-FSW)

tool friction stir welding that differ from standard FSW. One is the considerably increased loading of the tool. Especially the strength and lifetime of the pin is a major limiting factor for the process (see Fig. 3.4(a)). The process stability especially in thin sheet welding is another critical point. The transient temperature and material flow behaviour can lead to instabilities that cause defective welds and may damage the tool. These instabilities are not found in standard FSW as the material temperature and flow is more constrained due to the presence of a backing. An example for the occurrence of unstable material flow is given in Fig. 3.4(b). Although BT-FSW is mainly used for thin sheets of light metals, it has proven to be suitable for challenging joining tasks like stainless steel [46] and thick sections as shown by Dalder et al. [47] and Threadgill et al. [48]. Neumann [3] and Edwards and Sylva [49] have collocated recent applications of the technology. The reported applications range from high speed trains to Delta II rocket tanks and the space shuttle.

Neumann et al. [3, 50] present work on BT-FSW that directly precedes the work conducted for this study. He evaluates three basic empirical pin designs and shows the feasibility of the process for 4-mm-thick sheets of AA2024 T351. It is an widely used material in aircraft industry and has been studied by many groups. Publications on standard FSW on this alloy can readily be found in literature. Tensile properties are published by Lockwood et al. [51] as well as fracture examinations by Sutton et al. [52]. Literature is available on material models [53], the hardness [54], the precipitation phenomena [55] and the hot extrusion behaviour [56] As it is a rather old alloy, it is well understood in many ways and has been joined successfully
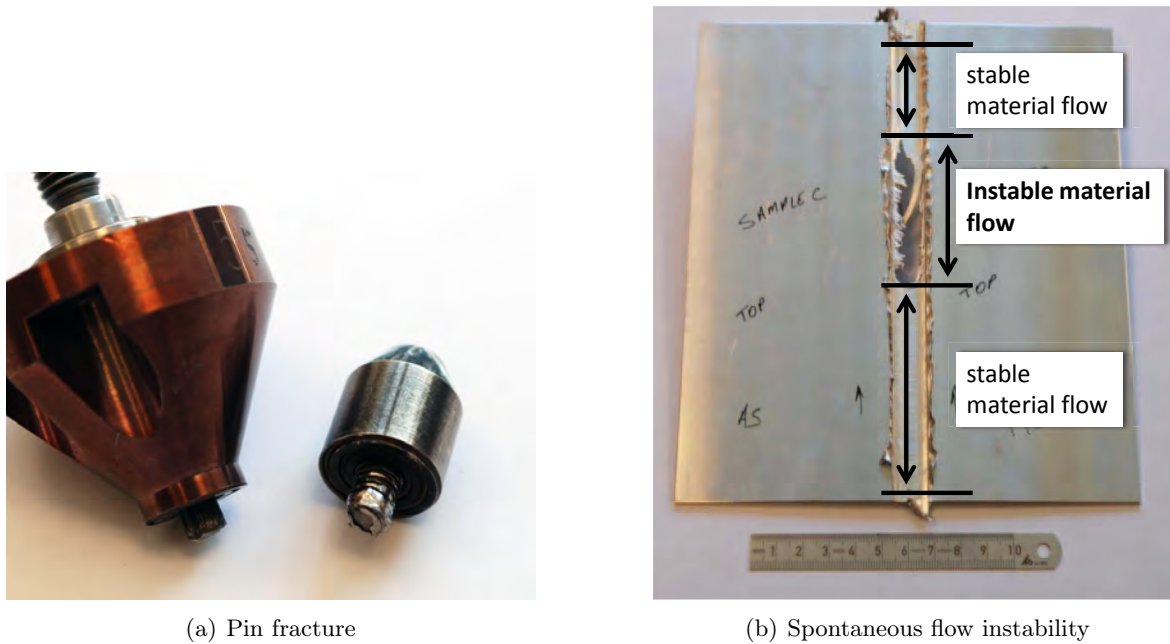
(a) Pin fracture
(b) Spontaneous flow instability

Figure 3.4: Challenges in BT-FSW

not only by standard FSW but also by BT-FSW [3].

3.2 Modelling

Modelling of FSW has been a major interest of many researchers in the last decade. Most models developed in this work are influenced by the work of Schmidt et al. [57, 58, 59, 60, 61, 62, 63, 64, 65, 66, 64] and Colegrove et al. [67, 68, 22, 69, 70]. There is a large quantity of published work on different aspects of the FSW process. This section describes different aspects that are of interest to modelling.

3.2.1 Thermal Models

Thermal modelling is a central part of modelling FSW. Many of the properties of a final weld can be derived directly from the thermal history of the work piece [64]. Almost every process model in the field of FSW, be it microstructural, CFD or thermo-mechanical, incorporates a thermal model or uses input data generated by one. There are various types of thermal models including fully analytical, numerical and also mixed formulations.

When setting up a thermal model of the FSW process, it is most important to find an appropriate representation for the heat generated at the interface between the tool and the work piece.

3.2.1.1 Fully Analytical Approaches

Several approaches have been made to model heat generation and the temperature fields present during welding. Long before the FSW process was even developed, Rosenthal [71] derived an analytical solution for the temperature distribution caused by a moving line heat source on an infinite plate. This solution can be applied to FSW models as a first estimate, as it is analytical and very fast to evaluate [72]. A constant line source through the thickness of the plate is expressed in Equation (3.1) (see also [73]).

$$T = T_0 + \frac{Q}{2\pi k t_{plate}} e^{-\lambda u_{weld}\xi} K_0(\lambda u_{weld} r) \qquad (3.1)$$

where K_0 is the modified Bessel function of the 2nd kind and 0th order, T_0 is the initial temperature, Q is the heat input, π is a constant, k is the thermal conductivity, t_{plate} is the plate thickness, ρ_{mat} is the materials density, c_p is the specific heat capacity, λ is $\frac{\rho_{mat}c_p}{2k}$, u_{weld} is the welding speed, ξ is the distance projected on to the welding direction and r is the radial distance from the tool.

The analytical code iSTIR based on Rosenthal's equations is a thermal model of the FSW process including the thermal asymmetric distribution under the tool shoulder. It has been applied to hot and cold welding conditions and to both similar and dissimilar friction stir welded joints [24].

The quality of the predictions can be satisfactory when one is looking at the far field or when one is interested in a rough estimate of the time at elevated temperatures. The approach is certainly not capable of predicting the thermal field in the vicinity of the tool as several important factors are neglected. These factors are the difference in thermal properties between tool material and work piece material, the influence of the tool size and shape on the distribution of the generated heat and, most importantly, the convective energy transport by the deforming work piece material. Therefore this kind of model is insufficient as an input for further detailed investigations concerning material flow, forces and torques, microstructure or residual stresses.

3.2.1.2 Analytical Heat Sources

A more detailed investigation is possible with the help of numerical (often finite element based) techniques. The most comprehensive way to do this is to predict the heat generation and transport by including all relevant effects like friction and plastic dissipation into a fully coupled multi-physics time dependent numerical thermo-mechanical model. This is linked to excessive computational effort and requires precise knowledge of all relevant physical interactions, which is not available today. Therefore it is convenient to derive an analytical heat source model which is easy to evaluate and can be integrated into a purely thermal model. The input variables for such a model can be of physical significance e.g.:

- tool rotational speed ω

- welding speed u_{weld}

- plate thickness t_{plate}

- frictional coefficient μ

- assumed process forces F

- input of heat Q

but they can also consist of purely empirical parameters [74, 75]. It is important how heat is generated and distributed in the heat source. A point heat source has a uniform total heat output while any extended heat source shape can have a heat output as a function of spatial coordinates. Some common analytical heat sources shapes are illustrated in Fig. 3.5 (also see [61]). A common approach is to have a linear dependence of heat generation on the r coordinate of a polar coordinate system as illustrated in Fig. 3.6(a). Here the heat generation is proportional to the frictional velocity $v_{friction}$ defined in

$$v_{friction} = \omega r, \tag{3.2}$$

where ω is the angular velocity of the tool and r is the distance from the assumed heat source centre. This is based on the assumption that there is a linear relationship between interaction velocity and heat generation. As the interaction between tool and work piece is not only based on friction but also on plastic deformation and the frictional velocity is only meaningful if the work piece does not move or deform at all, this assumption can be doubted. It does not account for the differences in temperature at different locations of the tool, their effect on the material properties and the implication on heat generation.

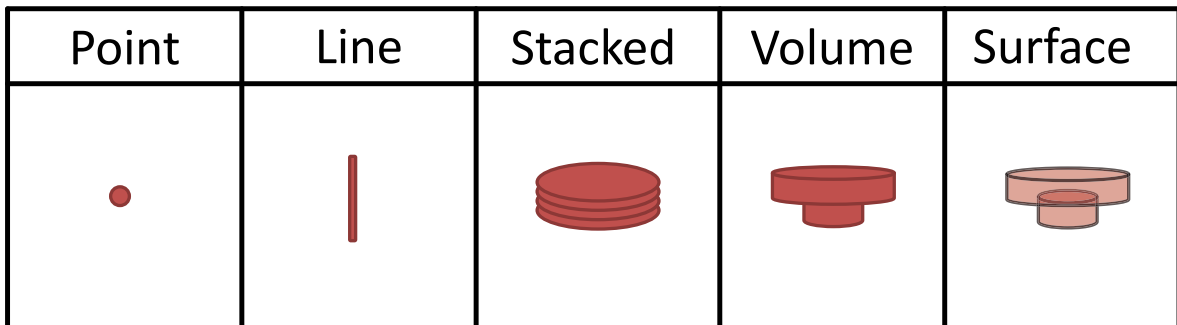Selected references on analytical heat source models are provided in the appendix, Tab. D.1.

Point	Line	Stacked	Volume	Surface

Figure 3.5: Analytical heat source shapes

(a) Analytical linear heat source
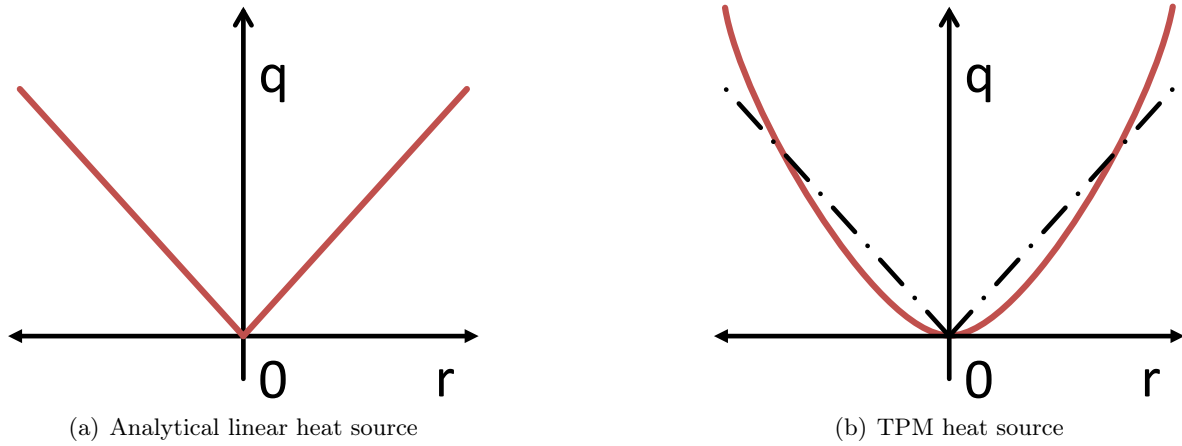
(b) TPM heat source

Figure 3.6: Energy distribution in spacial heat sources [2]

3.2.1.3 Contact Condition

The heat generation from the tool is influenced by the contact condition between tool and base material. For this contact condition one can distinguish between sliding, sticking, or partial sliding and sticking as described by Schmidt et al. [64, 59] and Uyyuru and Kailas [7]. It is therefore convenient to define a contact state variable as proposed by Schmidt et al. [59] in

$$\delta = \frac{\omega_{matrix}}{\omega_{tool}} \in [0, 1]. \tag{3.3}$$

Here δ is the contact state variable, ω_{matrix} is the shear layer angular velocity and ω_{tool} the tool angular velocity. This contact state variable facilitates the formulation of analytical heat sources and shear layers and is capable of representing any combination of sliding and sticking at the tool interface. In most cases the contact state is an input parameter to heat source models as well as material flow models. This is problematic as there is no way of determining the contact condition experimentally in an accurate way. The assumption of a contact state can have significant influence on the model predictions though. Therefore it is strongly encouraged to choose a model formulation where the contact state is not needed or is an output rather than an input of the model.

3.2.1.4 Calibrating Parameters

Any FSW model requires certain input parameters for the behaviour of the material, the heat generation or the boundary conditions. There are several possibilities to gain these input parameters. When directly modelling FSW temperature fields, it is usually important to know the power source [76] as a heat input. With this parameter the heat source formulations can be calibrated. The total heat output of virtually any heat generation formulation can be fitted to an experimentally determined value. This usually does not allow for a prediction of other

conditions than the ones investigated experimentally, as the interaction between the process parameters and the heat generation remains unclear.

A simple but not physically meaningful approach is to calibrate a power dependent variable of a model to minimise the difference between the model temperature prediction and experimental temperature measurements [24, 59]. Once again the predictive capabilities are very limited. A related approach uses measurements of power such as machine power consumption or, more elaborately, torque at the tool to directly calculate the dissipated heat [77, 74]. Some assumption has to be made on the distribution of the heat input to the shoulder and pin. Energy dissipation other than the desired friction (e.g. due to vibration and acoustic noise emission) might influence the results.

The heat source has also been directly modelled using contact pressure p and Coulomb's friction coefficient μ as input parameters [1, 78]. In a first step this yields a shear stress according to

$$\tau_{friction} = \mu p. \tag{3.4}$$

This shear stress can be used as a boundary condition in the model or to directly calculate a heat input due to friction using

$$q_{friction} = \tau_{friction}\omega r. \tag{3.5}$$

Here $q_{friction}$ is the heat flow per surface area due to friction, $\tau_{friction}$ is the shear stress due to friction, ω is angular velocity and r is the distance from the heat source centre. This method has to deal with the difficulties of experimentally determining μ as a function of the temperature T and possibly other influencing quantities like strain rate or relative velocity. It can be doubted that a linear friction law captures the relevant effects with sufficient accuracy. The contact pressure can be found from material flow or from fully coupled models, but is usually taken as a mean pressure derived from experimentally determined forces.

3.2.1.5 Thermal Pseudo-Mechanical (TPM) Heat Sources

A promising new way of determining heat input without having to do experimental calibration for every new set of welding parameters is the TPM approach proposed by Schmidt et al. [64]. The method is based on the knowledge of the plastic behaviour of the work piece material at elevated temperature rather than the friction phenomena within the process. The yield stress (more precisely the flow stress) of all materials that are suitable for FSW is a function of temperature. It dramatically decreases once the temperature approaches the solidus or melting temperature. That decrease is a natural limit to shear stresses present during welding. This is of fundamental importance as the shear stresses are the driving forces of heat generation as given by

$$q_{total} = \dot{\gamma}\tau_{friction} + (\omega r - \dot{\gamma})\tau_{yield}, \tag{3.6}$$

where q_{total} is the total heat flow, $\dot{\gamma}$ is the shear rate, $\tau_{friction}$ is the shear stress due to friction and τ_{yield} is the shear yield stress. Using the contact state variable (Eq. (3.3)) and Coulomb's law (Eq. (3.4)) Eq. (3.6) can be expressed as

$$q_{total} = \omega r \left(\delta \tau_{yield} + (1 - \delta) \mu p \right), \tag{3.7}$$

where p is the contact pressure and μ is Coulomb's friction coefficient. As long as the contact state is not pure sliding ($\delta \neq 0$) it can be stated that

$$\tau_{interface} = \tau_{friction} = \tau_{yield}, \tag{3.8}$$

where $\tau_{friction}$ is the shear stress due to friction and $\tau_{interface}$ the shear stress at the interface between tool and workpiece. This can readily be assumed because $\delta = 0$ implies no material motion and therefore no weld at all. Eq. (3.8) yields the TPM heat source equation as proposed by Schmidt and Hattel [64, 65, 66, 64]

$$q_{total} = \omega_{tool} r \tau_{yield}, \tag{3.9}$$

which is prescribed as a boundary condition at the interface between the tool and the work piece. The only a priori unknown input parameter is the shear yield stress of the material which is a function of temperature. Once this data has been determined experimentally, no further calibration is needed when changing other process parameters like welding speed, tool rotational speed or plate thickness. It should be noted that this heat source formulation does not depend on the contact state. The resulting heat source output can be compared to the linear analytic heat source shown in Fig. 3.6(a). The TPM heat source generally predicts higher values of q for large values of r where the temperature is low, τ_{yield} is high and much heat is generated. For very low values of r the TPM heat source predicts lower heat output as compared to the linear analytic model, as the temperature is very high and τ_{yield} very low. A typical TPM heat source graph is shown in Fig. 3.6(b). The thermal model developed in this study (see Section 5.1) features such a TPM heat source.

A unique capability of the TPM heat source is to predict the machine torque M_T from a numerical simulation with only thermal degrees of freedom. This is done by integrating the temperature dependent material flow stress $\tau_{yield}(T)$ multiplied with the distance to the rotational axis of the tool r over the contact surface of the tool and the work piece according to

$$M_T = \int_{\partial\Omega} \tau_{yield}(T) r \, dA. \tag{3.10}$$

This assumes the stresses to be in tangential direction only, which has to be taken into account when working with complex geometry features on the pin.

3.2.1.6 Numerical Implementations

When it comes to the implementation of (FE) numerical thermal models, there are two important choices to be made [57]: One choice is between using a Lagrangian or an Eulerian frame. The Lagrangian frame implementation assumes that the material is associated with the models element mesh. No material is exchanged between elements. In the Eulerian frame an additional convective motion of material through the mesh is possible. This allows for a static mesh and still includes energy transported by moving material. The second choice is between a time dependent and a steady state formulation.

The simplest case of a FSW thermal model is an Eulerian model with fixed mesh that captures the welding speed by moving the material through the entire plate. Such a model is usually solved in steady state formulation as the geometry of the model is static as presented by Colegrove et al. [79]. Unfortunately, experimental welds begin with a cold work piece, tool and machine. Therefore it takes a considerable amount of time to approach the steady state. An estimation of this transient heat up time can be made from transient thermal models [2]. It can be stated that most experimental setups in a laboratory will not reach a steady state. The influence of the heating up of tools and machine have to be considered. A purely Eulerian model cannot capture this effect accurately. On the other hand a purely Lagrangian model cannot account for the material moving around the tool in a shear layer. Therefore mixed formulations of transient models are the most promising choice.

In the last decade several numerical models for the FSW process have been derived using various codes and levels of detail. An overview of the available numerical thermal models is provided in the appendix, Tab. D.2.

3.2.2 Flow Models

The material flow around the pin has been modelled in different ways. There are approaches that prescribe analytical velocity fields to determine stresses and strains of the welded material [80]. The velocity fields are generated by superposition of circumventing, vortex and torsion velocity components. Although this is helpful to increase the understanding of the formation of different material flow patterns, it cannot be readily used in a predictive way for new process parameters. The focus of this study is to predict the forces and torque acting on the tool. The material flow resulting from the tool rotation in general and the pin features in particular is of interest as well. Therefore a Computational Fluid Dynamics (CFD) or Computational Solid Mechanics (CSM) approach is needed.

3.2.2.1 CFD Flow Modelling

The most common approach in flow modelling of FSW is to solve a formulation of Navier-Stokes equations

$$\rho(u \cdot \nabla)u = \nabla \cdot [-pI + \eta(\nabla u + (\nabla u)^T)] \tag{3.11}$$

$$\rho \nabla \cdot u = 0 \tag{3.12}$$

in a computational fluid dynamics (CFD) framework, where ∇ is the Nabla operator defined as $\left(\frac{\partial}{\partial x}, \frac{\partial}{\partial y}, \frac{\partial}{\partial z}\right)$, u is the velocity vector, and η is the viscosity. This includes the assumption that the plasticised material in the shear layer around the tool can be treated as a fluid. It has been shown by Aukrus and LaZghab [81] that aluminium alloys can be described as a shear thinning liquid at sufficiently high temperatures. It can be shown that the Reynolds number in FSW is below the expected laminar to turbulent transition [57]. Therefore laminar flow can be assumed. Common software for the solution of the CFD models are FLUENT [67, 68, 22] and COMSOL [57, 66].

First approaches include 2D Eulerian models by Seidel and Reynolds [82], Schmidt [57] and Colegrove and Shercliff [68]. It can be stated that a 2D model of the material flow around the tool cannot be used to predict forces or torque acting on the tool. The material flow is not constant or linear in the depth direction, so that the forces and torque found in a 2D representation cannot be extrapolated. Still, even advanced flow models like the one proposed by Colegrove and Shercliff [69] are solved in 2D because of limited computational resources and time. A similar limitation is also true for any axial symmetric flow model like the one developed by Colegrove [70]. The reason for this is the asymmetry of the material flow. Plastic material from the advancing side is swept around the retreating side giving rise to a force in transverse direction due to the Magnus effect [11] as illustrated in Fig. 3.7.
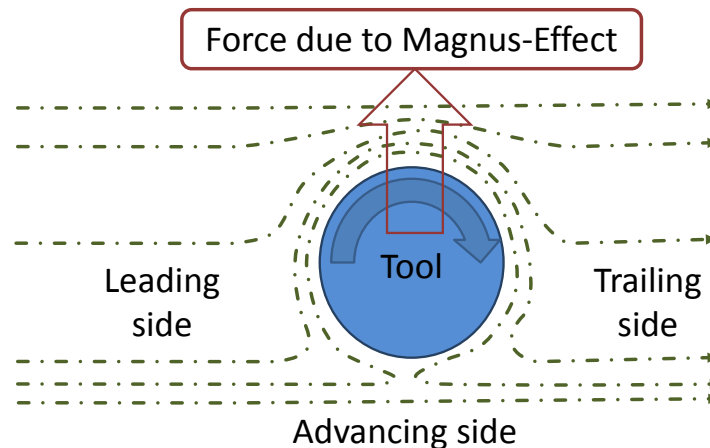

Figure 3.7: Schematic plot of magnus effect in FSW

Some work has been extended to 3D models [67]. The primary interest here was to include the convective heat transport of the shear layer into a thermal model. The heat generation is calibrated to fit experimental data. As the material and heat generation model used in this work is very basic, the flow has to be considered a rough approximation sufficient for the task at hand but insufficient for force predictions. Tool features are not included.

Featured tools have been considered in later work by Colegrove and Shercliff [22], Schmidt and Hattel [66] and Atharifar et al. [11]. A common limitation of these works is the use of a steady state solution. As featured tools are not rotationally invariant, these solutions can only be considered an approximation of a snapshot of the material flow. As they cannot consider the history of the material flow, the accuracy of the predictions is limited. The actual dynamic variation of the conditions within a rotation of the tool cannot be determined.

The material flow depends on the contact condition between tool and work piece (see Section 3.2.1.3). It relates the tool rotational speed with the velocity of the welded material at the tool interface. This interface velocity governs the entire material flow around the tool. This has been investigated by prescribing different contact conditions [66]. Although recent studies do not assume pure sticking condition anymore [11], the contact condition is chosen as a constant. This remains problematic. As in thermal models, the contact condition should not be an input to a flow model, because it cannot be accurately determined experimentally.

The validation of material flow models has been attempted in different ways. One is by comparing predicted forces to experimental forces [11]. Another is by adding marker material to an experimental weld and using analytical techniques like X-ray imaging, X-ray tomography and metallography (sectioning) to investigate the deformation of these [63]. This technique can provide an exact measure for the shear layer size. Some attempts have also been made to determine velocities within the shear layer from the deformation of the markers. The accuracy of these velocity measurements may be doubted because of several reasons. In order to obtain an interpretable marker pattern the interaction with the marker must be less than one rotation of the tool to avoid aliasing. Therefore the tool must be stopped in the exactly right moment with a very harsh deceleration. Even if this can be realised, it cannot be assumed that the flow in this situation is comparable to a continuous welding situation because the velocity is dominated by the deceleration and does not correspond to the nominal parameters.

Several flow models include a thermal model with different degrees of coupling. In a simple case the interaction is limited to the heat transported along with the flowing material [67]. A fully coupled approach includes heat generation by viscous dissipation [11]. For the sake of simplicity a decoupled investigation may be preferred if a reasonably accurate thermal model is available. Such a thermal model will need to include some information on the material shear layer. Therefore an iterative approach is needed. Another approach can be to integrate a flow model as local model into a larger thermal model. This has been demonstrated by Carbone et al. [83] and Schmidt and Hattel [66] using COMSOL. Flow models can use different material

models ranging from very basic assumptions to experimentally validated models taking into account the temperature and strain rates [81, 84, 85]. An overview of selected CFD flow models is provided in the appendix, Tab. D.3.

3.2.2.2 CSM Flow Modelling

An alternative way of modelling the material flow around the tool is by solving for plastic deformation in a solid mechanics FEM framework. This computational solid mechanics (CSM) method usually requires an ALE formulation and a re-meshing strategy to accommodate the large deformations. A further challenge for this modelling approach is the need to deal with topological changes and void formation and closure. Therefore most ALE FSW models are implemented in commercial software for forging and related processes such as DEFORM-3D [86, 7] or FORGE3 [87]. Another common commercial code for mechanical material flow models is ABAQUS [88, 89, 90].

When considering the dimensionality and time dependence of the model the same restrictions are valid as in CFD. Therefore 2D Eulerian approaches like the one reported by Xu et al. [88] cannot provide the desired outputs. The computational resources needed for 3D calculations are generally very high. The model reported by Schmidt [57] is solved in no less that 14 days (3GHz single core PC) even when using mass scaling to achieve an acceleration of a factor of 1000. A major bottleneck here is the contact between tool and welded material that has to be solved with high resolution.

Due to this limitation some studies focus on single process steps like the plunging step [91]. Here a Johnson-Cook material law and a constant friction coefficient of 0.3 (taken from literature) are applied. The comparison of this model to experimental data still reveals large discrepancies in the predicted forces. Zhang et al. [89] add an upper limit (saturation) to the frictional stress to prevent unrealistically high stresses that exceed the material strength as shown in Fig. 3.8. The model is validated by comparing the plastic strain predictions to microstructural features of the cross section of experimental welds. This is a promising qualitative approach. In more recent work the rate-independent plasticity was replaced by a rate-dependent constitutive model. Unfortunately, the used friction coefficient has not been published. Buffa et al. [86] achieve a better correspondence between predicted and experimental forces after calibrating the friction coefficient. Still a constant value of 0.46 is assumed. It is problematic to generalise these results as the contact conditions and friction coefficient depend on many influencing parameters that are not known in detail. One of the most advanced CSM model available presented by Guerdoux and Fourment [87] uses a Norton law Eq. (3.13) for friction and thus takes into account the temperature dependence in $K(T)$ and the relative velocity Δv_s.

$$\tau_{friction} = -\alpha_f K(T) \|\Delta v_s\|^{p-1} \Delta v_s \tag{3.13}$$
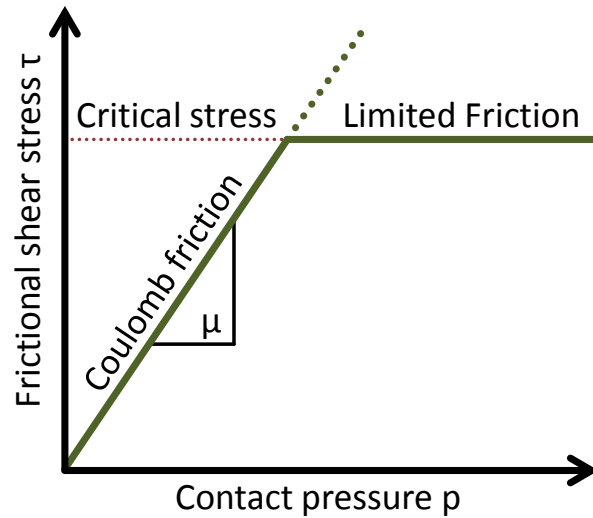
Figure 3.8: Limited friction law in CSM models

The coefficients a_f and p are calibrated using experimental force measurements. The model can be solved in a transient frame and therefore in principle be used to show the evolution of volumetric welding defects like tunnels and excessive flash. Still the accuracy is limited. A featured tool is represented by additional prescribed velocity components on the surface of the geometrically smooth tool. This can be used to show that there is an influence of such velocities on the formation of the joint. It cannot be used however to actually find the influence of a certain tool geometry on these velocities. Therefore more work is needed to allow for knowledge based tool development.

An overview of the available solid mechanics flow models is provided in the appendix, Tab. D.4.

3.2.2.3 Material Models

The information on the material behaviour needed for all models can be acquired from different sources. Basic physical relationships can be expressed analytically on the basis of well known physical constants only. More often assumptions have to be made on parameters in such equations e.g. the friction coefficient. These assumptions are often derived from experimental experience [53]. Many material parameters can be readily found in literature [92]. Unfortunately, the validity limits of published results are often not explicitly stated. In more complex situations it is possible to fit experimental data with arbitrary curves [93] or calibrate the needed parameters of a physically sound formulation by dedicated experiments.

The most important material characteristic in the context of FSW flow modelling is the hot deformation behaviour. The flow stress as a function of temperature and other parameters needs to be predicted. A basic approach is to use tabulated data as is done for the TPM heat source. The basic model taking into account temperature T and strain rate $\dot{\epsilon}$ is a power law Eq. (3.14) that can also be expressed as Eq. (3.15) using the universal gas constant R and the

Zener-Hollomon parameter Z as defined in

$$\dot{\epsilon} = A\sigma^n \exp\left(-\frac{Q}{RT}\right) \tag{3.14}$$

$$Z = A\sigma^n \tag{3.15}$$

$$Z = \dot{\epsilon}\exp\left(\frac{Q}{RT}\right). \tag{3.16}$$

This can be successfully fitted to experimental data by the parameters A, n and Q as shown by Zhang and Baker [94] for AA6082. A similar approach is the inverse hyperbolic sine law Eq. (3.17) [22] that is also used in this study (see Eq. (5.14) (page 51) and Eq. (5.17)).

$$Z = A(\sinh \alpha\sigma)^n \tag{3.17}$$

This can be prescribed as it is or extended by including an empirical softening regime near the solidus temperature of the material [69].

The modelling activities in terms of material behaviour are, however, not limited to flow stress. For aluminium alloys there are also many approaches of formulating material models with a different focus. The metallurgical reactions in the HAZ are investigated by Bjørneklett et al. [95] as is the microstructure evaluation as a function of temperature and strain rate. They have been modelled in general [96, 53, 97] and in the context of FSW [98].

The above mentioned investigations usually deal with a single alloy or alloy families. In some cases the temper of the material also plays an important role for the selection of the best model representation of the behaviour of a certain material [94]. Not all alloys and tempers have been examined experimentally, and the quality of the results is not homogeneous for those that have been. Therefore the generalisation that would be needed in order to apply a material law to different alloys has not been achieved yet. This is a limiting boundary condition when trying to formulate a general FSW model today.

3.2.3 BT-FSW Specific Modelling

Very few models published in literature explicitly deal with BT-FSW. These include work by Deloison et al. [99] and Hersent et al. [100] as well as Neumann et al. [3, 50] and Hilgert et al.[2, 101]. The main reason for this seems to be the limited availability of experimental work on BT-FSW. Many ideas for the modelling of standard FSW can be directly used in modelling of BT-FSW. Still the focus of the models needs to be slightly different as the critical boundary conditions are not the same in both process variations. Especially tool loading is usually not the driving force in single sided FSW. This may also be a reason for the fact that one cannot find much systematic treatment of tool design in literature. There are some promising numerical studies featuring tool design but their focus is on the influence of tool shape on the material flow [68, 102]. The loading of the tool and the resulting stresses are not

investigated. Therefore there is a strong need for work in this field to move to a knowledge based tools design.

3.2.4 Summary and Conclusions

- Promising approaches for numerical thermal models of FSW are available. They can be applied to BT-FSW with minor modifications. Purely Eulerian (steady state) models are not well suited for process development as the experimental welding length is usually insufficient to reach a quasi-steady-state. Time-dependent purely thermal models with dynamic geometry are desirable.

- The material flow and the acting forces can be modelled in a solid mechanics (CSM) or fluid dynamics (CFD) approach. The fluid dynamics approach is favourable as it requires less computational effort and avoids problems generated from excessive re-meshing. A 3D model is needed because neither 2D nor 2.5D axis-symmetric models can capture the asymmetric material flow and the resulting process forces.

- The development of a transient CFD model with featured tools is desirable for accurate force predictions. Only such a model can be used to evaluate the tool loads of featured tools and therefore provide valuable input for knowledge based tool development.

- The contact state between the tool and the deforming material is needed as an input (in one way or another) for most thermal and material flow models. As this quantity cannot be accurately determined experimentally, the predictive capabilities of such models are very limited. The contact state must be an output of a flow model or combined process model.

- A coupled solution of temperature evolution and material flow is possible. The computational resources needed for this kind of models are very large. In order to be a useful tool in process development a model should be capable of generating predictions sufficiently fast. Therefore decoupling the different physical interactions as much a possible is desirable.

- There is a lack of systematic scientific work on tool development. This is most important for bobbin tools. They have to produce sound welds comparable to standard FSW tools while withstanding considerably harsher loading conditions. A trial and error development in this field is very expensive and time consuming and has delayed the implementation of economic industrial applications of the BT-FSW process.

Chapter 4

Experimental

4.1   Hardware Implementation

The welding experiments were conducted on the FlexiStir device at HZG/WMP. This versatile experimental welding machine has been developed to conduct in-situ welding experiments in the synchrotron facilities of DESY in Hamburg, Germany. It is a compact machine driven by 13 servo electrical motors allowing for flexible modes of operation. The machine with mounted BT-FSW welding head can be seen in Fig. 4.1.

Within the scope of this study the hardware has been upgraded with a three dimensional piezoelectric force measurement system. The system comprises four 3D Kistler sensors to measure the welding force and lateral force additional to the force in Z-direction. These measurements make X-force controlled welding possible (see Section 6.3.2). An additional set of 1d piezoelectric force sensors was mounted in the welding head to measure the Z-forces acting on the lower shoulder and pin only. The two Z-force channels therefore allow for an evaluation of the forces acting within the gap between the two shoulders. This is used for the Z-force controlled welding process (see Section 6.3.2). A schematic view of the force sensor setup in the welding head is given in Fig. 4.2. The FlexiStir is controlled by a programmable logic controller (PLC) programmed and operated using CoDeSys (3S-Smart Software Solutions) which conforms to the international industrial standard IEC 61131-3. The controller software has been expanded to reflect the changes in hardware and to enable various process control strategies (see Section 6.3.1) and data acquisition (see Section 4.3).

4.2   Welding Experiments

Welds were carried out with various process parameter combinations and control strategies. In order to preserve comparability all welds evaluated in this study were performed on specimens made of AA2024 in T351 condition and have one of two different geometries. The geometry of the specimens is defined in Fig. 4.3. The first variant features a run-in notch in the centre line
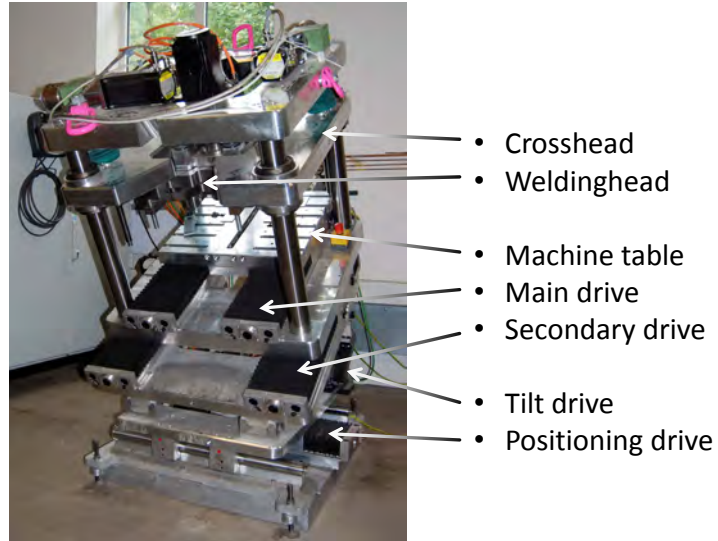
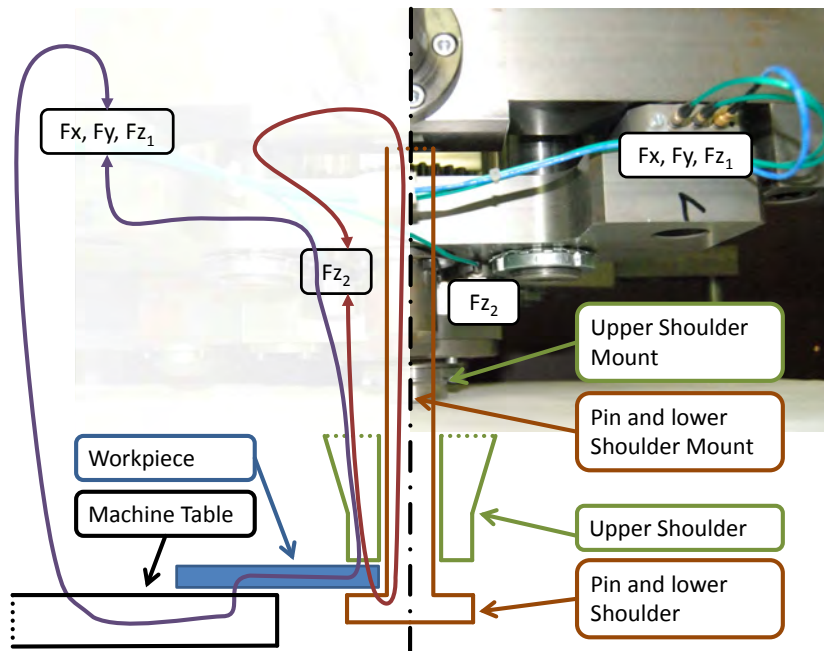Figure 4.1: FlexiStir experimental welding machine

Figure 4.2: Force measurement in the FlexiStir BT-FSW welding head

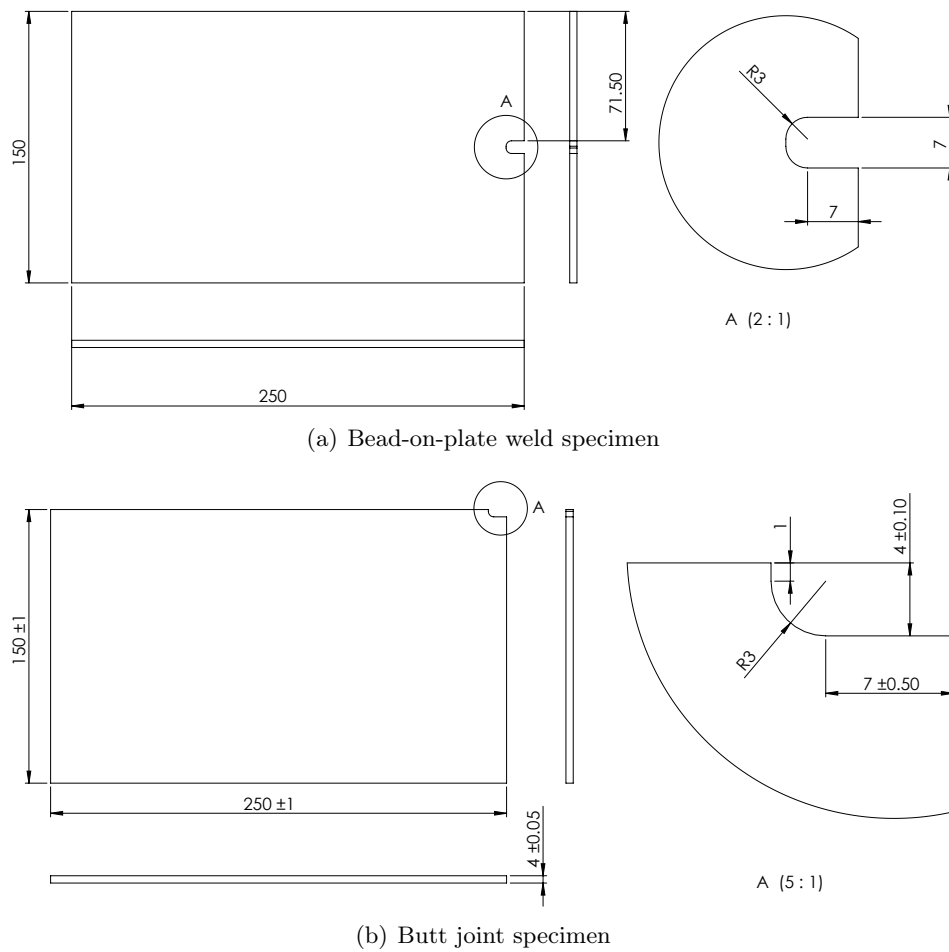(a) Bead-on-plate weld specimen

(b) Butt joint specimen

Figure 4.3: Geometry and dimensions of the welded specimens

and is used for bead-on-plate weld studies as shown in Fig. 4.3(a). The other features a half run-in notch at a corner (Fig. 4.3(b)). These specimens are combined to form one complete run-in notch and used for butt joints. The nominal composition of the material used is given in Tab. 4.1. In the course of the work two batches of material where used. Hardness and tensile tests were performed to ensure equivalent material properties and behaviour. No significant differences where observed. Still all tensile tests presented in Section 7.1.4.2 were performed on welds that were initially made or repeated with the second material batch to avoid any influence from the base material.

Three campaigns of welding experiments for AA2024 are described in this study. Investigations and welding campaigns in Magnesium AZ31, AA5454 and AA2219 have been conducted and will by published elsewhere.

The first campaign is referred to as baseline experiments. They were performed according to the state of the art of tooling and process control on the FlexiStir welding machine as it was at the beginning of this work. The welding speed for these welds was 0.3 mm/s at 1200RPM.

Elements [wt%]	Si	Fe	Cu	Mn	Mg	Cr	Zn	Ti	Others (each)	Others (total)	Al
Min.	-	-	3.8	0.3	1.2	-	-	-	-	-	
Max.	0.5	0.5	4.9	0.9	1.4	0.1	0.25	0.15	0.05	0.15	bal.

Table 4.1: Nominal chemical composition of AA2024

The process was gap (i.e. distance between the shoulders) controlled (see Section 6.3.1.1).
The second campaign is referred to as controller development experiments. The tools used are the same as for the baseline experiments, while the process is Z-force controlled using an additional in-plane-force overload protection for the run-in of the tool implemented by a XY-force controller. Experiments with varying gap force were performed at 600-800 RPM for welding speeds from 0.5 to 2.0 mm/s. These experiments are used to validate most of the models predictions.

The third campaign is referred to as tool validation experiments. The tools used for these experiments were developed based on numerical models and the experiences gathered from tool manufacturing. The process was controlled according to the results of the controller development experiments.Tab. 4.2 lists the parameter sets for all welding conditions discussed within this work. The process parameters were chosen with respect to previous experience, the evaluation of proceeding experiments and the numerical predictions of tool loads and temperature as discussed in Section 5.1.5.2 and Section 6.2.2. The aim of the experiments was to generate different welding conditions to validate the numerical models and to increase productivity and joint quality while avoiding damage to the tool.

campaign	tool rotation [1/min]	welding speed [mm/s]	z-force target [kN]	id
baseline	1200	0.3	(gap controlled)	B_01 - B_05
controller development	1000	0.9	2.9	C_01
	1000	0.9	2.6	C_02
	1000	1.2	2.6	C_03
	1000	1.2	3.0	C_04
	800	0.5	1.5	C_05
	800	0.5	2.5	C_06
	800	0.7	2.5	C_07
	800	0.9	2.5	C_08
	800	1.1	2.5	C_09
	800	0.9	2.7	C_10
	800	0.9	2.9	C_11
	800	0.9	3.3	C_12
	800	1.2	3.0	C_13
	800	1.2	3.2	C_14
	800	1.2	3.4	C_15
	800	1.5	3.5	C_16
	600	0.9	2.9	C_17
	600	0.9	3.2	C_18
	600	1.0	3.0	C_19
	600	1.0	3.4	C_20
	600	1.0	3.7	C_21
	600	1.2	3.2	C_22
	600	1.2	3.4	C_23
	600	2.0	4.0	C_24
tool validation	600	1.0	2.7	T_01
	450	2.0	4.0	T_02
	500	1.2	3.0	T_03
	400	1.0	3.0	T_04
	350	1.2	3.0	T_05
	350	1.5	3.0	T_06
	350	2.2	3.1	T_07

Table 4.2: Parameters for all welds discussed in this study

4.3   Data Acquisition

During all welding experiments in the set-up described in Section 4.1 and Section 4.2, measured data is collected from the piezoelectric force sensors as well as from the machine controller. For the sake of simplicity the in-plane forces from all four 3D sensors are summed up to form a single value for F_x in X direction and F_y in Y direction for the output in the log file. The single sensor values are only used in torque calculation. The torque acting on the tool can be measured in two independent ways. The first uses the 3D force sensors of the machine head. When the individual forces in X direction and in Y direction are known along with the positions Δx_{sensor} and Δy_{sensor} of the sensors relative to the tool, the torque can be calculated according to

$$M_T = \sum_{i=1}^{4} F_{x_i} \Delta y_{sensor_i} - F_{y_i} \Delta x_{sensor_i}. \tag{4.1}$$

Here F_{x_i} and F_{y_i} are the forces measured by a single sensor while Δy_{sensor_i} and Δx_{sensor_i} are the corresponding distances. The second method to estimate the torque is to use the motor current. This is done independently for both spindle motors according to

$$M_T = \frac{U_{motor} I_{motor}}{\omega}, \tag{4.2}$$

where U_{motor} is the motor voltage, I_{motor} is the motor current and ω is the rotational velocity. With this approach the torque of the lower shoulder and pin M_{lower} and the torque of the upper shoulder M_{upper} can be evaluated independently and summed up to the total torque according to

$$M_T = M_{lower} + M_{upper}. \tag{4.3}$$

The difference in accuracy of these two methods is discussed in Section 5.1.6.

All relevant quantities including forces, torque, welding speed and shoulder gap are recorded to a log file at a maximum frequency of 200 Hz. There are two modes of data logging available. The continuous logging is always active as a default setting. It is initiated when the welding process starts. The recorded samples are written to the controller's file system. This technique can be used for welds with virtually infinite duration. The data rate is not constant though, as the file system reacts in a asynchronous way. The mean data rate is close to the ideal 200Hz, but gaps of up to 0.1s can occur. As the data collated this way is insufficient for certain analyses like Fourier transform, a second logging option has been implemented. This burst mode log is triggered by the user and records a limited amount of samples into a preallocate array within the controller's RAM. This guarantees maximum speed at constant frame rates. The recorded and logged data is used for model validation and process control. Examples are provided in Figure 5.33 and Section 6.3.3.

For selected joints, type-K thermocouples are positioned on the specimens and the joining

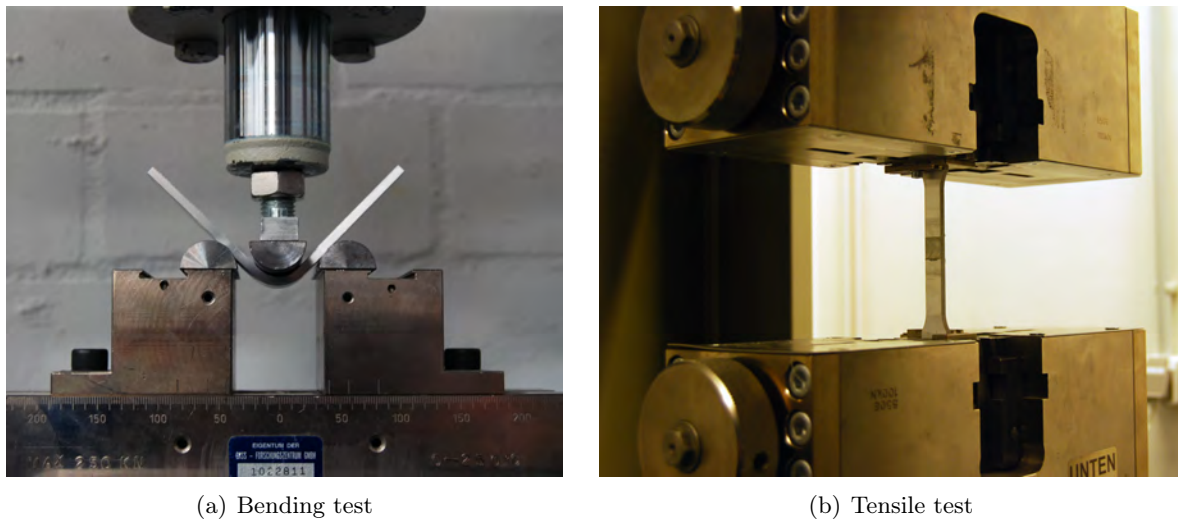(a) Bending test

(b) Tensile test

Figure 4.4: Mechanical testing setup

process is recorded with an InfraTec ImageIR infrared thermal camera. The thermocouple data is used to calibrate and validate the thermal camera output. These results are described in Section 5.1.5.2.

After welding, several specimens are taken from the joints for bending tests, metallography evaluation, hardness testing and tensile testing. Due to the limited welding length available, not all these tests are conducted on every individual joint but on welds performed with the same process parameters and control settings. As a steady welding state is not completely reached in the present experimental setup, this is a source for scatter. The bending test uses a three-point-bending setup on a manually operated hydraulic press. The geometry of the specimen and fixture are shown in Fig. 4.4(a). These tests are performed for all welds that have not been discarded after optical inspection (see Section 7.1.1). This test allows for a fast qualitative evaluation of the joint quality. The width of the specimens is 20mm, the length is 150mm and the thickness is the plate thickness of nominally 4mm. No machining is applied to the specimen aside from the extraction out of the welded sheet. Results are provided in Section 7.1.2. A Leica DM IRM light microscope is used to asses the joint quality and detect the presence of volumetric defects (see Section 7.1.3). Additionally the geometric shape of the shear layer (thermal-mechanically affected zone TMAZ) is determined on the macrographs. This is needed for the validation of the shear layer predictions of the flow model. Hardness measurement is conducted as 5HV0.5 hardness line profiles in the middle of the plate thickness on the cross section of the welds using a Zwick/Roell ZHV hardness testing machine. The location and coordinate origin of the measured line is shown in Fig. 4.5. The measured profiles are reported in Section 7.1.4.1.

Tensile specimens are prepared according to the specifications given in Fig. 4.6. They are

tested with a Zwick / Roell 100kN tensile testing machine according to DIN EN 10002. A displacement rate of 0.6mm/min is chosen. The setup is shown in Fig. 4.4(b) The results are presented in Section 7.1.4.2.
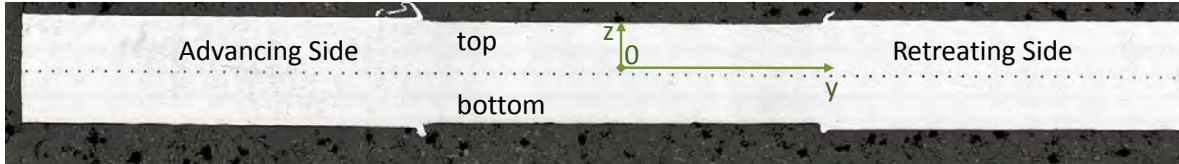

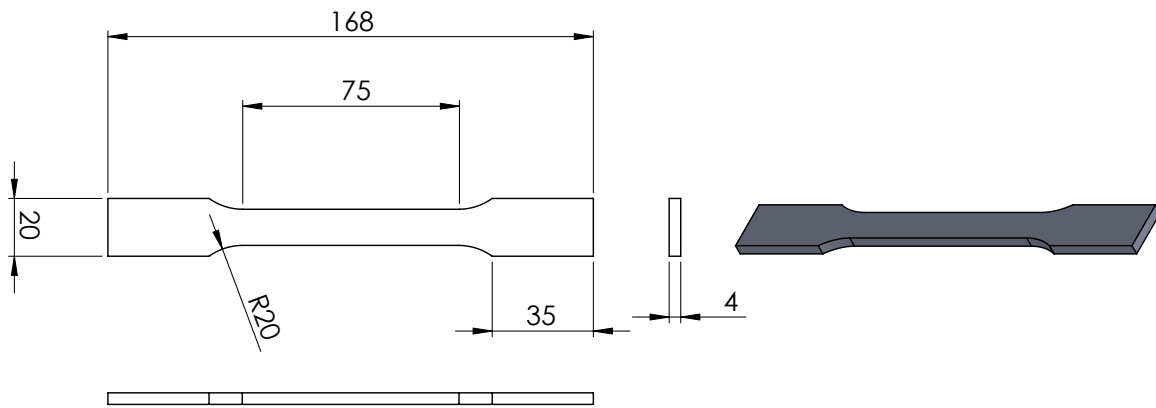Figure 4.5: Location of the microhardness measurements

Figure 4.6: Geometry and dimensions of the tensile specimens

Chapter 5

Process Modelling

5.1 Thermal Modelling

The thermal model used for all temperature predictions in this work is based on own previous work on TPM models for bobbin tool FSW [2, 101]. The Moving Geometry (MG) model described in these studies has been extended using deformed meshes to achieve a smooth motion of the tool in between the discrete time steps. This approach will be referred to as Advanced Moving Geometry Model AMGM and is described in detail in Section 5.1.2.

5.1.1 Thermal Pseudo-Mechanical (TPM) Heat Source

The implemented TPM heat source relies on input data on temperature dependent shear yield stress. This can be derived from tensile yield stress data provided in [103] by using the relationship from

$$\tau_{yield} = \frac{\sigma_{yield}}{\sqrt{3}}, \tag{5.1}$$

where τ_{yield} is the shear yield stress and σ_{yield} is the tensile yield stress. The resulting data is listed in Tab. 5.1 and plotted in Fig. 5.1.

5.1.2 Advanced Moving Geometry Model (AMGM)

The AMGM extends the MG model for BT-FSW that uses discrete time steps with intermediate mapping to account for the moving tool of a FSW weld in a purely thermal FE model. The original concept allows for fast predictions of transient thermal fields including an accurate representation of the geometric entities involved in the joining process. A drawback of the approach is the large amount of intermediate mapping. This is not only time consuming but also involves numerical interpolation and may influence the accuracy of the results. To limit the amounts of mapping steps a new concept is introduced to the MG model.

In the AMGM the motion of the tool between two remeshing and mapping steps is represented
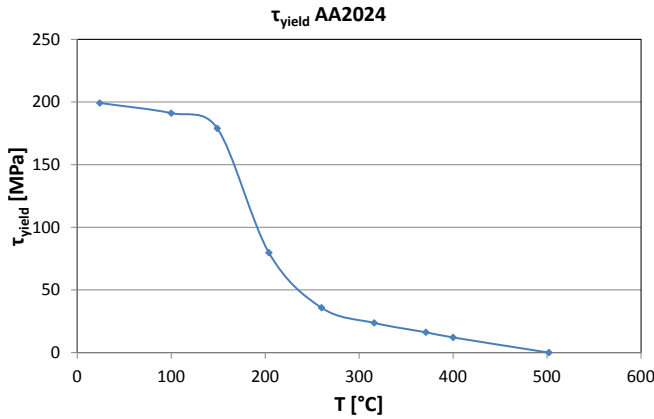
Figure 5.1: Calculated shear yield stress

Temp. [°C]	σ_{yield} [MPa]	τ_{yield} [MPa]
24	345	199.2
100	331	191.1
149	310	179.0
204	138	79.7
260	62	35.8
316	41	23.7
371	28	16.2
400	21	12.1
502*	0	0

*: Cutoff value added (see [65])

Table 5.1: Shear yield data [2]
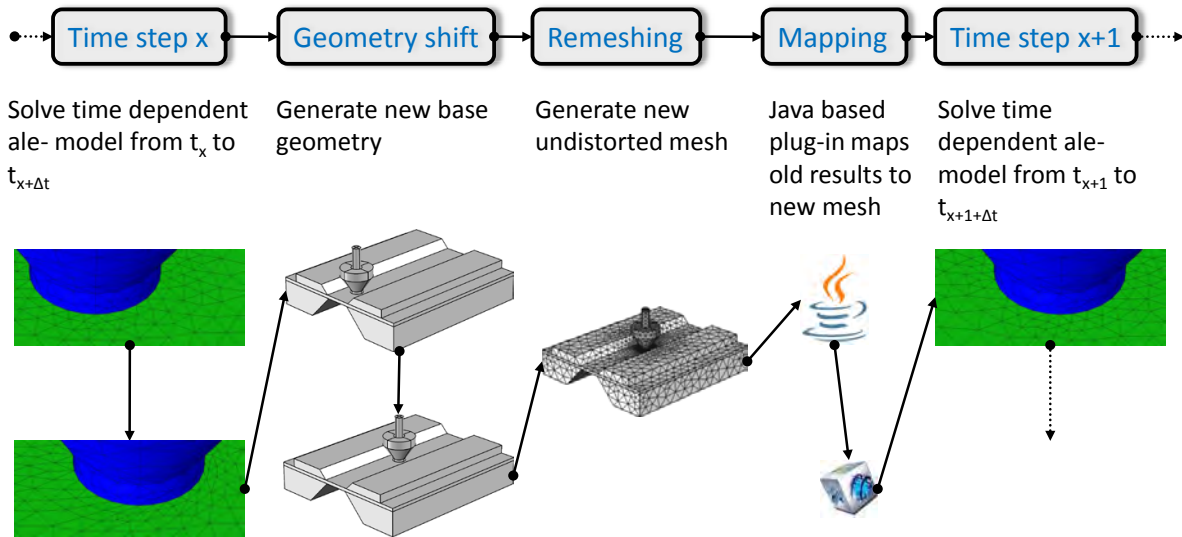
Figure 5.2: Schematic plot of the AMGM

by a deformation of the mesh. Now the limiting factor for the size of the discrete time steps is no longer the smooth representation of the tool motion, which implies a maximum advance per time-step of a fraction of the shoulder diameter, but the deterioration of mesh quality. The amount of deformation achievable in between two remeshing sequences is now considerably extended. This leads to faster predictions. The model's reliability is improved as the position of the tool is now represented correctly not only at the discrete time steps but also at any solver-time-step in between. A schematic of the AMGM approach is given in Fig. 5.2. Fig. 5.3 shows the mesh deformation and remeshing of one iteration of the AMGM.

The implementation of the AMGM is not done in Matlab script as was the original MG model due to the change of strategy of Comsol Multiphysics FE software. The most favourable user API is now provided for JAVA programming language. This has been used for all implementations of user features described in this study for Comsol versions above 4.0. The remeshing

(a) Initial mesh

(b) Deformed mesh

(c) After re-meshing and mapping
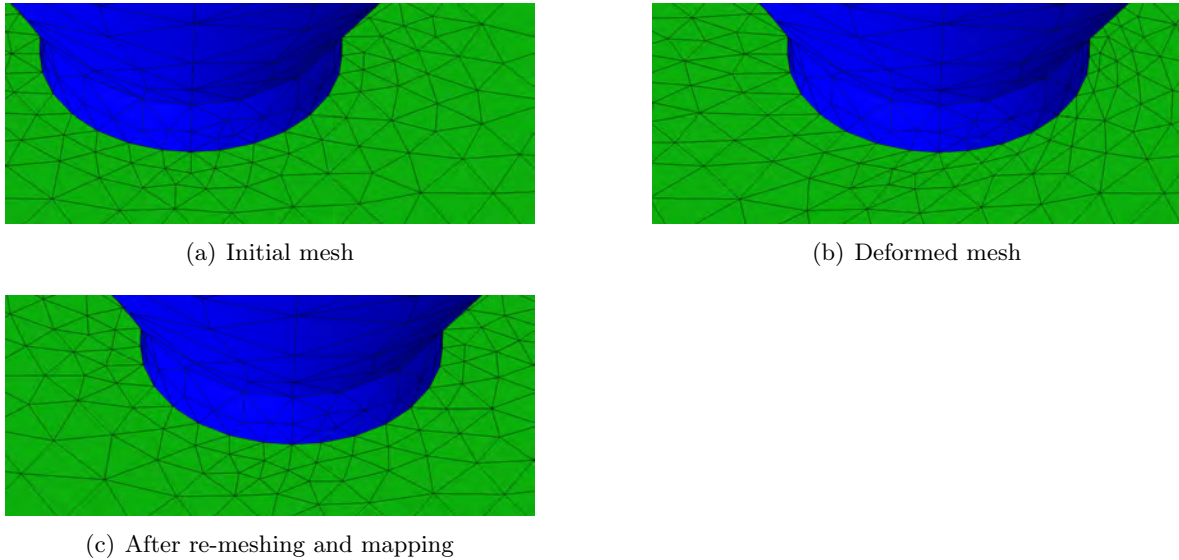
Figure 5.3: Mesh deformation and re-meshing within one iteration of the AMGM

and mapping is done in a custom set of java classes. Abbreviated versions of these can be found in Appendix C. The mesh deformation is implemented using the predefined Moving Mesh (ALE) physics interface. The location of the tool is parametrised as a function of time while the workpiece mesh is allowed to freely deform to accommodate the motion. The location of the deformed mesh nodes is solved for in a segregated solver step before solving for the temperature. The governing equation for the free mesh deformation is the predefined Laplacian smoothing with second order geometry elements.

This adds a considerable number of degrees of freedom to the model. As the coupling between temperature and tool location is unidirectional by nature, the segregated solver approach does not noticeably increase solution time. Note that the maximum Java heap size of Comsol needs to be increased to run longer AMGM simulations. When available 8GB are recommended.

The AMGM is a mixed Lagrangian and Eulerian model. The motion of the tool is defined in a Lagrangian frame. Thus the exact geometry of the experimental setup can in principle be included in the model. The level of detail of the experimental setup that needs to be included in the enmeshed model depends on the duration of the simulated weld as well as the used materials. Very short and fast welds can be accurately represented by the workpiece and a small part of the tool. Longer and slower welds have to include the clamping of the plates as well as larger regions of the tool and welding head. This is due to the transient effect of tool and machine heating.

The motion of the plasticised material in the vicinity of the pin is modelled in an Eulerian frame. This means that heat flow corresponding to material motion through the Lagrangian mesh is prescribed using a volumetric convective heat flow boundary condition. This allows to capture the asymmetric conditions present in FSW in the thermal model without the need to

couple a mechanical model to predict the material deformation in a Lagrangian frame. This is important as a fully coupled model cannot be solved in reasonable time with present computational resources. As the aim of the thermal model is to save time in process development, it needs to be sufficiently fast to perform many iterations for result maps and optimisation in a multidimensional parameter space.

The shape and velocity field of the plasticised material extruded around the pin must still be known as a input parameter to the thermal model. An educated guess is possible from the knowledge of the microstructure present in welded joints (see Fig. 3.3). In order to get best results, it is possible to use a CFD model to compute the shear layer (see Section 5.2). As this is a time consuming operation, it is not suggested to perform time dependent CFD simulations for every parameter and geometry combination. The impact of the shear layer shape on the overall temperature field is small compared to the computational cost of the predictions. It is sufficient to use an analytical shear layer model that has been calibrated with a sufficient number of CFD predictions. An analytical shear layer model (ASLM) like this is described in Section 5.1.3.

5.1.3 Analytical Shear Layer Model (ASLM)

The temperature field in the vicinity of the tool is not only defined by the heat generation in the heat source, but also by the convective heat transport that occurs with the plastic material that is extruded around the pin and forms the shear layer. It is important to consider this convective heat transfer in order to get precise predictions of the temperature distribution. This can be seen from the Péclet number as defined in

$$Pe = \frac{\rho c_p u_c L}{k}, \tag{5.2}$$

where ρ is the material density, c_p is the specific heat capacity, u_c is the characteristic velocity, L is the characteristic length and k is the thermal conductivity. In the case of a bobbin tool shear layer the characteristic length can be defined to be the shoulder radius (in this case $\approx 7.5mm$) and the characteristic velocity can be defined as the maximum tangential tool velocity. At 600 RPM this would be $\approx 150mm/s$. The resulting Péclet number in this case is ≈ 23. This high value indicates that the convective heat transfer cannot be ignored.

The ASLM model used in this study is based on previous work by Schmidt et al. [61] on standard FSW tool shear layers and own work [2]. It is used to define an analytical velocity field for the work piece material in the close vicinity of the tool. This velocity is used to generate convective heat flux resembling the material moved around the tool in a shear layer. Fig. 5.4 shows the magnitude of material velocity in the area between the two shoulders with and without a shear layer present. The model uses a polar coordinate system based on r and z directions, as in this application the shear layer can be assumed to be close to axis symmetric.
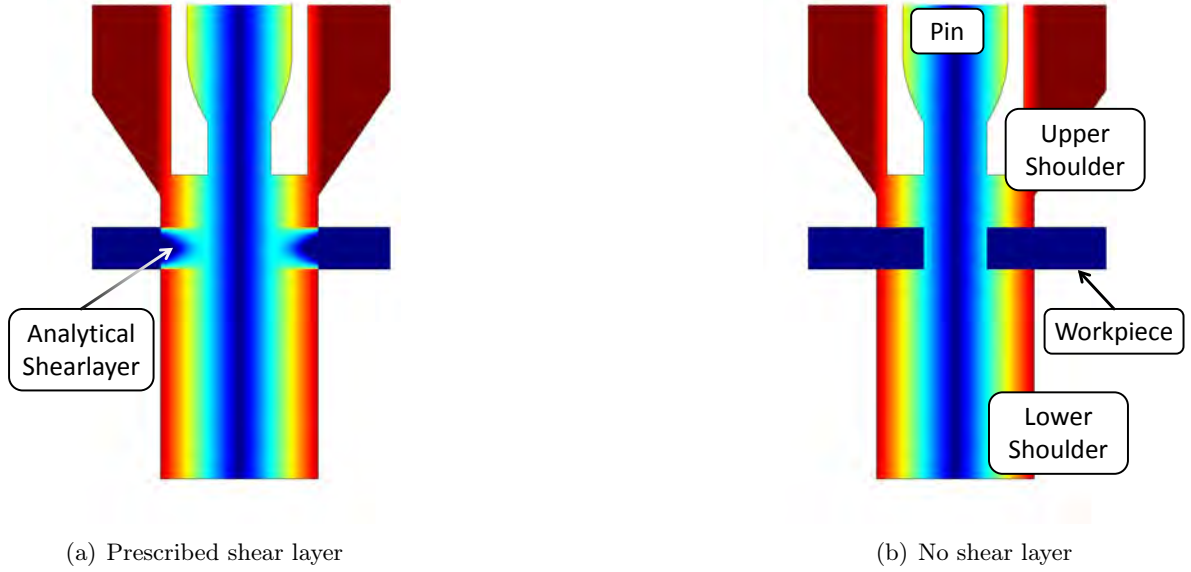
(a) Prescribed shear layer

(b) No shear layer

Figure 5.4: Material velocity

This assumption can be made as the Magnus effect and the acting forces are of no importance here (see Section 3.2.2.1). The velocity output of the model is based on the coordinates dr and dz that give the local distances to the tool in r and z direction (see Fig. 5.5).

The model consists of six equations. Eq. (5.4) and Eq. (5.5) deal with the distance to the tool shoulders, Eq. (5.6) controls the designed boundary shape of the shear layer, Eq. (5.3) and Eq. (5.7) deal with the distance from the tool pin, and Eq. (5.8) defines the velocity field.

$$dr = r - R_p \tag{5.3}$$

$$dz = \frac{t_{plate}}{2} - |z| \tag{5.4}$$

$$\zeta = \frac{2dz}{t_{plate}} \tag{5.5}$$

$$R_* = (1 - \zeta^{m_{shape}}) \cdot R_s + \zeta^{m_{shape}} \cdot R_m \tag{5.6}$$

$$\rho = \frac{dr}{R_* - R_p} \tag{5.7}$$

$$v_{sl} = \omega r \cdot \sqrt{1 - (\zeta^{m_z} \cdot \rho^{m_r})^2} \tag{5.8}$$

Here dr is the normal distance from tool pin surface, r is the distance from the heat source center to the point of interest, R_p is the tool pin radius, dz is the normal distance from the nearest tool shoulder surface, t_{plate} is the plate thickness, z is the Z-coordinate, ζ is the normalized dz, R_* is the shear layer outer boundary radius, m_{shape} is the shear layer shape control variable, R_s is the tool shoulder radius, R_m is the shear layer minimum outer radius, ρ is the normalized dr, v_{sl} is the shear layer tangential velocity, m_z is the shear layer shape
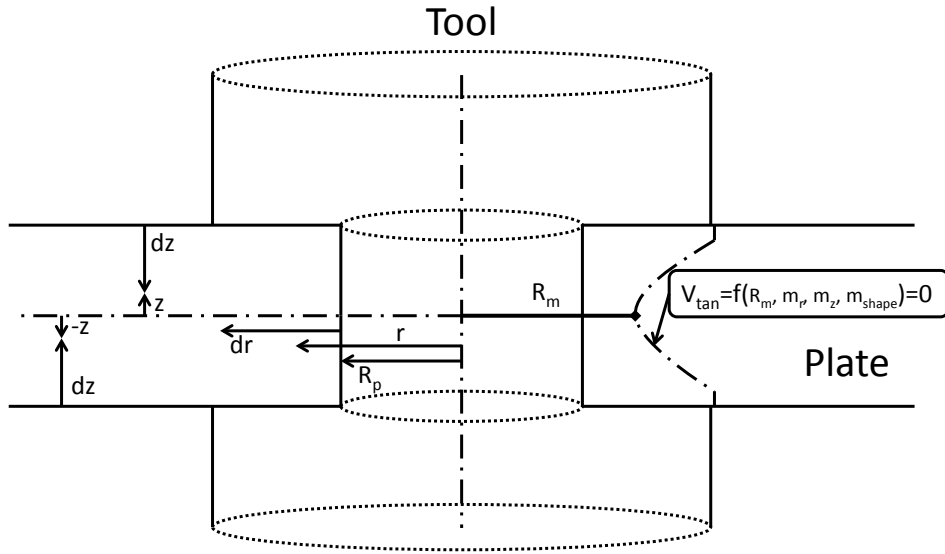
Figure 5.5: Shear layer model coordinates

control variable for z direction and m_r is the shear layer shape control variable for r direction. The resulting tangential velocity field v_{sl} can then be split up into x and y components and added to the convective flux term u of Eq. (5.10). It is mandatory to define a cutoff distance in r direction for the shear layer, which should be equal or near the shoulder radius. This can be done using regular expressions or by defining a suited sub domain of the work piece representation in the model. Else the continuity guaranteed by the formulation will extend the shear layer to a virtual infinitely large rotating shoulder, which is of course undesired. The model uses fitting variables m_z, m_r, m_{shape} and R_m to provide flexible control over the horizontal and vertical shearing velocities characteristics as well as the shape of the shear layer's inner boundaries. Fig. 5.6 shows different possible shear layer shapes with the parameters given in Tab. 5.2.

parameter set	m_z	m_r	m_{shape}	R_m
a	1	1	1	4.5mm
b	0.5	0.5	0.5	4.5mm
c	2	2	2	4.5mm
d	1	1	1	6.0mm
e	0.5	0.5	0.5	6.0mm
f	2	2	2	6.0mm

Table 5.2: Shear layer parameters
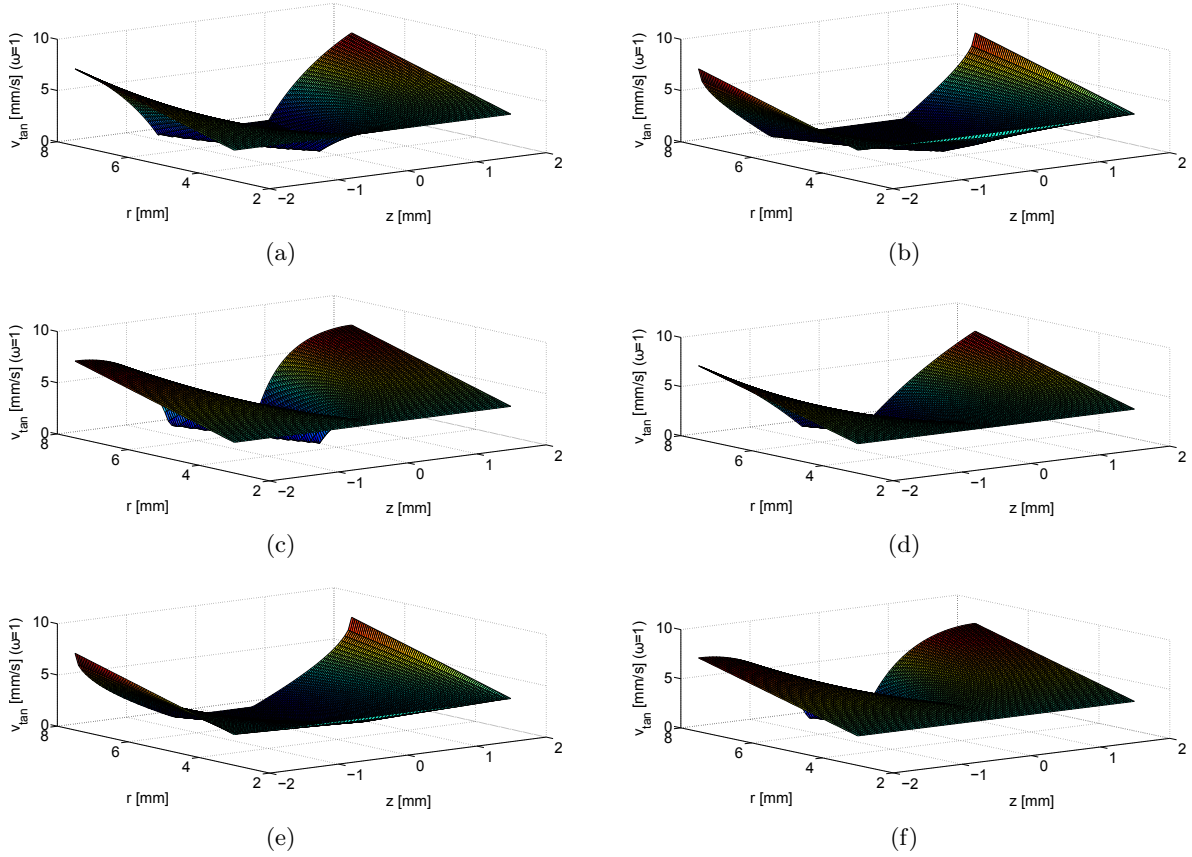
Figure 5.6: Shear layer shapes (see Tab. 5.2)

5.1.4 Material Definition and Boundary Conditions

Boundary conditions representing the physical environment of the modelled domain as well as the heat generation by the heat source are applied to groups of boundaries. The material properties for the different domains of the model are considerably different. Especially the different values of thermal conductivity need to be considered for the work pieces made of aluminium and the tool, clamps as well as the machine table made of steels. Fig. 5.7 shows the different material groups of the model. Fig. 5.8 shows the different boundary groups of the model.

The tool rotation is represented using convective flow according to Eq. (5.9). This is implemented by prescribing the convection term u in the heat transfer equation Eq. (5.10) in the region defined in Fig. 5.8(e).

$$\mathbf{u} = \begin{bmatrix} \omega y \\ -\omega x \\ 0 \end{bmatrix} \tag{5.9}$$

$$\rho c_p \frac{\partial T}{\partial t} + \rho c_p \mathbf{u} \nabla T = \nabla(k \nabla T) \tag{5.10}$$

In the same way the shear layer is represented using the analytical shear layer model (see Section 5.1.3). All convective terms are superposed to generate the Comsol convective flux term.

The work piece and clamp surface as well as the tool surfaces, except for the upper one connected to the machine spindle, are set to have a constant heat transfer coefficient $h = h_{air}$. Thus heat is transferred to the surrounding air at room temperature $T_{inf} = (273.15 + 20)K$ according to Eq. (5.11) on the boundaries marked on Fig. 5.8(a).

$$-\mathbf{n}(-k\nabla T) = q_{total} + h(T_{inf} - T) \tag{5.11}$$

Here $\mathbf{n}$ is the surface normal vector, k is the thermal conductivity, T is the temperature, ρ is the density, c_p is the specific heat capacity, u is the convection term in the heat transfer equation, h is the heat transfer coefficient, q_{total} is the prescribed inward surface heat flux and T_{inf} is the external temperature. In the same way heat transfer is realised at the interface between tool and machine using $h = h_{spindle}$ on the interface defined in Fig. 5.8(c) and at the cut off edges of the table using $h = h_{table}$ as shown in Fig. 5.8(b).

At the boundaries that represent the interface between the tool and the workpiece as shown in Fig. 5.8(d) the q_{total} term of Eq. (5.11) is used to define the TPM heat generation according to Eq. (3.9).
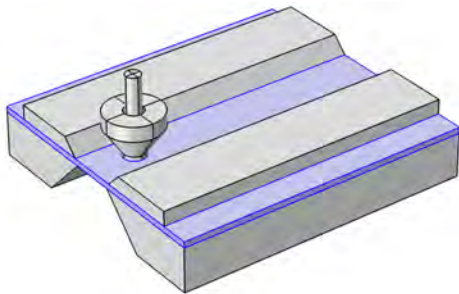
(a) Work piece made of AA2024
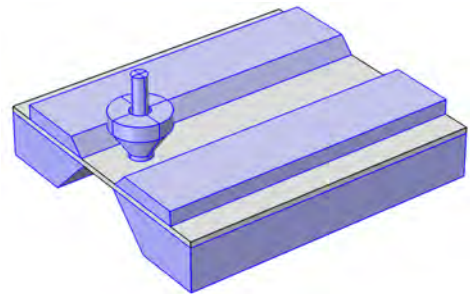
(b) Tool, clamps and table made of high-strength steel

Figure 5.7: AMGM material definition

(a) Convection to air

(b) Convection to table

(c) Convection to machine spindle

(d) Prescribed TPM heat source

(e) Convective tool rotation
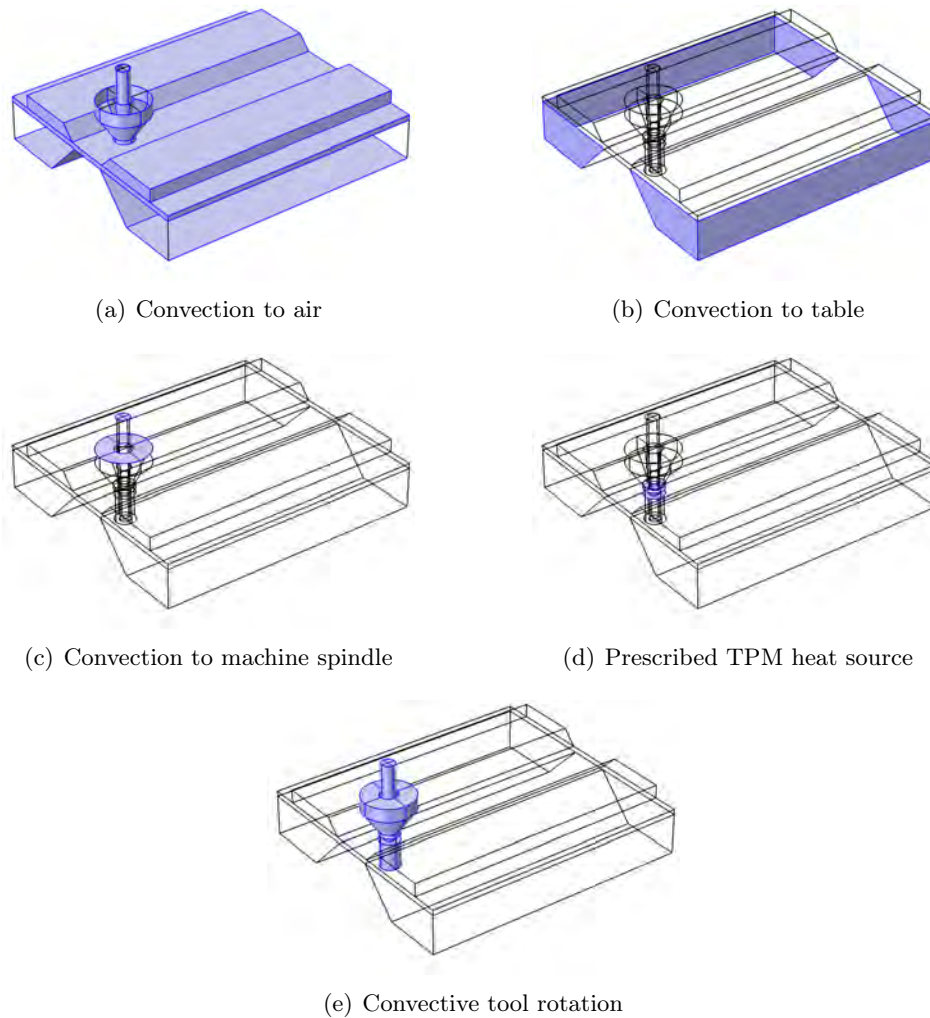
Figure 5.8: AMGM boundary conditions

### 5.1.5 Predictions and Validation

5.1.5.1 Thermal Field Prediction

Fig. 5.9 shows an example of the transient thermal field prediction of the AMGM. The parameters used are 800RPM and a welding speed of $2mm/s$. The transient character of this short weld can be clearly seen by the heating of the tool and clamps. The curve plotted along with the temperature field overview is taken from the centre of the weld line along the welding direction. The origin of the coordinate system is in the centre of the plate.

The influence of the joining parameters on the peak temperature and the time at elevated temperatures is plotted in Fig. 5.10. Here the time at elevated temperature is measured as dT_{500}, which is the time span for which the material at a given point has a predicted temperature above 500K. The samples chosen here correspond to those used to illustrate
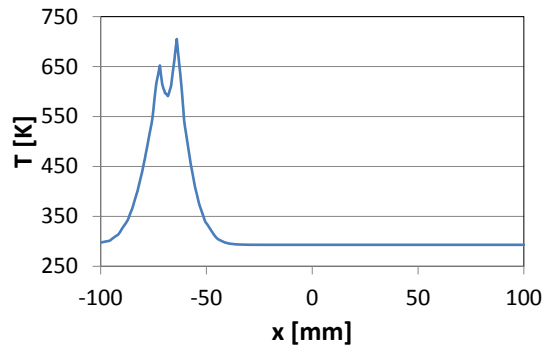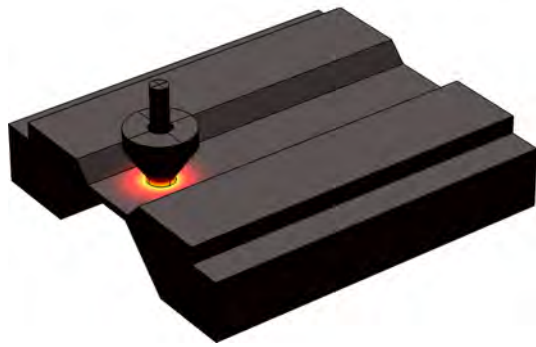
(a) Temperature field at t=1s
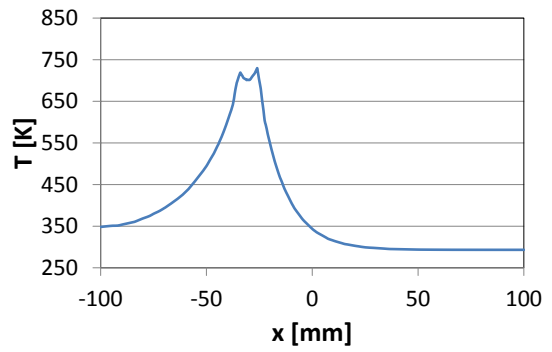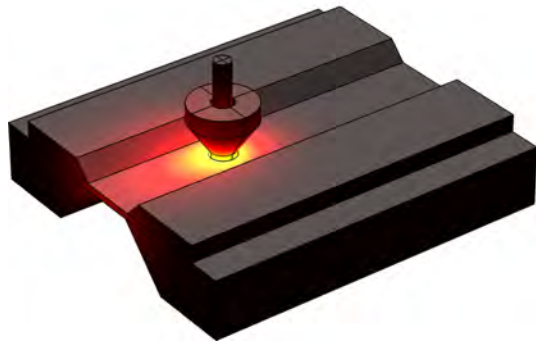
(b) Temperature field at t=20s
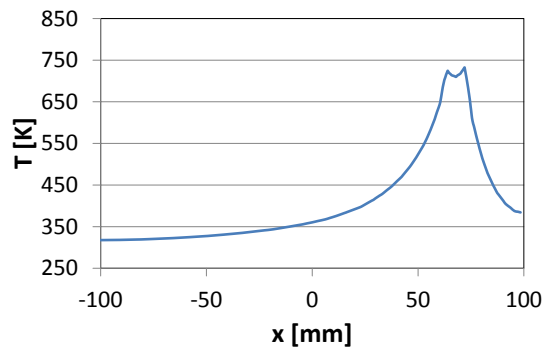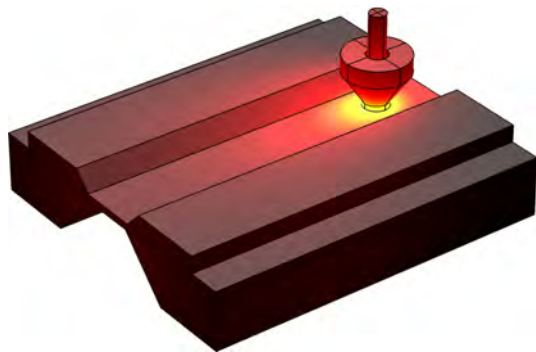
(c) Temperature field at t=69s

Figure 5.9: Thermal field prediction

(a) Peak temperature prediction
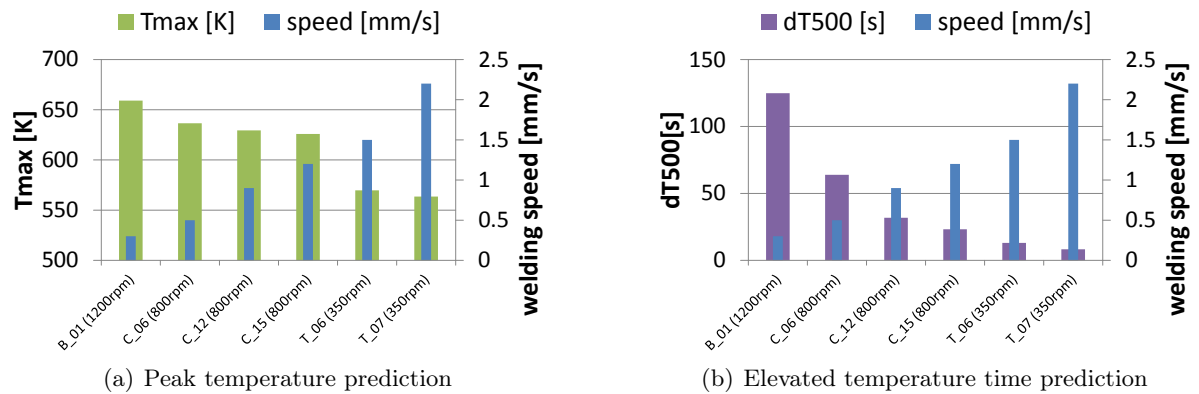

(b) Elevated temperature time prediction

Figure 5.10: Peak temperature and elevated temperature time prediction

micro hardness changes as function of process parameters in Fig. 5.14. The temperature data for the line graphs is extracted 7.5 mm from the centre line on the retreating side of the weld in the centre of the plate. This location is chosen as it corresponds well with the average location of minimal hardness found in the experimental evaluation.

5.1.5.2 Temperature Field Validation

The temperature predictions of the AMGM as well as the MG model have been validated with thermocouples as described in detail by Hilgert et al. [2]. Additionally, the temperature field of selected welds was recorded using a infrared thermo-camera. The calibration of these measurements was performed with K-type thermocouples. Fig. 5.11(a) shows a thermograph of a C_20 weld (600 RPM, $1mm/s$) from the trailing side. The line indicated on this figure is used to visualise the comparison of the measured and predicted temperature. Fig. 5.11(b) shows this comparison. Results and problems with emissivity correction and geometric mapping of the thermograph to the plate coordinate system are discussed in Section 5.1.6.
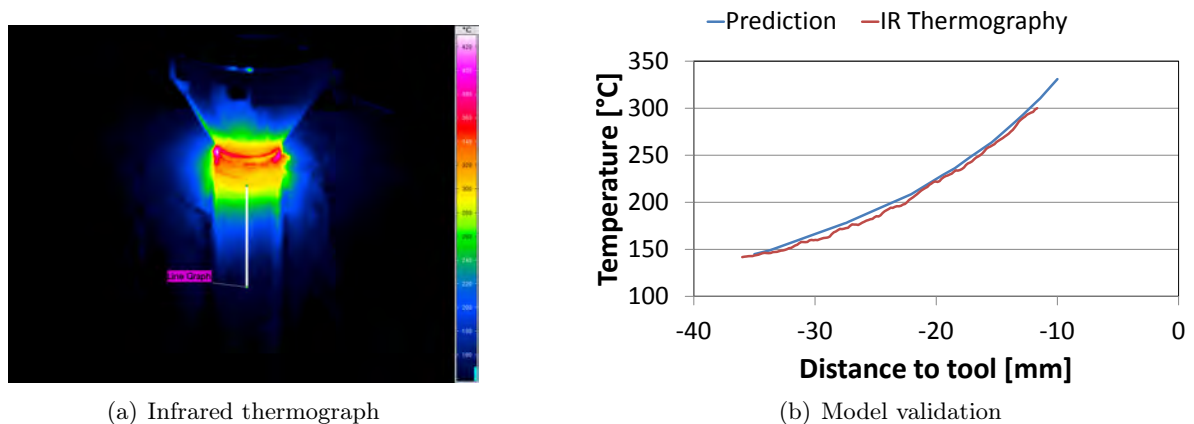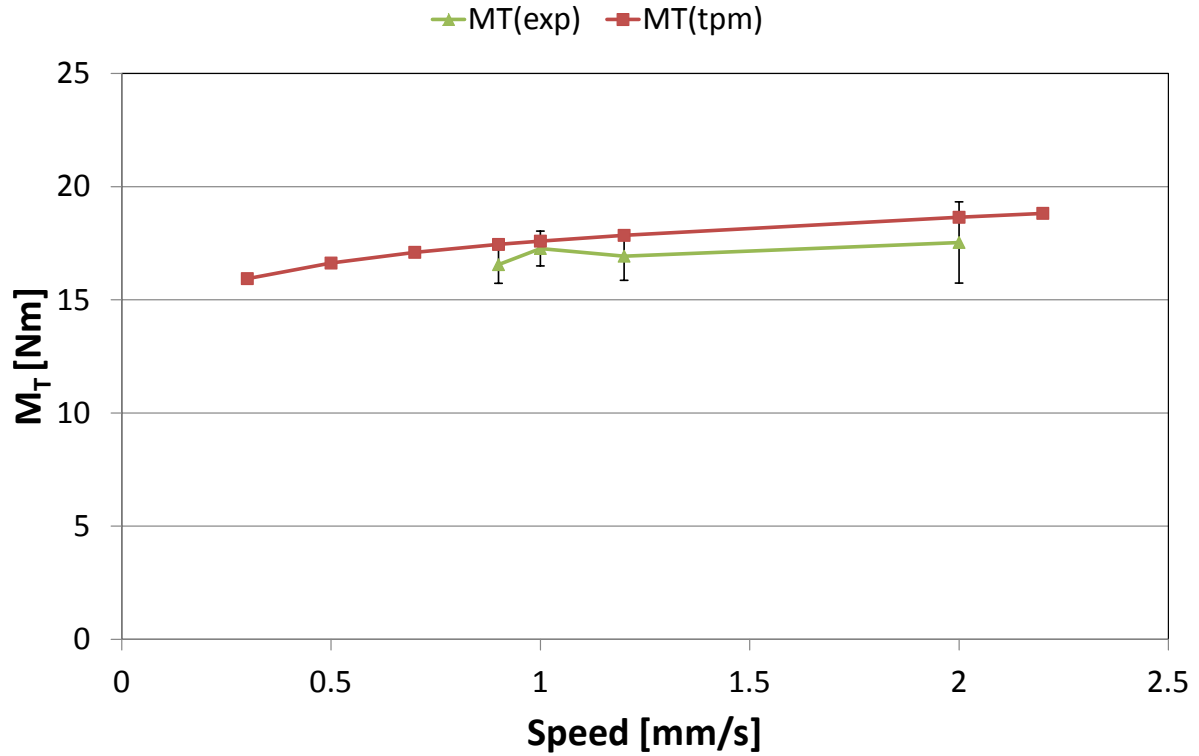

(a) Infrared thermograph

(b) Model validation

Figure 5.11: Infrared thermograph

Figure 5.12: Predictions for the torque M_T

5.1.5.3 TPM Torque and Energy Prediction

As described in Equation (3.9) the TPM heat source can be used to predict the acting torque on the tool from the resolved shear stresses on the tool surface. A series of predictions for welds with 600 RPM are shown in Fig. 5.12 together with experimental validation data from motor current (see Section 5.1.6). From this the line-energy can be derived, which is an important characteristic value of the process. It is calculated according to

$$q_l = \frac{M_T \omega}{u_{weld}}. \tag{5.12}$$

The line-energy predictions and validation for the same conditions as in Fig. 5.12 are given in Fig. 5.13.

5.1.5.4 Weld Zone Size Prediction

The size of the weld zone (i.e. the zone between the outer boarders of the HAZ on both sides of the weld) can be predicted by the thermal model. A basic approach is to define a limit temperature at which softening sets in as proposed by Preston et al. [53]. There a value of 175°C is assumed for short time temperature stability. The predictions can be validated by microhardness measurements. The microhardness profiles for a series of welds from the
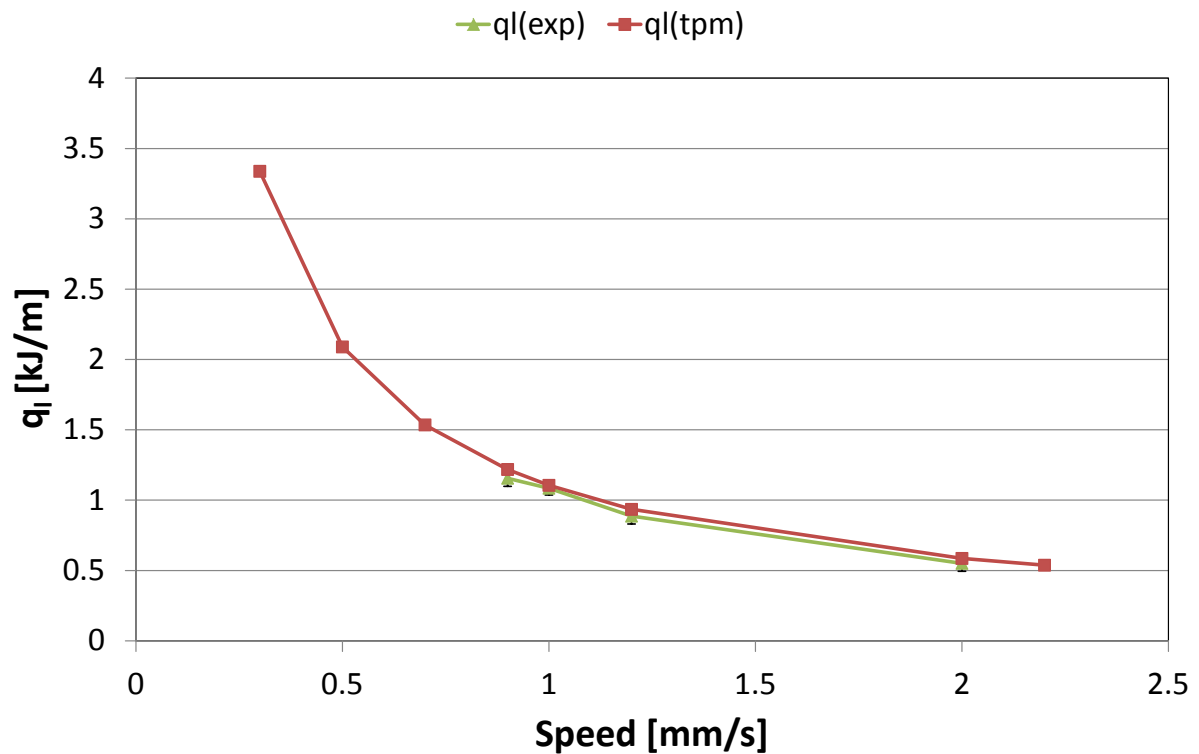
Figure 5.13: Predictions for the line energy q_l

controller development campaign are plotted in Fig. 5.14. The measured microhardness profiles reveal the size of the weld zone. It is defined to be the distance between the points on the advancing and retreating side, where the measured microhardness reaches the base material value (see Section 7.1.4.1). The weld zone can be correlated to the peak temperature at the respective locations. A comparison between the experimentally determined weld zone width (location of base material microhardness) and the maximum extent of the region that has been heated to a peak temperature above 225°C and above 250°C is given in Fig. 5.15.
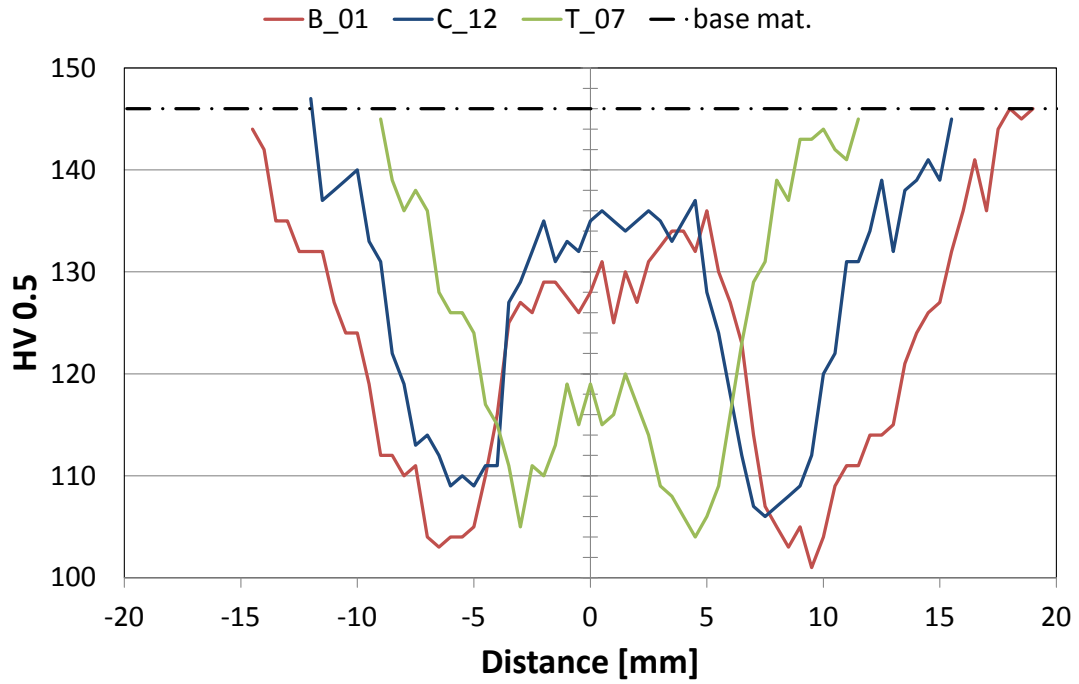
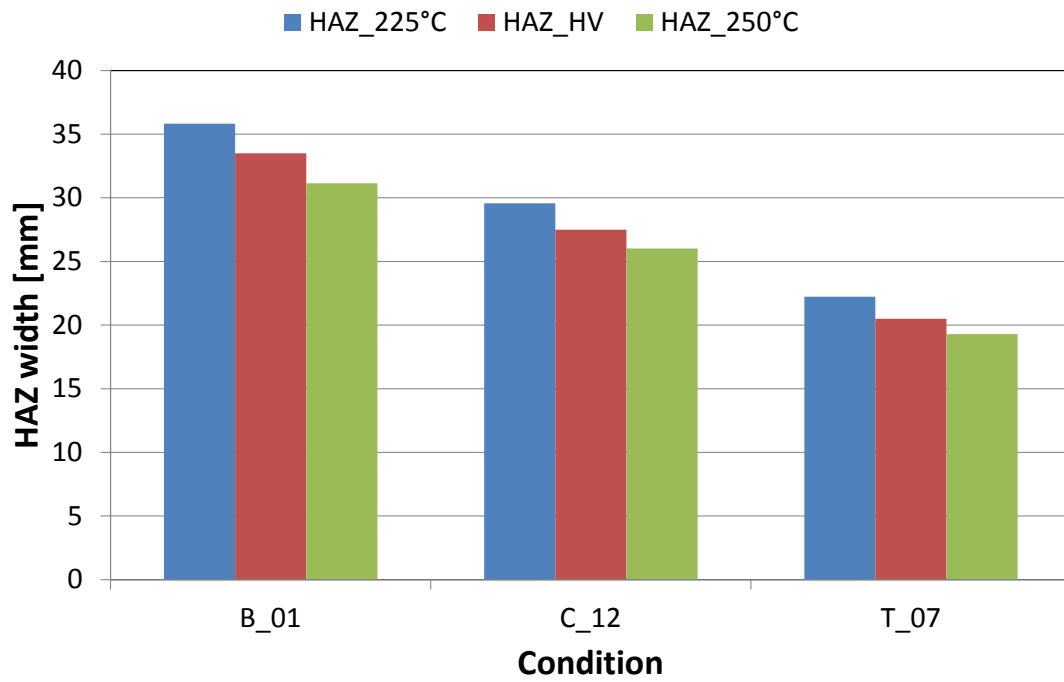Figure 5.14: Microhardness evaluation for different welding speeds

Figure 5.15: Weld zone width correlation to peak temperature

5.1.6 Discussion

The temperature predictions of the AMGM have been validated with earlier existing predictions using the MG model [101] and also with new experimental data. It can be stated that the difference in the predicted temperature field between the MG model and AMGM is very small and can be neglected if the MG model is solved with a sufficiently small step size. This has been expected as the physical assumptions and boundary conditions have not been changed. The faster prediction speed is by far the most important benefit of the transition from the MG model to the AMGM. A comparison with the IR camera measurements show a good agreement. This measurement technique is, however, not easy to apply to BT-FSW welds on the FlexiStir machine, as the field of view is geometrically very limited. Only the trailing side can be readily accessed in an acceptable angle. Reflections from the welding head additionally complicate the measurements. Calibration of the emission coefficient with thermocouple data cannot be avoided. The mapping of the acquired thermographic data to the coordinate system of the plate used in the models is needed. The accuracy of this mapping is limited by spacial resolution of the IR camera but most of all by its limited depth of focus. The transformation of the coordinates also includes the angle of view, which is not easy to determine accurately. The accumulated spacial uncertainty leads to a fairly large systematic error.

As the numerical model yields good results in comparison to the thermocouple measurements, it does not seem practical to use the IR camera as a temperature measurement technique for this process and machine as a standard technique. It may still be used for special validation purposes, though, as it is the only way to measure the cooling of the stirred material directly. A thermocouple at this location is bound to be destroyed by the process. The thermal field predictions are valuable for comparison between different joining conditions. They are needed as an input for the CFD model as well. As the predictions contain the complete thermal history for every location of the welded material, these predictions can also be used in the future to attempt to predict mechanical properties of the resulting welds.

The torque predictions have been successfully validated with experimental measurements for different process parameters (see Fig. 5.12). In this context the torque acting on the Tool can be measured in two independent ways (see Section 4.3). An example of the results is plotted for welding condition C_21 (see Tab. 4.2). Here Fig. 5.16 shows the torque calculated from the in-plane forces and Fig. 5.17 shows the torque estimated from the motor current. As can be seen in Fig. 5.16 and Fig. 5.17, the two available methods of torque measurement do not lead to comparable results. The values calculated from the force sensors according to Eq. (4.1) cannot be considered realistic. This is clear from the negative values for the torque recorded during the run-in of the weld. It is impossible to find negative torque values in a FSW setup. The mean value of around 50Nm seems unrealistic too, as the tools used in this study cannot resist the stresses acting at such a torque (see Section 6.2.1). Therefore it has to be concluded that this method of torque measurement is not feasible with the current hardware. The reason for
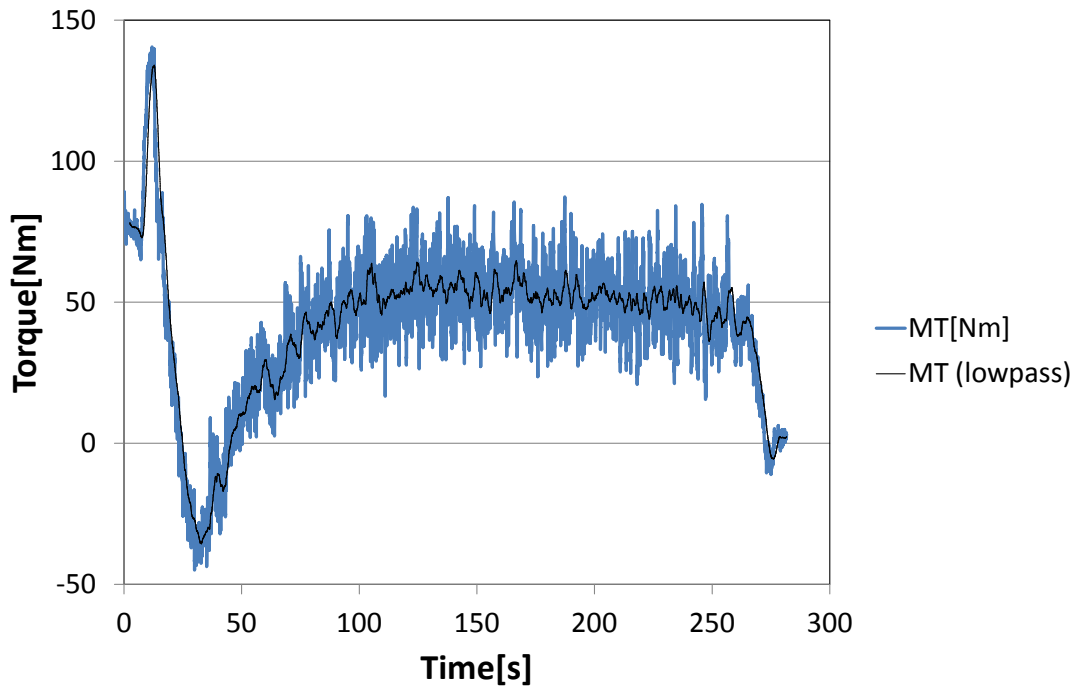
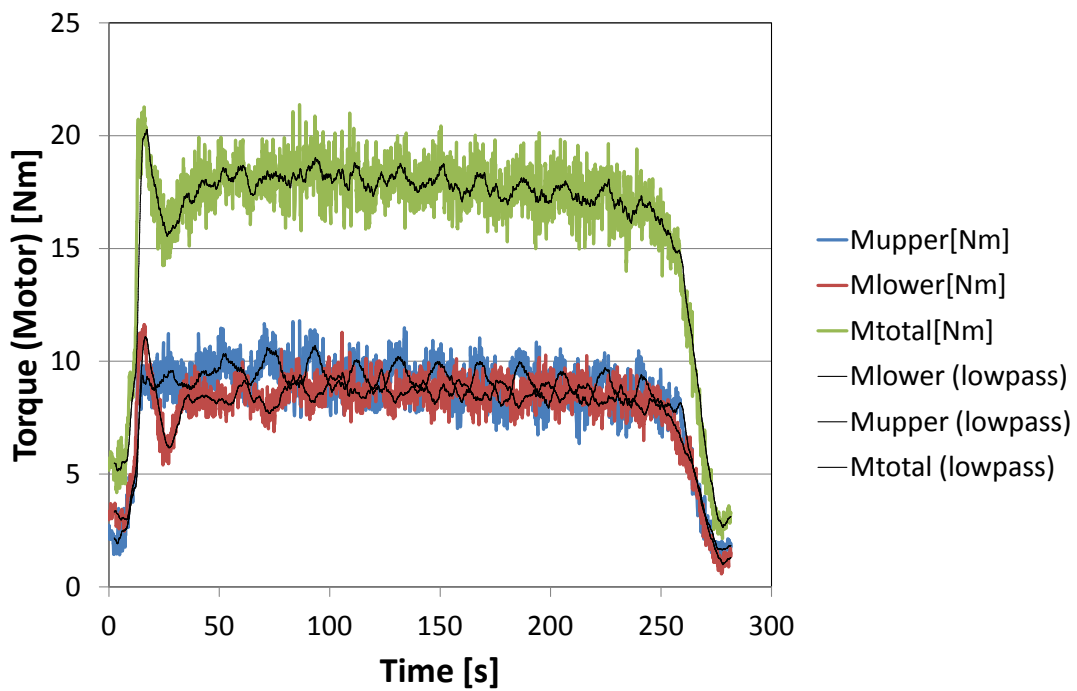Figure 5.16: Torque calculated from the in-plane forces

Figure 5.17: Torque estimated from the motor current

this is that the force signal recorded by the sensors due to a force acting on the tool ($\approx 250N$ per sensor and direction) is one order of magnitude larger than the (nominal) force signal due to a torque acting on the tool ($\approx \frac{50Nm}{30cm\cdot 8} = 21N$ per sensor and direction). Therefore small systematic errors in the distribution of the force to the force sensors have a large effect on the measured torque. A dedicated torque sensor would be needed to solve this problem. The torque estimation from the motor current gives promising results that correspond very well with the predicted values (see Fig. 5.12). Therefore it is suggested to rely on this technique until a dedicated torque sensor has been implemented. In most cases it will be sufficient to run a thermal model to get an idea whether the chosen process parameters can be handled by the tool and welding machine in terms of torque.

The derived value of line energy is a useful indicator for the thermal loading of the base material. It can be thought of as a combination of the peak temperature and the time at elevated temperature (compare Fig. 5.10). Usually low line energy is desirable.

The thermal field predictions are valuable for comparison between different joining conditions. They are furthermore needed as an input for the CFD model. As the predictions contain the complete thermal history for every location of the welded material, these predictions can also be used to predict mechanical properties of the resulting weld. A basic example for this is the size of the weld zone. As can be seen from Fig. 5.15, the onset of softening at the boundary of the HAZ occurs at peak temperature between $225°C$ and $250°C$. This value is higher than the limit of short time temperature stability of $175°C$ as proposed by Preston et al. [53]. This may be due to a different conception of how short "short time" is. It does not seam realistic to perform a FSW joint of AA2024 completely below this temperature. Therefore a softened HAZ cannot be completely avoided. The size of the weld zone can, however, be accurately predicted from the thermal model.

5.2 Flow Modelling

The material flow around the pin is of major importance for the formation of the joint as well as for the resulting process forces. This material flow is a function of temperature, viscosity and tool geometry. Two versions of a material flow model have been developed for this study. The first one is a steady state model using a rotational symmetric tool (cylindrical pin and flat shoulders). This model is meant to predict the shear layer size and shape for different process conditions in a fast and general manner. The inputs are a temperature field predicted by the AMGM, the welding speed u_{weld} and tool RPM along with material data for the constitutive equation of viscosity Eq. (5.17). This model is referred to as standard flow model or CFD model. The second version is the rotating featured pin model (RFPM). It uses the same material model as the standard flow model but includes a rotating mesh domain to represent a featured pin. This model is time dependent and can be used to get refined predictions of
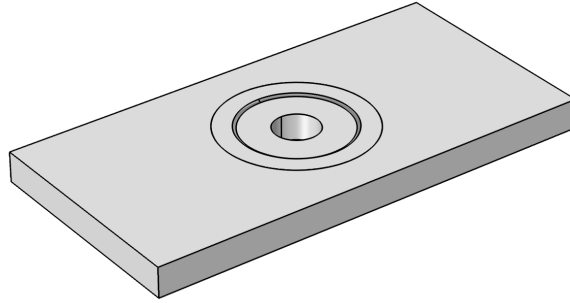
Figure 5.18: Geometry of the simple flow model

material flow, tool torque and welding forces as a function of tool design. It can also be used to evaluate the loads acting on the tool. These are important inputs to the mechanical model of the tool (see Section 6.2.1).

5.2.1 Geometry, Equations and Boundary Conditions

5.2.1.1 Geometry

The geometry (see Fig. 5.18) consists of a part of the base material sheet. The tool pin is cut out of the plate. The tool shoulders are imprinted as boundaries on the top and bottom surface of the workpiece. The domain of the plate is chosen sufficiently large so that the material flow on both the inlet and the outlet surface is parallel to the welding direction and has the same homogeneous velocity as the nominal welding speed. This means that any softening and stirring in the vicinity of the pin and shoulders is captured within the modelled domain. The material at the outer boundaries can be considered solid although is has a finite but very high viscosity.

5.2.1.2 Equations

The governing equation is the Navier-Stokes equation (as expressed in Eq. (3.11) and Eq. (3.12)). This steady state formulation needs to be extended to the time dependent version for transient models

$$\rho \frac{\partial u}{\partial t} + \rho(u \cdot \nabla)u \quad = \quad \nabla \cdot [-pI + \eta(\nabla u + (\nabla u)^T)]. \tag{5.13}$$

The viscosity is defined using the inverse hyperbolic sine law (see Section 3.2.2.3) [81, 84] for the material flow stress. It is a function of temperature and shear rate. The standard form in terms of effective deviatoric flow stress $\bar{\sigma}$ and effective strain rate $\dot{\epsilon}$ is given in Eq. (5.14). This needs to be converted to a system of the effective viscosity η_{eff} and the shear rate $\dot{\gamma}$ for

Parameter	Value
α	$1.6 \cdot 10^{-8} [m^2/N]$
A	$e^{19.6} [s^{-1}]$
Q	$1.4880 \cdot 10^5 [J/Mol]$
n	4.27

Table 5.3: Material parameters for AA2024 [104]

flow modelling. This is done by applying Eq. (5.15) and Eq. (5.16) to Eq. (5.14) which results in Eq. (5.17).
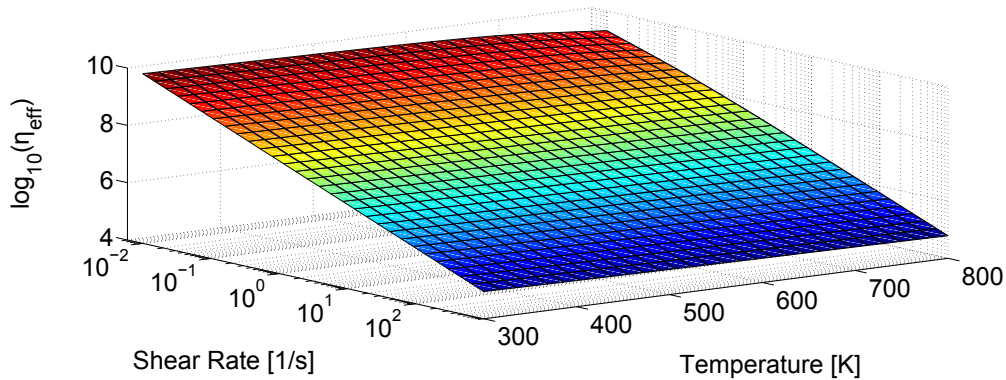
$$\bar{\sigma} \;\; = \;\; \frac{1}{\alpha} sinh^{-1} \left(\frac{\bar{\dot{\epsilon}} e^{(Q/(RT))}}{A} \right)^{1/n} \tag{5.14}$$

$$\eta_{eff} \;\; = \;\; \frac{\bar{\sigma}}{3\bar{\dot{\epsilon}}} \tag{5.15}$$

$$\dot{\gamma} \;\; = \;\; \sqrt{3}\bar{\dot{\epsilon}} \tag{5.16}$$

$$\eta_{eff} \;\; = \;\; \frac{sinh^{-1} \left(\frac{\dot{\gamma} e^{(Q/(RT))}}{\sqrt{3}A} \right)^{1/n}}{\alpha\dot{\gamma}\sqrt{3}} \tag{5.17}$$

Here R is the universal gas constant and α, A, Q, and n are material properties. For the alloy AA2024 these constants are taken from Sheppard [104] and are given in Tab. 5.3. The resulting effective viscosity η_{eff} for the range of temperature and shear rate that is of interest in this context is plotted in Fig. 5.19.

Figure 5.19: Effective viscosity η_{eff}

As the viscosity is described by a very nonlinear function, a parametric solver approach can help to achieve convergence. Hereby the effective viscosity is ramped up using a convergence parameter n_{conv} going from 10 to 1 according to Eq. (5.18). The necessity of this approach as well as the selection of the range of the convergence factor depend on the solver settings and
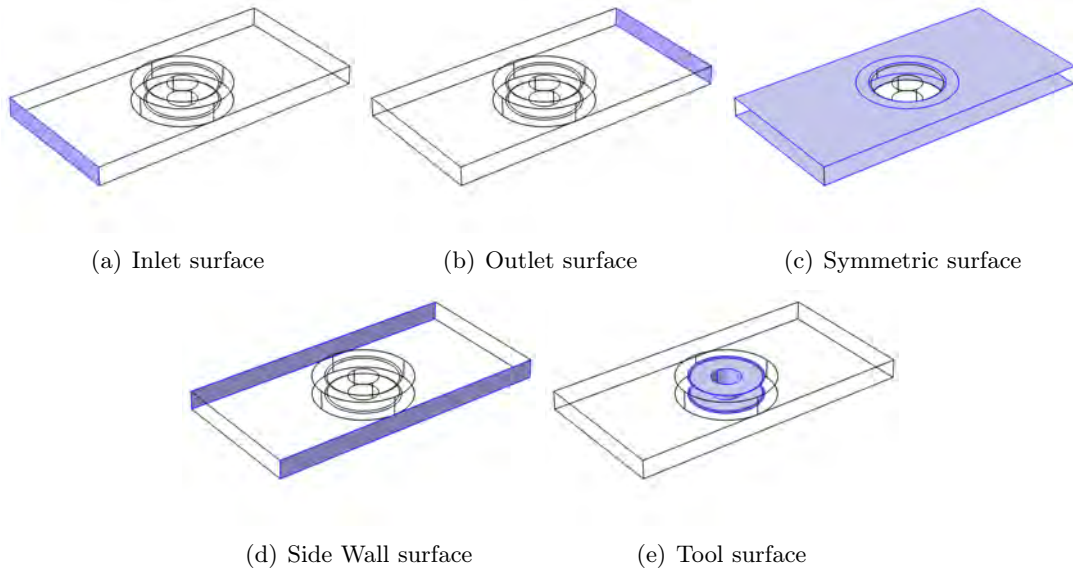
(a) Inlet surface   (b) Outlet surface   (c) Symmetric surface

(d) Side Wall surface   (e) Tool surface

Figure 5.20: CFD model boundary conditions

the complexity of the geometry under investigation.

$$\eta_{conv} \quad = \quad \eta_{eff}(\dot{\gamma}, T)^{(1/n_{conv})} \tag{5.18}$$

5.2.1.3   Boundary Conditions

Fig. 5.20 shows the different boundary groups of the CFD model. The boundary conditions
of the inlet surface (Fig. 5.20(a)) define a constant material flow velocity in welding direction.
The same is true for the side walls as shown in Fig. 5.20(d). This represents the actual
behaviour of the material, which does not deform outside a small shear layer around the tool.
The outlet surface (Fig. 5.20(b)) prescribes a constant relative pressure of zero. The free
surface (Fig. 5.20(c)) of the plate is set to a slip condition so that no material can leave the
plate. The pin and shoulder surfaces (Fig. 5.20(e)) prescribe a defined tangential velocity
$v_{tangent}$ compatible with the tool's rotation speed ω according to

$$v_{tangent} \quad = \quad \delta\omega_{tool}r. \tag{5.19}$$

Here r is the distance from the tool axis, ω_{tool} is the tools angular velocity and δ is the contact
state variable $(0 < \delta < 1)$ that defines the ratio of sticking and slipping at the interface as
explained in Section 3.2.1.3. It should be stated here that δ is not necessarily prescribed as
an input to the model in this equation. In the normal mode of operation of the model it is a
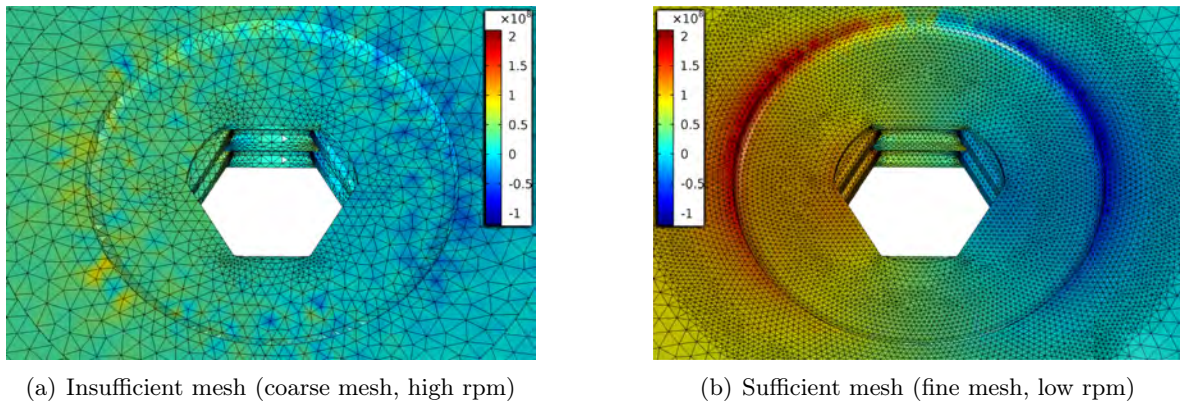predicted quantity as described in Section 5.2.4.

(a) Insufficient mesh (coarse mesh, high rpm)

(b) Sufficient mesh (fine mesh, low rpm)

Figure 5.21: Mesh density dependency of the pressure field solution [Pa]

5.2.1.4 Mesh

As known for FE models, insufficient mesh density leads to arbitrary results. In the CFD models this can be seen best when plotting the pressure field p for meshes with insufficient and sufficient mesh density as done in Fig. 5.21. The pressure field for high rpm (high shear rates) cannot be represented with coarse meshes. This has to be emphasised as the velocity field predicted in such cases does not show such an obvious dependency on the mesh density. Therefore the mesh density should always be validated with respect to the pressure distribution.

5.2.2 Rotating Featured Pin Model (RFPM)

Steady state solutions of the material flow are helpful to estimate the force and torque response on the tool and the size of the expected shear layer. The influence of tool geometry cannot be considered for tools that are not rotationally symmetric. It should be emphasised that the ratio between static volume and dynamic/swept volume of a FSW tool is important for the joint quality. Therefore the limitations of a steady state approach may be considered severe. A model has been developed to allow for transient material flow simulation of arbitrary pin geometries. This model is referred to as rotating featured pin model (RFPM). Fig. 5.22 shows the boundary and mesh groups of this model that differ from the ones in the CFD model described above.

The main concept is to define a rotating mesh domain (Fig. 5.22(a)) including the imprints of the tool and a stationary mesh domain (Fig. 5.22(b)) representing the work piece. In order to be able to couple these two domains in a meaningful way, the rotating mesh must have an outer shape that is rotationally invariant. A coupling can then be defined on the interface (Fig. 5.22(d)) of the static and the dynamic domains to enforce flow continuity. The tool boundaries (Fig. 5.22(c)) are now defined as moving (rotating) walls. The rotation of the tool

(a) Rotating mesh domain

(b) Static mesh domain

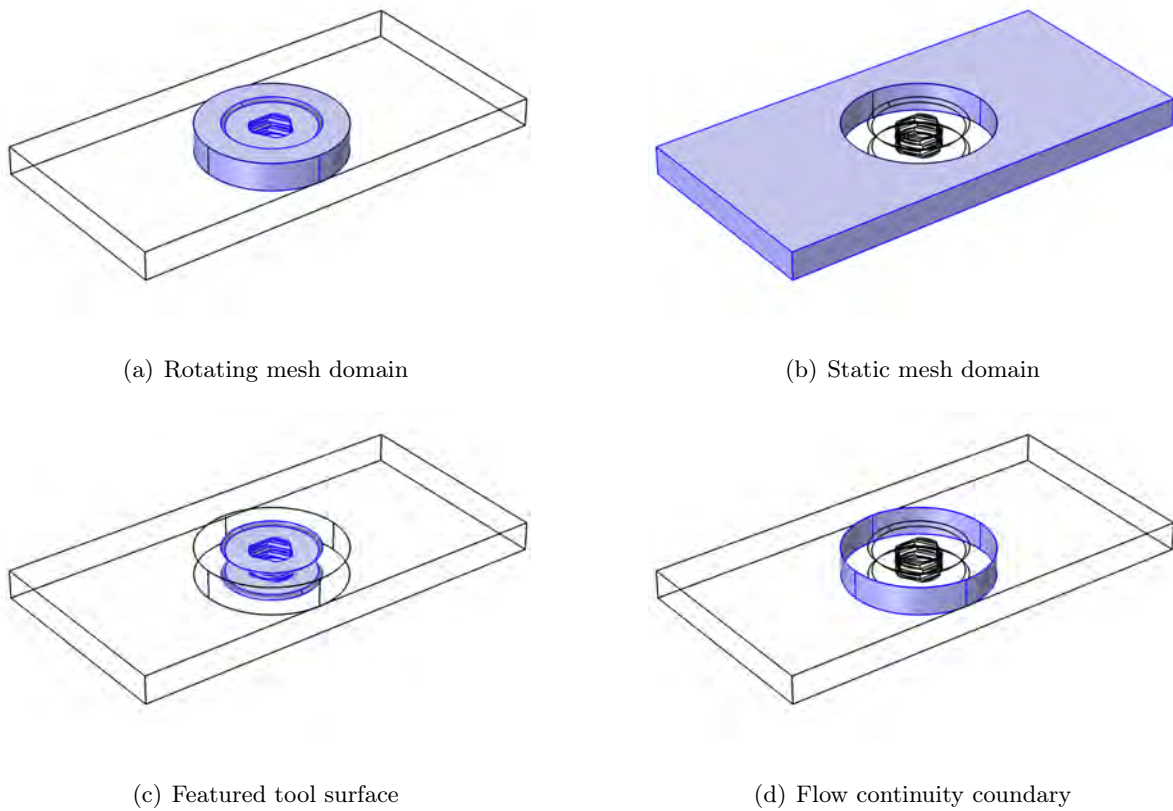(c) Featured tool surface

(d) Flow continuity coundary

Figure 5.22: RFPM boundary conditions and mesh groups

imprinted in the moving mesh domain is illustrated in Fig. 5.23.

With this model the transient influence of the tool features can be evaluated. In principle it would be possible to run the RFPM based on the complete transient thermal history of a joint to predict the transient force history with a resolution far below a single tool rotation. This is not feasible due to the excessive computational power that would be needed to do so. As the information for single tool rotations will change very gradually during the weld, the gain of knowledge from such an approach cannot justify the cost. The model is rather intended to be used to take snapshots at several locations throughout the weld. The thermal field is taken from the AMGM at the appropriate time and kept constant. First a stationary solution is computed as a starting point for the transient predictions. This stationary solution only gives an estimation of the flow as the boundary conditions are constant here. Then several transient tool rotations are simulated in the RFPM until there is no significant change from one rotation to the next. This converged situation is used to derive the quantities of interest like mean forces and resolved tool loading.
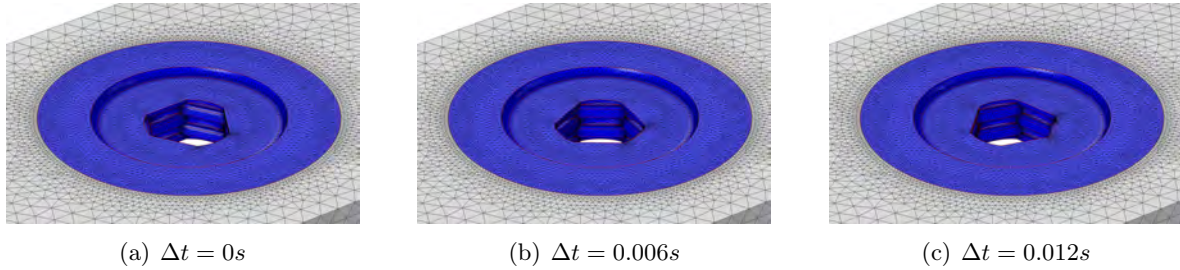
(a) $\Delta t = 0s$ (b) $\Delta t = 0.006s$ (c) $\Delta t = 0.012s$

Figure 5.23: Rotating tool in RFPM mesh

5.2.3 Calibration with Artificial Neural Networks

The analytical shear layer model described in Section 5.1.3 is designed to save computational time. It is meant to eliminate the need for CFD calculations for each combination of process parameters. In order to achieve this goal, it is mandatory to determine the input parameters for the shear layer shape equations in a fast but reliable way. It is proposed to train an artificial neural network (ANN) with the predictions of the CFD model for a set of process parameter combinations. The well trained neural network is then used to chose the analytical shear layer parameters with almost no computational effort.

Artificial neural networks represent a qualified tool for solving complex inverse problems like the determination of the input parameters for the ASLM. An introduction to ANNs in materials science and computational mechanics is given by Sumpter and Donald [105] and Yagawa and Okuda [106].

The artificial neural network used for this purpose is composed of an input layer, two hidden layers and an output layer. The input layer consists of two neurons representing the process parameters welding speed and tool rotational speed as these are the controlling parameters of the CFD model. The hidden layer consist of three neurons each. The output layer consists of four output neurons representing the calibration parameters for the analytical shear layer model m_{shape}, m_r, m_z and R_m. The topology is plotted in Fig. 5.24. The neural weights are indicated by the colour of the neural connections where red indicates a small (negative) weight and green indicates a high weight.

The training patterns are created by fitting the parameters of the analytical shear layer model to the flow field predictions of the CFD model at the retreating side of the weld. The fitting is performed using the nonlinear minimisation capabilities from Matlab's Optimisation Toolbox. Training is done by the resilient backpropagation *Rprop* algorithm as described in detail by Riedmiller and Braun [107].

Of course the prediction of the ASLM is only a rough approximation of the actual shape and velocity profile of the material flow around the tool. The true material flow is not axisymmetic, but has a pronounced difference between the retreating and advancing side. It has to be emphasised that the calibration of the ASLM is done from steady state solutions of flow
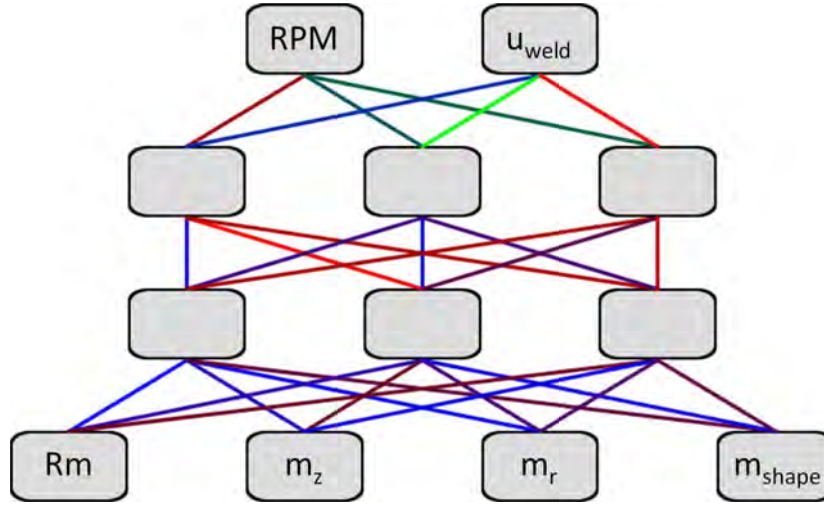
Figure 5.24: Topology of the artificial neural network

around tools with simplified geometry. This is sufficiently accurate to reproduce the temperature difference between the advancing and retreating sides when looking at the far field of temperature distribution. For a detailed investigation of the time-dependent formation of a shear layer around a tool with realistic geometrical features, a different approach must be taken as described in Section 5.2.2.

An artificial neural network was trained with a total of 64 data patterns generated from CFD results for various input parameters. These range from 400RPM to 1200RPM for the tool rotation and $0.5[mm/s]$ to $5[mm/s]$ for the welding speed. The comparison between trained and predicted values is plotted in Fig. 5.25. The blue dots correspond to a pattern that has been used for training. The red dots correspond to validation patterns that have not been used for training. Fig. 5.26 shows the predictions for the shear layer parameter fields.

5.2.4 Predictions

For validation of the model and easier interpretation of the results, derived values are calculated from the CFD models predictions. Most important are the in-plane welding forces, the gap force and the torque. These are then compared to experimental data (see Figure 5.33). The force in welding direction F_x is found by integrating the pressure over the inlet surface and outlet surface according to

$$F_x = \int_{\partial\Omega} pdA. \tag{5.20}$$

The outlet surface is used to define the relative pressure value of zero so it can be omitted in the integration. Analogous to that the force in the gap F_g and the lateral welding force F_y are found by integrating the pressure over the corresponding boundaries. The torque M_T acting

(a) R_m

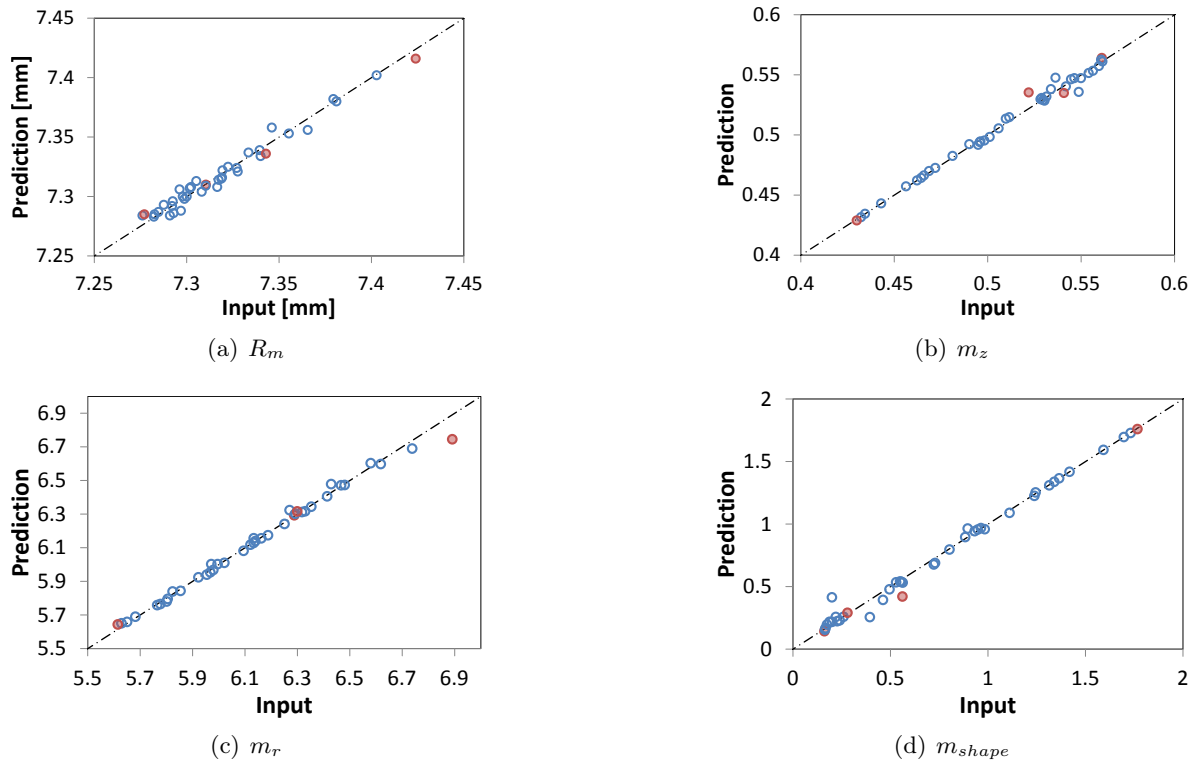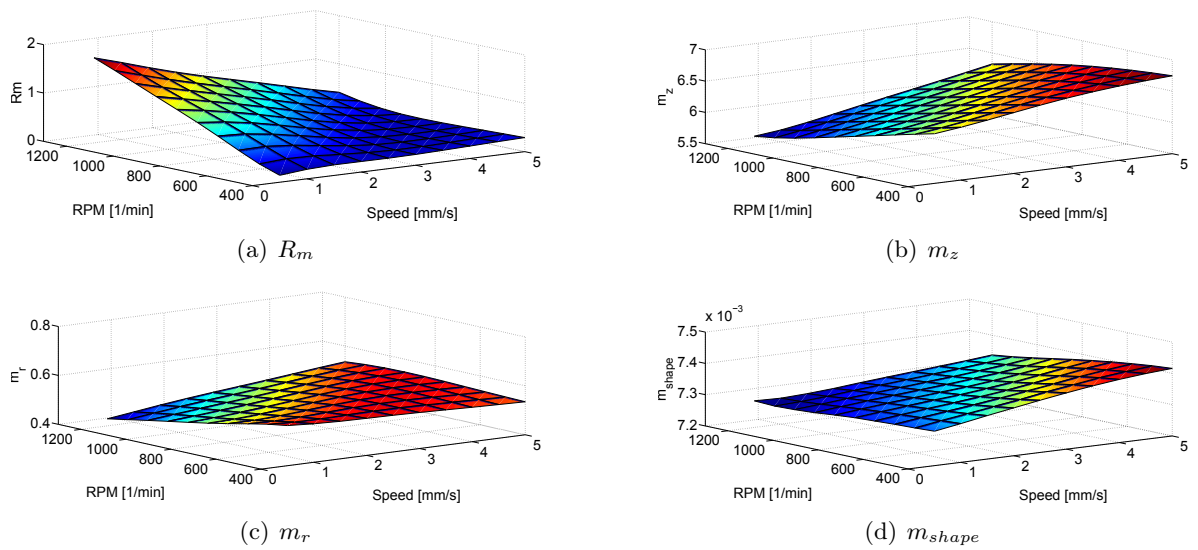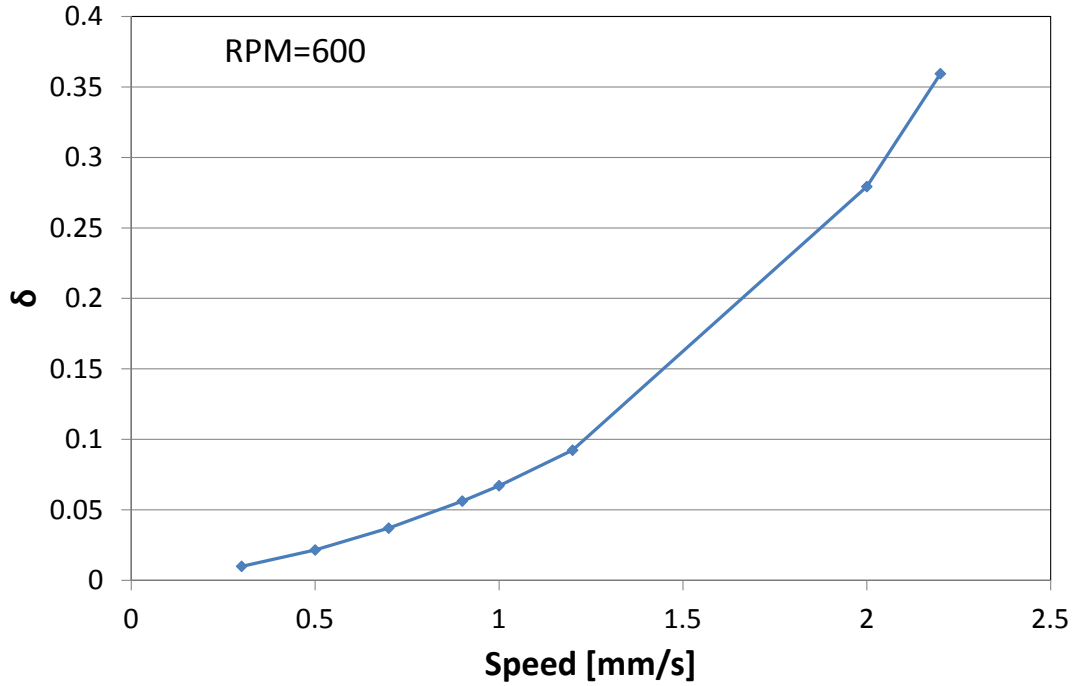(b) m_z

(c) m_r

(d) m_{shape}

Figure 5.25: Comparison between the trained and the predicted values for the shear layer parameters - blue dots correspond to a pattern that has been used for training, red dots correspond to validation patterns that have not been used for training

(a) R_m

(b) m_z

(c) m_r

(d) m_{shape}

Figure 5.26: Predicted values for the shear layer parameters

Figure 5.27: Predictions for the contact state variable δ

in the pin can be calculated according to

$$M_T \quad = \quad \int\limits_{\partial\Omega} (f_{v_x} \cdot y - f_{v_y} \cdot x)dA. \tag{5.21}$$

Here f_v is the viscous force per area acting on a location on the pin surface and x and y are the distances from the tool axis.

When combining Eq. (5.21), Eq. (5.19) and Eq. (3.10), a global constraint can be applied to the torque variable defining a constant value known from the thermal model (see Section 5.1.5.3) and validated experimentally (see Fig. 5.12). This is done by adding a single additional degree of freedom (named δ) to the model that is calculated in such a way that the acting torque is equal to the desired value. This way the contact state variable δ can be determined. As an alternative the desired contact state can be prescribed, of course. Then the torque can be in principle predicted from the CFD model. This, however, is only useful if an experimental evidence for a certain contact state is found. Fig. 5.27 shows the predicted delta values as a function of welding speed for a tool rotation of 600 RPM. The sensitivity of the predictions of the torque M_T and the welding force F_x on the contact state δ are shown in Fig. 5.28. The implication of this is discussed in Section 5.2.5.3.

The velocity profile in the vicinity of the featured pin is predicted by the RFPM. Such a prediction is plotted in Fig. 5.29. The outer contours of the predicted shear layer can be used to validate the models. An example of a shear layer velocity profile predicted with the CFD
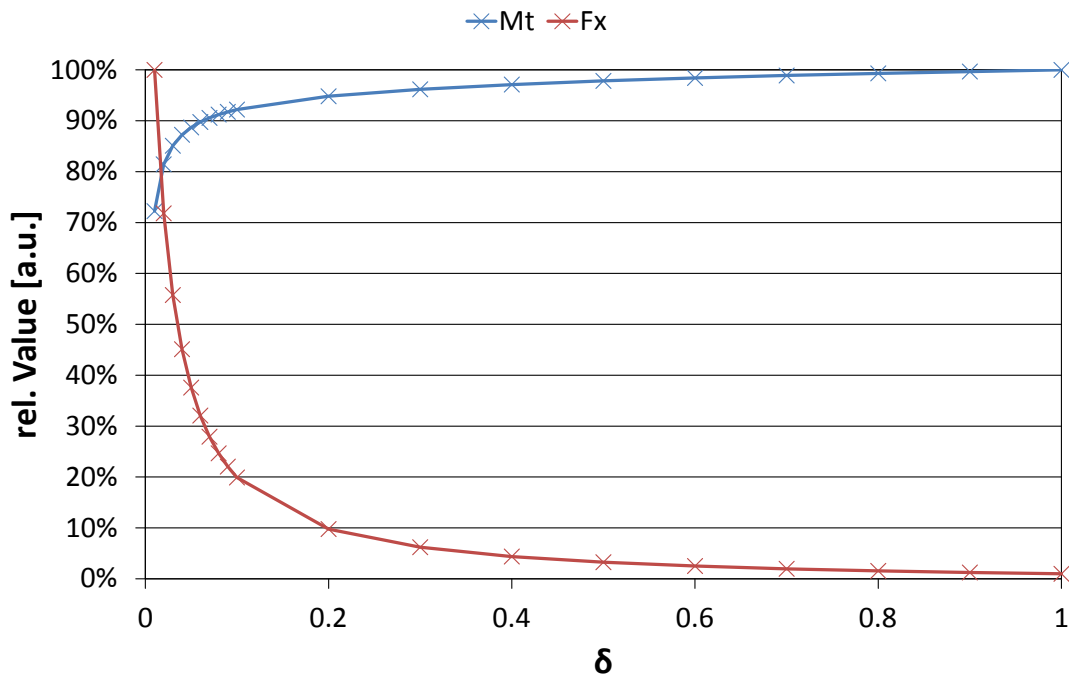
Figure 5.28: Sensitivity of the torque and forces on the contact state variable δ

model is compared to the macrograph of the corresponding experimental weld in Fig. 5.30. The pressure acting on the pin surface can be extracted from the RFPM and used as an input to the mechanical model of the tool as described in Section 6.2.1. A snapshot of such a pressure distribution for the corresponding joining conditions C_19 (baseline tool) and T_01 (improved tool) can be found in Fig. 5.31.

5.2.5 Results and Discussion

5.2.5.1 Shear Layer

The prediction of shear layer sizes using the CFD model has been validated using micrographs of stir zones from experimental welds. The predictions are reasonably accurate and the calibration of the ASLM using ANNs is possible. It can be observed that the trained neural network is able to predict the inputs for the analytical shear layer model with adequate precision (see Fig. 5.25). More training patterns are desirable to extend the valid range of prediction. While the prediction of the shear layer shape shows good agreement with experimental observations (see Fig. 5.30), the absolute value of the predicted shear layer velocity is not easy to validate experimentally.

The difference in shear layer size for different process parameters is rather small. The most important parameter controlling the size is R_m. It ranges from 7.28mm to 7.41mm for the investigated parameters. Therefore it may be questioned whether the prediction of the shear layer size is imperative for process development. The shear layer shape and velocity profile
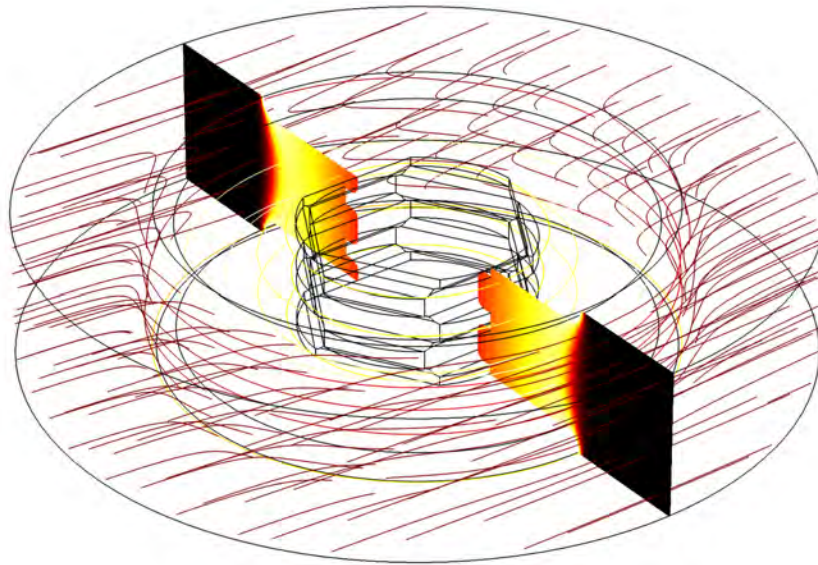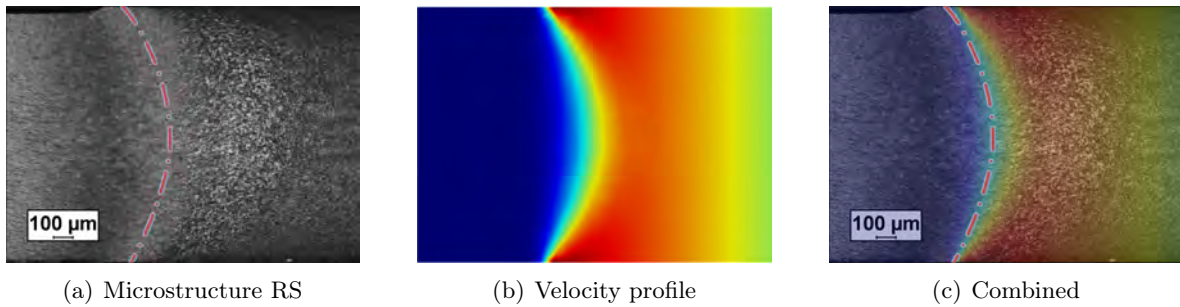
Figure 5.29: Velocity profile prediction in the vicinity of the featured pin
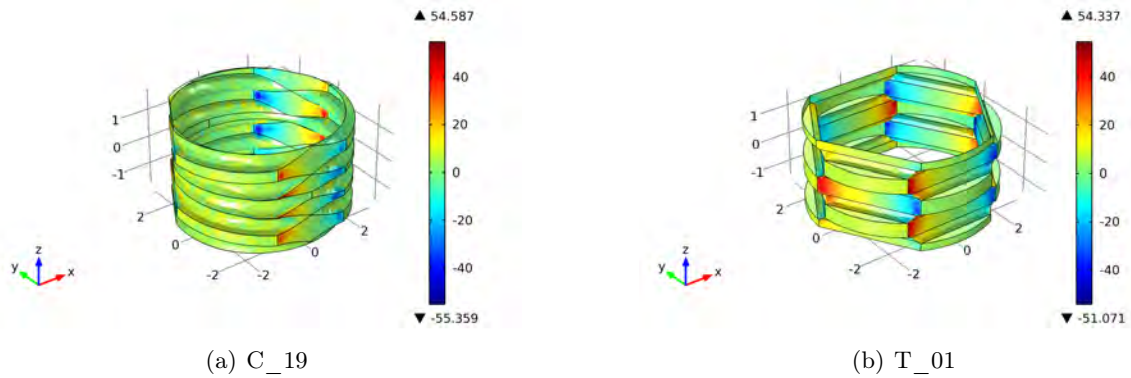

(a) Microstructure RS   (b) Velocity profile   (c) Combined

Figure 5.30: Comparison between a predicted shear layer (red color indicates high velocity) and the microstructure

(a) C_19   (b) T_01

Figure 5.31: Relative pin pressure predictions for 600RPM and $1mm/s$

is mainly controlled by the parameters m_r, m_z and m_{shape}. While the velocity slope at the interface between the tool and the shear layer does not change much ($0.43 < m_z < 0.56$ and $5.64 < m_r < 6.75$) the shape of the outer limit of the shear layer is more variable ($0.14 < m_{shape} < 1.76$). Still the impact of an accurate knowledge of the shear layer geometry as a function of process parameters on the thermal field prediction can be neglected in many cases, as the amount of transported thermal energy is dominated by R_m. One can choose to use a set of standard parameters for the ASLM to create thermal predictions for novel process conditions rather than calibrating these with CFD calculations. If, on the other hand, a parametric CFD study is to be done anyway to acquire process force predictions, the shear layer data can be used as a byproduct.

5.2.5.2 Pin Pressure Distribution

In Fig. 5.31 it can be seen that the predicted relative pressure acting on the pin can reach negative values that exceed the absolute pressure on the model (normal atmosphere at 0.1MPa). Therefore the resulting absolute value of pressure at the surface of the pin is negative in some areas. This can be interpreted as tensile stresses acting on the surface. Such a state is not conservative in CFD models. The formulation ensures continuity and cannot predict the formation of a void in a case where adhesion between the welded material and the tool is weaker than the tensile loads at the interface. This must be considered when comparing predictions with experimental results. As no experimental data is available on the maximum adhesion stress, further work is needed here to come to a consistent formulation that can deal with adhesion failure and void formation.

5.2.5.3 Forces and Torque

The torque acting on the tool can be predicted from both the TPM heat source as given in Eq. (3.10) and the CFD models. The first approach is energy based and thus only yields a value for the total torque. The CFD models allow for a prediction of viscous force per area on the tool-to-workpiece interface. The CFD torque and force predictions are very sensitive to the contact state δ as can be seen in Fig. 5.28. An increasing amount of sticking (higher values of δ) lead to higher torque values and lower forces in welding direction. The increase in torque results from the greater amount of deformation that is introduced into the modelled material in sticking condition. The shear thinning material law limits this increase in torque. It is also responsible for the decrease of the force in welding direction. The viscosity in the shear layer is smaller in the sticking condition which makes it easier for the tool to be moved along the weld line.

The sensitivity is very pronounced for the force prediction. The values for small δ (sliding condition) are two orders of magnitude larger than the values for pure sticking. The realistic values for δ are found by comparing the torque predictions of the TPM and the CFD approach.

Therefore the validation of the TPM torque predictions in Section 5.1.5.3 and Section 5.1.6 is applicable here. The values found are in the sensitive range of $\delta < 0.4$ (see Figs. 5.27 and 5.28). As the torque is not as sensitive to δ as the force, the force predictions must be considered to be less accurate in general as a consequence of the uncertainty in the determination of δ.

Forces acting on the pin can be predicted by the CFD models. For tool development knowledge of these forces is needed to estimate the loading conditions on the tool. As these can be highly dependent on the tool features, it is recommended to run the RFPM for a set of representative process parameter combinations and then check the stresses resulting from the predicted forces in the mechanical model. The force predictions are validated with the force measurements on experimental joints and show an acceptable quality. For simplicity the resulting total in-plane force F_{xy} is discussed as an example here. The experimental force values and standard deviations used for this comparison are taken for quasi-steady state situations (Z-force controlled) in the centre of the weld line. Fig. 5.32 shows a comparison of the F_{xy} predictions of the steady state CFD, a mean value over one tool rotation of the transient RFPM and the mean experimental force value. Results for two welding conditions are presented. One is a slow condition with the baseline tool (C_19, 600RPM, 1mm/s) and the other is a fast condition with the improved tool (T_07, 350RPM, 2.2mm/s).

Fig. 5.33 shows a comparison of a force prediction of the RFPM as a function of the tool rotational angle and the corresponding force measurement data for welding condition C_19. This figure additionally includes the predictions for the similar conditions (T_01, 600RPM, 1mm/s) when using the improved tool design. It has to be stated here that the curves in Fig. 5.33 are not synchronised. It is not possible with the present experimental setup to extract the exact tool angle in the global coordinate system. Therefore the experimental curve is generated from the timestamps of the force measurement and an assumedly constant RPM value. The phase shift is a priori unknown. However, several tendencies can be found from the numerical and experimental results:

- The force predictions of both CFD model and RFPM are in reasonable agreement with the experimental force measurements. As expected, the CFD predictions show a larger deviation from the experimental value (see Fig. 5.32) as they do not take into account the exact tool geometry. They also generally predict higher forces. All predictions slightly over-predict the experimental value. This is conservative with respect to tool design.

- The experimental force signal has a low resolution within a single tool rotation. Even in burst mode logging no more than 200Hz are possible. This corresponds to only 20 data points per revolution for the given example at 600 RPM. It is not feasible to accurately validate the predicted force curves within one tool rotation of the RFPM with the present experimental setup. It can be doubted that a faster force measurement alone can resolve this problem, as the scatter of the overall force signal is rather large.
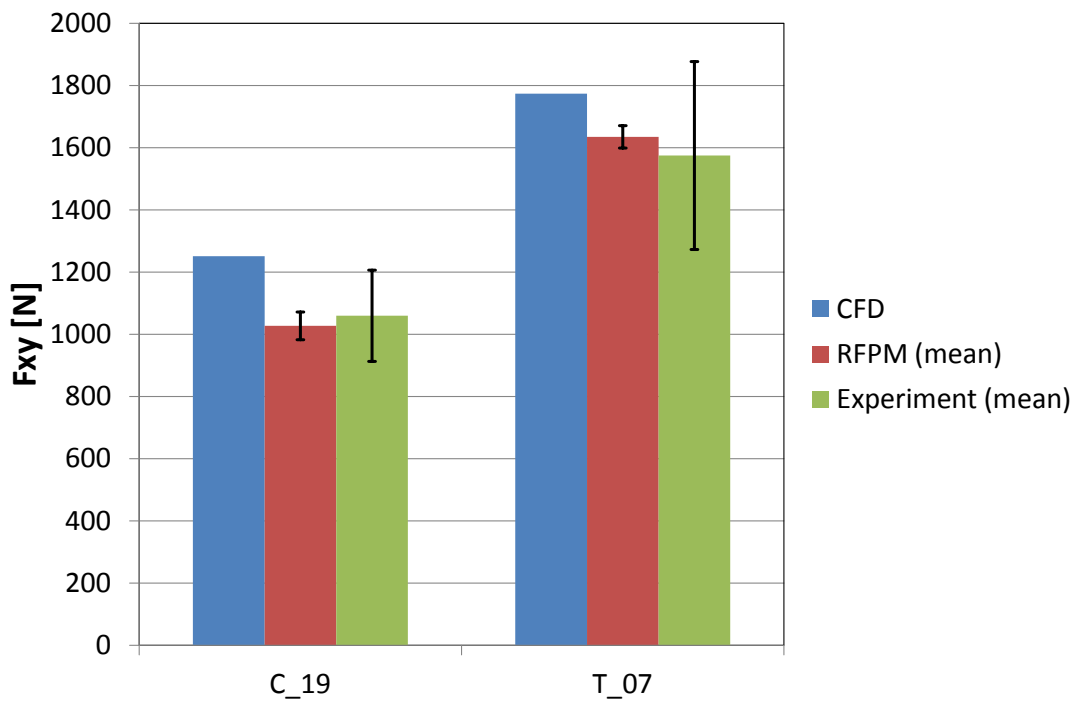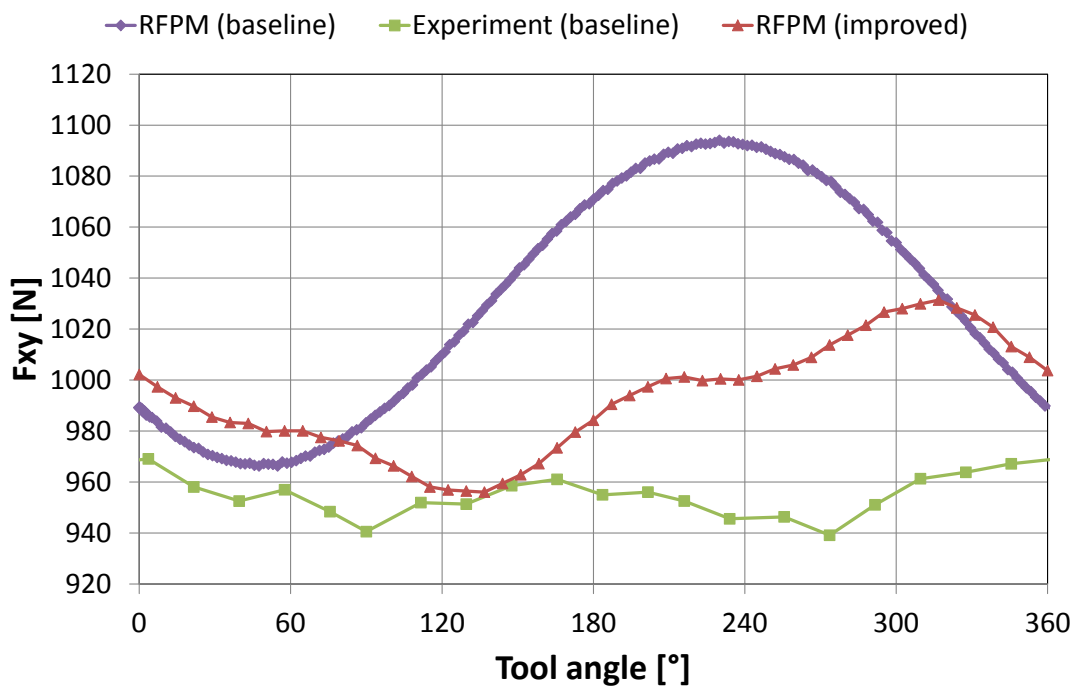
Figure 5.32: In-plane forces prediction and validation

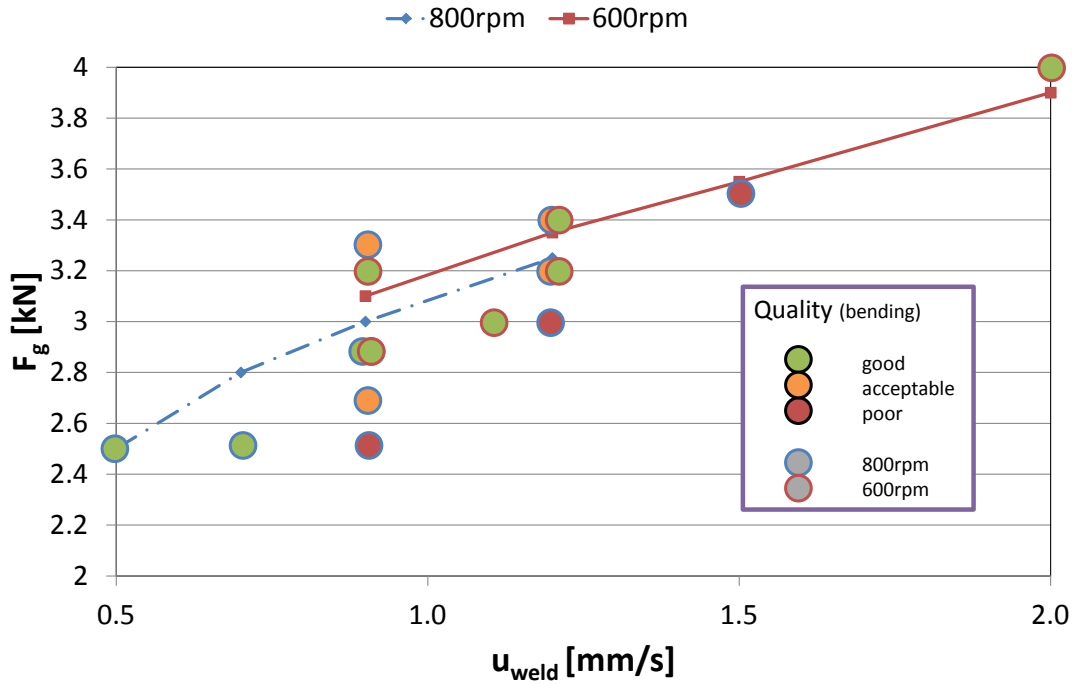
Figure 5.33: In-plane forces within one tool rotation

Figure 5.34: Predictions for the gap forces F_g and validation: curves are predicted, dots are experiments

- The improved tool has a 3-fold rotational symmetry of the features in the XY-plane. Therefore a periodic force signal of three times the tool rotational speed could be expected. This is not predicted by the model. The prediction is closer to a force signal periodicity of one per revolution. This seems to be in agreement with experimental data although the limitations mentioned above need to be considered. An explanation for this is not evident from the models flow field prediction and has not been proposed yet.

- For comparable process parameters the predicted mean in-plane forces for the improved tool are 3.3% lower than for the baseline tool. The maximum predicted in-plane forces is 5.7% lower. More important than this small decrease in absolute force value is the 51% reduction in the standard deviation. This could help to reduce vibrations during the process.

The gap force for a sound weld can also be predicted by the CFD model (see Section 5.2.4) analogous to Eq. (5.20). The model has been validated by comparing predictions made for a set of welding speeds at 600 to 800 RPM (conditions C_XX) to the experimental observations. For each of the predicted data points a validation weld with different controlled gap force levels has been performed.

The quality of each section has been assessed by bending tests (see Section 7.1.2). The results are plotted in Fig. 5.34. Green colour indicates the best performing bending specimen. Several tendencies can be found from the numerical and experimental results:

- The predicted gap forces can be used to perform sound welds with the Z-force controller. This is very helpful to define a basic parameter set as a starting point for further optimisation. The validity limits for different RPMs need to be considered. No acceptable results were found for 800RPM above 1.2mm/s while the agreement is good for 600RPM up to 2mm/s. This shows that not any predictable welding condition is actually weldable. Additionally further factors such as peak temperature and acting forces need to be considered.

- The needed gap force increases almost linearly with increasing welding speed for the investigated range of parameters. This is very helpful as a simple empirical gap force equation can be defined. This can be of the form $F_g := A + B u_{weld}$ and can be predicted from as little as two runs of the CFD model.

- The change in predicted gap force for changed RPM is rather small. Experimental results show that 800RPM welds have a tendency towards lower quality than 600RPM welds at the same gap force level even though the predicted values are similar. This may be due to other effects related with the higher heat input of 800RPM welds.

5.3 The Process Model - Summary and Conclusions

In this chapter the numerical models that have been developed according to the objectives of this work (see Section 2.1) are introduced. Together they can be thought of as a process model. This process model consists of three parts. One is the thermal model with TPM heat source that uses an advanced moving geometry approach to predict the transient temperatures acting at any time and location during the welding process. This model is a purely thermal model and can therefore be run fast with very little demand for computational resources. The second one is a CFD model that predicts the material flow around the tool and the forces acting on it. This model needs the input of the thermal model. As the thermal model gives best results when calibrated with a correct shear layer shape predicted by the flow model the entire modelling schema is by nature iterative.

The final part of the process model is the mechanical model for the tool loads. It can be run with nothing more than the predictions of the other parts of the process model and basic knowledge of the tool material properties at elevated temperatures. Therefore tool design can be performed up to a certain degree without the need of experiments. An overview of the entities and quantities involved in the process model development and the interactions between them is given in the flow chart Fig. 5.35. A step by step description of the work flow and a description of how to use the models in process development is given in Section 8.1.

Based on the information gained from the models described above, further modelling attempts are possible to gain a deeper understanding of the BT-FSW process. The evolution of microstructure based on the temperature history can be modelled. This effort can be based
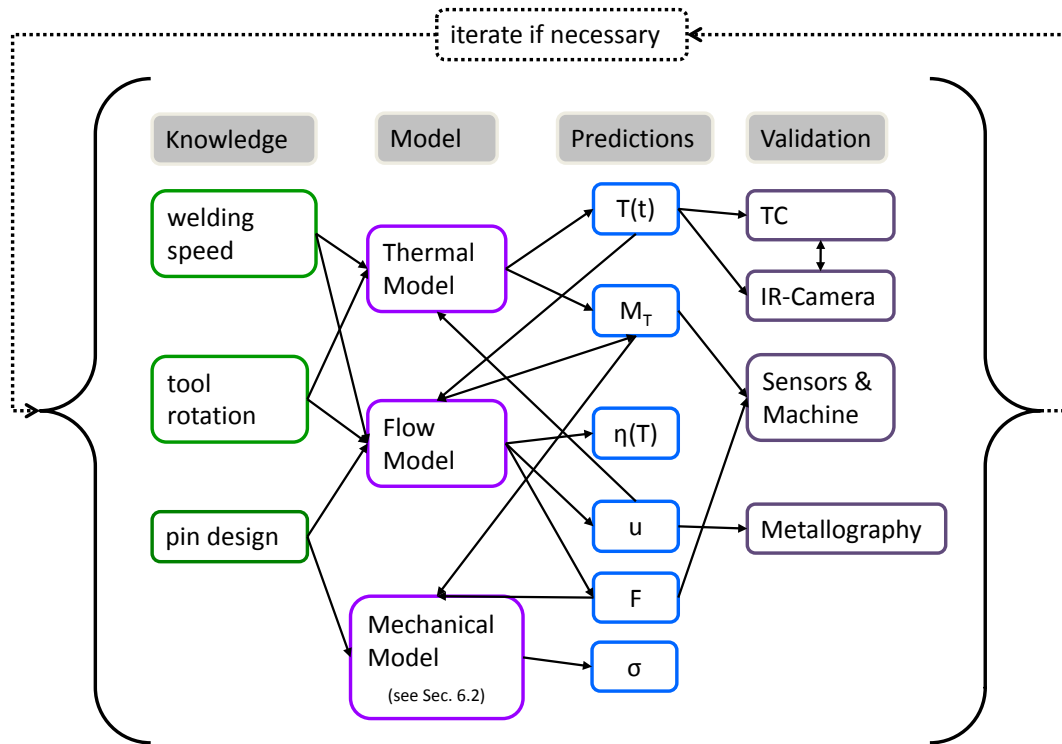
Figure 5.35: Flowchart of the process development schema

on successful existing approaches (see Section 3.2.2.3). The residual stresses can be modelled using the temperature field and the applied loads from the tool and clamping.

Thermal Model

- A thermal model has been developed based on a TPM heat source.

- It can predict the transient temperature field of the process using a moving geometry.

- The shear layer around the tool is represented analytically with a model based on inputs from the flow models.

- The energy input to the joint and the torque acting on the tool are outputs rather that inputs of the model.

- The predicted temperature fields have been validated experimentally with thermocouples and infrared thermography.

- The predicted machine torque has been validated experimentally with motor current measurements.

Flow Model

- The material flow around the tool has been modelled for both simple tools in steady state and (transient) rotating featured tools. The first assumes a tool with axial symmetry for basic predictions, the other can deal with featured tools at the cost of increased demand for computational resources.

- The predicted shear layer shape is used to calibrate the thermal model.

- The material is treated as liquid with nonlinear temperature and strain rate dependent viscosity. Measures have been taken to achieve convergence of the model in spite of the strong non-linearity of this material model.

- Forces and torque acting on the tool are predicted. They can be used to assess tool design, clamping setup and other relevant quantities like required machine stiffness.

- The contact condition at the interface between tool and welded material can be predicted and is not needed as an input.

Chapter 6

Implementation

6.1 Tooling

6.1.1 Tool Loading

A bobbin tool is subject to very demanding conditions of operation. It has to withstand complex three dimensional mechanical loading at high temperatures. For aluminium and magnesium based light alloys the temperature of the tool can rise up to 500°C. The main mechanical loads acting in the pin are superimposed torsion and bending as well as tension. A schematic illustration of the loading condition is given in Fig. 6.1. Therefore bobbin tool design has two major aspects. One is to know the forces and the resulting loads on the tool during welding. The other is to find a tool material that can meet these requirements and allows for tools to be manufactured in an economic way. While the forces on the tool can be determined experimentally as well as numerically, the resulting stresses of a complex featured tool can only be determined by numerical modelling (see Section 6.2.1). As the manufacturing of a prototype for a new tool design is an expensive and time consuming task, it is reasonable to use a numerical model to predict the acting forces first (see Section 5.2). Within the scope of this study, an improved tool design was developed. It is based on a set of aspects that have been found to be important and are described below.

6.1.2 Tool Materials

The selection of the tool material is very important for the BT-FSW process. Here it plays a more prominent role as compared to standard FSW because of the severe loading condition of the pin. The tool material is the major limiting factor for welding speed and thus productivity. The most important material parameter for metallic tool materials is the yield stress at elevated temperatures. In the case of welding aluminium or magnesium the test temperature can be chosen to be 500°C. Higher temperatures would lead to bulk melting of the work pieces and do not occur in the process. The use of other high temperature materials as bobbin tool
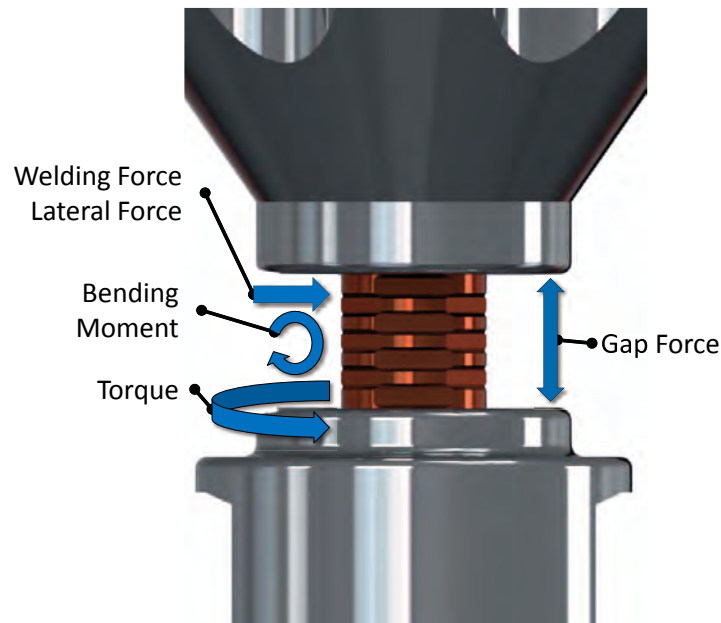
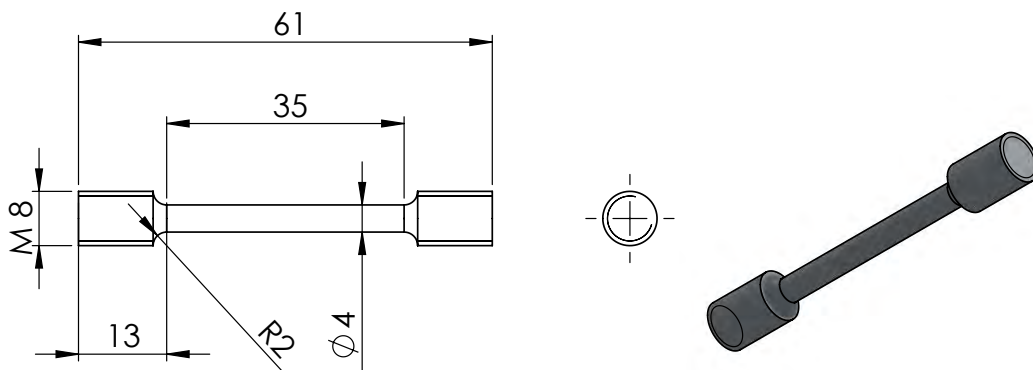Figure 6.1: Schematic illustration of the tool loading

Figure 6.2: Geometry and dimensions of the hot tensile specimens

pins has been considered. Ceramic materials are in principle suited for the high temperatures and loads. The application of cubic boron nitride in the classical FSW tooling for steel welding proves this. The high amount of tensile stresses in bobbin tools is the most challenging aspect from a technological point of view. The most important argument against ceramic tool materials still is the cost of manufacture and the limited machineability of complex features.

Hot tensile tests have been performed to qualify four different tool material candidates. The tests where conducted on a MTS tensile testing machine at 500°C based on the standard DIN EN 10002-5. The specimen dimensions and geometry are given in Fig. 6.2. This shape was selected due to its good representation of a common bobbin tool pin. The candidate materials are known under their commercial names Marax, Hotvar, TSP01 and MP159. The composition is provided in Tab. 6.1. The heat treatment used for the tool materials was

Name	Composition	Standard
Marax	X2NiCoMo18-9-5	DIN 1.6358
Hotvar	55CrMoV10-23-9	-
TSP 01	X80CrCoMoVNb6-3-3-1-1	-
MP159	CoNiCrFeMoTi36-26-19-9-7-3	AMS 5841-5843

Table 6.1: Tool material composition

derived from the suggestions of the manufacturer:

Marax anneal at 800-1000°C; age 3 hours at 460°C;

Hotvar anneal at 1060°C; oil quench at 220-550°C; immediately age 3 times for 1 hour at 580°C;

TSP 01 anneal at 1100°C; oil quench at 220-550°C; immediately age 3 times for 1 hour at 580°C;

MP159 anneal at 1050°C (for 4 hours); water quench; age 4 hours at 660°C;

Four samples of each of the tool material candidates have been tested. The results are listed in Tab. 6.2. Not all tests could be evaluated properly because sliding occurred at the extensometer. The values that are listed without an explicit tolerance could not be determined for a sufficient number of specimens. A comparison of the recorded force-displacement curves suggests a very low scatter of these values as well. A comparison of the engineering $\sigma - \epsilon$ curves for the different materials is given in Fig. 6.3.

Material	$Rp_{0.2}[MPa]$	$E[GPa]$
Marax	1447	$158 \pm 5.0\%$
Hotvar	$1246 \pm 0.9\%$	$166 \pm 0.0\%$
TSP 01	1395	163
MP159	$1561 \pm 0.3\%$	$205 \pm 0.8\%$

Table 6.2: Results of the hot tensile tests

6.1.3 Tool Cleaning

After welding aluminium or magnesium alloys the concave features of the pin are usually filled with work piece material. This does not necessarily yield any problems when welding the same alloy with the same tool in a consecutive experiment. The excess material is mechanically removed during the run-in phase of the process. This is different when excessive material is entrapped in the gap between the upper shoulder and the pin. If this material cools down after welding a defined movement of the actuator that defines the gap size is often no longer possible. Even if a sufficiently large force can be applied to overcome the friction in the gap
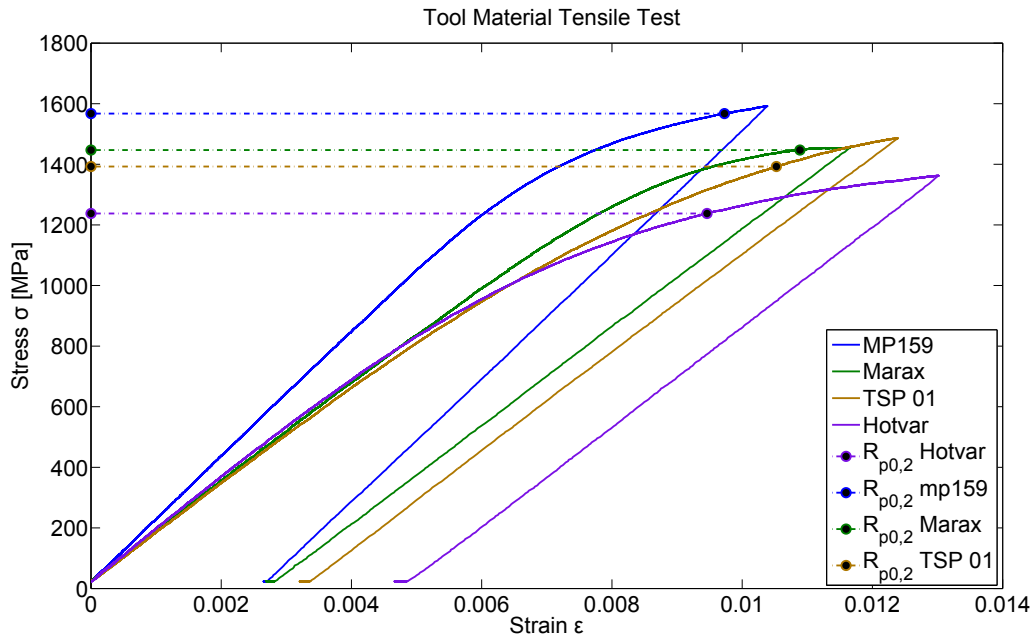
Figure 6.3: Comparison of the engineering $\sigma - \epsilon$ curves for tool materials at $500°$C

and effectively control the gap size, it is still not possible to perform another Z-force controlled weld, as the gap force cannot be accurately determined when large frictional forces counteract any positioning of the pin actuator. When a used tool is to be reused for an other alloy it needs to be cleaned to prevent contamination of the weld.

It has proven convenient to use chemical cleaning where needed. Aluminium alloys can be removed from steel tools in a solution of sodium hydroxide within a few minutes to a few hours depending on the chosen concentration. A concentration of 10 to 20 g/l has proven efficient. The duration of tool cleaning can be efficiently reduced when operating at elevated temperatures ($40°$C) and stirring the solution. Magnesium alloys can be chemically dissolved in a similar procedure using acetic acid. This method has a considerable advantage over mechanical tool cleaning, as the latter can lead to excessive wear of the pin features.

When performing a parametric study, it is suggested to chemically clean the tool prior to each welding experiment. This guarantees maximum comparability by eliminating any influence of the tool precondition. A comparison between a bobbin tool after welding and after cleaning is provided in Fig. 6.4.
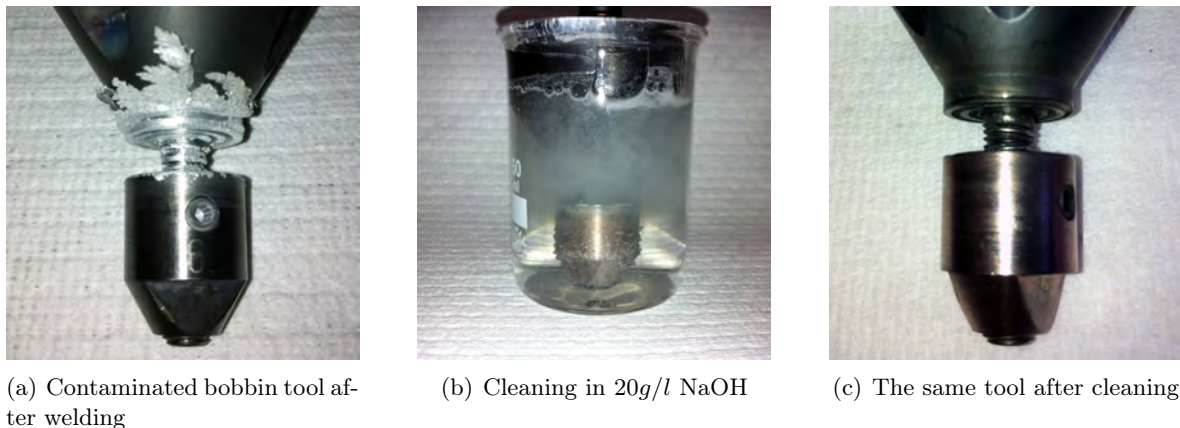
(a) Contaminated bobbin tool after welding

(b) Cleaning in $20g/l$ NaOH

(c) The same tool after cleaning

Figure 6.4: Tool cleaning

6.1.4 Tool Design

6.1.4.1 Empirical Bobbin Tool Design

The most simple bobbin tool design possible is monolithic. Such a tool has a fixed distance between the two shoulders and can thus only be used for a single thickness of joints. The advantage of this design is the low cost of manufacturing and the high mechanical robustness of the tool. A main drawback is the lack of control of the force acting between the shoulders. This force results from the thickness mismatch between the tool gap and the work piece. It is a function of temperature due to thermal expansion. The change in gap force due to thermal expansion can be very large. For the tool, work piece size and material used in this study the additional pin tensile stress due to a temperature change from room temperature to the operating condition (400K difference) has been determined from a simple FE Model. It includes an axis symmetric representation of a 4-mm-thick AA2024 workpiece and a HotVar tool (see Section 6.1.2) with a $\varnothing$ 6mm pin and $\varnothing$ 13mm shoulders. The material chosen is a linear elastic model with temperature dependent material properties. The results are shown in Fig. 6.5.

In this scenario the increase in tensile stress in the pin has a maximum of 355MPa. The loads on the pin considerably increase as the joint is heated up. As the gap needs to be predefined to allow a start of the weld in cold material, the additional loads can easily lead to tool fracture as soon as the working temperature has been reached. If the tool can carry the loads, the result of the thermal expansion mismatch can be a too small welding gap leading to significant flash formation and a weld that is thinner than intended. Additionally the higher gap forces can lead to undesired thermo-mechanical conditions in the shear layer giving rise to material flow instabilities.

It is widely accepted in the FSW community that controlling the process parameters severely improves the joint quality [12, 108, 109].
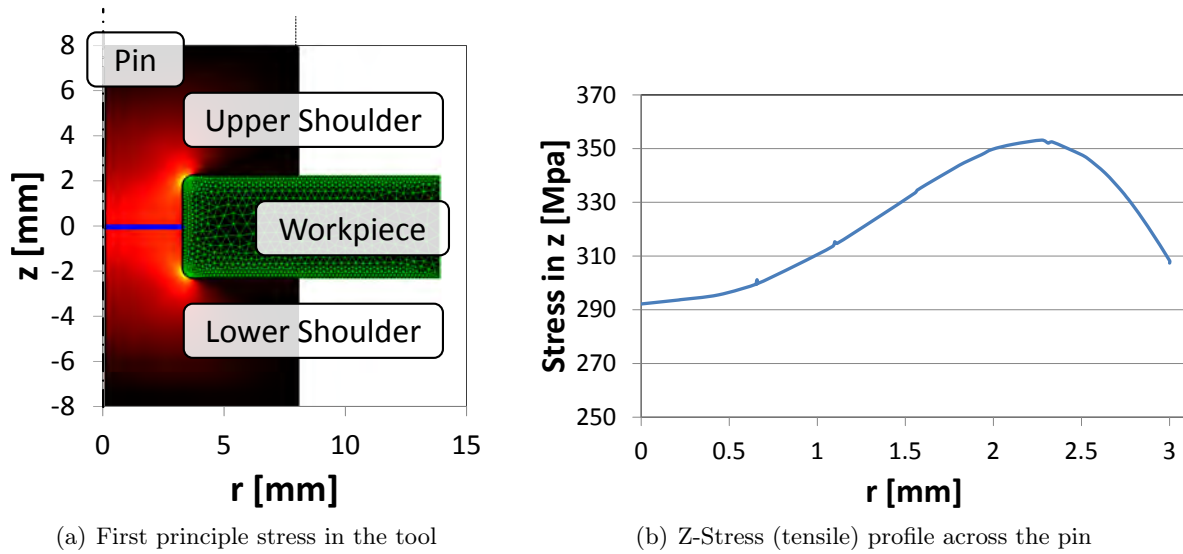
(a) First principle stress in the tool

(b) Z-Stress (tensile) profile across the pin

Figure 6.5: Additional pin stress due to 400K temperature rise in pin and workpiece

A common approach is to control the force acting between the shoulders of a bobbin tool by adjusting the gap thickness or pin length (see Section 6.3.1.2) [3]. In order to achieve this relative motion, the tool is split up into at least two pieces. The upper shoulder features a hole trough which the pin is inserted. The lower shoulder can be fabricated as part of the pin or attached as an additional component. The relative motion of the pin in the upper shoulder can be generated by an additional actuator. An example of such a tool with gap size control capability is provided in Fig. 1.3. A drawback of this design is the inherent problem of hot material from the workpiece being extruded into the gap between the upper shoulder and the pin. Therefore tool cleaning is often required (see Section 6.1.3).

A tool with separated upper shoulder and pin can also be used to define different rotational velocities for both shoulders. Theoretical considerations suggest that this can help to achieve better control of the heat input and the temperature field formation. There are three different possible regimes to choose from. A small relative velocity in the gap between pin and upper shoulder can be realised with most tool designs and materials. Depending on the motor technology and controller, such a small relative velocity may not be avoidable. It results from using two individual motors for the upper shoulder and the combined lower shoulder and pin. A large relative velocity can lead to excessive frictional heat generation in that gap. Fig. 6.6 shows a thermograph of the heat generation of a tool with large relative velocity after only a few seconds of rotation without any external load. The heat generation at the interface between the tool and the workpiece is limited by the lower high temperature strength of the work piece. The frictional heat generation in the gap between the pin and the upper shoulder is not limited in this way. The additional heat input may damage or completely destroy a tool that is not equipped with a suitable friction and heat protection. Such a protection can

(a) Before rotation
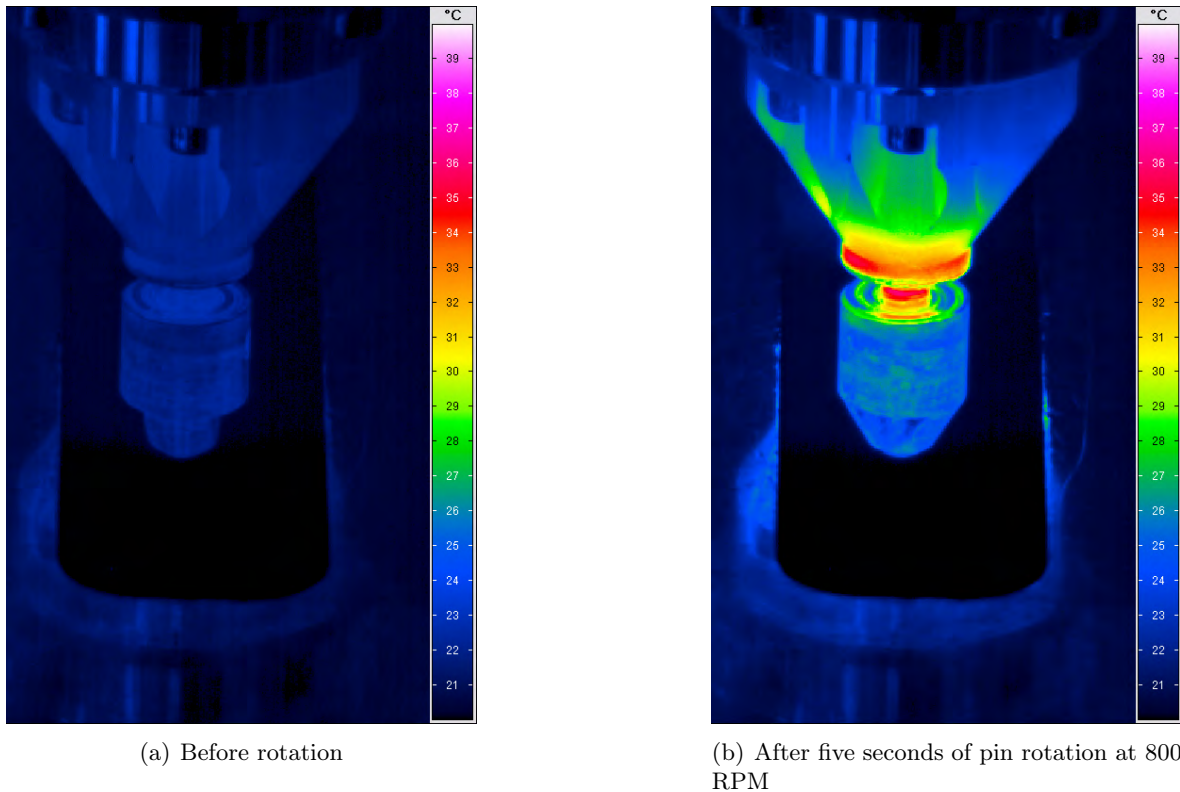

(b) After five seconds of pin rotation at 800 RPM

Figure 6.6: Tool heat generation due to relative velocity (steel on steel)

be realised by ceramic inlays like those included in the improved tool design developed in this study. Fig. 6.7 shows the effect of the inlays. The test conditions are the same as for Fig. 6.6 but the time at 800 RPM is extended to one minute. The rise in temperature is minimal. In a next step of development the lower shoulder can be decoupled from the pin. This way the complete heat input is generated by the pin. Details can be found in a patent by Hilgert and dos Santos [110].

The design of the pin features has been mainly empirical in the past (e.g. [3]). The pin design used for the baseline experiments (B_XX) as well as the controller development experiments (C_XX) within this study can be seen in Fig. 6.8. The threads included in this design are inspired by standard FSW tooling. For these it was found that enhanced material transport towards the root of the weld is often needed to avoid root defects and tunnels.

When comparing the tools to the original drawings of the pin features (see Fig. 6.8) it can be observed that the computer aided design does not ideally correspond to the shape that was actually manufactured. Such deviations make process development extremely difficult as there is insufficient repeatability. It is further impossible to reach an in-depth understanding of the interaction of the tool design and the process results when the tool shape is not known with sufficient accuracy. Therefore the improved tool features are designed with respect of
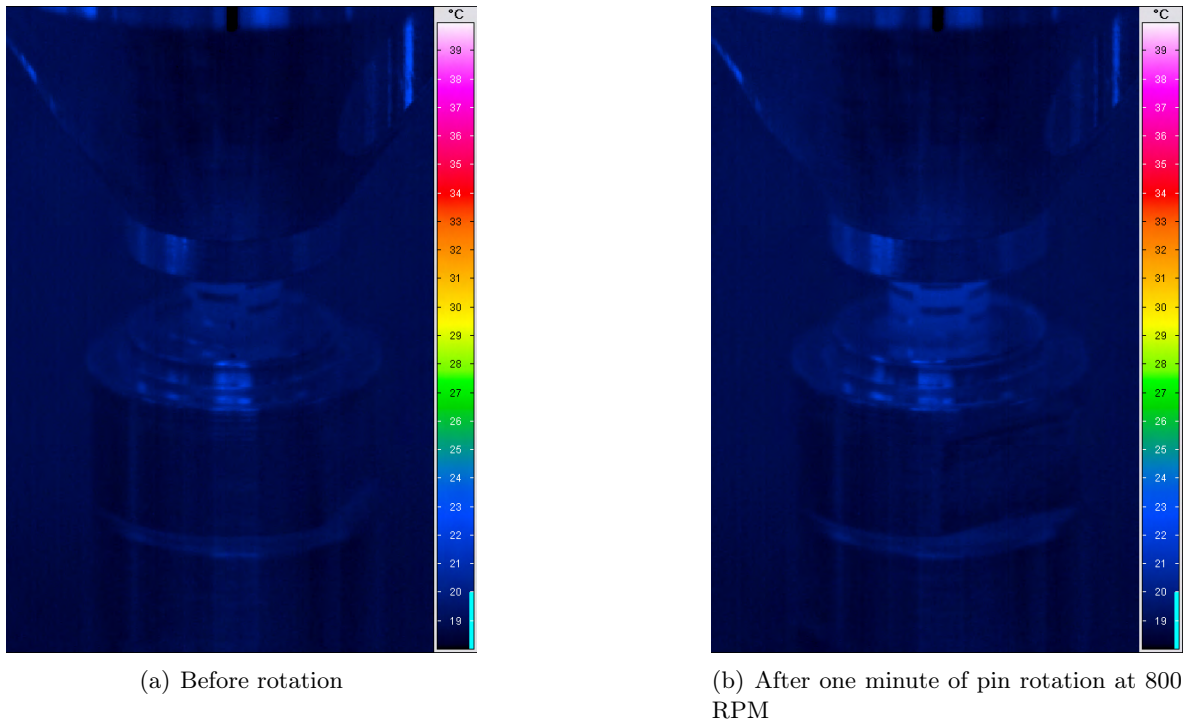
(a) Before rotation

(b) After one minute of pin rotation at 800 RPM

Figure 6.7: Tool heat generation due to relative velocity (Al_2O_3 inlay)

machinability (see Section 6.4.3). This leads to the desired reproducibility of the pin shape as can be seen in Fig. 6.9. The improved bobbin tool design does incorporate threads. This is a consequence of the experimental observations of the joint microstructure described and discussed later in Section 7.3.3.

6.1.4.2 Simulation Based Tool Design

In order to avoid costly trial and error iterations in tool design, the loads acting on the tool in service need to be known as precisely as possible. From these loads the acting stresses can be deduced and compared to the allowable stresses of the respective tool material. This procedure involves aspects that can be dealt with experimentally and some that can only be provided by a numerical model. In any case experimental data in tool development is always linked to a full scale tool hardware manufacturing iteration. It is therefore desirable to obtain predictions of the acting temperatures, loads, and stresses from numerical calculations only. The predictions for temperature and loads are provided by the process model developed for this study (see Chapter 5). The predictions of the resulting tool stresses is described in the following Section 6.2.

The starting point for numerical tool development can either be a simple basic geometry like a cylindrical pin with no features or a knowledge based approach with an existing geometry to be optimised. The first step in the tool development schema is to predict the temperature
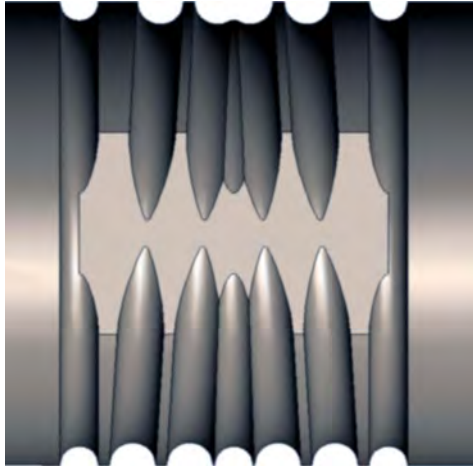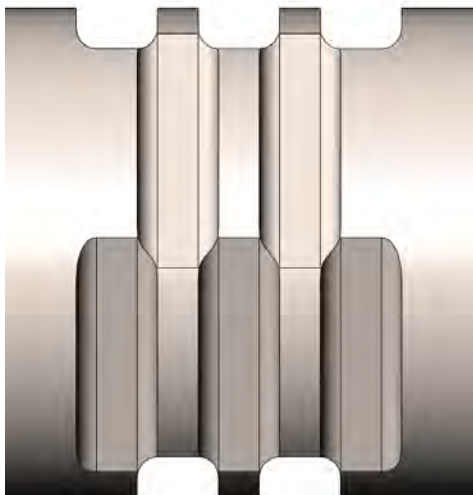
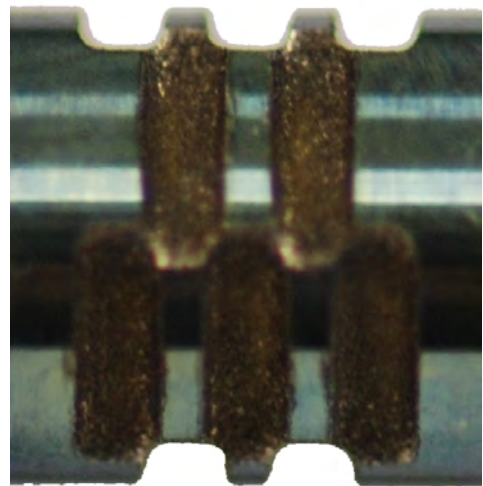(a) Empirically designed threaded bobbin tool pin (as designed)

(b) Empirically designed threaded bobbin tool pin (as manufactured)

Figure 6.8: Empirical bobbin tool pin feature design

(a) Improved bobbin tool pin (as designed)

(b) Improved bobbin tool pin (as manufactured)

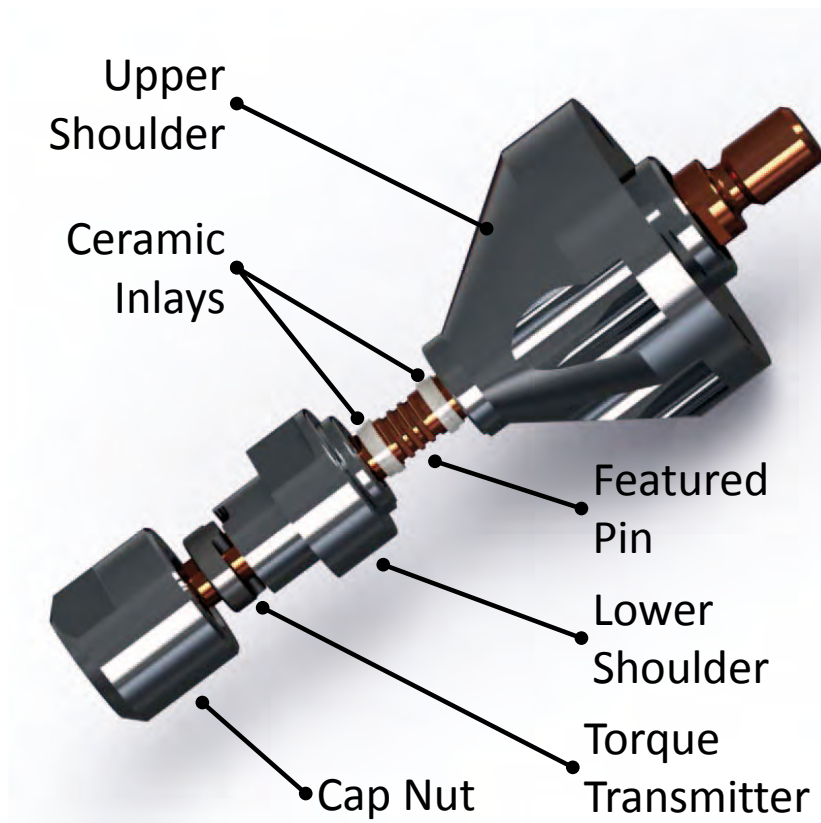Figure 6.9: Improved bobbin tool pin feature design

Figure 6.10: Improved bobbin tool assembly

the tool will have during operation (see Section 5.1.2) and the forces that will be acting (see Section 5.2). The second step is to predict the stresses in the tool (see Section 6.2.1) and compare them to the allowable stress of the desired tool material (see Section 6.1.2) at the defined temperature. Now tool features and tool material can be changed until a satisfactory result is achieved. As the acting loads are a function of the tool features to a certain degree, a run of the material flow model for featured tools (see Section 5.2.2) is needed per iteration for best precision. The actual shape of the material shear layer can be used to further qualify a tool design.

The improved tool design developed using the models and experiments described in this study is presented in Fig. 6.10. Apart from the pin features and the tool material, some changes where made to the mechanical setup of the tool. The lower shoulder is now a multi-part design which allows for easy assembly and disassembly with a well defined position on the pin. There are inlays made of Al_2O_3 inserted into the gaps between the pin and shoulders to reduce friction, wear and heat transfer due to relative motion of the pin.
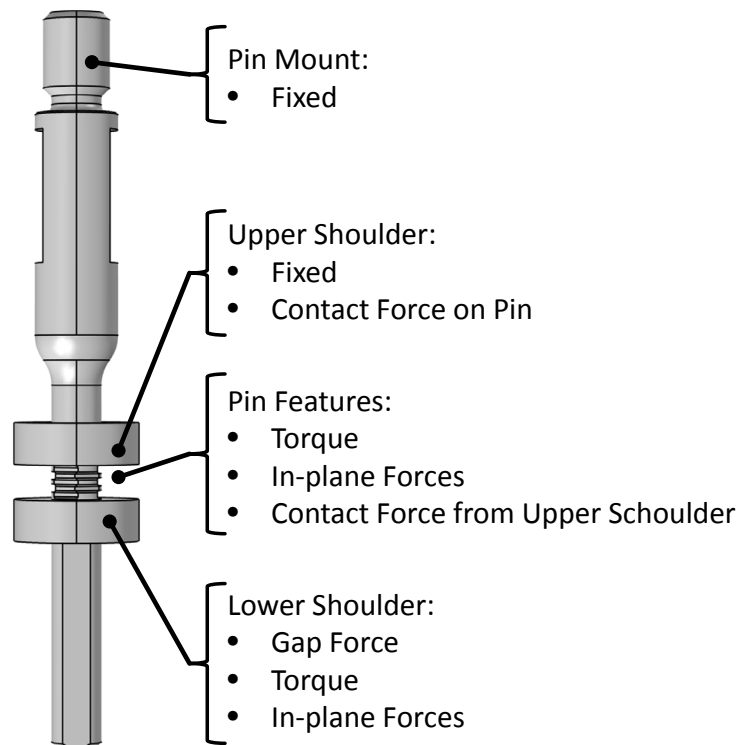
Figure 6.11: Geometry and interactions of the mechanical model

6.2 Mechanical Modelling

6.2.1 Model Implementation

When the loads acting on the tool are known from either experimental measurements or a model (CFD or RFPM), a simple mechanical model can be used to compare the maximum stress acting in the critical regions of the tool to an allowable value based on the material properties of the tool material (see Chapter 6 and Section 6.2.2). It is sufficient to use a linear elastic material model, as plastic deformation should not occur in the tools. If the predicted stresses for a parameter set exceed the yield stress of the material at any critical location, it is not recommended to use these tools for that parameter set.

The modelled geometry includes the pin and idealised parts of the shoulders for the application of boundary conditions. The interactions are summarised in Fig. 6.11. An example for the mesh density required for the pin can be found in Fig. 6.12. The governing equations of the mechanical model are not described in greater detail here, as they can be considered very basic.

In order to be able to quickly compare different tool designs and estimate stress characteristics
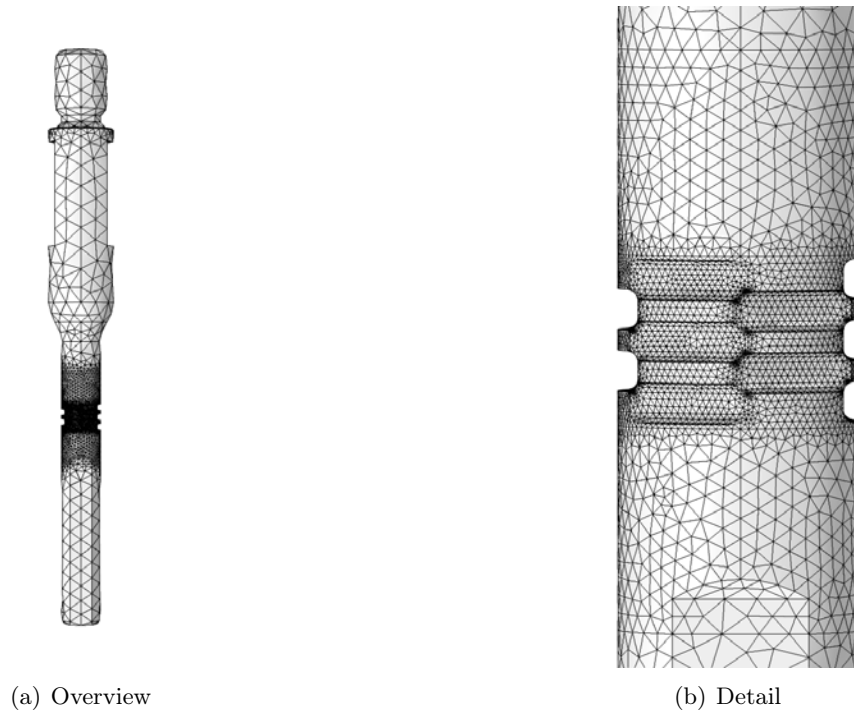
(a) Overview

(b) Detail

Figure 6.12: Mesh density needed by the mechanical model

a test-case scenario is used including several load cases listed in Tab. 6.3. It has to be stated that the load in welding and lateral direction can be combined to only one load in the plate-plane. As the pin is not axis-symmetric the rotation will lead to different reactions to the applied load as a function of the rotation angle. Therefore the test-case scenario uses F_x and F_y so that a mean and a max value can be estimated. In critical cases it may be needed to test a larger number of force vectors to find the maximum occurring stresses with sufficient precision. In principle it is also possible to run the mechanical model in a transient frame. Then the realistic transient loading histories from the RFPM could be evaluated. This might be needed in the future when studying the fatigue behaviour of the tool. The last load-case has been derived from the magnitude of loads commonly acting during the welds performed within this study to allow for a fast comparison of tool candidates. If the distribution of the loads is not known in detail (e.g. from the RFPM) all loads are applied in a conservative way. The in-plane force Fxy is applied at the interface between lower shoulder and pin. This result in a maximum bending moment. The torque is distributed to the upper shoulder, lower shoulder and pin in a ratio of 47%, 47% and 6% resulting in an effective torque on the pin of 53%. These values are found from the RFPM and are a reasonable approximation of the torque distribution for all geometries considered. Results and predictions of the mechanical model are provided in the context of tool design in chapter Chapter 6. The discussion of these can be found in Section 6.4.2

Load-Case	M_T [Nm]	F_x [kN]	F_y [kN]	F_g [kN]
A	1	0	0	0
B	0	1	0	0
C	0	0	1	0
D	0	0	0	1
E	10	1	1	3

Table 6.3: Load-cases for the mechanical model

Load-Case	Baseline $\sigma_{Mises_{max}}$ [MPa]	Improved $\sigma_{Mises_{max}}$ [MPa]	rel. change [%]
A	503	645	128.2
B	854	785	92.9
C	813	809	99.5
D	120	145	120.8
E	1401	1194	85.2
Fracture	1811	-	-

Table 6.4: Predicted tool stress

6.2.2 Tool Loading Prediction

The stresses acting in the tool are predicted by the mechanical model (see Section 6.2.1). These predictions are used in the tool development process. The predicted loads for candidate designs are compared among each other and to the material limits (see Section 6.1.2 and Tab. 6.2). Fig. 6.13 shows the response of the final pin design to the simple load-cases listed in Tab. 6.3. The reaction to the most complex combined load-case E is shown in detail in Fig. 6.15(b). These predictions can be compared to those for the baseline tool design. The stress response to the same load conditions is given in Fig. 6.14 and Fig. 6.15(a). The maximum stress values for all cases presented here are listed in Tab. 6.4.

The mechanical model predictions are also helpful when choosing process parameters for existing tools. Fig. 6.16 shows the load acting in a baseline tool in a condition that can lead to pin fracture (see Section 7.2.1). The overload can be predicted and thus such welding conditions can be avoided.
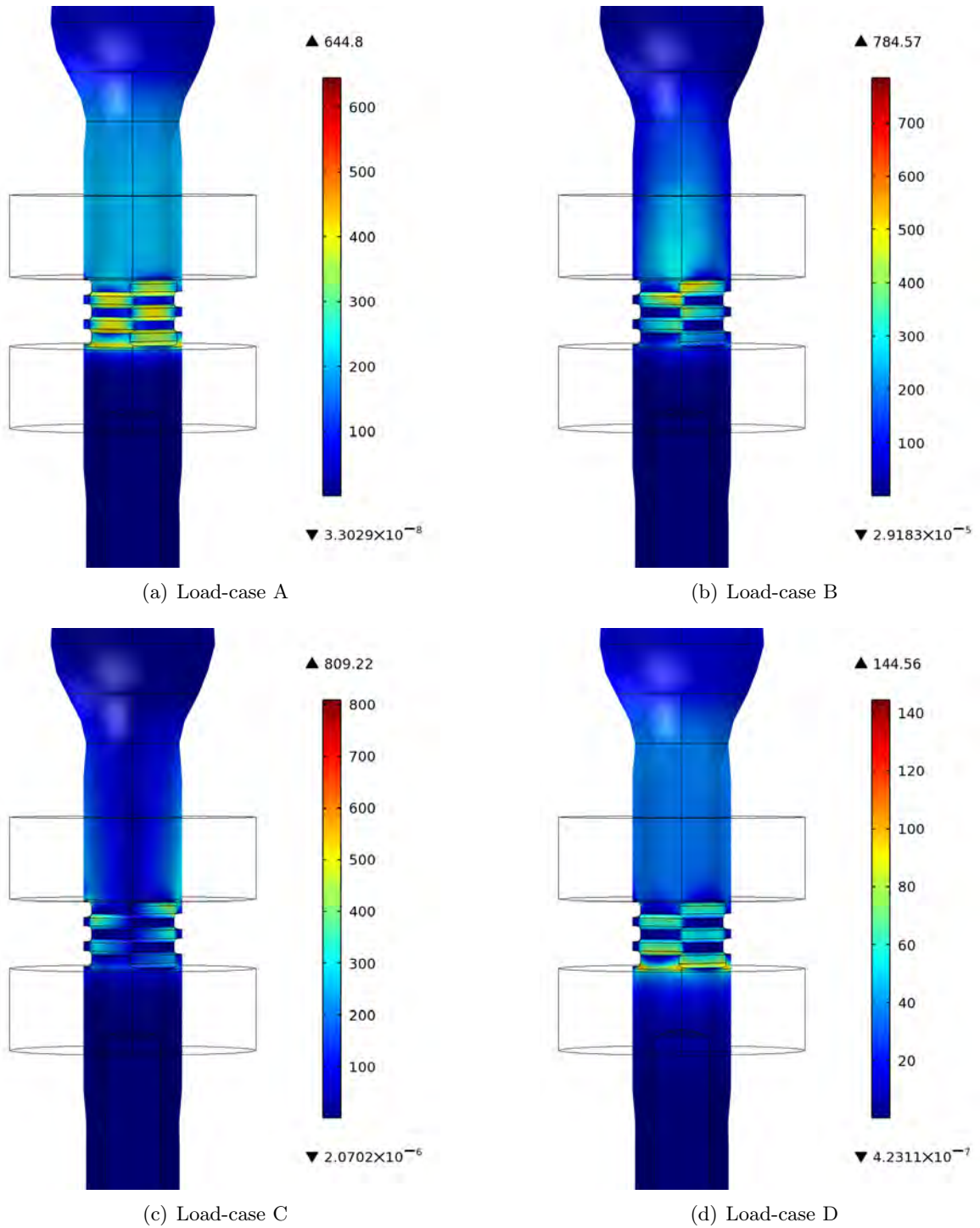
(a) Load-case A

(b) Load-case B

(c) Load-case C

(d) Load-case D

Figure 6.13: v. Mises stress response to simple load-cases

(a) Load-case A

(b) Load-case B

(c) Load-case C
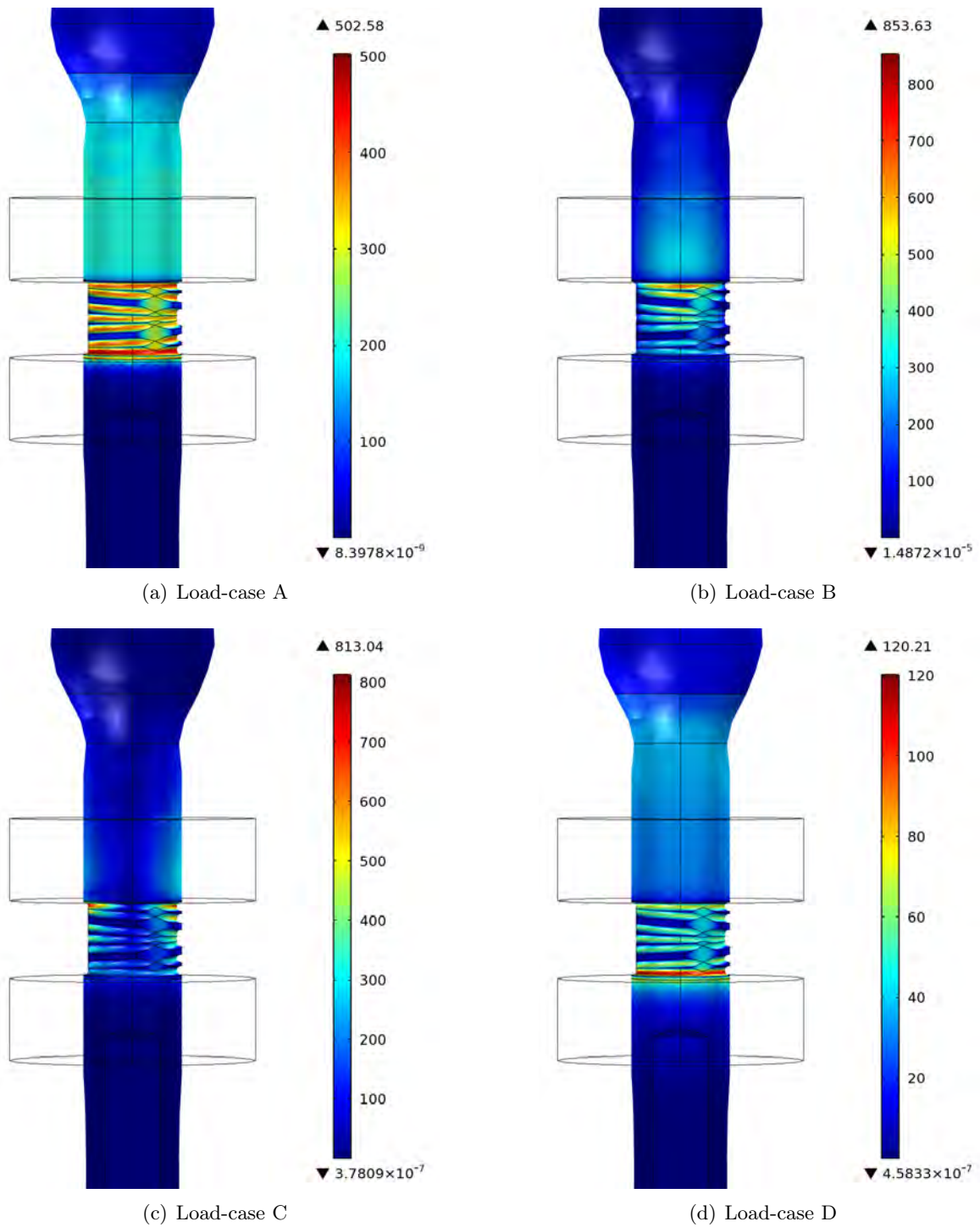
(d) Load-case D

Figure 6.14: v. Mises stress response to simple load-cases (baseline tool)
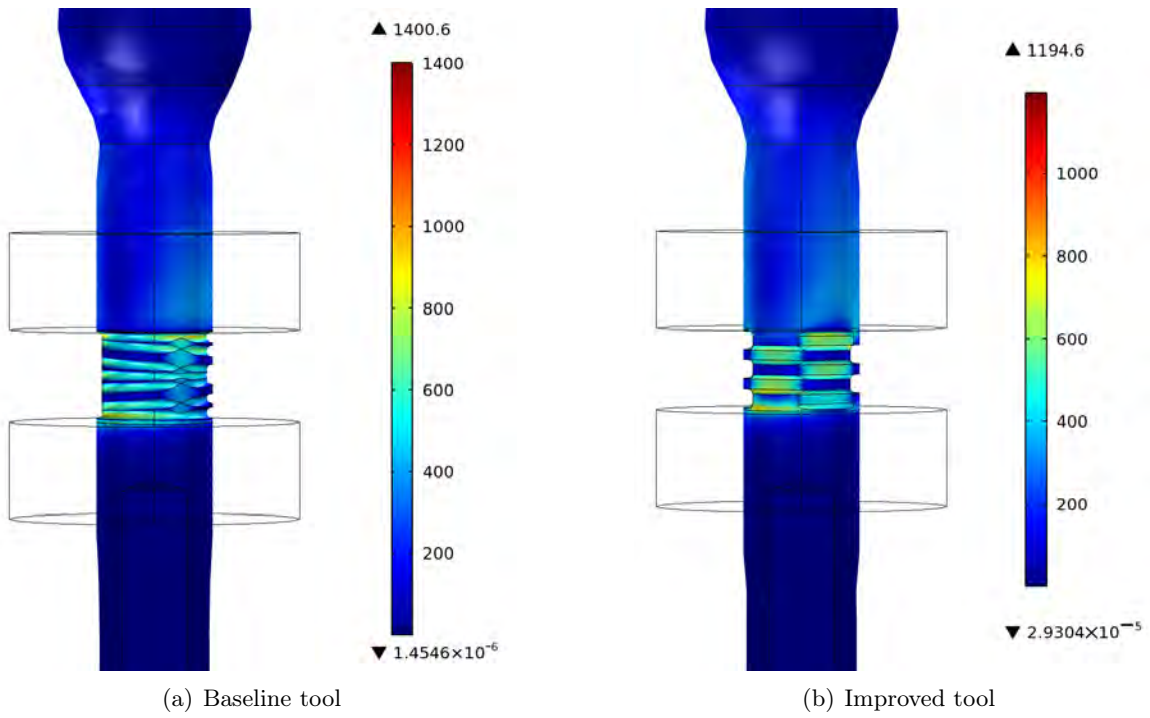
(a) Baseline tool

(b) Improved tool

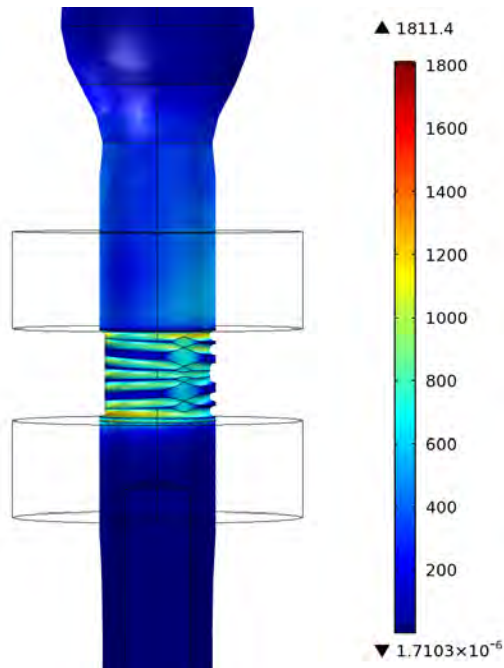Figure 6.15: v. Mises stress response to complex load-case

Figure 6.16: v. Mises stress response of the baseline pin to the fracturing load-case

6.3 Process Control

6.3.1 Process Control Strategies

In BT-FSW the main process parameters are usually considered to be welding speed, tool rotational speed and force between the shoulders. While rotational speed and welding speed are externally applied by any welding machine, the force between the shoulders can either be controllable or result from the geometric properties and the applied conditions. Not all combinations of process parameters lead to a stable joint formation. The accessible process window is limited by several quantities. High welding speeds result in high loads on the tool. The same is true for excessive gap forces. Insufficient gap force or tool rotational speed can lead to insufficient heat generation. The consequence of this is a milling process rather than a joining process as material is not plasticised but cut or chipped. Too high heat inputs can lead to excessive softening of the material and formation of large flashes. For most materials excessive heat input results in a massive degradation of the material properties. Therefore the process parameters must be chosen with regard to these limitations.

As the process is not static but very transient in nature for most cases it is important not only to choose adequate initial parameters but to control them throughout the weld. Especially when attempting to perform short welds that are by nature more transient in their behaviour and usually do not reach a steady state it is desirable to control the process variables like temperature and forces to reduce quality gradients in the joint. This does not mean that process control is not important for long welds, of course. The possible approaches are described in this section.

6.3.1.1 Static Parameters

The most elementary strategy in process control is static parameter control. This means that the welding speed and tool rotation are defined and then kept constant throughout the joint. This is possible on most welding machines whether they are specialised FSW machines or adapted milling machines of any kind. Usually this functionality is already implemented in the hardware in the form of an integrated controller. A static parameter process does usually not keep the gap force constant, as it is a resulting variable more than a basic process parameter. The constant quantity is rather the nominal gap size or nominal distance between the shoulders. This results from intrinsic limitations of the tool (monolithic design) or the welding machine (no measuring capability for the gap force). As mentioned above this strategy does not provide best results for short welds. The parameters needed to achieve a sound run-in are not optimal (if even usable) for the rest of the joint. Once the tool has heated up and thermal expansion mismatches have lead to a change in gap force (see Fig. 6.5) the physical boundary conditions are very different from the initial ones.

6.3.1.2 Z-Force Control

With monolithic tools no direct control of the force between the shoulders is possible. The acting force results directly from the gap between the shoulders and the work piece thickness. Both are a function of temperature because of thermal expansion. Therefore the acting forces can usually not be kept constant throughout a weld. This can results in inhomogeneous joints. The most common approach to solve this issue is to apply a Z-force control through a tool with variable gap size (see Figure 6.5). If the gap can be directly controlled and the force acting on the upper and lower shoulder can be measured a full feedback controller can be implemented (see Section 6.3.2). The controller will then attempt to adjust the gap size until the desired z-force is achieved. This is the best option to guarantee constant pressure on the plasticised material of the shear layer and helps to achieve homogenous weld quality. Additionally such a controller helps to efficiently prevent tool overload.

6.3.1.3 X-Force Control

Independent of the gap size and gap force, the force acting in the welding direction can be used to control the welding speed (see Section 6.3.2) It may also be considered to control the x-force by variation of the tool RPM. This can be implemented on any welding machine as long as force measurements can be conducted at the tool or at the work piece during welding. One possible aim of an X-force controller is to keep the physical conditions in the weld constant. As heat generation is a function of travel speed and RPM (as is the X-force), a controlled X-force can help to limit the temperature variation (for advantages and disadvantages of this controller strategy see also Section 6.3.1.4). A more important field of application of this control strategy, however, is the overload protection of the tool. If the force in X-direction or the combined XY-force is limited by such a controller, the risk of tool fracture can be decreased. This strategy can also be used to control the acceleration of the tool during the run-in step.

6.3.1.4 RPM Based Control

An alternative option to X-force control is the RPM based process control. The tool rotational speed can be controlled based on different input variables. The best results can be expected from a direct temperature measurement in the process zone. As this is seldom possible, there are alternative approaches. The X-force can be used as a feedback signal. The advantage of an X-force based RPM controller over a X-force controller as described in Section 6.3.2 is that the productivity (welding speed) of the process is kept constant. This is also important as the time a region of the welded material stays at elevated temperatures is essential for metallurgical processes like precipitation dissolution and may have large influence on the final mechanical properties. This interaction time should be constant to allow for reproducible

mechanical properties. The drawback of this controller is that it does not protect the tool from overloading as the Z-force and X-force controllers do. At high welding speeds the RPM controller will ramp up tool rotations to produce sufficient heat to soften the material in order to meet the X-force feedback signal. This increase in RPM can cause considerable changes in the applied torque. A controller that counteracts an increased load (increasing measured X-force) with another increasing load (increased RPM) is not very conservative in terms of tool protection.

6.3.1.5 Torque Based Control

It is possible to control the energy input to the weld by applying a measured torque or machine power signal as a feedback to a controller for one of the welding parameters. In this way the control target can be to keep the line energy constant. Due to the inherent oscillation of the torque and the limitations due to tool strength, this controller type is not suitable as a sole control strategy. It is possible, though, to combine it with Z-force and X-force control to form a hybrid strategy. In principal, the gap may be used to provide constant Z-force, the welding speed may be limited for tool safety by a XY-force controller and the torque or line energy is kept constant by adjusting the RPM.

6.3.1.6 Manual Interaction

In many cases an improvement of the weld quality can be achieved by an experienced operator through manual interaction with the welding machine. This can include basic operations like adjusting the welding speed or tool rotation of the welding machine based on the visual inspection of the current joint or other feedback. This operation mode can have advantages over strictly programmed computer controlled welding in cases where only the experience of the operator allows for the right call of action. The inherent drawback is the need for a skilled operator, which contradicts one of the main economical advantages of FSW. The reproducibility is very limited in welds with manual interaction as timing and extent of the interaction not only depend on the operator but also on his or her level of concentration. This effect can be seen in Section 7.3.4 when comparing the standard deviation of mechanical properties of the state-of-the-art welds [3] that where produced with manual Z-force control and the fully automated welds of this study.

6.3.2 Controller Implementation

Within the scope of this study, a XY-force controller and a Z-force controller have been designed and implemented for the FlexiStir device. This has been made possible due to the hardware improvements described in Section 4.1. RPM based control has not been chosen for the current hardware as tool safety is considered high priority and direct temperature
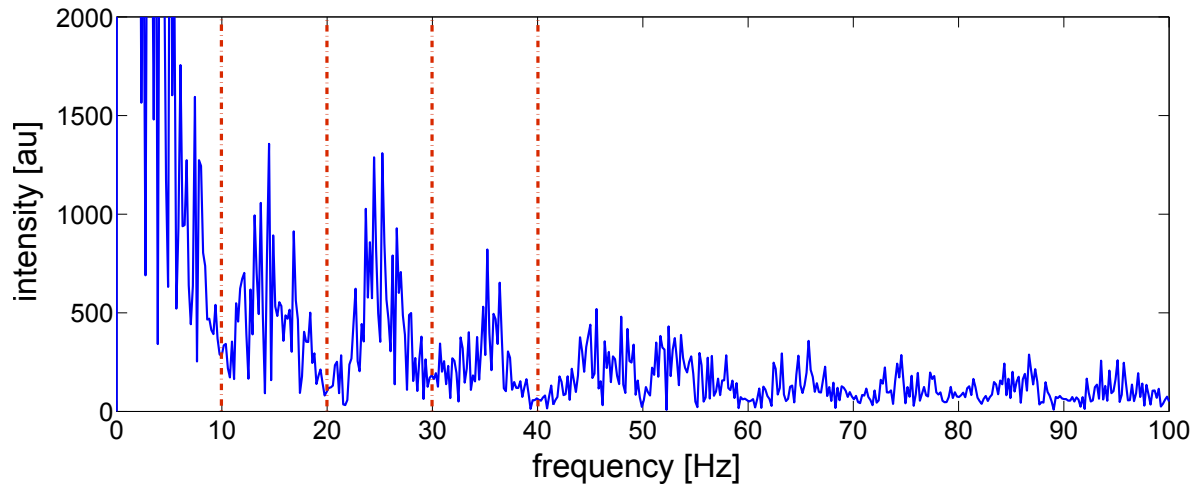
Figure 6.17: Frequency spectrum of the force signal during a BT-FSW weld with 600 RPM

measurement at the tool is not available. A torque based feedback has not been used as the torque and power measurements lack precision and no further improvement of the process is to be expected. A dedicated torque sensor might open up new opportunities for future work on this topic.

The z-force control needs to handle two degrees of freedom. One is the position of the upper shoulder and thus the entire welding head. It is adjusted using the main traverse of the FlexiStir. The other is the size of the gap between the two shoulders. This is adjusted using the pin retraction actuators. The inputs for the controller are the force acting between welding head and machine frame (Z1) and the force acting between the welding head and the lower shoulder (F2) (see Fig. 4.2). The force measurement runs at the same frequency as the machine controller. This is in the region of 200Hz. As the recorded force signal is noisy and contains higher frequency components it is not suited as an input for the force control routine (see Fourier spectrum in Fig. 6.17). The frequency component that corresponds to the spindle rotation is in the range of 6.6 to 20 Hz (400 to 1200 RPM). In the given example 600 RPM (10 Hz) are used. This frequency does not show up in the frequency plot directly but the harmonic spacing reveals the influence of the rotational speed on the force oscillation. All harmonics up to 100 Hz can be found as minima of the intensity distribution. Therefore the controller should use a floating average of at least 20 samples corresponding to 0.1s. This filter is applied to the force signal and acts as a low pass filter.

The controller routine for the z-force control is implemented as a constant step width feedback controller. The filtered force signal is compared to the desired value. If the deviation is greater than a tolerance value the machine will move the corresponding actuator by a defined step size. This step size is chosen to be 0.01mm which is the smallest reasonably controllable distance. During the movement of the actuator no new adjustment is commanded. The dynamic of

this strategy is limited but by far sufficient to control the process for the achievable welding speeds. The advantage of this control strategy is the high robustness and minimal possibility of unstable conditions. The Z1 desired value is basically zero which means that all the Z-force acting on the work piece is balanced between the shoulders and does not lead to a resulting force on the machine frame. The tolerance band for this value can be chosen fairly large (100N or more) as these forces do not significantly influence the resulting process. It may be beneficial in some cases to apply a small resulting Z-force on the work piece. This can be the case if rigid clamping is difficult to achieve due to geometrical limitations. This effective down force can help to eliminate vibrations on the workpiece. If the parts to be joined are not plates but more complex extrusions, the temperature of the upper and the lower surface can be very different. In these cases it may also have a positive effect on the homogeneity of the joint (e.g. the amount of flash on the upper and lower side) to choose a small offset for the Z1 force. The desired Z2 or gap force value is a major process parameter comparable to the gap size in non controlled welds. This parameter must be optimised. Predictions of the optimal pressure are an output of the flow model (see Section 5.2).

The XY-force control only needs to handle one degree of freedom. This is the welding speed or machine table velocity. The controller is implemented as a constant step controller for the table velocity. This controller can be used as a run-in controller as well. In this case it guaranties a soft start of the welding speed and therefore prolongs tool lifetime.

Z-force and XY-force controller are independent of one another and can be controlled from a single screen of the Codesys visualisation for the FlexiStir control program. Both can be turned on and off during welding and a manual control of the involved process parameters is possible for those degrees of freedom currently not used by a controller. The visualisation is plotted in Fig. 6.18.

6.3.3 Controller Output

The gap size evaluation during a Z-force controlled weld is plotted in Fig. 6.19. The forces and welding speed during the run-in controlled by a X-force controller is plotted in Fig. 6.20. Here $F_{inplane}$ is the combined F_x and F_y. The user defined force limit for the run-in is F_{limit}. The controller output u_{weld} is the welding speed as commanded to the table motors. The target velocity after run-in u_{target} is the nominal welding speed.
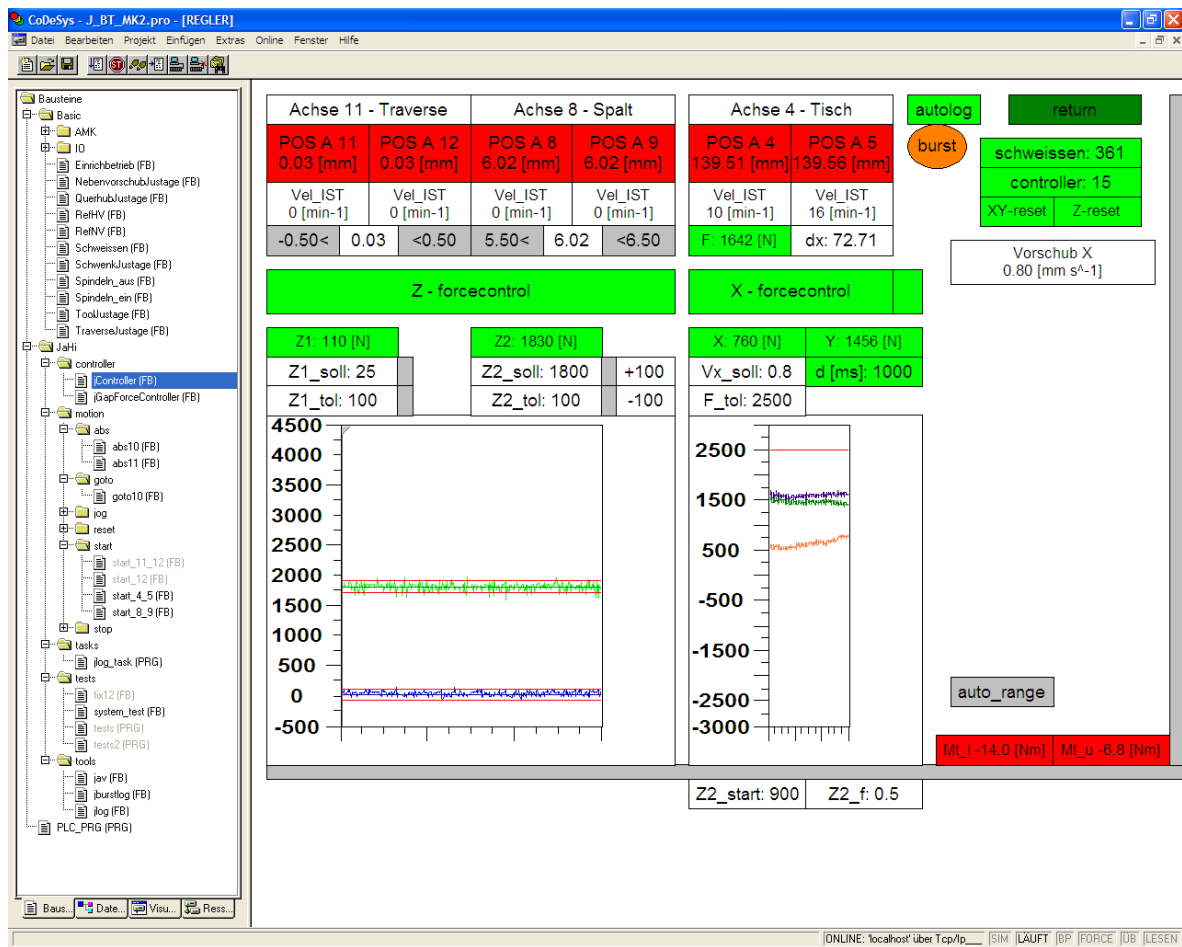
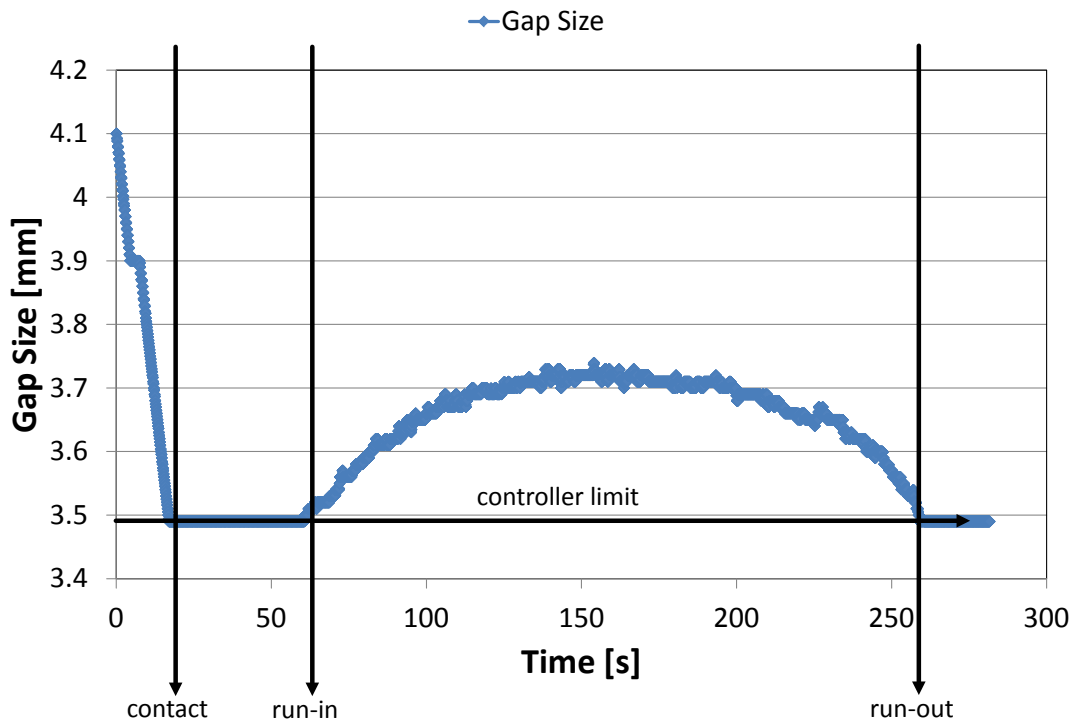Figure 6.18: Controller implementation for the FlexiStir device

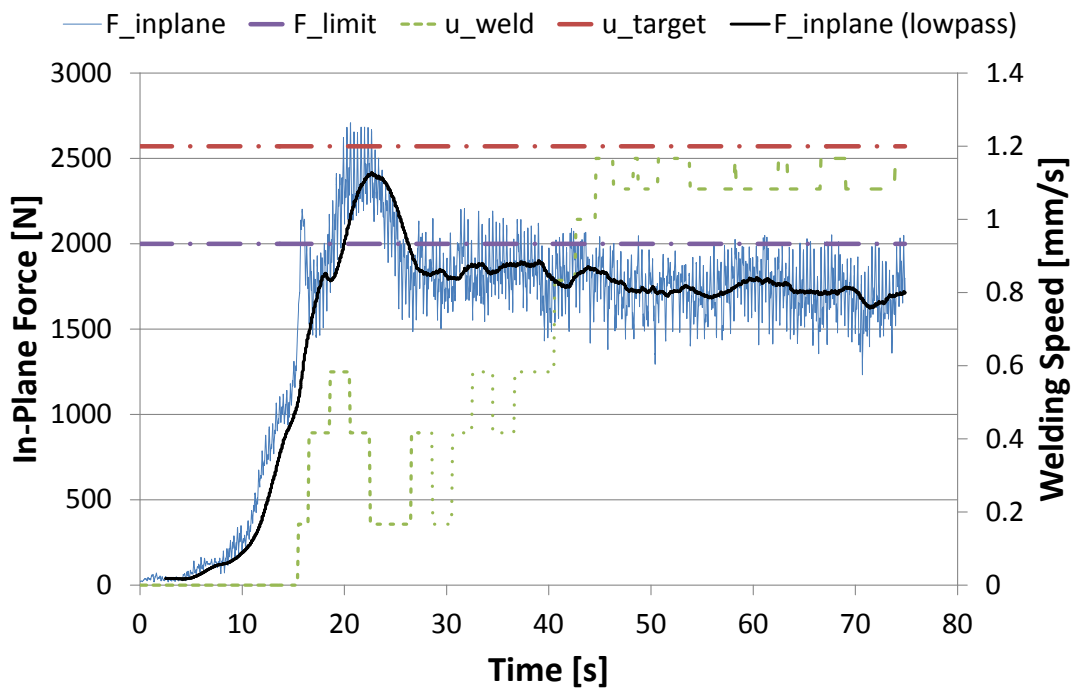Figure 6.19: Gap size evaluation during a Z-force controlled weld

Figure 6.20: Force and speed evolution during an X-force controlled run-in

6.4   Discussion

6.4.1   Tool Material

The tool steel Marax has been suggested as a tool material by Neumann [3]. Although it is a promising material in terms of high temperature strength, it has to be kept in mind that the heat treatment is done at a temperature of 460°C. This is not very much higher than the operating temperature of the tools. Therefore the long time performance of the material may be deteriorated by the process temperature. Hotvar has been established as a standard tooling material for FSW tools at HZG. The heat treatment is done at 580°C which is well outside the range of common process temperatures. Unfortunately, the strength of Hotvar is inferior to Marax as well as the other material candidates. This is not very problematic in standard FSW but may be insufficient to meet the demands in BT-FSW. The powder-metallurgical high speed steel TSP01 has been suggested by Brunzel et al. [111] from the experiences with the delta-N tool concept. The material performance is very good. Unfortunately, the commercial availability is unsatisfactory.

The final material candidate is the cobalt based alloy MP159. It has been successfully used in industrial fabrication of high speed trains with BT-FSW in Japan [112]. The mechanical performance is superior to all other considered materials and the availability, machinability and price are satisfactory. Therefore MP159 is the most promising candidate for highly loaded bobbin tool pins. The shoulders can in principle be manufactured from any of the tested materials. Due to the different coefficients of thermal expansion it may not be ideal to use a combination of different materials. It is therefore suggested to use MP159 for the shoulders as well. As these are not subject to considerable wear the additional cost is negligible. The transition from Hotvar as a tool material for the baseline tools to MP159 as a tool material for the proposed improved tools leads to an improvement in yield strength of 25%. This value can be considered a direct gain in tool productivity.

6.4.2   Tool Stress Modelling

As no plasticity is allowed in the tool, the mechanical model described in Section 6.2.1 uses a linear elastic material law. The geometric non-linearity may be neglected as the global deformation is small. It is therefore in principle possible to calculate different load cases by superposition and scaling of normalised load cases. This makes the mechanical model fast and easy to use. An detailed experimental validation of this model is unfortunately not possible. It can be stated that the predicted stresses for all welding conditions that have been successfully tested experimentally are below or only slightly above the experimentally determined yield stress of the tool material. The experimental load case leading to tool fracture has been modelled (see Fig. 6.16 and Tab. 6.4). The maximum stress predicted in this case is above 1800MPa. This is clearly above the yield strength of Hotvar (1246MPa) which is the tool

material used in that case. The exact value of the peak stress cannot be trusted as the model itself is linear elastic. In the real tool the maximum stress will be lower due to plastic deformation and load redistribution. Still it can be stated that tool failure is very probable once the yield stress of the tool material is considerably exceeded. This is even more critical as the loading is by nature cyclic and fatigue cracking will damage the tool.

The baseline tool design has been compared to the proposed improved tool design in terms of maximum stress for several load cases (see Figs. 6.14, 6.15(a), 6.13 and 6.15(b) and Tab. 6.4). The interaction of pin features and load combination is complex. The comparison shows that the new tool design has to withstand lower stresses in the combined load case although not for all basic load cases. The improvement for the realistic combined load case E is significant. The maximal tool stress is only $\approx 85\%$ of the baseline value. This is important as the objective to reach the highest possible productivity and thus highest welding speed can only be reached when the tool loading is decreased along with tool material improvement.

The achievable precision in the mechanical model is limited by the manufacturing tolerances of the tool features. As shown in Fig. 6.8(a) and Fig. 6.8(b) the resulting geometry of a manufactured pin may differ strongly from the designed shape. The more complex the tool design, the worse is the deviation in production. Therefore it must be emphasised that the mechanical model cannot be successfully used for a fully automatic optimisation scheme as the optimisation results may not be transferable to the final tool. It is a task for the tool developer to keep an eye on the tradeoff between tool complexity, feasibility of production and stress response (see Section 6.4.3).

6.4.3 Tool and Feature Design

There are two major aspects to consider when defining the shape of the pin features. One is material mixing, the other is tool stress increase due to notch effects. The fist can be estimated using the RFPM and the predicted shear rates and velocity profiles, the second can be calculated using the mechanical model. The approach of tool design using this framework is by nature iterative.

The improved bobbin tool developed in this study is the result of this procedure. Once a basic design was chosen based on previous knowledge, several iterations were performed. The pin features are designed in a way suited for production by electrical discharge machining. This results in a major gain in reproducibility (see Fig. 6.9). At the same time the tool cannot have the theoretically optimal shape in terms of minimal stresses and best material transport.

The ceramic inlays tested in this study have shown very promising results in terms of friction and thermal insulation (see Fig. 6.6 and Fig. 6.7). The design needs to be improved, however, in terms of mechanical reliability, as a failure of such an inlay in the upper shoulder can damage the pin and shoulder through excessive wear (see Fig. 7.15(a)). A design review is recommended.

6.4.4 Controller Strategy

It can be stated that Z-force control is strongly recommended for any welding task. This is due to the complex interactions resulting from thermal expansion of the tool and workpiece. The resulting time dependent and position dependent forces not only result in a heterogeneous quality of the joint but also decrease tool lifetime due to overloading. In many conditions the gap needed to obtain a sound weld at the beginning of the joint line will lead to a destruction of the tool due to excessive Z loads after a short welding distance, while a gap suitable for the steady state conditions does not lead to a stable and defect free weld during run-in at all. The gap size evolution shown in Fig. 6.19 shows that the nominal gap size has to be adjusted by a total of more than 5% of its nominal value to keep the Z-force constant.

XY-force control can help to ensure homogeneous welding conditions but is not mandatory in all cases. It has proven very helpful when performing trial welds with exploratory parameters, geometries or new materials. The XY-force can reach detrimentally high values if the process does not generate sufficient heat for a fully developed shear layer. In such cold welding cases the pin may fracture during run-in before the operator has a chance to intervene. An XY-force control limiting the welding speed in such a way that the tool forces stay well below the critical region (defined by mechanical testing of the tool or numerical simulation) allows to find suitable process parameters without risking tool fracture. The evolution of XY-force controlled welding speed as shown in Fig. 6.20 shows that the run-in phase into cold material can be rather complex in terms of resulting forces.

6.4.5 Weld Stability

Weld instability is often observed in thin sheet welds in aluminium and magnesium alloys. This phenomenon only occurs in fixed gap processes. Using Z-force control eliminates the instability.

The reason for the instability is assumed to be the excessive heating of the shear layer to an extent where plasticised material can exit the weld at the sides of the shoulders. This leaves a cavity and the pressure state in the process zone changes drastically. More material is extruded through the cavity until no weld is formed anymore. The material between the shoulders is kept there and rotates with the tool. At this point the heat generation is sufficiently reduced and the tool and the remaining material between the shoulder cool down. After sufficient cooling the material flow may stabilise again. As the tool enters cold material at some point the friction is sufficient to abrade and deform the material stuck between the shoulders sufficiently to again form a cavity there. Now sufficient frictional heating can take place again to re-enter the stable process of material transport and deposition.

The critical overheating is assumed to be caused by increasing gap forces as a consequence of thermal expansion coefficient mismatch between the tool and the plates. In Z-force controlled welds this phenomenon is avoided by keeping the acting forces constant.

6.5 Implementation - Summary and Conclusions

Tool Design

- The material for improved tools has been selected based on experimental evaluation of four material candidates suggested by different sources within the scientific community. A increase of yield strength of 25% was realised by the choice of the best available tool material.

- It was established that due to thermal expansion mismatch all advanced bobbin tools should have Z-force control capability.

- Tool design needs to be simple enough to allow reproducible manufacturing.

- The selection of features can be aided by numerical simulations of loads and stresses. The suggested tool design leads to a maximum stress of only 85% of the baseline design in a standard load case. Still, a purely numerical tool optimisation is not possible so far, as the limits in machinability need to be considered.

Mechanical Model

- The stresses acting in a tool are modelled based on the loads found either experimentally or predicted numerically. It is possible to find all loads that are required from numerical predictions only. In principle this allows for tool development without experimental prototyping

- Different tool designs can be compared based on standard load cases or realistic loading conditions.

- The feasibility of desired process parameters for a defined tool can be assessed. If excessive stresses are found, either the process parameters or the tool design need to be altered.

Process Control

- The welding process can be controlled by applying a combination of possible control strategies. For the present study a Z-force and a XY-force controller have been implemented in hardware and software of the welding machine.

- Tool failure because of thermal expansion coefficient mismatch can be avoided by controlling the force acting in the tool gap. Weld instability can be avoided in the same way.

- The loads acting on bobbin tools during the run-in process step can be reduced by a XY-force controller. The welding speed is gradually reached instead of instantaneously. This helps to prevent tool failure.

- The achievable productivity can be increased by the reduction of tool loads through process control.

Chapter 7

Joint Quality Improvement

7.1 Joint Characterisation

7.1.1 Visual Inspection

Visual inspection often gives a good impression of the joint quality. A set of examples for surface conditions are given in Fig. 7.1. The corresponding process parameters for the poor surface are constant-gap welding, 1200 RPM and $0.3mm/s$ welding speed. This type of flashy surface is found for all constant-gap joints (see Section 6.3.1.1) and Z-force controlled joints with excessive target force. The good surface condition is achieved for all Z-force controlled joints with correct target force. The presented example is condition T_06 (Z-force controlled at 3.0kN with 350 RPM and $1.5mm/s$ welding speed).

(a) Poor weld surface condition
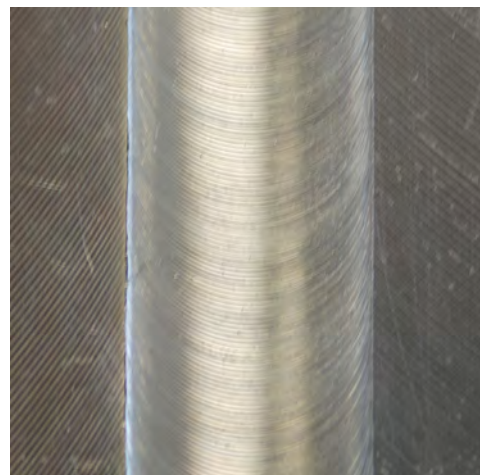
(b) Fine weld surface condition

Figure 7.1: Weld surface conditions

(a) Overview   (b) Bend angle determination   (c)   Extended   test (180°)
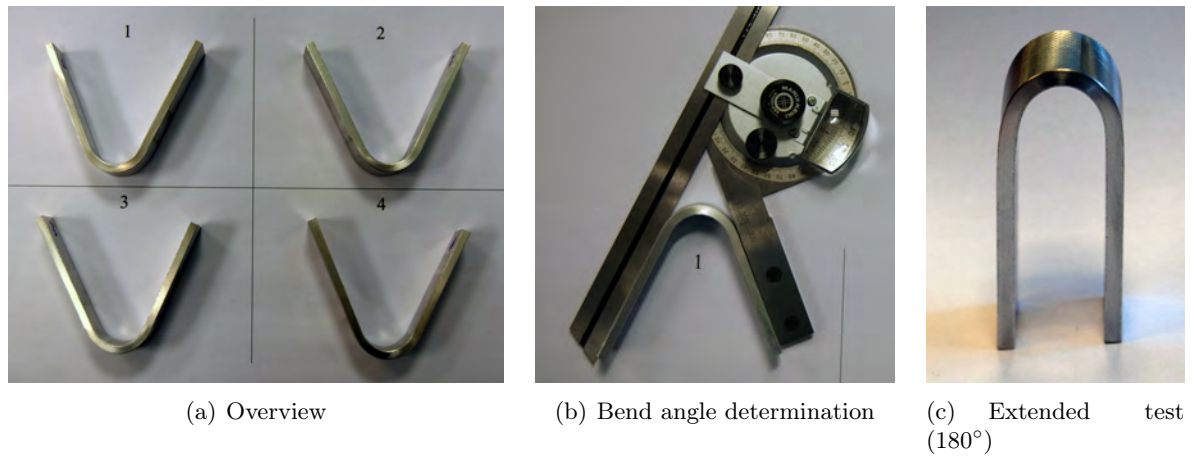
Figure 7.2: Bending test of base material

7.1.2   Bending Tests

Bending tests of the base material show that the ductility is sufficient to allow reproducible bending angles above 130°(see Fig. 7.2). This is the largest bending angle that can be produced using the specified setup according to ASTM E290. After this angle testing was continued with an extended bending test using a bench vice. No fracture occurred even at 180° (see Fig. 7.2(c)). Visual inspection and optical microscopy do not reveal any crack initiation at this bending angle.

The bending test results for the best performing welding conditions of the different campaigns are given in Tab. 7.1.

campaign	condition id	bending angle α [°]
baseline	B_01	42
controller development	C_06	71
	C_07	75
	C_22	72
	C_24	74
tool validation	T_04	130+
	T_05	130+
	T_07	130+

Table 7.1: Bending test results of welded joints - a plus sign (+) indicates no fracture at maximum bending angle

For some welded conditions the bending test has been extended until fracture. Such an extended bending test specimen for T_05 condition is shown in Fig. 7.3. This sample showed initial cracking at $\alpha \approx 158°$.

Figure 7.3: Extended bending specimen (T_05)

7.1.3 Microstructure

The base material is a rolled sheet. The pancake-like microstructure with elongated grains in rolling and traverse direction can be seen in Fig. 7.4. As this base microstructure is invariant to rotations along the thickness direction, the influence on the joining process from the specimen orientation is expected to be small. Still all joints are performed along the rolling direction to avoid any systematic error due to deviations in the base material behaviour.

The microstructure of the welded joints is influenced by the tool geometry as well as the process parameters. Fig. 7.5 shows three cross section macrographs of different sound welding conditions done with the baseline tool. A typical stir zone to shear layer transition for the advancing and the retreating side with the baseline tool design is shown in Fig. 7.6. The typical defects occurring in joints with the baseline tool design are located in the upper and lower stir zone. They can consist of volumetric defects (voids) or regions with abnormally large grain sizes or both. Fig. 7.7 shows examples for such defects. The sources for these defects are discussed in detail in Section 7.3.3. The microstructure of the welds done with the improved tool differs from the ones found in joints made with the baseline tool. A typical cross section is shown in Fig. 7.8. These results are discussed in detail in Section 7.3.2.

7.1.4 Mechanical Properties

7.1.4.1 Hardness Measurements

The hardness of the base material was tested with different procedures. A line of 20 indents was made with 10HV0.2, 10HV0.5 and 5HV0.5. The statistic evaluation leads to mean hardness values of 143.4 ± 6.1 for 10HV0.2, 147.5 ± 2.8 for 10HV0.5 and 146.3 ± 2.3 for 5HV0.5. As 10HV0.2 shows an intolerable amount of systematic scatter it was not used on welded joints.

5HV0.5 was chosen as it allows faster evaluation than 10HV0.5 with comparable accuracy and spacial resolution. This procedure was used for all hardness measurements within this study.

7.1.4.2   Tensile Tests

The base material tensile test results are summarised in Tab. 7.2 together with the best tested welding conditions from all welding campaigns. The stress-strain curves are given in Fig. 7.9.

Name	$R_{p0,2}$ [MPa]	Rm [MPa]	A [%]
Base Material	343.48 ± 0.58	488.97 ± 0.57	18.02 ± 0.63
B_01	270.72 ± 3.78	396.8 ± 4.21	3.20 ± 0.32
C_22	287.39 ± 2.12	412.14 ± 2.09	4.82 ± 0.17
T_07	294.03 ± 3.45	428.66 ± 2.95	6.46 ± 0.05

Table 7.2: Tensile tests results

The strength and ductility evolution is shown in Fig. 7.10. The fracture mode of all base material and welded specimens is comparable and can be seen in Figs. 7.11, 7.12 and 7.13. It is a ductile 45° fracture across the entire specimen. In the case of all welded specimens the fracture seems to initiate at one of the shoulder marks. In the constant-gap condition B_01 as shown in Fig. 7.12, the fracture path points into the SZ. In the force controlled cases the fracture occurs outside the TMAZ as shown in Fig. 7.13. It should be noted here that the fracture does not always occur at the same side of the weld.

(a) 5x (as polished)

(b) 10x (color etch)
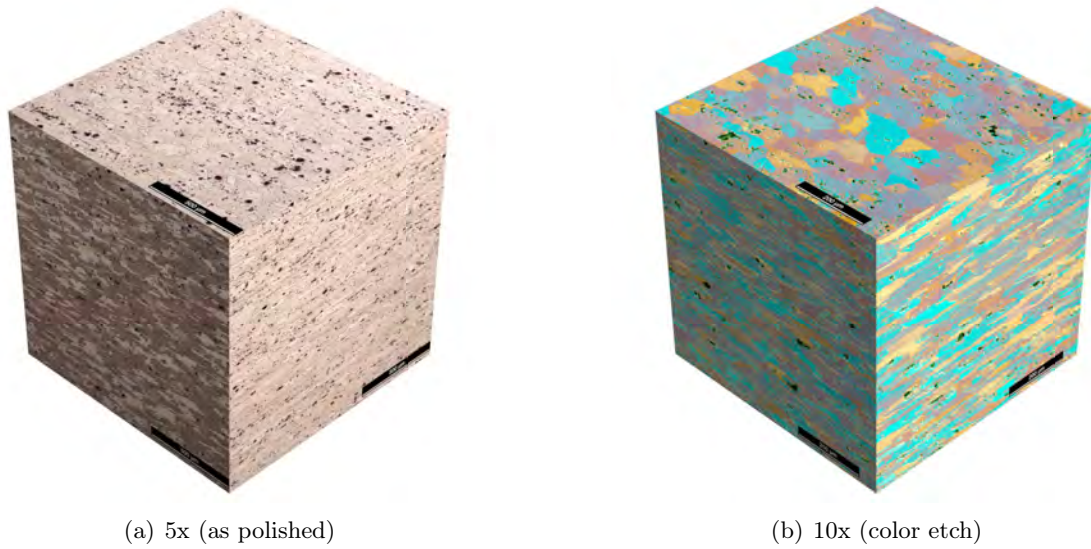
Figure 7.4: Base material microstructure

(a) C_06

(b) C_02

(c) C_16
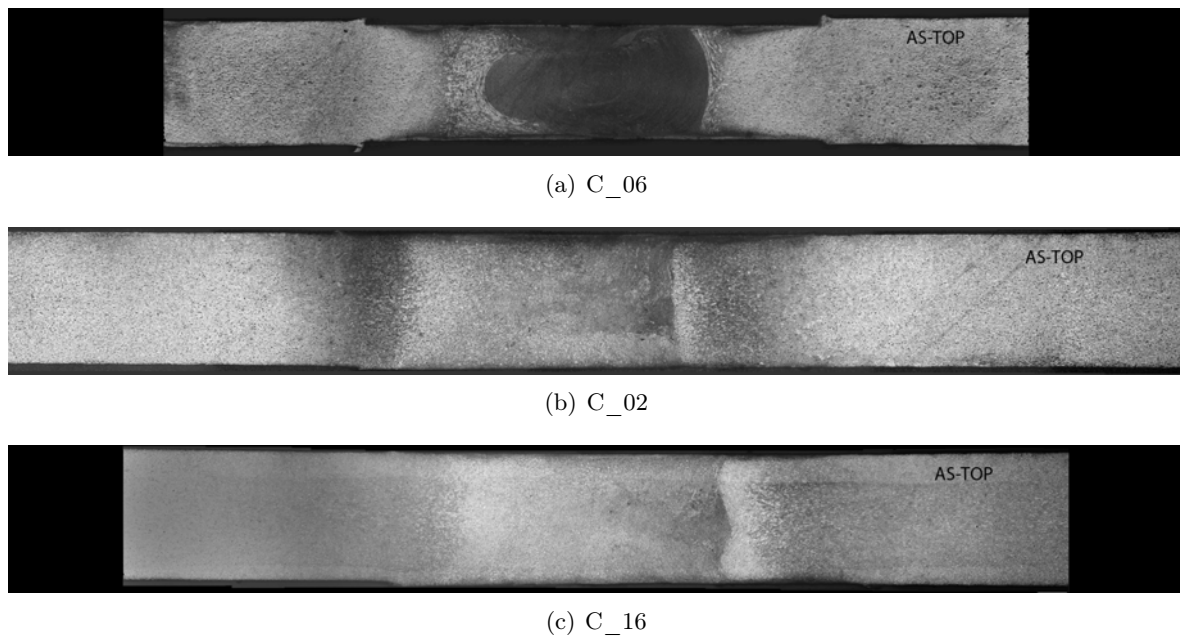
Figure 7.5: Typical microstructure of sound joints welded with the baseline tool

(a) Retreating side

(b) Advancing side
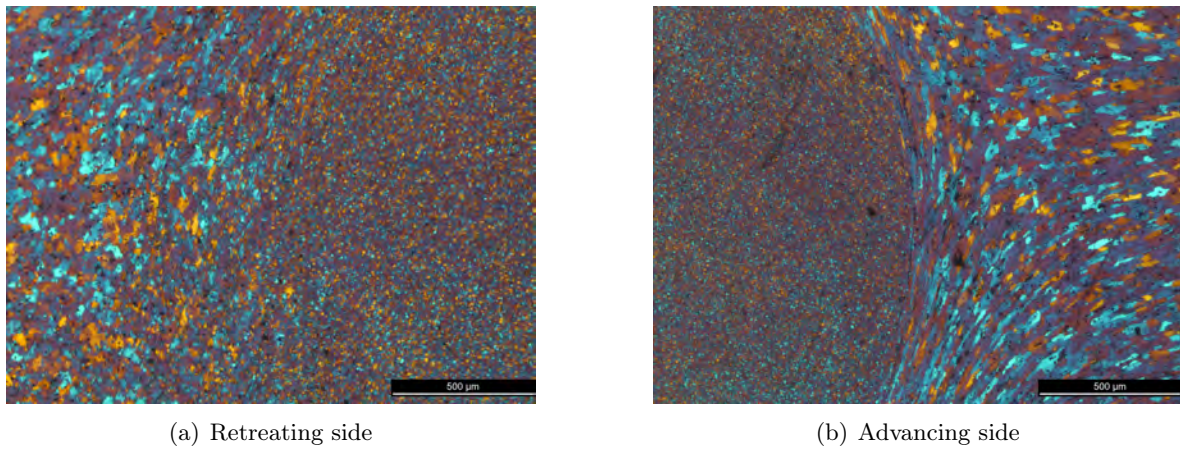
Figure 7.6: Typical transition between shear layer and SZ microstructure (baseline tool)

(a) Voids (Overview, C_09)

(b) Voids (C_09)

(c) Abnormally large grains (C_24)
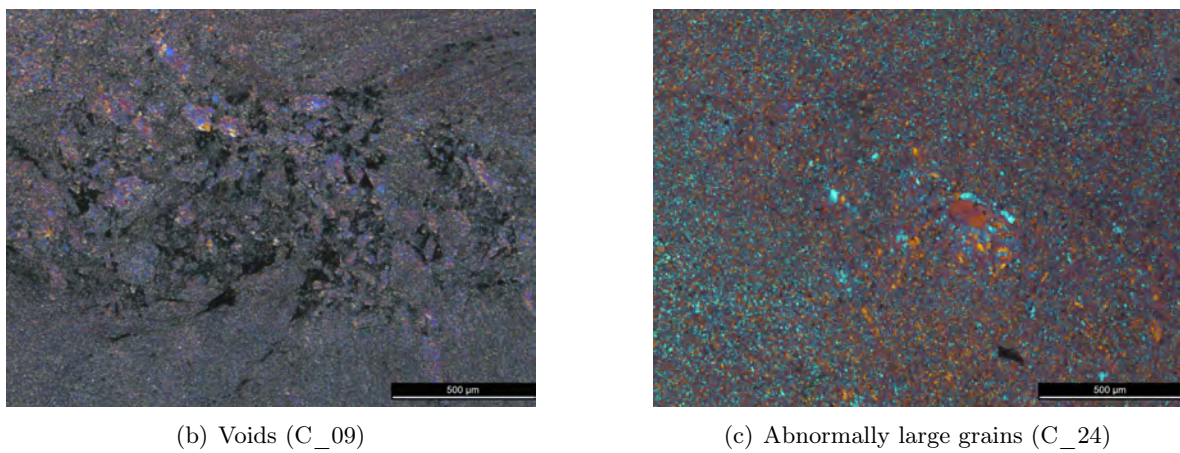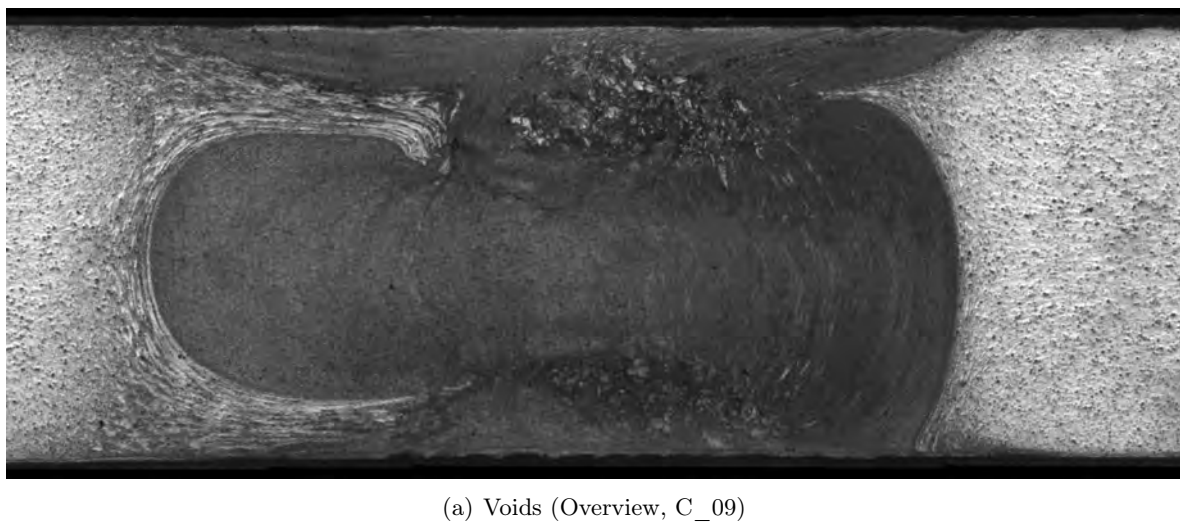
Figure 7.7: Typical defects in the microstructure of joints welded with the baseline tool
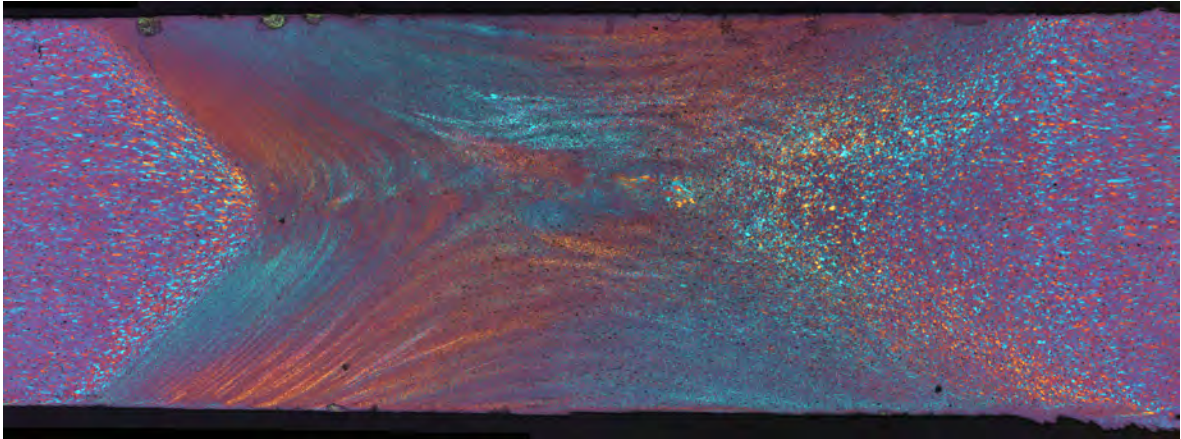
Figure 7.8: Typical microstructure of joints with welded with the improved tool
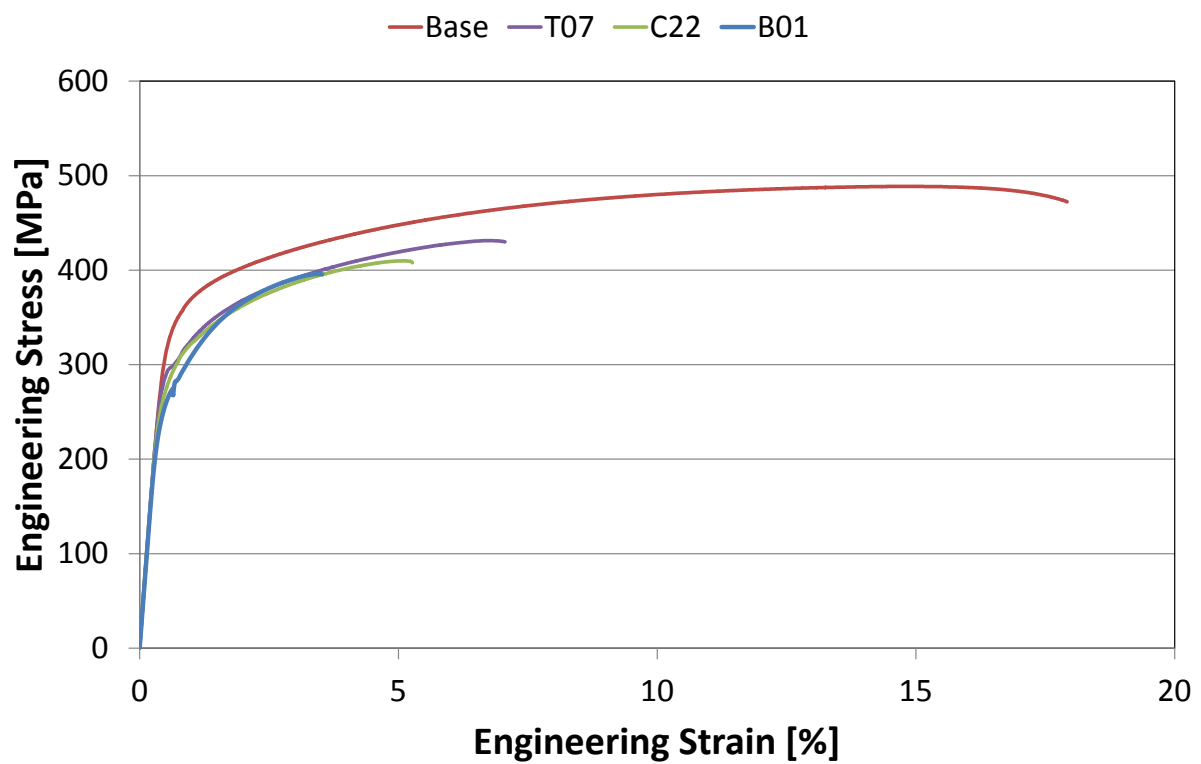
Figure 7.9: Stress-strain curves

(a) Strength

(b) Ductility
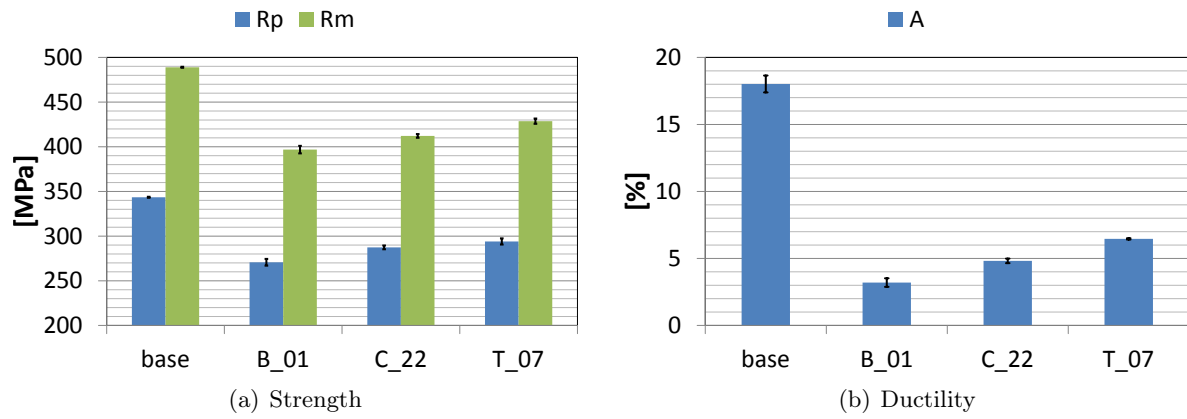
Figure 7.10: Overview of tensile test results

(a) Base material side

(b) Base material bottom
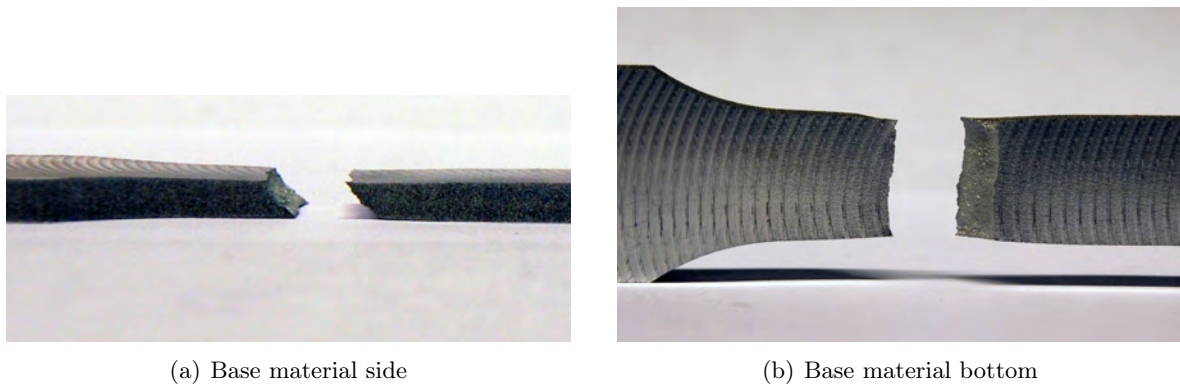
Figure 7.11: Fracture appearance of the base material tensile specimens

(a) B_01 joint bottom

(b) B_01 joint top

(c) B_01 joint side
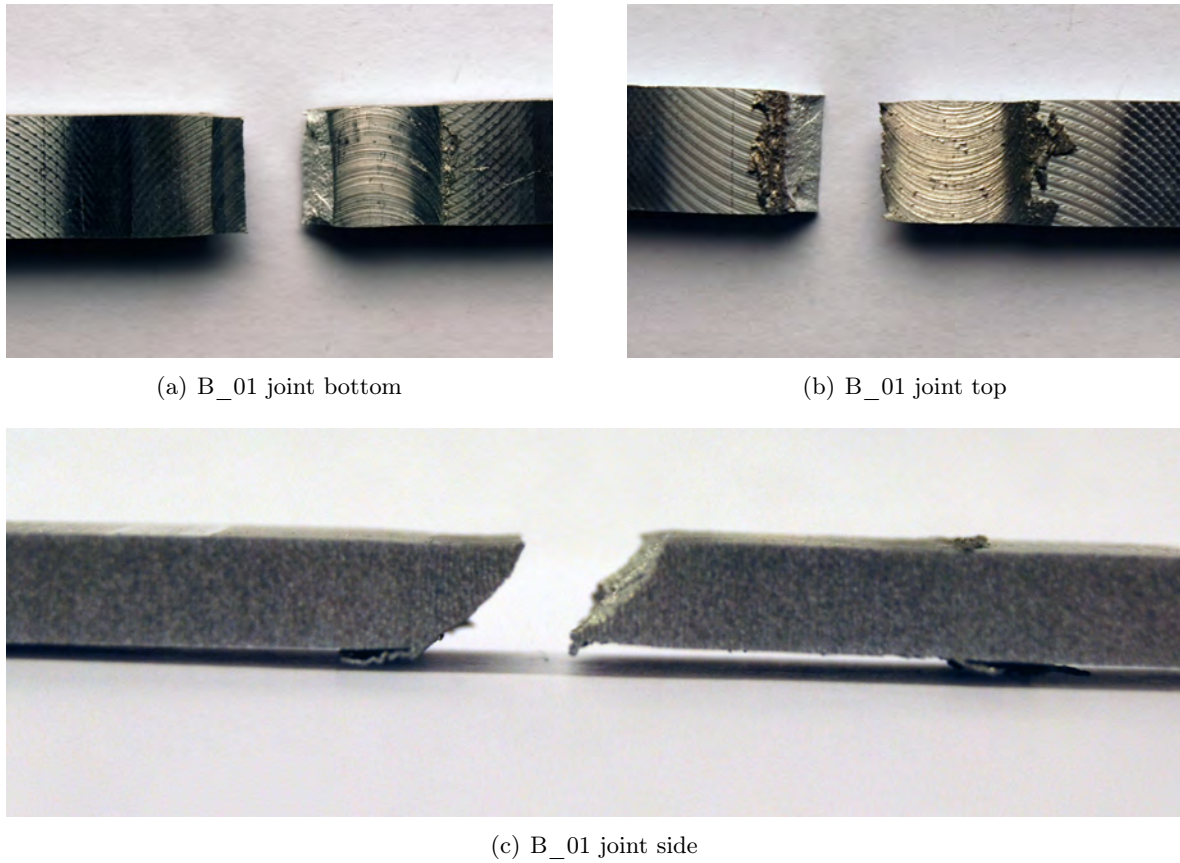
Figure 7.12: Fracture appearance of the welded tensile specimens B_01
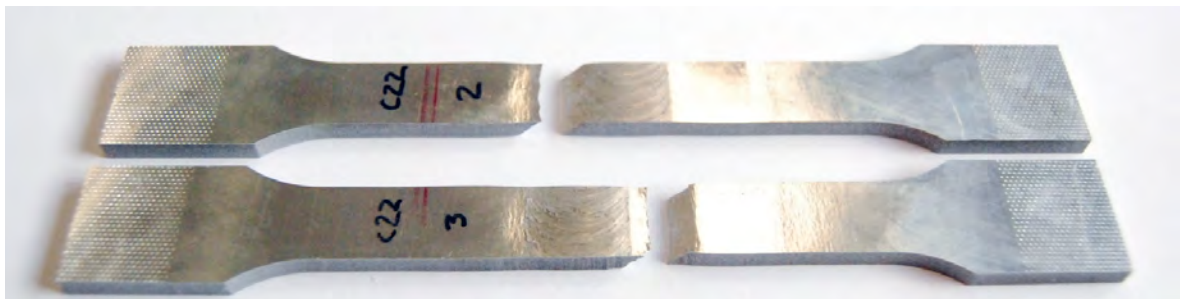
Figure 7.13: Fracture mode of the welded tensile specimens C_22

7.2 Tool Performance

7.2.1 Pin Fracture

The maximum loading capability of the baseline tool was determined experimentally. The loads on the pin were increased by choosing harsher process parameters until a pin fracture occurred while welding 1.5mm/s at 800rpm with Z-Force controlled at 3.5kN. The loading history of the weld is plotted in Fig. 7.14. The conditions were used to model the stresses acting in the pin in the condition of failure (see Table 6.4). No other pin fractured in the force controlled experiments.
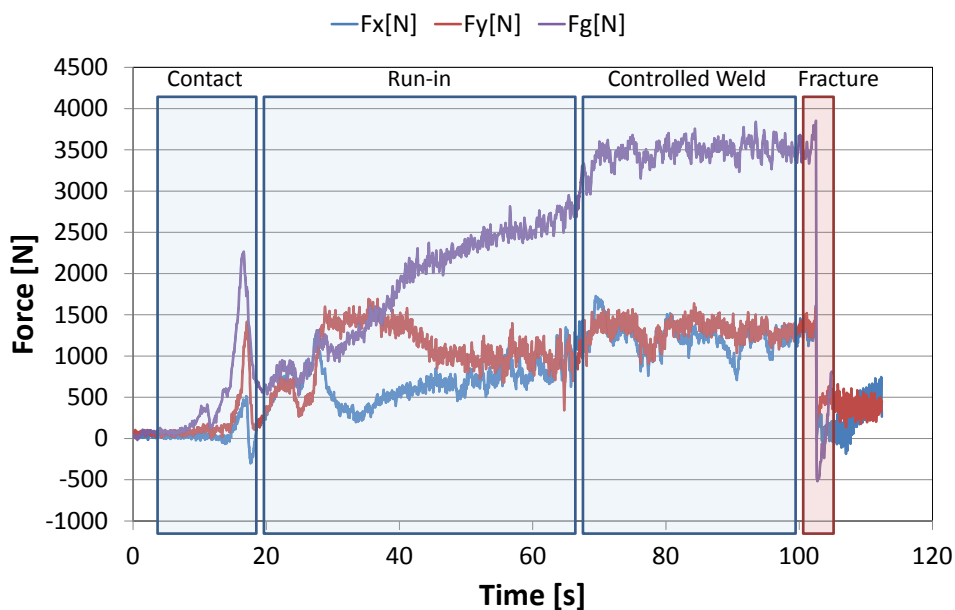

Figure 7.14: Loading history trace of a weld with fractured pin

7.2.2 Tool Wear

Tool wear due to contact with aluminium is very limited. A source for excessive wear is debris from a fractured upper shoulder ceramic inlay. In such a case the surface of the pin at the interface with the upper shoulder is considerably damaged as shown in Fig. 7.15(a). This needs to be considered when applying ceramic inlays (see Section 6.4.3). The torque transmitter for the lower shoulder can show signs of wear and plastic deformation due to overload as shown in Fig. 7.15(b) after a large number of experiments. Failure of this part has not been observed. The current material used for this part is a mild steel. A future material selection offering increased yield strength at elevated temperatures while preserving sufficient amount of ductility may be beneficial for this part.
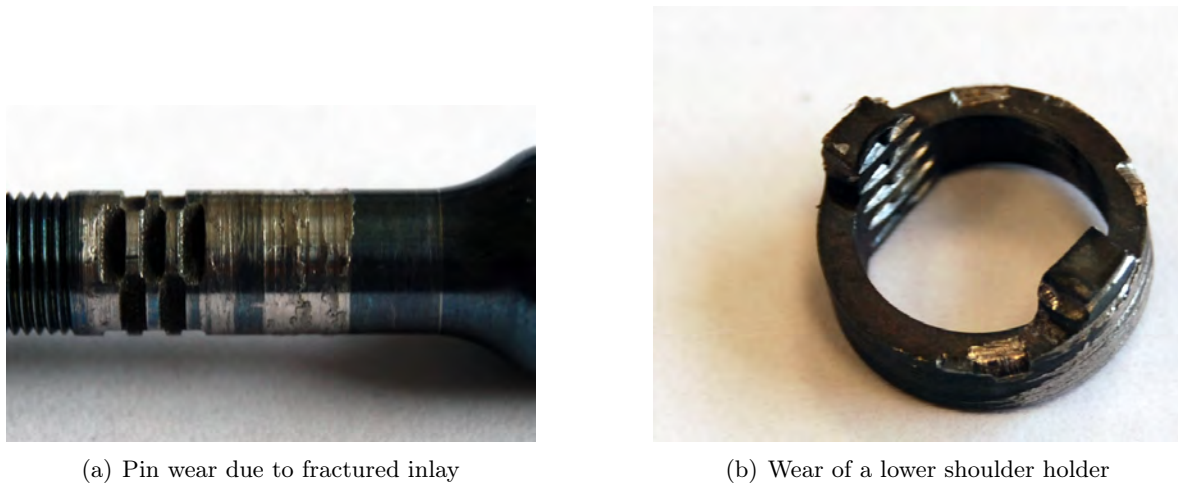
(a) Pin wear due to fractured inlay

(b) Wear of a lower shoulder holder

Figure 7.15: Tool wear

7.3 Discussion

7.3.1 Quality Assessment

The quality of the weld is defined by several factors: The strength of a good weld is determined by the softened HAZ or TMAZ. A simple criterion for mechanical weld quality is the bending angle α reached in a bending test. When the specimen fails, the crack should be outside the SZ as shown in Fig. 7.16(a) to make sure that no macroscopic defects are present. This can be explained by the hardness profiles found for all welds in this material (see Fig. 5.14). The softening of the welded material for the alloy investigated in the present study is due to precipitate dissolution and coarsening (overaging). For the currently available process conditions the softest zone is always outside the SZ. This can be explained by two effects. The minor contribution may be deducted from significantly reduced grain size in the stir zone that may contribute to a slightly increased hardness. More important is the reprecipitation of the strengthening particles. This only occurs in regions of the weld where the peak temperature was sufficiently high to dissolve a considerable amount of precipitates as opposed to just coarsen them.

A more quantitative method of assessing the weld quality is based on measuring the maximum softening or the minimum hardness. It can be seen from Fig. 5.14 that increasing the welding speed from $0.3mm/s$ (B_01) to $0.9mm/s$ (C_12) gives a slight increase in minimum hardness. This is due to the lower peak temperature as well as the lower time at elevated temperatures (see Fig. 5.10). Sample B_01 with very low speed of $0.3mm/s$ and high RPM shows the lowest minimum hardness of all tests. When the welding speed is further increased from $0.9mm/s$ (C_12) to $2.2mm/s$ (T_07), no additional gain in minimum hardness is reached. As the stir zone is also considerably softer in T_07 condition, it can be stated that the dissolution
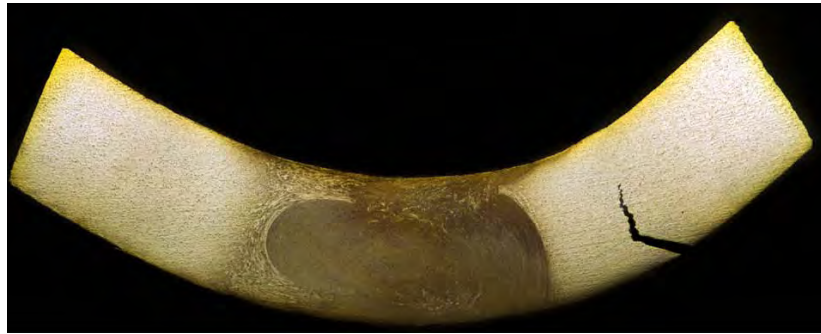
(a) failed outside the welded zone
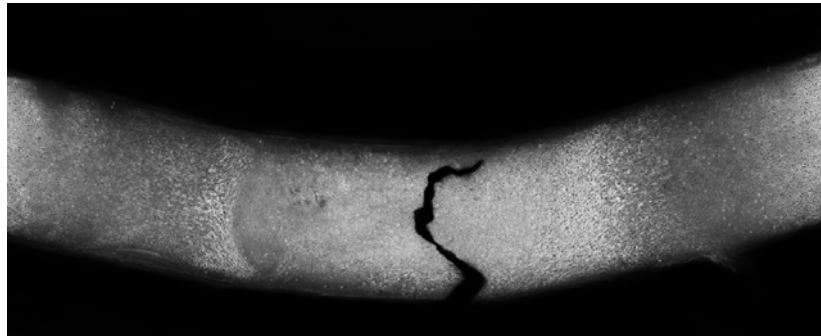
(b) failed inside the welded zone

Figure 7.16: Bending specimen with different failure locations

and reprecipitation is not happening completely anymore within the shorter time at elevated temperatures linked to this faster and colder condition. Therefore it can be assumed that a further increase in welding speed may finally lead to a joint with no post weld ageing in the stir zone. In order to predict this behaviour and thus define targets for further development of tooling and process parameters, microstructure evolution models (see [97]) based on the available transient temperature history can be utilised (see flowchart Figure 5.35).
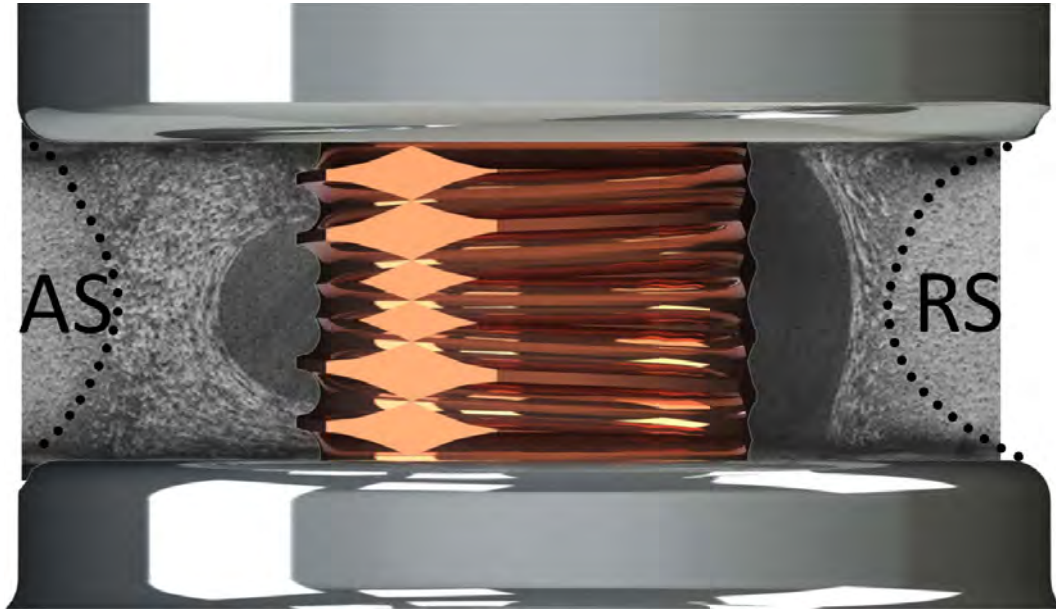
7.3.2 Joint Microstructure

The microstructure of the welds performed with the baseline tool configuration (B_XX and C_XX) show different shapes of the micro structural regions for different process parameter ranges (see Fig. 7.5). The slow and hot condition C_06 has a very convex stir zone shape with the largest diameter in the centre. In this condition the threads on the pin are able to transport the hot material towards the centre of the plate efficiently. This effect is not as pronounced in the higher speed condition C_16 and cannot be observed at all in the high RPM condition C_02. It can be concluded here that the threads perform as expected only in very hot conditions with low RPM. The threads are inspired by standard FSW tooling where enhanced material transport towards the root of the weld is often needed to avoid root defects

and tunnels (see Chapter 6). As these problems are not common in BT-FSW threads have not been added to the improved tool design.

A common microstructural feature is the difference in transitions from the SZ to the outer region of the shear layer between the advancing and the retreating side. On the advancing side this transition is very harsh with a high gradient in grain size and shape. On the retreating side the transition is much more gradual. The harsh transition on the advancing side is considered detrimental to the weld quality as a sharp interface in the softest region of the joint (see Fig. 5.14) is present and can act as a preferential crack-path. The microstructure typically observed in welds done with the improved tool differs significantly from those produced with the baseline tool (see Fig. 7.17). The SZ region is not widest in the centre of the plate but has a symmetric shape with the smallest diameter in the centre. The largest diameter is close to the shoulder diameter. The concave shape of the SZ corresponds to the shape of the TMAZ. The deformed region is symmetric and does not contain strong gradients or complex bonding line shapes. The transition in grain size is much smoother even at the advancing side of the joint. This is considered beneficial to the joint quality (see Tab. 7.1). The reason for the difference in material flow and thus microstructure zone shapes is the lack of threads on the pin.

7.3.3 Microstructure Anomalies

Several joints made with the baseline tool configuration exhibit defects in the microstructure. As shown in Fig. 7.7 the two types of common defects are volumetric defects (voids) and abnormally large grains in the stir zone. Both can occur simultaneously at the same location. Voids are not found without the presence of large grains, but large grains do occur without any voids. The presence of extended voids is very detrimental to the joint quality. Such a defect can be easily identified with a bending test. The presence of abnormally large grains in the stir zone does not necessarily deteriorate the joint quality (see C_24). It can be considered a pre-step to void formation: Larger grains are continuously ripped out of the outer regions of the shear layer to SZ interface. They can survive the joining process without being further deformed and thus reduced in grain size if they end up in a region of reduced forging pressure and shear rate. Such a region of insufficient forging pressure could not only be a possible explanation for large grains in the stir zone. If the forcing pressure drops even further voids will be formed at the same location. That could explain the experimental observation. The conditions leading to defect formation can be linked with the threads on the pin. They favour a material transport towards the centre of the joint and a reduced pressure at the location where the material is coming from. In Fig. 7.7(a) it can be seen that the material is extruded into the stir zone from above and below while the stir zone itself develops in the centre of the plate. This material flow pattern does not seem to be beneficial. This is another reason for not including threads on a bobbin tool pin.

(a) Baseline (C_06)
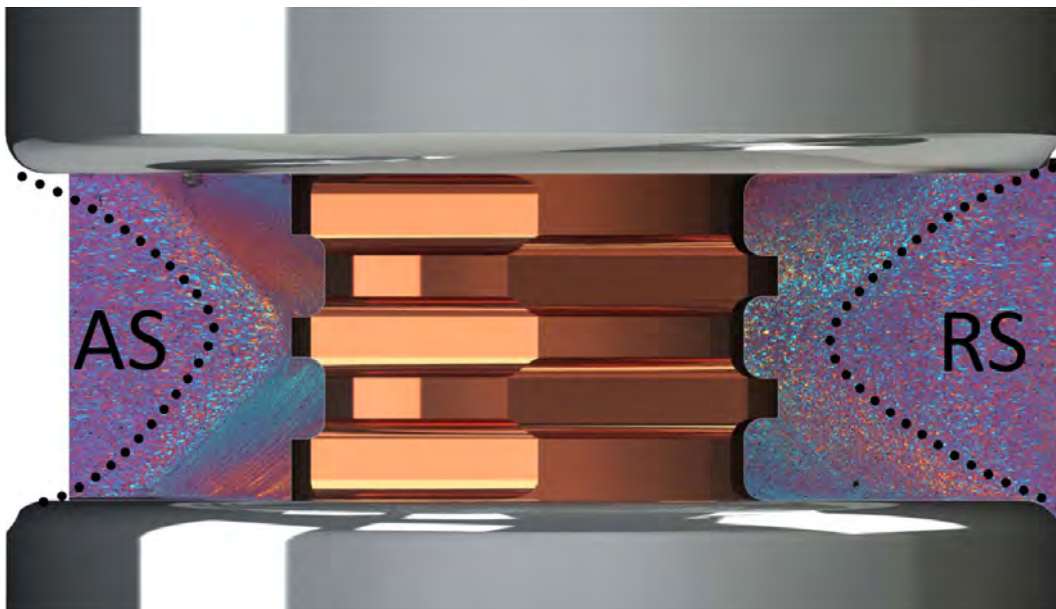
(b) Improved (T_06)

Figure 7.17: Tools and resulting microstructure zone shapes

7.3.4 Quality Improvement

The highest bending angle reported for 4mm AA2024 BT-FSW joints by Neumann [3] is 70°. All of these bending tests have failed inside the stir zone. The highest value obtained in the present study for the baseline tool is 75° with failure outside of the stir zone. The joints made with the improved tool do not fail in the bending test up to 130° (see Tab. 7.1 and Fig. 7.3). The values determined for some specimens using a bench vice for extended bending until fracture should not be compared with the ASTM bending test values on a one-to-one ratio. Still, the values of $\approx 160°$ and more prove the large gain in quality resulting from the new tool due to its improved mechanical strength and the process parameters that are available because of this strength.

The best tensile weld efficiency (traverse tensile strength) reported by Neumann [3] is $\approx$83% with a base material UTS of 469MPa. The baseline experiments of this work conducted on the FlexiStir show an efficiency of 81% with a base material UTS of 489 MPa. The average tensile R_m of the experiments (397 MPa) is already higher than the maximum reported value (388 MPa). This means that the starting point for optimisation of the process within this study is at the state of the art. Any improvements above these values can be considered a step forward in process development. The best weld efficiency found in this study for force controlled experiments with the baseline tool design is 84% (C_22). The best weld efficiency with the improved tool design is 88% (T_07) which can be considered a good value for an precipitation hardened alloy. The achievable joint efficiency for standard FSW of 2024T351 is found to be 87% by Lockwood et al. [51]. Post weld heat treatments might further increase this where needed. As reported by Aydin et al. [113] for 2024T4 joints, a post weld heat treatment to T6 condition increased the tensile joint efficiencies from 79% to 87%. Of course this cannot be compared to a T3 or T351 temper on a one-to-one basis. Tensile results in comparison with the state of the art are plotted in Fig. 7.18. An overview of the tensile weld efficiency is plotted in Fig. 7.19.

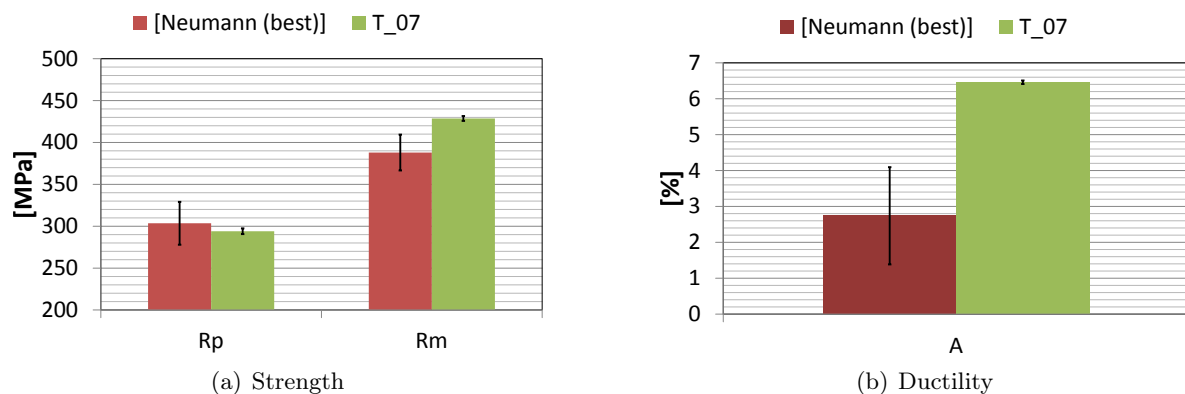

(a) Strength   (b) Ductility
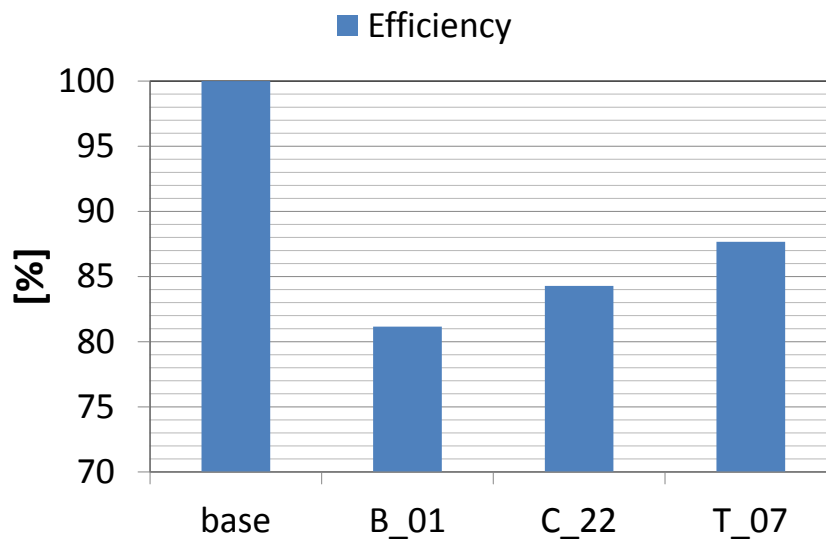
Figure 7.18: Overview of the tensile test results

Figure 7.19: Overview of the tensile weld efficiency

When comparing the weld efficiency in Fig. 7.19 with the characteristic values for heat input in Fig. 5.10 a trend is obvious. Lower peak temperatures and dwell times at elevated temperatures result in improved joint efficiency. Therefore a further decrease of the heat input is desirable. The potential for this decrease in the BT-FSW process is limited by the heat generation of the two shoulders. In standard FSW the Delta-N approach suggested by Brunzel et al. [111] is an attempt to decrease heat input by decoupling the pin and the shoulder and reducing the shoulder RPM. For BT-FSW this concept has been expanded to both shoulders. The resulting Stationary Shoulder Bobbin Tool Friction Stir Welding process (SSBT-FSW) has been invented and filed as patent by Hilgert and dos Santos [110] (see Appendix B).

As can be seen in Fig. 7.18(b), the maximum ductility reached in the past was 2.7%. The best condition presented in this work reaches 6.5%. This large increase in ductility is believed to be a result of the increased homogeneity of the joints. As shown in Fig. 7.13, the force controlled joints fail on either side of the specimens. Especially the welding conditions of the tool validation campaign (T_XX) have a much more uniform microstructure (see Fig. 7.17).

It should be noted that the increase of strength, ductility and efficiency mean values is accompanied with a large decrease of scatter. A comparison of the standard deviations in Fig. 7.18 shows that the automatic process control used in this study leads to a much more reproducible process as compared to the manual process control (see Section 6.3.1.6).

With increasing welding speed and decreasing peak temperatures the size of the HAZ can be reduced (see Fig. 5.15 and Fig. 5.10). This can be considered a gain in weld quality. The size of the softened zone can be predicted by the thermal model (see Section 5.1.5.4).

7.4 Joint Quality Improvement - Summary and Conclusions

- Improved process control and tooling has helped to considerably increase the productivity and quality of the BT-FSW joints produced in this study. The joint efficiency has been increased from 82% [3] to 88%. The maximum ductility has been increased from 2.7% to 6.5%.

- The improved tool design developed with the aid of numerical models has proven successful. It can be used for a larger parameter window due to the resulting superior mechanical properties. The microstructural defects that are common for the threaded baseline tool can be avoided completely.

- The weakest region of the joint is between the HAZ and the TMAZ. The softening in this region due to precipitation coarsening and dissolution cannot be avoided. The size of the heat affected zone can, however, be predicted using the thermal model and reduced by choosing faster and colder process parameters.

- Based on the results of the work the SSBT-FSW process has been invented and filed as patent.

Chapter 8

Summary and Conclusions

8.1   Summary

The objectives of the work (see Section 2.1) were to develop numerical models for the relevant physical interactions of bobbin tool friction stir welding in order to use them to develop improved hardware and software and improve process stability, quality and productivity.

In a first step baseline welding experiments based on the prior state of the art were conducted on the existing welding machine FlexiStir. The results of these experiments were used to determine the relevant physical interactions that needed to be included in the numerical models and the technological challenges of the process. The key observations and conclusions were:

- The mechanical strength of the tools was a limiting factor. The process parameters that could be examined with the welding machine and tools at that time were limited to excessively slow welds with very high RPMs. The reason for this was identified to be the fixed gap process control strategy that favoured tool fracture because of thermal expansion mismatch (see Fig. 6.5). It was concluded that the gap size needs to be controllable to avoid these problems.

- The forces in welding direction and lateral direction could not be measured. The selection of process parameters on a trial-and-error basis lead to tool failure due to overload. It was concluded that the expected process forces need to be known before welding. A model of the material flow is needed to predict the acting forces. Such a model needs to include information on the temperature field. Therefore a thermal model is needed.

- The process temperature does not reach a steady state within the available experimental welding length. It needs to be considered transient. Therefore it was concluded that all model predictions need to consider the different situations at the beginning, centre and end of the welds.

- The baseline tool had been designed based on empirical knowledge of standard FSW

tooling. The manufactured tools had a strong deviance from the complex computer aided design. They included sharp notches that acted as stress-raisers and favoured fracture. It was concluded that improved tools need to be designed in a way that allows for reproducible production. The definition of the tool size and the design of the pin features requires best possible knowledge of the expected loads and the tool material properties. Therefore a prediction of the transient forces acting on a rotating arbitrarily shaped pin is required. Such a model was not yet available at that time. A mechanical model is needed to find the stresses acting in the tool based on the external loads. Mechanical testing of tool material candidates is needed at appropriate temperatures.

Based on these conclusions the welding head was upgraded with additional sensors to measure all forces and the torque acting on the tool. The software of the machine was extended with a series of feedback loops to control the force in the gap between the tool shoulders and the welding speed. Process control strategies were developed and tested. These changes made a wider process parameter window accessible for experimental observations while still using the baseline tool. This wider range of available experimental data facilitated the development and validation of the numerical process model.

The process model framework consisting of a thermal model, two versions of a material flow model and a mechanical model. All elements of the process model can best be understood in their interaction and impact on the tool and the process when following the principle work flow as described below. It is the result of the experiences gathered throughout the work on knowledge based process development of FSW processes:

First the material to be joined and the geometric properties of the desired joint are defined. The temperature dependent shear yield stress of the material needs to be known. It can either be determined experimentally or taken from the literature. With this information a first run of the thermal advanced moving geometry model (AMGM) (see Section 5.1 and Section 5.1.2) can be performed. An initial guess for the input parameters needs to be made. The welding speed can be chosen based on the desired productivity, the tool rotational speed (RPM) needs to be within the capabilities of the available welding machine. The parameters for the analytical shear layer model (ASLM) (see Section 5.1.3) can be set to a default value at this stage. If a basic tool geometry (pin and shoulder radii) has not been defined a starting guess needs to be made as well.

The result of this first run of the thermal model will be a prediction of the transient temperature fields and an estimate of the machine torque needed to perform the weld. If either of these is far outside the acceptable range, that has to be defined regarding the material to join and the machine capabilities, the welding speed and RPM or tool size need to be adjusted.

The thermal field predictions can now be enhanced by calibrating the ASLM with predictions of the CFD model (see Section 5.2 and Section 5.2.3) for the chosen tool size and work piece material and thickness.

Precise material flow and joining force predictions can be produced by running the rotating featured pin model (RFPM) (see Section 5.2.2). This model requires the definition of the tool features. Iterative runs can be performed to compare the effect of different tool designs. This model can be run for a short time (several tool rotations) at various times throughout the formation of the joint, taking as an input the transient temperature field predicted by the AMGM. This way the transient process forces can be predicted. If these exceed the desired range, another iteration with altered process parameters or tool geometry can be performed. Finally, the predicted temperature, force and flow fields can be used for further evaluation. The mechanical loads can be used to estimate stresses acting in the tool (see Section 6.2.1) and to compare these to the allowable values (see Chapter 6 and Section 6.1.2). The shear rates, forces and temperatures can also be inputs for micro structure models which again can be inputs for residual stress models. The later two are not described in detail in this work but will be published elsewhere upon completion (see Figure 5.35).

The described work flow can thus help to design the welding process including parameters and tooling. By combining TPM and CFD models, the contact condition δ could be eliminated from the list of necessary inputs to the process model. This is an important step towards a self-contained fully numerical prediction of a priori unknown process conditions and results. The amount of preliminary experiments can be reduced. This saves time and cost.

The process model was used as described above to develop an improved bobbin tool design. This tool design was manufactured using the new tool material MP159 that was selected based on the comparison of mechanical performance of four tool material candidates suggested by the scientific community. The new tools were tested successfully. They allow for higher welding speeds and thus higher productivity while at the same time they lead to an improved joint quality.

The models described in this study can help to predict the transient behaviour of a bobbin tool weld. This knowledge alone does, however, not always enable the operator to find a constant set of process parameters that fulfil all the required limits in terms of productivity, load and temperature. Therefore another aspect investigated in this work is the process control strategy (see Section 6.3.1). A versatile feedback controller has been implemented on the machine controller. The force acting between the shoulders can be controlled as well as the force acting on the pin in the in-plane direction.

8.2 Conclusions

From the results of the numerical and experimental work the following conclusions can be drawn:

- Process development in the field of FSW and BT-FSW in particular can be effectively supported by numerical modelling. Especially a thermal TPM model can predict valu-

able information with very limited cost in terms of computational time and model adaption. It can therefore be recommended to model the thermal field of any novel joint configuration and check the peak temperatures and maximum torque to identify possible problems with the chosen process parameters. This may prevent damage to the tool, welding machine and workpiece. Parametric studies can easily be performed. The information on the transient thermal field found from the thermal model with the inputs of the CFD and ANN-calibrated ASLM is a very important basis for further scientific evaluation of the microstructural behaviour of BT-FSW joints. The data can be used as a starting point for several further investigations that depend on accurate thermal histories.

- In terms of tool development the RFPM in combination with a mechanical model can be used to find the performance limits of a given design and check novel tool designs before manufacturing. This can save a lot of time and money. Within the scope of the presented work the stresses acting in the tool for a standard load case have been reduced by 15% this way. By selecting the most suitable material, an additional gain of 25% in tool strength could be realised. This allows for significantly higher allowable process loads and thus extends the accessible process window. Also a desirable symmetric material flow in the stir zone can be achieved by a robust tool design.

- A deeper understanding of the conditions present during welding allows for significant improvement of process productivity and quality. By choosing the process parameters based on the knowledge of heat input and expected process forces, the welding speed and thus productivity was increased by a factor of $\approx$10. Tool fracture is not a common issue any longer. The mechanical quality of the joints is significantly improved. The performance in bending was increased by over 120%. The Ductility was increased by 140% and the tensile joint efficiency was improved by 7% to an absolute value of 88%. This is achieved by the combination of lower heat input, higher welding speed and the increased homogeneity of the microstructure.

- As the interaction between tool geometry and weld quality is not jet known in sufficient detail, it is not possible today to develop a tool with ideal joining capabilities from modelling only. More work on this field may further decrease the necessary iteration cycles including hardware manufacturing. Within the limits of the manufacturing process for the tools, computer based geometry optimisation is a possible means of further tool performance increase.

- The general trend towards complex integral structures gives rise to new challenges for bobbin tool technology. Robotic solutions may gain a higher importance for industrial applications in this field. As the stiffness of such systems is inherently limited it is mandatory to consider a minimisation of process loads during tool development.

Appendix A

Lists

List of Figures

List of Tables

References

[1] Ø. Frigaard, Ø. Grong, and O.T. Midling. A process model for friction stir welding of age hardening aluminum alloys. *Metallurgical and materials transactions A*, 32(A):1189–1200, 2001.

[2] J. Hilgert. Modeling bobbin tool friction stir welding. Diploma Thesis, 2009. Technische Universität Hamburg-Harburg.

[3] T. Neumann. *Untersuchung der Schweißbarkeit der Aluminiumlegierung AL 2024 mit Hilfe des Rührreibschweißverfahrens mit einem kraftautarken Werkzeug "Bobbin-Tool"*. PhD thesis, TU Ilmenau, 2010.

[4] W.M. Thomas, E.D. Nicholas, J.C. Needham, M.G. Murch, P. Templesmith, and C.J. Dawes. Friction stir welding. GB 9125978.8, 1991. Patent.

[5] R.S. Mishra. Preface to the viewpoint set on friction stir processing. *Scripta Materialia*, 58(5):325–326, 2008.

[6] K.J. Colligan and R.S. Mishra. A conceptual model for the process variables related to heat generation in friction stir welding of aluminum. *Scripta Materialia*, 58(5):327 – 331, 2008. Viewpoint set no. 43.

[7] R.K. Uyyuru and S.V. Kailas. Numerical analysis of friction stir welding process. *Journal of Materials Engineering and Performance*, 15(5):505–518, 2006.

[8] W.J. Arbegast. A flow-partitioned deformation zone model for defect formation during friction stir welding. *Scripta Materialia*, 58(5):372–376, 2008.

[9] L. Ke, L. Xing, and J. Indacochea. Material flow patterns and cavity model in friction-stir welding of aluminum alloys. *Metallurgical and Materials Transactions B*, 35(1):153–160, 2004.

[10] X.K. Zhu and Y.J. Chao. Effects of temperature-dependent material properties on welding simulation. *Computers and Structures*, 80:967–976, 2002.

[11] H. Atharifar, D. Lin, and R Kovacevic. Numerical and experimental investigations on the loads carried by the tool during friction stir welding. *Journal of Materials Engineering and Performance*, 18(4):339–350, 2009.

[12] R.S. Mishra and Z.Y. Ma. Friction stir welding and processing. *Materials Science and Engineering: R: Reports*, 50(1-2):1 – 78, 2005.

[13] R. Nandan, T. DebRoy, and H.K.D.H. Bhadeshia. Recent advances in friction-stir welding - process, weldment structure and properties. *Progress in Materials Science*, 53(6):980 – 1023, 2008.

[14] G. Cam. Friction stir welded structural materials: beyond Al-alloys. *International Materials Reviews*, 56:1–48(48), 2011.

[15] J.R. Ding and P.A. Oelgoetz. Auto-adjustable pin tool for friction stir welding. US 5,893,507, 1999. Patent.

[16] W.M. Thomas, K.L. Johnson, and C.S. Wiesner. Friction stir welding - recent developments in tool and process technologies. *Advanced Engineering Materials*, 5(7):5867–5877, 2003.

[17] J.-Q. Su, T.W. Nelson, R. Mishra, and M. Mahoney. Microstructural investigation of friction stir welded 7050-T651 aluminium. *Acta Materialia*, 51:713–729, 2003.

[18] P. Cavaliere, E. Cerri, L. Marzoli, and J.F. dos Santos. Friction stir welding of ceramic particle reinforced aluminium based metal matrix composites. *Applied Composite Materials*, 11(l):247–258, 2004.

[19] A. Kostka, R.S. Coelho, J. dos Santos, and A.R. Pyzalla. Microstructure of friction stir welding of aluminium alloy to magnesium alloy. *Scripta Materialia*, 60(11):953 – 956, 2009.

[20] S. Sheikhi, R. Zettler, and J.F. dos Santos. Fortschritte beim Rührreibschweißen von Aluminium, Magnesium und Stahl. *Mat.-wiss. u. Werkstofftech.*, 37(9):762–767, 2006.

[21] L. Bertling and N. Harlfinger. Innovative Fügeverfahren zur Herstellung von Al-Leichtbaustrukturen im Schienenfahrzeugbau. *Mat.-wiss. u. Werkstofftech.*, 30:290–299, 1999.

[22] P.A. Colegrove and H.R. Shercliff. 3-dimensional CFD modelling of flow round a threaded friction stir welding tool profile. *Journal of Materials Processing Technology*, 169:320–327, 2005.

[23] G.E. Cook, R. Crawford, D.E. Clark, and A.M. Strauss. Prediction of temperature distribution and thermal history during friction stir welding: input torque based model. *Industrial Robot: An International Journal*, 31(1):55–63, 2004.

[24] P. Vilaça, L. Quintino, and J.F. dos Santos. iSTIR - analytical thermal model for friction stir welding. *Journal of Materials Processing Technology*, 169(3):452–465, 2005.

[25] P.L. Threadgill. Terminology in friction stir welding. *Science and Technology of Welding & Joining*, 12:357–360(4), 2007.

[26] S. Lomolino, R. Tovo, and J.Fna dos Santos. On the fatigue behaviour and design curves of friction stir butt-welded al alloys. *International Journal of Fatigue*, 27:305–316, 2005.

[27] G. Buffa, L. Fratini, and R. Shivpuri. Finite element studies on friction stir welding processes of tailored blanks. *Computers & Structures*, 86(1-2):181 – 189, 2008.

[28] N. Kamp, A. Sullivan, and J.D. Robson. Modelling of friction stir welding of 7xxx aluminium alloys. *Materials Science and Engineering: A*, 466(1-2):246 – 255, 2007.

[29] A. Sullivan and J.D. Robson. Microstructural properties of friction stir welded and post-weld heat-treated 7449 aluminium alloy thick plate. *Materials Science and Engineering: A*, 478(1-2):351 – 360, 2008.

[30] W. Xu, J. Liu, G. Luan, and C. Dong. Microstructure and mechanical properties of friction stir welded joints in 2219-T6 aluminum alloy. *Materials & Design*, 30(9):3460 – 3467, 2009.

[31] P. Dong, F. Lu, J.K. Hong, and Z. Cao. Coupled thermomechanical analysis of friction stir welding process using simplified models. *Science and Technology of Welding & Joining*, 6:281–287, 2001.

[32] A.P. Reynolds. Flow visualization and simulation in FSW. *Scripta Materialia*, 58(5):338 – 342, 2008. Viewpoint set no. 43.

[33] D.G. Hattingh, C. Blignault, T.I. van Niekerk, and M.N. James. Characterization of the influences of fsw tool geometry on welding forces and weld tensile strength using an instrumented tool. *Journal of Materials Processing Technology*, 203(1-3):46 – 57, 2008.

[34] K.J. Colligan and J.R. Pickens. *Friction Stir Welding and Processing III*, chapter Friction Stir Welding of Aluminium Using a Tapered Shoulder Tool, pages 161–170. TMS, 2005.

[35] C.G. Derry and J.D. Robson. Characterisation and modelling of toughness in 6013-T6 aerospace aluminium alloy friction stir welds. *Materials Science and Engineering: A*, 490(1-2):328 – 334, 2008.

[36] S.W. Williams. Welding of airframes using friction stir. *Air & Space Europe*, 3(3-4):64 – 66, 2001.

[37] E. Schofer. Rührreibschweißen - Wärmearmes Verbinden von Aluminiumlegierungen. *Materialwissenschaft und Werkstofftechnik*, 30(11):693–696, 1999.

[38] A. Toskey, W. Arbegast, C. Allen, and A. Patnaik. *Friction Stir Welding and Processing III*, chapter Fabrication of alumnium box beams using self - reacting and standard fixed pin friction stir welding, pages 171–178. TMS, 2005.

[39] C.L. Campbell, M.S. Fullen, and M.J. Skinner. Welding head. US 6199745, 2001. Patent.

[40] R.W. Carter. Auto-adjustable tool for selfreacting and conventional friction stir welding. US 6758382, 2004. Patent.

[41] H. Loitz, J.P. Wulfsberg, J. v.d. Wense, A. v. Strombeck, C. Schilling, and J.F. dos Santos. Vorrichtung zum Verbinden von Werkstücken nach der Methode des Reibrührschweißens. OE 10 2004 028 560, 2005. Patent.

[42] NASA. Marshall's friction stir welding technology successfully commercialized by two companies. News Release 02-009 01/23/02, NASA Marshall Space Flight Center, Huntsville, Ala., http://www.msfc.nasa.gov/news/news/releases/2002/02-009.html, 01 2002.

[43] C.B. Smith, S.M. Gillis, and L.M. Cerveny. Self-clamping friction stir welding device. US 2010/0006622, 2010. Patent.

[44] M.R. Eller, D.P. Roussel, and Z. Li. Friction stir welding apparatus and method. US 2010/0140321, 2010. Patent.

[45] K.A. Burton and M.P. Matlack. Counter-rotating spindle for friction stir welding. US 2006/0102699, 2006. Patent.

[46] W.M. Thomas, C.S. Wiesner, D.J. Marks, and D.G. Staines. Conventional and bobbin friction stir welding of 12/steel using composite refractory tool materials. *Science and Technology of Welding 38; Joining*, 14:247–253, 2009.

[47] E.N.C. Dalder, J.W. Pastrnak, J. Engel, R.S. Forrest, E. Kokko, K. Mc Ternan, and D. Waldron. Bobbin-tool friction-stir welding of thick-walled aluminum alloy pressure vessels. *Welding Journal*, 2007. UCRL-JRNL-233687.

[48] P.L. Threadgill, M.M.Z. Ahmed, J.P. Martin, J.G. Perrett, and B.P. Wynne. The use of bobbin tools for friction stir welding of aluminium alloys. *Materials Science Forum*, 638 - 642:1179–1184, 2010.

[49] R. Edwards and G. Sylva. *Trends in Welding Research 2005: Proceedings of the 7th International Conference*, chapter Recent Advances in Welding of Aluminum Alloys using a Self Reacting Pin Tool (SRPT) Approach with Application Examplesd, pages 191–199. AMS, 2005.

[50] T. Neumann, R. Zettler, J.F. dos Santos, P. Vilaça, and L. Quintino. *Analysis of Self-Reacting Friction Stir Welds in a 2024-T351 Alloy*, pages 55–72. Number IV in Friction Stir Welding and Processing. John Wiley & Sons, 2007.

[51] W.D. Lockwood, B. Tomaz, and A.P. Reynolds. Mechanical response of friction stir welded AA2024: experiment and modeling. *Materials Science and Engineering A*, 323(1-2):348 – 353, 2002.

[52] M.A. Sutton, A.P. Reynolds, B. Yang, and R. Taylor. Mode i fracture and microstructure for 2024-T3 friction stir welds. *Materials Science and Engineering A*, 354(1-2):6 – 16, 2003.

[53] R.V. Preston, H.R. Shercliff, P.J. Withers, and S. Smith. Physically-based constitutive modelling of residual stress development in welding of aluminium alloy 2024. *Acta Materialia*, 52(17):4973 – 4983, 2004.

[54] T.S. Parel, S.C. Wang, and M.J. Starink. Hardening of an Al-Cu-Mg alloy containing types i and ii s phase precipitates. *Materials & Design*, 31(Supplement 1):2 – 5, 2010.

[55] C. Genevois, D. Fabrègue, A. Deschamps, and W.J. Poole. On the coupling between precipitation and plastic deformation in relation with friction stir welding of aa2024 T3 aluminium alloy. *Materials Science and Engineering: A*, 441(1-2):39 – 48, 2006.

[56] X. Duan and T. Sheppard. Simulation and control of microstructure evolution during hot extrusion of hard aluminium alloys. *Materials Science and Engineering A*, 351(1-2):282 – 292, 2003.

[57] H.N.B. Schmidt. *Modelling the Thermomechanical Conditions in Friction Stir Welding*. PhD thesis, Department of Manufacturing Engineering and Management, Technical University of Denmark, Lyngby, Denmark, 2004.

[58] H.N.B. Schmidt and J.H. Hattel. Heat source models in simulation of heat flow in friction stir welding. *International Journal of Offshore and Polar Engineering*, 14(4):294–304, 2004.

[59] H.N.B. Schmidt, J.H. Hattel, and J. Wert. An analytical model for the heat generation in friction stir welding. *Modelling and Simulation in Materials Science and Engineering*, 12(1):143–157, 2004.

[60] H.N.B. Schmidt and J.H. Hattel. A local model for the thermomechanical conditions in friction stir welding. *Modelling Simul. Mater. Sci. Eng.*, 13:77–93, 2005.

[61] H.N.B. Schmidt and J.H. Hattel. Modelling heat flow around tool probe in friction stir welding. *Science and Technology of Welding and Joining*, 10(2):167–186, 2005.

[62] H.N.B. Schmidt and J.H. Hattel. CFD modelling of the shear layer around the tool probe in friction stir welding. In *Friction Stir Welding and Processing III*. TMS (The Minerals, Metals & Materials Society), 2005.

[63] H.N.B. Schmidt, T.L. Dickerson, and J.H. Hattel. Material flow in butt friction stir welds in AA2024-T3. *Acta Materialia*, 54(4):1199–1209, 2006.

[64] H.N.B. Schmidt and J.H. Hattel. Thermal modelling of friction stir welding. *Scripta Materialia*, 58(5):332–337, 2008.

[65] H.N.B. Schmidt and J.H. Hattel. A thermal-pseudo-mechanical model for the heat generation in friction stir welding. In *Proceedings of the 7th International Symposium on Friction Stir Welding 2008*, 2008.

[66] H.N.B. Schmidt and J.H. Hattel. Thermal and material flow modelling of friction stir welding using comsol. In *Proceedings of the COMSOL Conference 2008 Hannover*, 2008.

[67] P.A. Colegrove and H.R. Shercliff. Experimental and numerical analysis of aluminium alloy 7075-T7351 friction stir welds. *Science and Technology of Welding & Joining*, 8:360–368, 2003.

[68] P.A. Colegrove and H.R. Shercliff. Two-dimensional CFD modelling of flow round profiled fsw tooling. *Science and Technology of Welding & Joining*, 9:483–492, 2004.

[69] P.A. Colegrove and H.R. Shercliff. CFD modelling of friction stir welding of thick plate 7449 aluminium alloy. *Science and Technology of Welding & Joining*, 11:429–441(13), 2006.

[70] P.A. Colegrove. Modelling the heat generation, temperature and microstructure of friction stir welds using comsol multiphysics. In *Excerpt from the Proceedings of the COMSOL Users Conference 2006 Birmingham*, 2006.

[71] D. Rosenthal. The theory of moving sources of heat and its application to metal treatments. *Trans. Am. Soc. Mech. Engrs.*, 68:849–866, 1946.

[72] A.A. Larsen, M. Bendsøe, J. Hattel, and H.N.B. Schmidt. Optimization of friction stir welding using space mapping and manifold mapping - an initial study of thermal aspects. *Structural and Multidisciplinary Optimization*, 38(3):289–299, 2008.

[73] Sindo Kou. *Welding Metallurgy*. Wiley-Interscience, 2002.

[74] J.W. Pew. A torque-based weld power model for friction stir welding. Master's thesis, Brigham Young University, December 2006.

[75] J.W. Pew, T.W. Nelson, and C.D. Sorensen. Torque based weld power model for friction stir welding. *Science and Technology of Welding & Joining*, 12(4):341–347, 2007.

[76] S.G. Lambrakos, R.W. Fonda, J.O. Milewski, and J.E. Mitchell. Analysis of friction stir welds using thermocouple measurements. *Science and Technology of Welding & Joining*, 8:385–390, 2003.

[77] M.Z.H. Khandkar, J.A. Khan, and A.P. Reynolds. Prediction of temperature distribution and thermal history during friction stir welding: input torque based model. *Science and Technology of Welding and Joining*, 8(3):165–174, 2003.

[78] Z. Zhang. Comparison of two contact models in the simulation of friction stir welding process. *J Mater Sci*, 43:5867–5877, 2008.

[79] P.A. Colegrove, M. Painter, D. Graham, and T. Miller. 3 dimesional flow and thermal modelling of the friction stir welding process. In *2nd Int. Symp. on Frition Stir Welding*, 2000.

[80] P. Heurtier, M.J. Jones, C. Desrayaud, J.H. Driver, F. Montheillet, and D. Allehaux. Mechanical and thermal modelling of friction stir welding. *Journal of Materials Processing Technology*, 171(3):348–357, 2006.

[81] T. Aukrust and S. LaZghab. Thin shear boundary layers in flow of hot aluminium. *International Journal of Plasticity*, 16(1):59 – 71, 2000.

[82] T.U. Seidel and A.P. Reynolds. Two-dimensional friction stir welding process model based on fluid mechanics. *Science and Technology of Welding & Joining*, 8:175–183, 2003.

[83] R. Carbone, A. Langella, and L. Nele. Numerical modelling of a time-dependent friction stir welding process with a moving tool using comsol script. In *COMSOL Users Conference 2007 Grenoble*. Dipartimento di Ingegneria dei Materiali e della Produzione - DIMP, 2007.

[84] S. Spigarelli, E. Evangelista, and H.J. McQueen. Study of hot workability of a heat treated AA6082 aluminum alloy. *Scripta Materialia*, 49(2):179 – 183, 2003.

[85] G. Becerra, J. Ramos-Grez, and J. Montecinos. Texture distribution and plane strain mechanical behavior of AA 7xxx plates of different thicknesses. *Journal of Materials Engineering and Performance*, 18(8):1144–1150, November 2009.

[86] G. Buffa, J. Hua, R. Shivpuri, and L. Fratini. A continuum based FEM model for friction stir welding–model development. *Materials Science and Engineering: A*, 419(1-2):389–396, 2006.

[87] S. Guerdoux and L. Fourment. A 3d numerical simulation of different phases of friction stir welding. *Modelling and Simulation in Materials Science and Engineering*, 17(7):075001, 2009.

[88] S. Xu, X. Deng, A.P. Reynolds, and T.U. Seidel. Finite element simulation of material flow in friction stir welding. *Science and Technology of Welding & Joining*, 6:191–193, 2001.

[89] H.W. Zhang, Z. Zhang, and J.T. Chen. 3d modeling of material flow in friction stir welding under different process parameters. *Journal of Materials Processing Technology*, 183(1):62 – 70, 2007.

[90] Z. Zhang and J.T. Chen. The simulation of material behaviors in friction stir welding process by using rate-dependent constitutive model. *J Mater Sci*, 43:222–232, 2008.

[91] S. Mandal, J. Rice, and A.A. Elmustafa. Experimental and numerical investigation of the plunge stage in friction stir welding. *Journal of Materials Processing Technology*, 203:411–419, 2008.

[92] T. Sheppard. Prediction of structure during shaped extrusion and subsequent static recrystallisation during the solution soaking operation. *Journal of Materials Processing Technology*, 177(1-3):26 – 35, 2006.

[93] S.M. Dörfler. Advanced modeling of friction stir welding - improved material model for aluminum alloys and modeling of different materials with different properties by using the level set method. In *Proceedings of the COMSOL Conference*, 2008. Hannover.

[94] B. Zhang and T.N. Baker. Effect of the heat treatment on the hot deformation behaviour of AA6082 alloy. *Journal of Materials Processing Technology*, 153-154:881 – 885, 2004.

[95] B.I. Bjørneklett, Ø. Grong, O.R. Myhr, and A.O. Kluken. A process model for the heat-affected zone microstructure evolution in Al-Zn-Mg weldments. *Metallurgical and materials transactions A*, 30(A):2667–2677, 1999.

[96] H.R. Shercliff and A.M. Lovatt. Modelling of microstructure evolution in hot deformation. *Philosophical Transactions of the Royal Society of London. Series A: Mathematical, Physical and Engineering Sciences*, 357(1756):1621–1643, 1999.

[97] Ø. Grong and H.R. Shercliff. Microstructural modelling in metals processing. *Progress in Materials Science*, 47(2):163 – 282, 2002.

[98] N. Kamp, A. Sullivan, R. Tomasi, and J.D. Robson. Modelling of heterogeneous precipitate distribution evolution during friction stir welding process. *Acta Materialia*, 54(8):2003 – 2014, 2006.

[99] D. Deloison, D. Jacquin, B. Gurin, C. Desrayaud, and F. Marie. Simplified models for bobbin-tool fsw process. In J. F. dos Santos, editor, *3rd FSW Modelling and Material Flow Visualisation Seminar*, Geesthacht, April 2008.

[100] E. Hersent, D. Piot, F. Marie, B. Guérin, D. Deloison, and S. Gourdet. Thermomechanical modelling and study of the microstructural evolution during bobbin tool friction stir welding of AA7449. In J. F. dos Santos, editor, *3rd FSW Modelling and Material Flow Visualisation Seminar*, Geesthacht, April 2008.

[101] J. Hilgert, H.N.B. Schmidt, J.F. dos Santos, and N. Huber. Thermal models for bobbin tool friction stir welding. *Journal of Materials Processing Technology*, 211(2):197 – 204, 2010.

[102] G. Buffa, J. Hua, R. Shivpuri, and L. Fratini. Design of the friction stir welding tool using the continuum based FEM model. *Materials Science and Engineering: A*, 419(1-2):381 – 388, 2006.

[103] *Metals Handbook*, volume 2. The American Society for Metals, Metal Park, OH, 9th edition, 1979.

[104] T. Sheppard. Extrusion of AA2024 alloy. *Materials Science and Technology*, 9:430–440(11), 1993.

[105] B.G. Sumpter and D.W. Noid. On the design, analysis, and characterization of materials using computational neural networks. *Annual Review of Materials Science*, 26(1):223 – 277, 1996.

[106] G. Yagawa and H. Okuda. Neural networks in computational mechanics. *Archives of Computational Methods in Engineering*, 3:435 – 512, 1996.

[107] M. Riedmiller and H. Braun. A direct adaptive method for faster backpropagation learning: the rprop algorithm. In *IEEE International Conference on Neural Networks*, volume 1, pages 586 – 59, 1993.

[108] L. Cederqvist, O. Garpinger, T. Hägglund, and A. Robertsson. Cascade control of the friction stir welding process to seal canisters for spent nuclear fuel. *Control Engineering Practice*, 20(1):35 – 48, 2012. Special Section: IFAC Conference on Analysis and Design of Hybrid Systems in Zaragoza, Spain, 16th-18th September, 2009.

[109] A. Razal Rose, K. Manisekar, and V. Balasubramanian. Effect of axial force on microstructure and tensile properties of friction stir welded AZ61a magnesium alloy. *Transactions of Nonferrous Metals Society of China*, 21(5):974 – 984, 2011.

[110] J. Hilgert and J.F. dos Santos. Vorrichtung zum Reibrührschweißen. DE 10 2011 015 831.6., 2011. Patentanmeldung.

[111] T. Brunzel, U. Henneboehle, F. Palm, J. Silvanus, and M. Pfeiffer. Reibrühr-Werkzeug sowie Verfahren und Vorrichtung zum Reibrühren. DE 102005030800 A1, 2007. Patent.

[112] T. Sato and T. Suda. *New Frontiers in Light Metals - Proceedings of the 11th International Aluminium Conference INALCO 2010*, chapter Finite Element Analysis of Friction Stir Welding Affected by Heat Conduction through the Welding Jig, pages 139 – 146. Number ISBN 978-1-60750-585-3. 2010.

[113] H. Aydın, A. Bayram, and İ. Durgun. The effect of post-weld heat treatment on the mechanical properties of 2024-T4 friction stir-welded joints. *Materials & Design*, 31(5):2568–2577, May 2010.

[114] Y.J. Chao, X. Qi, and W. Tang. Heat transfer in friction stir welding—experimental and numerical studies. *Journal of Manufacturing Science and Engineering*, 125(1):138–145, 2003.

[115] S.R. Rajesh, H.S. Bang, H.J. Kim, and H.S. Bang. Analysis of complex heat flow phenomena with friction stir welding using 3d-analytical model. *Advanced Materials Research*, 15 - 17:339–344, 2007.

[116] X.K. Zhu and Y.J. Chao. Numerical simulation of transient temperature and residual stresses in friction stir welding of 304l stainless steel. *Journal of Materials Processing Technology*, 146(2):263–272, 2004.

[117] S.R. Rajesh, H.S. Bang, W.S. Chang, H.J. Kim, H.S. Bang, C.I. Oh, and J.S. Chu. Numerical determination of residual stress in friction stir weld using 3d-analytical model of stir zone. *Journal of Materials Processing Technology*, 187-188:224–226, 2007.

[118] Z. Zhang and H.W. Zhang. Numerical studies on controlling of process parameters in friction stir welding. *Journal of Materials Processing Technology*, 209(1):241–270, January 2009.

Appendix B

Patent Application

Vorrichtung zum Reibrührschweißen

Die vorliegende Erfindung betrifft eine Vorrichtung zum Reibrührschweißen mit einem um eine Drehachse drehend antreibbaren Stift, der ein Antriebsende und ein freies Ende aufweist, wobei zwischen dem Antriebsende und dem freien Ende ein zylindrischer Eingriffsabschnitt vorgesehen ist, der sich axial in Richtung der Drehachse erstreckt und dessen Umfangsfläche zum Eingriff mit einem oder mehreren Werkstücken vorgesehen ist, mit einem ersten Schulterelement, das auf der zum Antriebsende weisenden Seite des Eingriffsabschnitts konzentrisch bezüglich der Drehachse um den Stift angeordnet ist und das eine zum Eingriffsabschnitt weisende sich senkrecht zur Drehachse erstreckende erste Anlagefläche aufweist, und mit einem zweiten Schulterelement, das auf dem zum freien Ende weisenden Seite des Eingriffsabschnitts konzentrisch bezüglich der Drehachse um den Stift angeordnet ist und das eine zum Eingriffsabschnitt weisende sich senkrecht zur Drehachse erstreckende zweite Anlagefläche aufweist, wobei sich die zweite Anlagefläche unmittelbar bis an den Eingriffsabschnitt erstreckt und wobei das erste Schulterelement zur Anlage an die erste Oberfläche und das zweite Schulterelement zur Anlage an die zweite, der ersten gegenüberliegenden Oberfläche eines oder mehrerer Werkstücke vorgesehen ist.

Das Prinzip des Reibschweißens beinhaltet, dass das Material eines oder mehrerer Werkstücke durch Reibung zwischen dem Werkstück und einem weiteren Werkstück oder einem Werkzeug zunächst plastifiziert wird und sich anschließend wieder verfestigt. Beim Reibrührschweißen werden zunächst die zwei zu verbindenden, in der Regel metallischen Werkstücke aneinander angelegt. Das kann beispielsweise heißen, dass zwei Metallplatten oder Bleche Oberfläche an Oberfläche übereinander gelegt werden (Überlappverbindung) oder aber so nebeneinander positi-

- 2 -

oniert werden, dass die schmalen Seitenflächen aneinander an-
liegen (Stumpfstoß-Verbindung). Danach wird ein Reibrühr-
schweißwerkzeug im Bereich der Kontaktfläche in das Material
von mindestens einem der beiden Werkstücke - z.B. über eine
Bohrung oder vom Rand her - eingeführt.

Durch eine Rotation des Werkzeuges wird der Reibrührvorgang
bewirkt, wobei das Werkzeug an wenigstens einem Werkstück
reibt und das Material von mindestens einem der beiden
Werkstücke plastifiziert. Dabei kann das Reibrührschweißwerk-
zeug optional entlang der Grenzfläche der beiden Werkstücke
bewegt werden. Das plastifizierte Material an der Grenzfläche
der beiden Werkstücke kühlt anschließend ab und bildet die
Schweißnaht, welche die beiden Werkstücke zusammenhält.

Aus dem Stand der Technik, wie beispielsweise der WO
2006/055530, sind bereits zahlreiche Vorrichtungen zum Reib-
rührschweißen bekannt. Allen diesen Vorrichtungen gemeinsam
ist ein im Wesentlichen zylinder- oder kegelförmiger Stift mit
einem Eingriffsabschnitt zum Eingriff mit mindestens einem
Werkstück und mit einem Schulterelement zur Anlage an die
Oberfläche des mindestens einen Werkstücks. Stift und Schul-
terelement werden drehend angetrieben, wobei der Stift z.B.
zwischen zwei zu verbindende und aneinander angelegte Werkstü-
cke so weit in die Werkstücke eindringt, bis das Schulterele-
ment an der Oberfläche der Werkstücke anliegt.

Durch die Reibung von Stift und Schulterelement an den
Werkstücken wird das Material im angrenzenden Bereich der
Werkstücke plastifiziert. Bei einer gleichzeitigen Vorwärtsbe-
wegung der Vorrichtung entlang der Kontaktfläche der beiden
Werkstücke wird von dem rotierenden Stift plastifiziertes Ma-
terial in Bewegungsrichtung des Stifts betrachtet hinter diese
transportiert, wo es sich mit weiterem plastifizierten Materi-

al der beiden Werkstücke verbindet und eine Schweißnaht bildet.

Um das Reibrührschweißwerkzeug an beiden Oberflächen abstützen zu können und die Werkstücke zueinander auszurichten bzw. aneinander zu drücken, kann eine Vorrichtung zum Reibrührschweißen mit einem ersten und einem zweiten Schulterelement – ein sogenanntes Bobbin-Werkzeug – verwendet werden, wobei das erste und das zweite Schulterelement an gegenüberliegenden Oberflächen des oder der Werkstücke anliegen. Eine derartige Vorrichtung ist beispielsweise aus der JP 2008/296285 oder aus der EP 1 738 856 B1 bekannt.

Problematisch bei der Vorrichtung zum Reibrührschweißen in Bobbin-Konfiguration ist jedoch, dass der Stift, um ein Drehmoment auf beide Schulterelemente zu übertragen und gleichzeitig an dem zu plastifizierenden Bereich des mindestens einen Werkstücks zu reiben, sehr hohe mechanische und thermische Lasten aufnehmen muss. Um die Vorrichtung nicht zu zerstören, wird die erreichbare Geschwindigkeit bei der Vorwärtsbewegung des Stiftes durch das Werkstück somit begrenzt, wodurch sich auch die Prozessdauer des gesamten Schweißprozesses verlängert. Die aus mechanischen Gesichtspunkten notwendige begrenzte Geschwindigkeit bei der Vorwärtsbewegung des Stiftes führt jedoch zu überhöhten Prozesstemperaturen im plastifizierten Bereich des Werkstücks und im Bereich des Stiftes, die sich einerseits negativ auf die Qualität der Schweißverbindung auswirken und andererseits den Stift selbst beschädigen können.

Außerdem liegen die Prozessgeschwindigkeiten bei Einsatz eines Bobbin-Werkzeugs deutlich unter den Prozessgeschwindigkeiten von konventionellen Reibrührschweißwerkzeugen. Aus diesen Gründen kommt dem Reibrührschweißprozess unter Einsatz von Bobbin-Werkzeugen bislang nur eine untergeordnete Bedeutung zu.

- 4 -

Ausgehend vom Stand der Technik ist es daher die Aufgabe der
vorliegenden Erfindung, eine Vorrichtung zum Reibrührschweißen
bereitzustellen, mit der die mechanische und thermische Belas-
tung des Stiftes sowie die thermische Belastung der Werkstücke
reduziert werden.

Diese Aufgabe wird dadurch gelöst, dass das zweite Schulter-
element mit dem Stift frei um die Drehachse drehbar verbunden
ist. Auf diese Weise überträgt der Stift kein Drehmoment auf
das zweite Schulterelement, sondern dreht sich frei relativ zu
diesem. Das zweite Schulterelement führt folglich keine Dreh-
bewegung gegenüber der Oberfläche des mindestens einen Werk-
stücks aus, weswegen auch keine aus der Drehbewegung resultie-
rende Reibung auftritt, die wiederum für eine zusätzliche Er-
wärmung des zweiten Schulterelements und des mindestens einen
Werkstücks verantwortlich wäre. Da sich die zweite Anlageflä-
che unmittelbar bis an den Eingriffsabschnitt des Stifts er-
streckt, ist es lediglich der Eingriffsabschnitt, der bei des-
sen Rotation Reibungswärme erzeugt. Das zweite Schulterelement
trägt nicht dazu bei.

Mechanische und thermische Belastung des Stiftes werden somit
reduziert. Auch die thermische Belastung des Werkstücks bzw.
der Werkstücke wird reduziert. Eine niedrigere maximale Werk-
stücktemperatur wiederum schlägt sich in einer höheren Quali-
tät der Schweißverbindung nieder. Außerdem kann bei niedrige-
rer thermischer und mechanischer Belastung des Stiftes eine
höhere Schweißgeschwindigkeit eingestellt werden, d.h. der
Stift kann mit höherer Geschwindigkeit vorwärts durch das Ma-
terial bewegt werden. Auf diese Weise kann zum einen die Tem-
peratur von Stift und Werkstück nochmals verringert werden.
Zum anderen werden so eine kürzere Prozessdauer und damit ein
effizienterer Schweißprozess möglich.

Zusammenfassend lässt sich feststellen, dass mit dem erfindungsgemäßen gegenüber dem zweiten Schulterelement frei drehenden Stift einer Beschädigung des Stiftes entgegengewirkt wird, eine höhere Qualität der Schweißverbindung erzielt wird und ein schnellerer, effizienterer Schweißprozess ermöglicht wird.

In einer bevorzugten Ausführungsform ist der Stift axial verstellbar mit dem zweiten Schulterelement verbunden. Auf diese Weise kann der Abstand des zweiten Schulterelements zu dem ersten Schulterelement und somit die Größe des Eingriffsabschnitts verändert werden, wodurch die Vorrichtung an verschiedene Werkstückabmessungen angepasst werden kann. Außerdem kann mit einem axial verstellbaren zweiten Schulterelement, das z.B. eine Vorspannkraft erfährt, Druck auf das Werkstück bzw. die Werkstücke ausgeübt werden, um eine bessere Abstützwirkung zu erzielen.

In einer weiteren bevorzugten Ausführungsform weist das zweite Schulterelement ein zweites, in der zweiten Anlagefläche vorgesehenes ringförmiges Zwischenstück aus Keramikmaterial auf, wobei das zweite Zwischenstück den Eingriffsabschnitt umgibt. Das zweite Zwischenstück ist konzentrisch bezüglich der Drehachse um den Stift herum, d.h. zwischen dem Eingriffsabschnitt des Stifts und dem zweiten Schulterelement angeordnet.

Zunächst dient das zweite ringförmige Zwischenstück zur thermischen Entkopplung von Stift und zweitem Schulterelement, wobei ein direkter Kontakt zwischen Stift und zweitem Schulterelement verhindert wird. Dieser Effekt wird durch die Verwendung von einem keramischen Material verstärkt, das eine sehr geringe Wärmeleitfähigkeit aufweist.

Ein solches Zwischenstück dient darüber hinaus als Gleitlager für den Stift in dem zweiten Schulterelement bzw. als Gleitla-

- 6 -

ger für das zweite Schulterelement an dem Stift. Der kerami-
sche Werkstoff des zweiten Zwischenstücks ist ebenso hochtem-
peraturbeständig wie hochfest und kann deshalb die hohen Tem-
peraturen des Stiftes wie auch die hohen Lagerkräfte und Mo-
mente des Stiftes aufnehmen, ohne beschädigt zu werden. Ferner
können Keramikgleitlager mit einer ausreichend glatten Ober-
fläche gefertigt werden, um eine reibungsarme Lagerung des
Stiftes sowohl in Bezug auf eine Drehung des Stiftes als auch
in Bezug auf eine axiale Relativbewegung zwischen Stift und
zweitem Schulterelement zu ermöglichen.

In noch einer weiteren bevorzugten Ausführungsform ist das
zweite Schulterelement als Hülse mit einer sich radial zur
Drehachse erstreckenden Bodenfläche und einer zylindrischen,
sich parallel zu Drehachse erstreckender Seitenwandung ausge-
bildet, wobei in der Bodenfläche die zweite Anlagefläche aus-
gebildet ist. Dabei ist es besonders bevorzugt, wenn das freie
Ende des Stifts von einem zylindrischen Träger umgeben ist,
der in axialer Richtung des Stifts verstellbar ist, und wenn
die Hülse drehbar an dem Träger gelagert ist. Diese drehbare
Lagerung kann beispielsweise über Wälzlager erfolgen. Beson-
ders bevorzugt ist es ferner, wenn das freie Ende des Stifts
mit einem Gewinde versehen ist, wobei der Träger auf das freie
Ende aufgeschraubt ist. Auf diese Weise kann die Position des
Trägers und damit des gesamten zweiten Schulterelements an dem
freien Ende des Stifts in einfacher Weise eingestellt werden
oder dieses ganz von dem Stift entfernt werden.

Mit einem solchen Aufbau des zweiten Schulterelements wird da-
her erreicht, dass der Stift frei drehbar um die Drehachse mit
dem zweiten Schulterelement verbunden ist, wobei gleichzeitig
die axiale Position des zweiten Schulterelements angepasst
werden kann.

Zwischen der Seitenwandung und dem freien Ende des Stifts ist in einer bevorzugten Ausführungsform ein Kugellager vorgesehen. Vorzugsweise können auch zwei Kugellager vorgesehen sein, die parallel und in Richtung der Drehachse beabstandet angeordnet sind. Die Verwendung von Kugellagern bietet eine im Wesentlichen reibungsfreie Lagerung, die auch axiale Lasten aufnehmen kann.

In einer anderen bevorzugten Ausführungsform weist der Träger eine sich senkrecht zur Drehachse erstreckende Gewindebohrung zur Aufnahme einer Fixierschraube auf, wobei in der Seitenwandung der Hülse eine koaxial zu der Gewindebohrung ausgerichtete Bohrung vorgesehen ist. Durch eine solche Fixierschraube, die z.B. von außerhalb der Hülse zugänglich ist, kann der aufgeschraubte Träger dann in einer Position bezüglich der Drehachse an dem freien Ende des Stiftes fixiert werden bzw. nach dem Lösen der Schraube von dem Stift entfernt werden.

Der Stift ist in noch einer anderen bevorzugten Ausführungsform fest mit dem ersten Schulterelement verbunden. Dabei ist es besonders bevorzugt, wenn der Stift einstückig mit dem ersten Schulterelement ausgebildet ist. Auf diese Weise rotiert die erste Schulter mit dem Stift mit und reibt an der Oberfläche des mindestens einen Werkstücks, wobei das Material des Werkstücks im an das erste Schulterelement angrenzenden Bereich plastifiziert wird.

In einer dazu alternativen, bevorzugten Ausführungsform ist der Stift frei um die Drehachse drehbar mit dem ersten Schulterelement verbunden. Dabei ist es besonders bevorzugt, wenn das erste Schulterelement ein erstes ringförmiges Zwischenstück aus Keramikmaterial aufweist und das erste Zwischenstück den Eingriffsabschnitt umgibt. Besonders bevorzugt ist es ferner, wenn der Stift axial verschiebbar mit dem ersten Schulterelement verbunden ist. Damit weist das erste Schulterele-

- 8 -

ment in den wesentlichen Punkten den gleichen Aufbau wie das zweite Schulterelement auf. Mit zwei frei um die Drehachse drehbar mit dem Stift verbundenen Schulterstücken kann die thermische und mechanische Belastung des Stifts wie in Verbindung mit dem zweiten Schulterelement beschrieben noch weiter reduziert werden ebenso wie die Qualität der Schweißverbindung weiter gesteigert werden.

Die vorliegende Erfindung wird im Folgenden anhand einer ein Ausführungsbeispiel darstellenden Zeichnung erläutert. Die Zeichnung zeigt in

Fig. 1   eine Seitenansicht eines Ausführungsbeispiels einer erfindungsgemäßen Vorrichtung zum Reibrührschweißen und

Fig. 2   einen Schnitt entlang der Drehachse des Ausführungsbeispiels aus Fig. 1.

In Figur 1 ist ein Ausführungsbeispiel einer erfindungsgemäßen Vorrichtung 1 zum Reibrührschweißen dargestellt. Die Vorrichtung 1 zum Reibrührschweißen weist einen Stift 3, ein erstes Schulterelement 5 und ein zweites Schulterelement 7 auf.

Der Stift 3 hat eine im Wesentlichen zylindrische Form und wird bezüglich einer Drehachse 9, die mit der Symmetrieachse des Stiftes 3 zusammenfällt, drehend angetrieben. Der Stift 3 weist ein Antriebsende 11 und ein dem Antriebsende 11 gegenüberliegendes freies Ende 13 auf. Am Antriebsende 11 erfolgt der drehende Antrieb des Stiftes 3 über einen nicht dargestellten Motor. Zwischen dem Antriebsende 11 und dem freien Ende 13 weist der Stift 3 einen zylindrischen Eingriffsabschnitt 15 auf, der vorgesehen ist, um drehend mit mindestens einem Werkstück einzugreifen. Der Eingriffsabschnitt 15 weist in dem vorliegenden Ausführungsbeispiel entlang seines Umfangs

mit einer axialen Ausdehnung eine strukturierte Umfangsfläche 17 auf, um bei dem Eingriff mit dem Material eines bzw. mehrerer Werkstücke eine höhere Reibung zu erzeugen. Wie in Fig. 1 erkennbar, weist der Eingriffsabschnitt 15 an seiner Umfangsfläche 17 eine gerillte Struktur auf.

Das erste, auf der zum Antriebsende 11 weisenden Seite des Eingriffsabschnitts 15 angeordnete Schulterelement 5 hat in dem vorliegenden Ausführungsbeispiel eine im Wesentlichen kegelförmige Gestalt und ist konzentrisch bezüglich der Drehachse 9 um den Stift 3 angeordnet, wobei der Kegel sich in Richtung des zweiten Schulterelements 7 zuspitzt. Ferner weist das erste Schulterelement 5 eine erste Anlagefläche 19 auf, die senkrecht zur Drehachse 9 angeordnet ist und zum Eingriffsabschnitt 15 hin gerichtet ist. Das erste Schulterelement 5 ist in dem vorliegenden Ausführungsbeispiel drehbar mit dem Stift 3 verbunden. Die im Wesentlichen kegelförmige Gestalt des ersten Schulterelements 5 erweist sich als vorteilhaft, um die bei der Reibung während einer linearen Bewegung der ersten Anlagefläche 19 an einem Werkstück entstehende Wärme möglichst gut aufnehmen und von der ersten Anlagefläche 19 wegleiten zu können.

Zwischen der ersten Anlagefläche 19 und dem Eingriffsabschnitt 15 des Stifts 3 weist das erste Schulterelement 5 ein erstes ringförmiges Zwischenstück 21 aus Keramikmaterial auf (siehe Figur 2). Das erste ringförmige Zwischenstück 21 dient zur thermischen Entkopplung von Stift 3 und erstem Schulterelement 5, wobei ein direkter Kontakt zwischen dem Stift 3 und dem ersten Schulterelement 5 im Bereich der ersten Anlagefläche 19 durch das erste Zwischenstück 21 unterbrochen wird. Das erste ringförmige Zwischenstück 21 ist vorzugsweise aus keramischem Material gefertigt, das eine geringe Wärmeleitfähigkeit aufweist. Außerdem ist keramisches Material hoch temperaturbe-

ständig und wird somit auch durch die bei dem Betrieb der Vorrichtung auftretenden hohen Temperaturen nicht zerstört.

Das zweite, auf dem zum freien Ende 13 weisenden Seite des Eingriffsabschnitts 15 angeordnete Schulterelement 7 umfasst in dem vorliegenden Ausführungsbeispiel eine zylinderförmige Hülse 23, die konzentrisch bezüglich der Drehachse 9 um den Stift 3 angeordnet ist, mit einer zylindrischen, sich parallel zur Drehachse 9 erstreckenden Seitenwandung 25 und einer sich radial zur Drehachse 9 ersteckenden Bodenfläche 27, die eine zweite, zum Eingriffsabschnitt 15 weisende und sich senkrecht zur Drehachse 9 erstreckende Anlagefläche 29 aufweist. Die zweite Anlagefläche 29 erstreckt sich unmittelbar bis an den Eingriffsabschnitt 15, sodass kein Zwischenraum verbleibt und auch kein weiteres Element zwischen Eingriffsabschnitt 15 und zweiter Anlagefläche 29 vorgesehen ist. Außerdem liegt die zweite Anlagefläche 29 gegenüber und im Wesentlichen parallel zu der ersten Anlagefläche 19, wobei beide Anlageflächen 19, 29 den Eingriffsabschnitt 15 in axialer Richtung begrenzen und dessen axiale Ausdehnung an verschiedene Werkstückdicken anpassen können. Beide Anlageflächen 19, 29 sind konzentrisch bezüglich der Drehachse 9 um den Stift 3 bzw. um die Enden des Eingriffsabschnitts 15 angeordnet und weisen zueinander, sodass die Schulterelemente 5, 7 zur Anlage an einander gegenüberliegende Oberflächen eines oder mehrerer Werkstücke vorgesehen sind.

Das zweite Schulterelement 7 weist ähnlich wie das erste Schulterelement 5 in der zweiten Anlagefläche 29 ein zweites ringförmiges Zwischenstück 31 auf. Das zweite Zwischenstück 31 dient hierbei nicht nur als thermisches Entkopplungselement zwischen Stift 3 und zweitem Schulterelement 7 bzw. zweiter Anlagefläche 29, sondern auch als keramisches Gleitlager für den gegenüber dem zweiten Schulterelement 7 rotierenden Stift 3. Keramische Gleitlager weisen eine hohe Festigkeit und

gleichzeitig eine hohe Temperaturbeständigkeit auf, was Voraussetzung für ein Lager ist, das bei der vorliegenden Erfindung eingesetzt werden kann.

Wie aus Fig. 2 ersichtlich, umfasst das zweite Schulterelement 7 ferner einen im Wesentlichen zylindrischen Träger 33, der das freie Ende 13 des Stiftes 3 konzentrisch bezüglich der Drehachse 9 umgibt und der über Kugellager 35 frei drehbar mit der Seitenwandung 25 der Hülse 23 verbunden ist. In dem vorliegenden Ausführungsbeispiel sind zur drehenden Lagerung des zweiten Schulterelements 7 an dem Stift 3 zwei Kugellager 35a, 35b vorgesehen, die in axialer Richtung voneinander beabstandet, im Wesentlichen parallel zueinander und senkrecht zur Drehachse 9 in der Hülse 23 zwischen der Seitenwandung 25 und dem Träger 33 angeordnet sind. Der Träger 33 weist auf seiner zum Stift 3 gerichteten inneren Oberfläche ein Innengewinde 37 auf, und der Stift 3 weist an seinem freien Ende 13 ein entsprechendes Außengewinde 39 auf, so dass der Träger 33 auf das freie Ende 13 des Stifts 3 aufgeschraubt werden kann. Dadurch ist der Stift 3 axial verstellbar mit dem zweiten Schulterelement 7 verbunden.

Der Träger 33 weist ferner eine sich senkrecht zur Drehachse 9 erstreckende Gewindebohrung 41 auf, die vorgesehen ist, um eine Fixierschraube 43 aufzunehmen, die in eingeschraubter Position an den Stift 3 anschlagen und mit diesem eingreifen kann. Das Eingreifen der Fixierschraube 43 mit dem Stift 3 dient dazu, die axiale Position des Trägers 33 in Bezug auf den Stift 3 und somit auch die axiale Ausdehnung des Eingriffsabschnitts 15 bzw. den Abstand zwischen der ersten und der zweiten Anlagefläche 19, 29 einzustellen. Um die Fixierschraube 43 für eine Einstellung zugänglich zu machen, ist in der Seitenwandung 25 koaxial zu der Gewindebohrung 41 eine Bohrung 45 vorgesehen.

Die Vorrichtung 1 zum Reibrührschweißen funktioniert wie
folgt. Zunächst werden zwei zu verbindende Werkstücke an den-
jenigen Flächen, die eine Verbindung eingehen sollen, aneinan-
der angelegt (nicht dargestellt). Daraufhin wird die zuvor be-
schriebene Vorrichtung 1 zum Reibrührschweißen mit dem Ein-
griffsabschnitt 15 entlang dieser zu verbindenden Flächen be-
wegt, wobei sich der Stift 3 relativ zu dem ersten Schulter-
element 5 eine Drehung ausführt und wobei die erste und die
zweite Anlagefläche 19, 29 an den Oberflächen des Werkstücks
bzw. der Werkstücke anliegen.

Aneinander angelegt heißt hier, dass entweder zwei im Wesent-
lichen flache Werkstücke, z.B. Platten oder Bleche, entlang
ihrer Stirnseiten, d.h. in der Regel der schmaleren Seiten,
aneinander gelegt werden und an diesen Flächen verbunden wer-
den (Stumpfstoß-Verbindung). In diesem Fall verläuft die Dreh-
achse 9 des Stifts 3 während des Schweißvorgangs parallel zur
Ebene, die durch die aneinanderliegenden Flächen definiert
ist.

Es kann aber auch heißen, dass die zwei Werkstücke überlappen,
d.h. Teile der Oberflächen übereinander gelegt und dann die
jeweils angrenzenden Flächen verbunden werden (Überlapp-
Verbindung). Hier verläuft die Drehachse 9 während des Schwei-
ßens dann senkrecht zu Anlageebene. Die Vorrichtung 1 kann
dann entlang der gesamten Kontaktfläche von einem Ende der an-
einander angelegten Werkstücke zum anderen bewegt werden oder
gezielt an einzelnen Orten eingebracht werden. Der Stift 3
kann vom Rand her in die Werkstücke eingebracht werden oder
eine Bohrung kann in den Bereich der Kontaktfläche der
Werkstücke eingebracht werden, wonach das zweite Schulterele-
ment 7 von dem Stift 3 abgeschraubt wird und der Stift 3 durch
die Bohrung geführt wird. Danach wird das zweite Schulterele-
ment wieder auf den Stift 3 aufgeschraubt und mit der Fixier-
schraube 43 so fixiert, dass beide Anlageflächen 19, 29 an den

jeweiligen gegenüberliegenden bzw. voneinander wegweisenden Oberflächen der Werkstücke oder des Werkstücks anliegen.

Durch die zuvor beschriebene frei drehbare Lagerung des zweiten Schulterelements 7 an dem freien Ende 13 des Stifts 3 wird das zweite Schulterelement 7 und damit die zweite Anlagefläche 29 durch die Drehung des Stifts 3 nicht mitbewegt. Die zweite Anlagefläche 29 reibt also auch nicht an dem Werkstück bzw. den Werkstücken. Auf diese Weise wird die thermische Belastung des Stifts 3 und des zweiten Schulterelements 7 gegenüber einem Reibrührschweißwerkzeug nach dem Stand der Technik mit zwei rotierenden Schultern reduziert. Im gleichen Zug wird die mechanische Belastung des Stifts 3 vermindert, da der Stift 3 kein Drehmoment auf das zweite Schulterelement 7 übertragen muss.

Mit einem solchen Aufbau sind als Folge der zuvor genannten Merkmale höhere Geschwindigkeiten möglich, mit denen sich die Vorrichtung 1 bzw. der rotierende Stift 3 entlang der zu verbindenden Flächen bewegt. Durch die höhere Geschwindigkeit der Vorrichtung 1 wird abermals die thermische Belastung auf Stift 3, zweites Schulterelement 7 und Werkstück verringert, da der Stift 3 kürzere Zeit an einem Ort rotiert, d.h. kürzere Zeit an dem selben Material reibt. Gleichzeitig wird die thermische Belastung des Werkstücks bzw. der Werkstücke reduziert, wodurch eine höhere Qualität der Schweißverbindung erreicht wird.

Alternativ kann auch das erste Schulterelement 5 fest an dem Stift 3 gelagert werden. Damit würde dann zwar die thermische und mechanische Belastung von Stift 3, erstem Schulterelement 5 und Werkstück aus oben genannten Gründen vergrößert, aber der Aufbau im oberen Teil der Vorrichtung würde sich vereinfachen.

P 84539
31.03.2011

Patentansprüche

1. Vorrichtung (1) zum Reibrührschweißen

    mit einem um eine Drehachse (9) drehend antreibbaren Stift (3), der ein Antriebsende (11) und ein freies Ende (13) aufweist,

    wobei zwischen dem Antriebsende (11) und dem freien Ende (13) ein zylindrischer Eingriffsabschnitt (15) vorgesehen ist, der sich axial in Richtung der Drehachse (9) erstreckt und dessen Umfangsfläche (17) zum Eingriff mit einem oder mehreren Werkstücken vorgesehen ist,

    mit einem ersten Schulterelement (5), das auf der zum Antriebsende (11) weisenden Seite des Eingriffsabschnitts (15) konzentrisch bezüglich der Drehachse (9) um den Stift (3) angeordnet ist und das eine zum Eingriffsabschnitt (15) weisende sich senkrecht zur Drehachse (9) erstreckende erste Anlagefläche (19) aufweist, und

    mit einem zweiten Schulterelement (7), das auf der zum freien Ende (13) weisenden Seite des Eingriffsabschnitts (15) konzentrisch bezüglich der Drehachse (9) um den Stift (3) angeordnet ist und das eine zum Eingriffsabschnitt (15) weisende sich senkrecht zur Drehachse (9) erstreckende zweite Anlagefläche (29) aufweist,

    wobei sich die zweite Anlagefläche (29) unmittelbar bis an den Eingriffsabschnitt (15) erstreckt und

    wobei das erste Schulterelement (5) zur Anlage an die erste Oberfläche und das zweite Schulterelement (7) zur Anlage an die zweite, der ersten gegenüberliegenden Oberfläche eines oder mehrerer Werkstücke vorgesehen ist,
    dadurch gekennzeichnet,

    dass das zweite Schulterelement (7) mit dem Stift (3) frei um die Drehachse (9) drehbar verbunden ist.

2. Vorrichtung nach Anspruch 1, dadurch gekennzeichnet, dass der Stift (3) axial verstellbar mit dem zweiten Schulterelement (7) verbunden ist.

3. Vorrichtung nach Anspruch 1 oder 2, dadurch gekennzeichnet, dass das zweite Schulterelement (7) ein zweites, in der zweiten Anlagefläche (29) vorgesehenes ringförmiges Zwischenstück (31) aus Keramikmaterial aufweist und

dass das zweite Zwischenstück (31) den Eingriffsabschnitt (15) umgibt.

4. Vorrichtung nach einem der Ansprüche 1 bis 3, dadurch gekennzeichnet, dass das zweite Schulterelement (7) als Hülse (23) mit einer sich radial zur Drehachse (9) erstreckenden Bodenfläche (27) und einer zylindrischen, sich parallel zu Drehachse (9) erstreckender Seitenwandung (25) ausgebildet ist und

dass in der Bodenfläche (27) die zweite Anlagefläche (29) ausgebildet ist.

5. Vorrichtung nach Anspruch 4, dadurch gekennzeichnet, dass das freie Ende (13) des Stifts (3) von einem zylindrischen Träger (33) umgeben ist, der in axialer Richtung des Stifts (3) verstellbar ist, und

dass die Hülse (23) drehbar an dem Träger (33) gelagert ist.

6. Vorrichtung nach Anspruch 5, dadurch gekennzeichnet, dass das freie Ende (13) des Stifts (3) mit einem Gewinde (39) versehen ist und

dass der Träger (33) auf das freie Ende (13) aufgeschraubt ist.

7. Vorrichtung nach einem der Ansprüche 4 bis 6, dadurch gekennzeichnet, dass zwischen der Seitenwandung (25) und

- 3 -

dem freien Ende (13) des Stifts (3) ein Kugellager (35) vorgesehen ist.

8. Vorrichtung nach einem der Ansprüche 5 bis 7, dadurch gekennzeichnet, dass der Träger (33) eine sich senkrecht zur Drehachse (9) erstreckende Gewindebohrung (41) zur Aufnahme einer Fixierschraube (43) aufweist und

    dass in der Seitenwandung (25) der Hülse (23) eine koaxial zu der Gewindebohrung (41) ausgerichtete Bohrung (45) vorgesehen ist.

9. Vorrichtung nach einem der Ansprüche 1 bis 8, dadurch gekennzeichnet, dass der Stift (3) fest mit dem ersten Schulterelement (5) verbunden ist.

10. Vorrichtung nach Anspruch 9, dadurch gekennzeichnet, dass der Stift (3) einstückig mit dem ersten Schulterelement (5) ausgebildet ist.

11. Vorrichtung nach einem der Ansprüche 1 bis 8, dadurch gekennzeichnet, dass der Stift (3) frei um die Drehachse (9) drehbar mit dem ersten Schulterelement (5) verbunden ist.

12. Vorrichtung nach Anspruch 11, dadurch gekennzeichnet, dass das erste Schulterelement (5) ein erstes ringförmiges Zwischenstück (21) aus Keramikmaterial aufweist und

    dass das erste Zwischenstück (21) den Eingriffsabschnitt (15) umgibt.

13. Vorrichtung nach Anspruch 11 oder 12, dadurch gekennzeichnet, dass der Stift (3) axial verschiebbar mit dem ersten Schulterelement (5) verbunden ist.

P 84539
31.03.2011

Zusammenfassung

Dargestellt und beschrieben ist eine Vorrichtung (1) zum Reibrührschweißen mit einem drehend antreibbaren Stift (3), der ein Antriebsende (11) und ein freies Ende (13) aufweist, wobei zwischen dem Antriebsende (11) und dem freien Ende (13) ein zylindrischer Eingriffsabschnitt (15) vorgesehen ist, mit einem ersten Schulterelement (5), das auf der zum Antriebsende (11) weisenden Seite des Eingriffsabschnitts (15) konzentrisch bezüglich der Drehachse (9) um den Stift (3) angeordnet ist und das eine zum Eingriffsabschnitt (15) weisende sich senkrecht zur Drehachse (9) erstreckende erste Anlagefläche (19) aufweist, und mit einem zweiten Schulterelement (7), das auf dem zum freien Ende (13) weisenden Seite des Eingriffsabschnitts (15) konzentrisch bezüglich der Drehachse (9) um den Stift (3) angeordnet ist und das eine zum Eingriffsabschnitt (15) weisende sich senkrecht zur Drehachse (9) erstreckende zweite Anlagefläche (29) aufweist. Die Aufgabe, eine Vorrichtung (1) zum Reibrührschweißen bereitzustellen, mit der die mechanische und thermische Belastung des Stiftes (3) sowie die thermische Belastung der Werkstücke reduziert werden, wird dadurch gelöst, dass das zweite Schulterelement (7) mit dem Stift (3) frei um die Drehachse (9) drehbar verbunden ist.
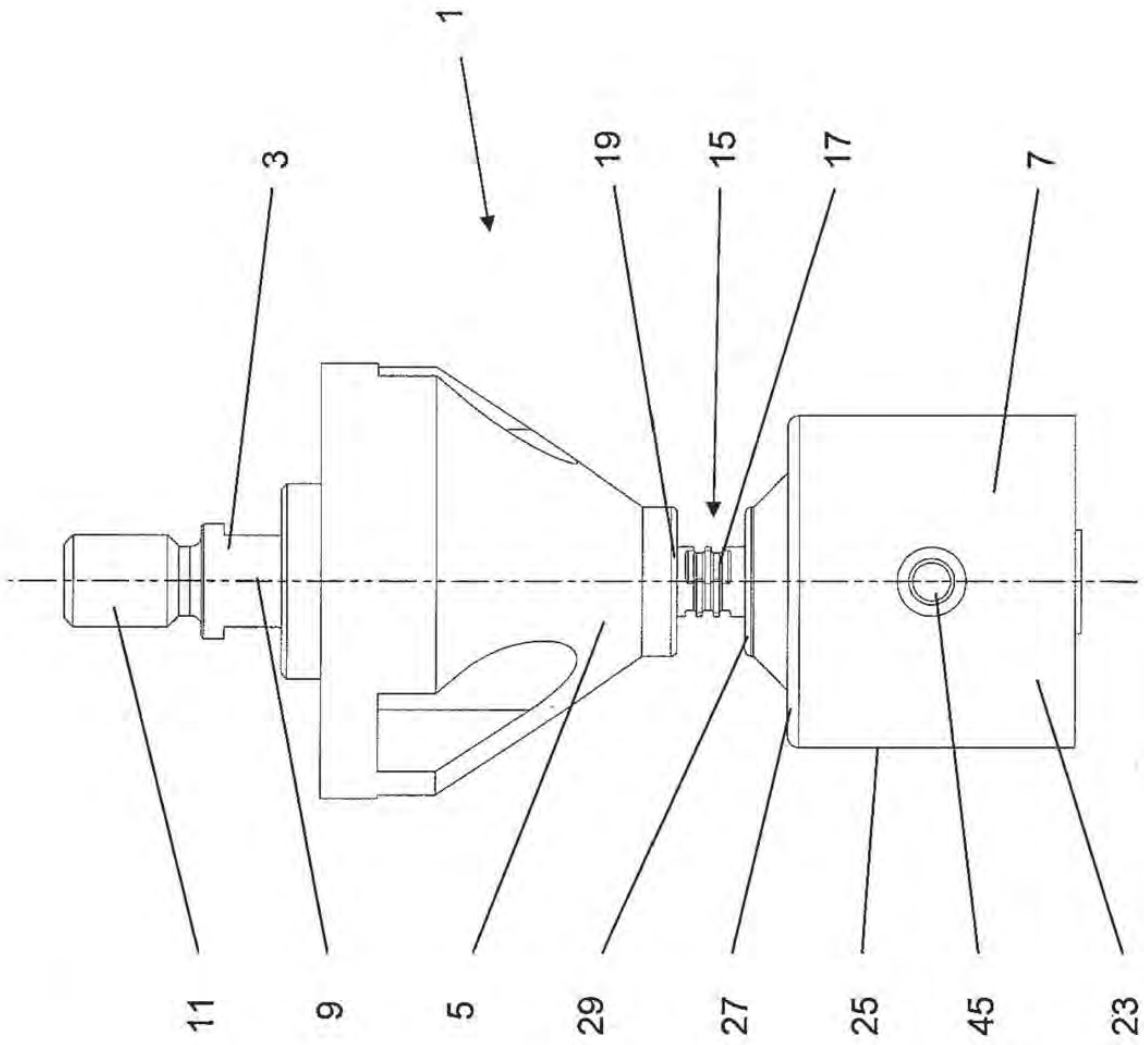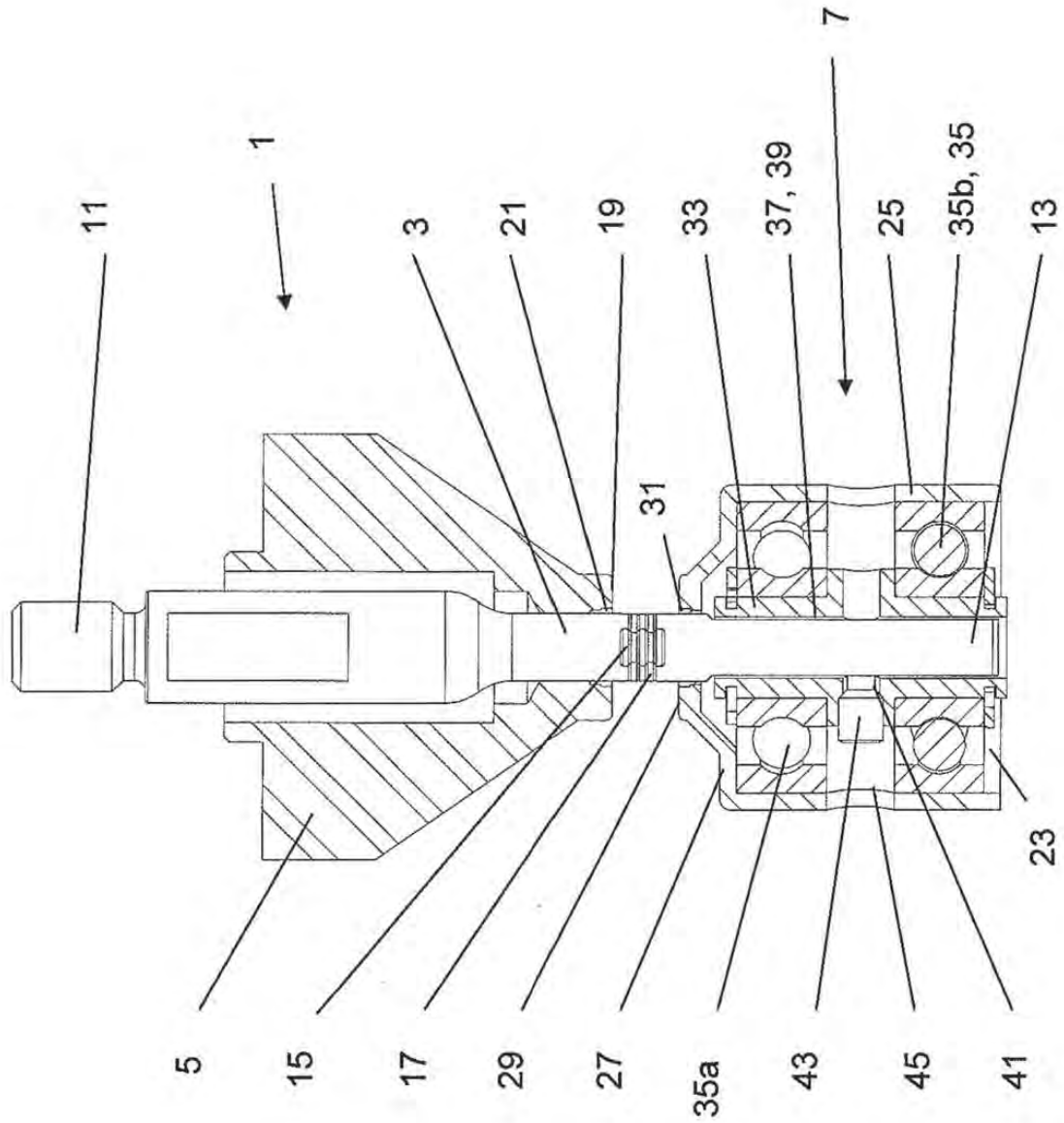
[Fig. 2]

1/2

Fig. 1

Fig. 2

Appendix C

AMGM Source Code

Listing C.1: code

```java
1  // java standard APIs
2  import java.util.*;
3  import javax.swing.*;
4  import java.net.*;
5  import java.lang.reflect.*;
6
7  // comsol APIs
8  import com.comsol.model.*;
9  import com.comsol.model.util.*;
10
11
12 public class MG_AMGM {
13
14   // static variables to save data inbetween mapping steps
15   static String[] args;
16   static MG_frame_adapter frame; // peer to graphical output window for user
          communication
17   static HashMap hash;   // persistent data stored inbetween mapping steps
18
19   // convenience call
20   public static void main(String[] a) {
21     args=a;
22     run();
23   }
24
25   // main work is done here
26   public static Model run() {
27     frame=new MG_frame_adapter(); // connect to graphical output peer
28     frame.setVisible(true);
29     frame.log("\r\n-running_AMGM-\r\n");
30     String tag = System.getProperty("cs.currentmodel");
```

```java
31    Model model = ModelUtil.model(tag); // get the COMSOL model object by the
          currentmodel property
32    hash=frame.getHash(); // get the persistent data hash
33    if (hash==null) {
34     frame.log("No_Hash_found...");
35     return model;
36    }
37
38    // be carefull with memory − it may be a limiting factor in large models
39    Runtime.getRuntime().gc();
40    double max=Runtime.getRuntime().maxMemory();
41    double total=Runtime.getRuntime().totalMemory();
42    double free=Runtime.getRuntime().freeMemory();
43    frame.log(String.format("free_memory:_%.2f%%_load:_%.2f%%", free/total*100.0,
          total/max*100.0));
44
45    try {
46     // figure out at which location of the weld we are
47     double MG_last=0;
48     if (hash.containsKey("MG_last")) MG_last=((Double)hash.get("MG_last")).
          doubleValue();
49     frame.log("MG_last_=_"+MG_last);
50     double MG_t=Double.parseDouble(model.param().get("MG_t"));
51     hash.put("MG_last", new Double(MG_t));
52     double MG_length=Double.parseDouble(model.param().get("MG_length"));
53     double uweld=Double.parseDouble(model.param().get("uweld_factor"));
54     double MG_end=MG_length/uweld;
55     boolean first=false;
56     if (MG_last>=MG_t) { // detect a new model run
57      frame.log("this_is_a_new_run!");
58      hash.put("MG_MAP_FAILED", new Integer(0));
59      first=true;
60     }
61
62     // in case the user wants to abbort the model run
63     if (hash.containsKey("STOP")) {
64      frame.log("**STOP_due_to_signal**");
65      return null;
66     }
67
68     frame.log("MG_t:_"+MG_t +"_(end:_" + MG_end + ")"+ "_=_"+String.format("%.2
          f%%",MG_t/MG_end*100.0));
69
70     SolverSequence solvestep = model.sol(args[0]); // find the COMSOL solution
          step from the calling arguments
71     SolverSequence init = model.sol(args[1]); // find the COMSOL initialisation
          step from the calling arguments
```

```
72    frame.log("start_running_init:_");
73    init.runAll(); // run the initialisation step in COMSOL
74    frame.log("done_running_init:_");
75
76    // if this is not the first step mapping of the previous results is needed
77    if (!first) {
78     map();
79    }
80
81    frame.log("start_running_solvestep_(extern)_");
82
83    // once again free as much as possible memory and clean up
84    Runtime.getRuntime().gc();
85    max=Runtime.getRuntime().maxMemory();
86    total=Runtime.getRuntime().totalMemory();
87    free=Runtime.getRuntime().freeMemory();
88    frame.log(String.format("free_memory:_%.2f%%__load:_%.2f%%_", free/total
          *100.0, total/max*100.0));
89    frame=null;
90    hash=null;
91    args=null;
92    }
93   catch(Exception e){
94    frame.log("AMGM_ERR:_"+e.toString());
95    for (StackTraceElement se : e.getStackTrace() ) frame.log("=>_"+se.toString
          ());
96   }
97   return model;
98  }
99
100 // mapping of the results is done here
101 static void map() {
102  frame.log("");
103  frame.log("MAPPING");
104  String tag = System.getProperty("cs.currentmodel");
105  Model model = ModelUtil.model(tag);
106  try {
107
108   // get all relevant data of the current soulution and new mesh and print
          some information for the user
109   SolverSequence source = model.sol(args[0]); // here is the old solution in
          the old mesh
110   SolverSequence target = model.sol(args[1]); // here is the new mesh waiting
          for a initial value to be mapped
111   String[] pnames = source.getPNames();
112   for (String s : pnames) System.out.println("pname:_"+s);
113   double[] U = target.getU();
```

```
114    frame.log("Target_vector_length:_"+U.length);
115    XmeshInfo xmi = target.xmeshInfo();
116    XmeshInfoDofs dofs = xmi.dofs();
117    String[] names = dofs.dofNames();
118    double[][] coords = dofs.coords();
119    frame.log("Target_coords_size:_"+coords.length+",_"+coords[0].length);
120    for (int i=0;i<coords.length;i++) for (int j=0; j<coords[0].length; j++)
           coords[i][j] *= 1000.0;
121    frame.log("Target_coords_mm=>m_");
122    int[] inames = dofs.nameInds();
123    double[] pvals = source.getPVals();
124    double pval=pvals[pvals.length-1];
125    pvals = new double[1];
126    pvals[0]=pval; //keep only last pval...
127    String[] expr = new String[1];
128    expr[0]="T";
129    double[] times=new double[1];
130    times[0]=pval;
131    frame.log("pval_(t):_"+pval);
132    HashSet<String> tags = new HashSet<String>(Arrays.asList(model.result().
           numerical().tags()));
133
134    // clean up older interpolation features in COMSOL and generate a new one
135    if (tags.contains("MG_map_interp")) {
136     model.result().numerical().remove("MG_map_interp");
137    }
138    if (tags.contains("MG_map_interp_")) {
139     model.result().numerical().remove("MG_map_interp_");
140    }
141    tags = new HashSet<String>(Arrays.asList(model.result().dataset().tags()));
142    if (tags.contains("dsetx")) {
143     model.result().dataset().remove("dsetx");
144    }
145    model.result().dataset().create("dsetx", "Solution");
146    model.result().dataset("dsetx").set("solution", source.tag());
147    model.result().numerical().create("MG_map_interp","Interp");
148
149    // configure the interpolation
150    model.result().numerical("MG_map_interp").set("expr", expr);
151    model.result().numerical("MG_map_interp").set("matherr", "on");
152    model.result().numerical("MG_map_interp").set("t", times);
153    model.result().numerical("MG_map_interp").set("coord", coords); // these are
           the coordinates of the new mesh
154    model.result().numerical("MG_map_interp").run();
155
156    // interpolate the values of the previous solution at the locations of the
           new mesh
```

```
157    double [][][][] result=model.result().numerical("MG_map_interp").getData();
158
159    // check all values for NaN results − these occure at geometry mismatches
           due to discretisation
160    int Nresult=model.result().numerical("MG_map_interp").getNData();
161    if (Nresult>0) {
162     frame.log("NData:␣"+Nresult);
163     int cnt=0;
164     int nan_cnt=0;
165     int inf_cnt=0;
166     int failed_cnt=0;
167     for (int i=0; i<U.length; i++) {
168      if (names[inames[i]].endsWith(".T")) {
169       U[i]=result[0][0][i];
170       if (Double.isNaN(U[i])) {
171
172        // if we are here we have mapping problems due to NaN results we fix
               them by searching the close vicinity of the desired location
173        nan_cnt++;
174        frame.log("");
175        frame.log("=>␣problem␣at␣"+i);
176        int p_cnt=0;
177        outer:for (double step=0.05;step<0.5;step*=2) { //iterate over step
178         for (int c_ind=0; c_ind<3;c_ind++){  //iterate over x,y,z
179          for (int sign=1; sign>−2; sign−=2) {  //iterate over sign
180
181           // another oppertunity to stop here
182           if (hash.containsKey("STOP")) {
183            frame.log("**STOP␣due␣to␣signal**");
184            return;
185           }
186
187           // interpolate values in the vicinity of the mesh point
188           p_cnt++;
189           model.result().numerical().create("MG_map_interp_","Interp");
190           try {
191            double[][] coords_=new double[3][2];
192            double[][][][] result_=null;
193            for (int j=0;j<3;j++) coords_[j][0]=coords[j][i];
194            coords_[c_ind][0] += (step*sign);
195            //frame.log(" => change coords ["+c_ind+"] by ("+(step*sign)+"): "+
                 coords_[0][0]+", "+coords_[1][0]+", "+coords_[2][0]);
196            model.result().numerical("MG_map_interp_").set("expr", expr);
197            model.result().numerical("MG_map_interp_").set("matherr", "on");
198            model.result().numerical("MG_map_interp_").set("t", times);
199            model.result().numerical("MG_map_interp_").set("coord", coords_);
200            model.result().numerical("MG_map_interp_").run();
```

```
201             result_=model.result().numerical("MG_map_interp_").getData();
202             U[i]=result_[0][0][0];
203          }
204        catch(Exception e){
205          frame.log("MG_MAP_INNER_ERR: "+e.toString());
206          for (StackTraceElement se : e.getStackTrace() ) frame.log("=> "+se.
                toString());
207        }
208        model.result().numerical().remove("MG_map_interp_");
209        if (!Double.isNaN(U[i])) {
210          frame.log("  => solved after "+p_cnt+" attempts");
211          break outer;
212        }
213
214          }
215        }
216      }
217
218      // if all fails the default is zero - if this happens check the model
            for discontinuities - then rerun
219      if (Double.isNaN(U[i])){
220        failed_cnt++;
221        frame.log("map failed => use 0");
222        U[i]=0;
223      }
224    }
225    cnt++;
226    }
227    }
228
229    // create new solution object from the found values and inform the user
230    target.setU(U);
231    target.setPNames(pnames);
232    target.setPVals(pvals);
233    target.createSolution();
234    frame.log("mapped.... dofs: "+cnt);
235    frame.log("Nan count: "+nan_cnt+ " Failed: "+failed_cnt);
236    int failed_before=((Integer)hash.get("MG_MAP_FAILED")).intValue();
237    hash.put("MG_MAP_FAILED",new Integer(failed_cnt+failed_before));
238    if ((failed_cnt+failed_before)>0) frame.log("SOME MAP STEPS HAVE FAILED!!!"
          );
239  }
240  else frame.log("nothing found...");
241  }
242  catch(Exception e){
243    frame.log("MG_MAP_ERR: "+e.toString());
```

```
244     for (StackTraceElement se : e.getStackTrace() ) frame.log("=>_"+se.toString
            ());
245   }
246   frame.log("");
247  }
248 }
```

Appendix D

Overview: Numerical Models of FSW

Author	Year	Description
Frigaard et al. [1]	2001	layered squares heat source
Chao et al. [114]	2003	standard linear heat source
Schmidt et al. [59]	2004	advanced heat generation and distribution
Schmidt et al. [61]	2005	overview on analytical heat sources
Rajesh et al. [115]	2007	3d analytical heat source

Table D.1: Selected References on Analytical Heat Source Models

Author	Year	Description	Code
Frigaard et al. [1]	2001	layered squares heat source	MATLAB
Chao et al. [114]	2003	including 3d tool	ABAQUS
Khandkar et al. [77]	2003	moving linear heat source	ABAQUS
Zhu et al. [116]	2004	inverse modeling	WELDSIM
Pew [74]	2006	empirical torque based model	custom
Rajesh et al. [115, 117]	2007	FEA using zone based analytical model	-
Zhang et al.[78, 78, 118]	2008	using Coulomb's friction	ABAQUS EXPLICIT
Schmidt et al. [64]	2008	advanced TMP model	COMSOL

Table D.2: Overview of the Available Numerical Thermal Models

Author	Year	Description	Code
Colegrove et al. [67]	2003	solid and liquid regions	FLUENT
Colegrove et al. [68]	2005	2d tool	FLUENT
Colegrove et al. [22]	2005	including tool	FLUENT
Schmidt and Hattel [62]	2005	2d tool	COMSOL
Colegrove et al. [69]	2005	including rotating tool	FLUENT
Colegrove et al. [70]	2005	2d-3d coupling	COMSOL
Atharifa et al. [11]	2008	including threaded tool, skew, sticking and sliding	FLUENT

Table D.3: Overview of the Available Flow Models

Author	Year	Description	Code
Xu et. al. [88]	2001	simple flow model	ABAQUS
Schmidt et.al. [60]	2005	ALE with coulomb friction	ABAQUS EXPLICIT
Buffa et al. [86]	2006	coupled, viscoplastic material	DEFORM
Uyyuru et al. [7]	2006	simple geometry, plastic material	DEFORM
Zhang et. al. [89]	2007	ALE flow with re-meshing and cut-off-friction	ABAQUS
Zhang et al.[78, 90, 118]	2008	investigating Coulomb's friction	ABAQUS EXPLICIT
Guerdoux et. al. [87]	2009	ALE with adaptive re-meshing	FORGE3

Table D.4: Overview of the Mechanical Deformation Models

Appendix E

Publications

Many aspects of the thesis have been published or are presently being published. A list of these publications follows:

Journal

[j1] J. Hilgert, J.F. dos Santos, and N. Huber. Shear layer modelling for bobbin tool friction stir welding. *Science and Technology of Welding and Joining*, 17(6):454–459, 2012.

[j2] J. Hilgert, H.N.B. Schmidt, J.F. dos Santos, and N. Huber. Thermal models for bobbin tool friction stir welding. *Journal of Materials Processing Technology*, 211(2):197 – 204, 2010.

Accepted by Journal

[sj1] L.L. Huetsch, J. Hilgert, K. Herzberg, J.F. dos Santos, and N. Huber. Temperature and texture development during high speed friction stir processing of magnesium az31. *Materials Science and Engineering A*, -:–, 2012.

Int. Conference (Peer Reviewed)

[icp1] J. Hilgert, H.N.B. Schmidt, J.F. dos Santos, and N. Huber. *Mathematical Modelling of Weld Phenomena 9*, chapter Moving Geometry Process Model for Bobbin-Tool FSW. Verlage der Technischen Universität Graz, 2010.

Int. Conference

[ic1] J. Hilgert, J.F. dos Santos, and N. Huber. Numerical simulation in bobbin tool fsw process development. In *Proceedings of the 9th International Symposium on Friction Stir Welding 2012*, 2012.

[ic2] J. Hilgert, J.F. dos Santos, and N. Huber. *Friction Stir Welding and Processing VI*, chapter Investigation of the Material Shear Layer in Bobbin Tool Friction Stir Welding, pages 187–193. TMS, 2011.

[ic3] J. Hilgert, L.L. Huetsch, J.F. dos Santos, and N. Huber. Material flow around a bobbin tool for friction stir welding. In *COMSOL Conference 2010, Paris*, 2010.

[ic4] J. Hilgert, H.N.B. Schmidt, J.F. dos Santos, and N. Huber. Moving geometry process model for bobbin tool FSW. In *Proceedings of the 8th International Symposium on Friction Stir Welding 2010*, 2010.

[ic5] J. Hilgert, H.N.B. Schmidt, and J.F. dos Santos. Bobbin tool FSW - a moving geometry model. In *COMSOL Conference 2009, Milano*, 2009.